MANIPULATION AND DETECTION OF SUPERPARAMAGNETIC BEADS WITH SPIN-VALVES

by

WENDY R. ALTMAN

B.S.E., Mercer University, Macon, Georgia, 2003

M.S., University of Colorado, 2009

A thesis submitted to the

Faculty of the Graduate School of the

University of Colorado in partial fulfillment

of the requirement for the degree of

Doctor of Philosophy

Department of Mechanical Engineering

2011

This thesis entitled:

Manipulation and Detection of Superparamagnetic Beads with Spin-Valves

written by Wendy R. Altman

has been approved for the Department of Mechanical Engineering

____

Victor M. Bright

____

Y.C. Lee

Date_____________

The final copy of this thesis has been examined by the signatories, and we find that both the content and the form meet acceptable presentation standards of scholarly work in the above mentioned discipline.

Altman, Wendy R. (Ph.D., Mechanical Engineering)

Manipulation and Detection of Superparamagnetic Beads with Spin-Valves

Thesis directed by Professor Victor M. Bright and Dr. John Moreland.

This work describes a new magnetic manipulation technique to trap, release, transport, and detect superparamagnetic beads (SPBs) with low-power and addressable spin-valves (SVs). Functionalized SPBs are used as "mobile substrates" or magnetic tags in numerous bioassays. Examples of applicable bioassays include protein and DNA purification, cell fractionation, enzyme immobilization, and immunoassays. SV technology is based on the giant magnetoresistance (GMR) effect and is commonly used in high-density magnetic recording heads and magnetic field sensors. The SV consist of two magnetic layers separated by a spacer layer. An antiferromagnetic (AFM) layer pins the magnetization of one ferromagnetic (FM) layer in one direction while the other FM layer remains free to rotate. When the two layers are parallel (low resistance state), the high magnetic field gradient will attract and trap a SPB. When the two layers are antiparallel (high resistance state), the gradient is low and the SPB will no longer be attracted to the SV; the SPB will be released. In addition to SPB capture and release, the stray fields from a trapped and magnetized SPB affect the SV resistance response, thus a trapped SPB can be detected. The scope of this thesis includes the design, fabrication, and characterization of the microfluidic and micro-electromechanical system (MEMS) to manipulate and detect SPBs with nonvolatile and locally addressable SVs.

DEDICATION

I would like to dedicate this work to my wonderful husband Eric. This work could not have been completed without his love, support, and extreme patience.

ACKNOWLEDGEMENTS

I would like to thank Professor Victor. M. Bright, my academic advisor and committee chairman, as well as my NIST advisors, Dr. John Moreland and Dr. Steven E. Russek, for their encouragement, support, and guidance. I am indebted to Prof. Y.C. Lee and Prof. Mark Borden for graciously serving on my committee. As a graduate student, I was fortunate and grateful to have access to the terrific facilities and personnel at the National Institute of Standards and Technology (NIST) through the NIST Professional Research Experience Program (PREP). I would like to especially thank Dr. Gary Zabow, Dr. Li-Anne Liew, Dr.^{2} Justin Shaw, Dr. Robert Usselman, Dr. Ranko Heindl, Dr. William Rippard, Dr. Mike Boss, Dr. Jay Koch, Dr. James Beall, Dr. Gene Hilton, Dr. Leila Vale, and Dr. Tom Cecil for their research advice and assistance in the cleanroom and laboratory. Also, I would like to thank Tony Kos for all his help with the hardware and computer equipment. The microfluidic component of this research was enhanced with the assistance of our Summer Undergraduate Research Fellowship (SURF) intern, Bruce Han.

TABLE OF CONTENTS

CHAPTER 5: SV CHARACTERIZATION 106

CHAPTER 6: SUPERPARAMAGNETIC BEAD (SPB) MANIPULATION ..123

LIST OF TABLES

LIST OF FIGURES

CHAPTER 1: INTRODUCTION

Thesis Goal

The goal of this thesis is to demonstrate the feasibility of using low power and individually addressable spin-valve (SV) devices for both manipulation and detection of functionalized micro-sized superparamagnetic beads (SPBs). Other research groups have focused on using the SV solely for sensing or detecting SPBs by means of the SV's magnetoresistance (MR) properties [1-8]; however, the focus of this work is to demonstrate both SPB manipulation and detection with SVs addressed locally by read lines and write lines. The magnetic hysteresis of the SV is harnessed to attract or release the SPB and the MR of the same SV is used to detect the SPB.

As depicted in Figure 1 (a), the SV consists of pinned (M_P) and free (M_F) magnetic layers separated by a metal spacer. The pinned layer on the bottom of the SV stack is biased with an antiferromagnet and requires a large applied magnetic field to change polarity. The unbiased free layer will change polarity in response to a low applied field. Figure 1 (b) illustrates a SV with both read and write lines. The SV's GMR is measured by means of the read line with sense current (i_r) and the SV is switched between low-resistance ON (M_F parallel to M_P) and high-resistance OFF (M_F antiparallel to M_P) states with a write-line current (i_w). The read-line GMR signal relays the SV state and, in tandem with an external in-plane bias field ($B_\perp$), establishes whether the ON SV is occupied by a SPB or vacant. The stray fields from the magnetized SPB alter the free-layer's switching properties and this change is detected by measuring the GMR. The field B|| globally switches all the arrayed SVs ON or OFF.

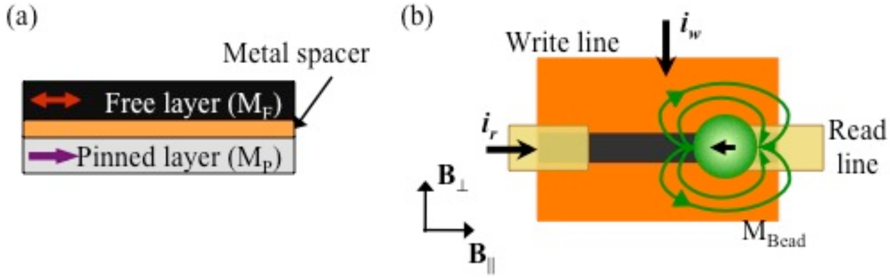

Figure 1: (a) Side view of SV stack consisting of magnetic free (M_F, thin-red arrow) and pinned (M_P, thick-purple arrow) layers separated by a metal spacer, (b) top-view illustration of a SV addressed with i_r, $B_{||}$, and i_w and showing the stray fields from a trapped SPB.

A schematic depicting SPB capture and release by means of an addressable SV is shown Figure 2. When the SV is ON (open magnetic flux), the SPB is attracted to the high magnetic field gradient located at both blunt ends of the SV. When the SV is OFF (closed magnetic flux), there is no longer a high magnetic field gradient located at both blunt ends of the SV resulting in the release of the SPB.

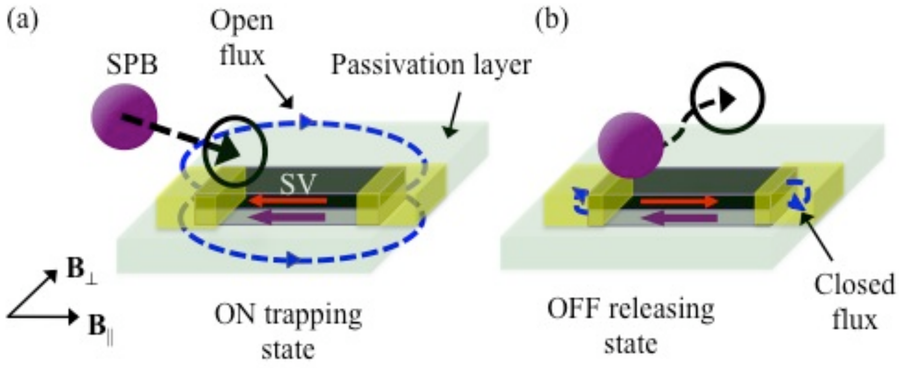

Figure 2: (a) SPB is attracted to and trapped by the ON SV's open magnetic flux, (b) SPB is released when the SV is turned OFF due to a lack of open flux.

Motivation

Precision control and detection of tagged biomolecules by means of surface functionalized magnetic beads in suspension will lead to considerable advancements in the fields of biotechnology, nanochemistry, and nano-medicine. Already, micro- and nano-sized SPBs are used for DNA purification, cell fractionation or selection, enzyme immobilization or biocatalysis, immunoassays, magnetic affinity chromatography, impurity extraction (*i.e.*, viruses from water), and magnetic support [9-10]. Pharmaceutical industries are interested in using magnetic systems to study the effects of drugs or external stimuli on cells [11]. High quality sperm fraction was demonstrated with SPBs; fraction isolates healthy spermatozoa from apoptic ones based on the intact membranes [12-13]. In biophysics, the SPBs can be used to position and manipulate biomolecules to study their molecular structure, structural organization, enzyme kinetics, and dynamic behavior. Finally, national security organizations are interested in magnetic systems for detection of hazardous chemical and biological warfare agents [14].

Biomolecule manipulation within a lab-on-a-chip (LOC), point-of-care (POC) device, or micro-total analysis systems (μTAS) can provide clinicians, doctors, scientists, and security personnel with a powerful handheld tool for diagnostics and sensing. A μTAS is a micro-electromechanical system (MEMS) capable of handling a sample from start to finish; the system both prepares and analyzes the sample.

Technologies to manipulate biomolecules include magnetophoresis, electrophoresis, and dielectrophoresis. Magnetophoresis is used to transport, stretch, twist, and uncoil biomolecules attached to a magnetic particle. Materials with different magnetic moments experience different forces when placed in a non-homogeneous magnetic field; the field gradient exerts a force on the magnetic material causing it to move. Common applications of magnetophoresis are protein purification, cell cytometry, and RNA isolation.

Electrophoresis is used to separate and analyze DNA and RNA fragments, and proteins based on size, shape, or charge. Electrophoresis is the motion of particles under the influence of a uniform electric field due to the charge difference between the particle and the surrounding fluid. The Western, Northern, and Eastern blots are common gel-electrophoresis techniques for detection of RNA, proteins, and lipids. Unlike magnetophoresis, the biomolecule of interest does not need to be attached to a carrier (e.g., SPB) to be manipulated.

Dielectrophoresis is the motion of dielectric particles under the influence of a non-uniform electric field. For a particle to be dielectric, it does not need to be charged, but it will need to be polarized. Because biological cells have dielectric properties, dielectrophoresis can be used to manipulate, transport, separate, and sort cells (e.g., cytometry). Optical tweezers [15] employ dielectrophoresis to manipulate biomolecules [16], to sort and classify cells [17], for cell fusion [18], and for intracellular surgery [19]. A dielectric bead can be trapped and manipulated by an extremely focused Gaussian laser beam; however, the laser can cause unwanted heating. Furthermore, the force and displacement are limited.

Magnetophoresis has some advantages over dielectrophoresis and electrophoresis. As the majority of biological materials are not magnetic (excluding red blood cells [20], ferritin, and magnetobacterium), magnetic manipulation has the advantage of being independent of the biological and chemical processes being evaluated [21-22]. In addition, magnetic beads are ideal for manipulating biomolecules and cells due to their comparable size scales: commercially available SPBs range from 10 nm to 5 μm in diameter, proteins are 5-50 nm, and cells are 10-100 μm [23]. Due to magnetic hysteresis, magnetic systems have the potential to enable fast, low-heat producing, and low-power consuming μ-TAS or POC devices.

Complementary metal-oxide-semiconductor (CMOS) compatible SV technology shows great potential for the control and detection of magnetic micro- and nano-SPBs in solution [24]. A small, fast, and easy-to-operate device utilizing microfluidics and MEMS technology will reduce the need for expensive and time-consuming laboratory testing. As shown in this body of work, low-power and individually addressable SV devices can capture, release, transport, and detect surface functionalized micro-SPBs suspended in solution. Already, other groups use SVs to detect single micro-SPBs and ensembles of nano-SPBs [1-8,25], but this is the first report of SPB transport by means of SVs. The long-term goal of this research is to integrate the manipulation and sensing capabilities of the SVs for nano-SPB bioassay applications.

Magnetism: A Brief Review

For over two hundred years, magnetism has been used to separate magnetic materials. In 1792, William Fullarton patented the process of separating iron minerals with a magnet for the mining industry [26]. Since then, the use of magnetism to manipulate materials has matured from the chemical and mining industries [27-29] to the biotechnology industry. Paralleling the growth of magnetic manipulation technologies, the materials manipulated have advanced from intrinsically magnetic material to surface-treated magnetic nano-structures.

The theory behind magnetic manipulation is simple. Materials with different magnetic moments experience different fields when placed in a non-homogeneous field. The magnetic field gradient exerts a force on the magnetic material inducing it to move. These field gradients are generated with permanent magnets or electromagnetic devices, such as current lines. Harnessing and sensing the field gradients within an integrated microfluidic and MEMS platform will enable precise translational and rotational control, as well as detection of SPBs for biological assays.

Magnetic Materials

The following section may be useful for readers new to the field of magnetism. If a more detailed review of magnetism is desired, please refer to the "Introduction to Magnetic Materials" by Cullity and Graham [30] or "Permanent Magnet and Electromechanical Systems" by Furlani [31].

Magnetic materials are classified by their susceptibility or the degree of magnetization a material exhibits in response to an applied field. The types of magnetic materials discussed in this research include diamagnetic, paramagnetic, ferromagnetic, antiferromagnetic, and superparamagnetic.

Diamagnetic material has a small negative susceptibility. When subjected to an applied magnetic field, the material has a weak bulk magnetization that opposes the field. All materials have diamagnetic properties even though the magnetization is most often weak.

Paramagnetic material (depicted in Figure 3) has a small positive susceptibility. In an applied magnetic field, the moment of the material will weakly align in the direction of the field. Examples of paramagnetic materials include tantalum, molybdenum, lithium, and magnesium.

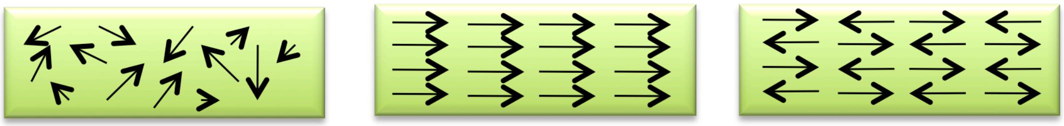

Paramagnetic Ferromagnetic Antiferromagnetic

Figure 3: Idealized atomic magnetic moments in paramagnetic, ferromagnetic, and antiferromagnetic materials.

Ferromagnetic (FM) material has a large positive susceptibility; the material retains its magnetic memory once an applied field is removed. As shown in Figure 3, the atomic moments are aligned parallel in a FM material. FM materials have two distinct properties: spontaneous magnetization and a magnetic ordering temperature. Unlike paramagnetic materials, FM materials saturate in moderate magnetic fields and at high temperatures (but below the Curie temperature). Examples of FM materials include iron, nickel, cobalt and Permalloy ($Ni_{20}Fe_{80}$).

Antiferromagnetic (AFM) material has atomic magnetic moments that align in a regular antiparallel pattern causing them to have no net magnetic moment (see Figure 3). Exchange bias or exchange anisotropy occurs in bilayers of FM and AFM thin films [32-33]. This exchange bias causes a shift in the hysteresis curve of the FM. Examples of AFM materials include IrMn, PtMn, and FeMn.

Superparamagnetism occurs only in micro[1]- and nano-particles. The nano-size of the particle allows the magnetization to randomly flip in response to thermal energy. Their magnetic susceptibility is much larger than paramagnets, thus the preface "super". As shown in Figure 4, when the particles are magnetized, they behave like magnetic dipoles and can be manipulated by magnetic field gradients. With no external field, their magnetization appears to be zero. Micro-SPBs are commonly composed of superparamagnetic nano-iron-oxide crystals embedded in a polystyrene matrix. Because the crystals may not be uniformly distributed in the matrix, the beads may not be uniformly magnetic [34]. Nano-SPBs disperse with no

---

[1] Micro-sized SPBs consisting of magnetic nano-particles embedded in a matrix are sometimes called non-remanent FM beads, not SPBs.

applied field; however, micro-SPBs tend to form chains and remain in chains once the field is removed because they have some remnance [35].

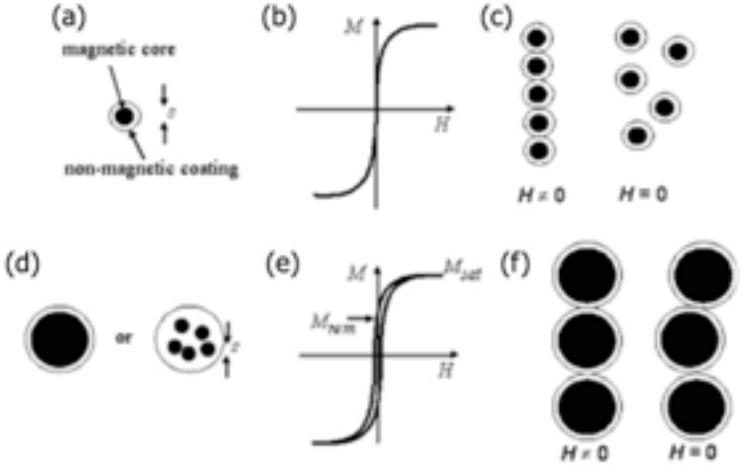

Figure 4: Difference between nano- (5-100 nm) and micro- (0.5-5 μm) SPBs. (a) One domain core of a nano-SPB, (b) Hysteresis free M-H curve of a nano-SPB, (c) Nano-SPBs disperse in no field, (d) Core of a micro-SPB, (e) M-H curve of micro-SPB with hysteresis, (f) Micro-SPB s form chains [35].

Hysteresis

Magnetic materials retain memory of an applied magnetic field after the field is removed, thus they exhibit hysteresis. A typical magnetization verses applied magnetic field curve for a FM material is shown in Figure 5. Both the major and one of the infinite minor loops (BCDE) are shown. The remnance is the magnetization of the material once the applied field is removed. The coercivity or coercive field is the magnetic field required to reduce the magnetization of the material to zero after being saturated.

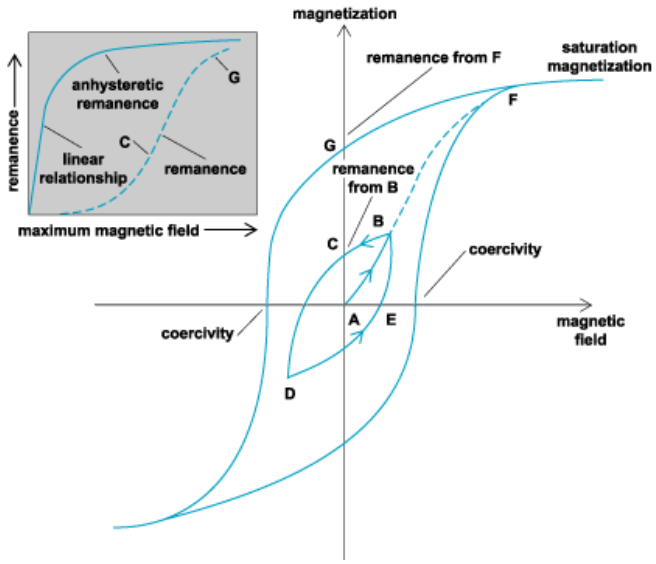

Figure 5: Typical magnetic hysteresis curve showing minor and major loops, remnance, and coercivity [36].

Giant Magnetoresistance (GMR)

Giant magnetoresistance (GMR) is a quantum-mechanical MR effect observed in thin-film structures of alternating FM and non-FM materials. In 2007, the Nobel Prize for Physics was awarded to Albert Fert [37] and Peter Grünberg [38] for discovering GMR. A significant (giant compared to resistance due to shape anisotropy) change in electrical resistance is observed when adjacent FM layers are aligned parallel or antiparallel. Figure 6 shows the GMR (shown as R/R) of Cr/Fe multilayers first deposited by the Fert group.

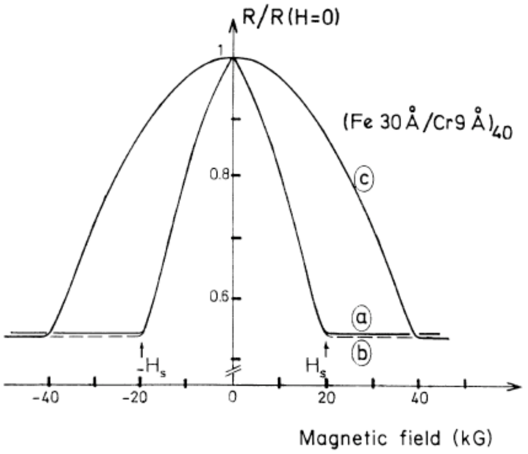

Figure 6: GMR of Fe/Cr multilayers [37].

Percent GMR is calculated by dividing the difference between the high parallel resistance and the low antiparallel resistance by the parallel low resistance (Equation 1). GMR is only observed in magnetic thin films because the layer thicknesses have to be smaller than or on the order of the mean free path for conducting electrons [39].

$$GMR = 100\frac{R_{\uparrow\downarrow} - R_{\uparrow\uparrow}}{R_{\uparrow\uparrow}} \tag{1}$$

Exchange Bias

Exchange bias or exchange anisotropy occurs in bilayers of FM and AFM thin films [32]. The moment of the FM layer couples to the moment at the interface of the AFM material, which results in the interfacial spins being pinned. This coupling causes a shift in the hysteresis curve of the FM layer (Figure 7) due to the extra energy needed to reverse both layers.

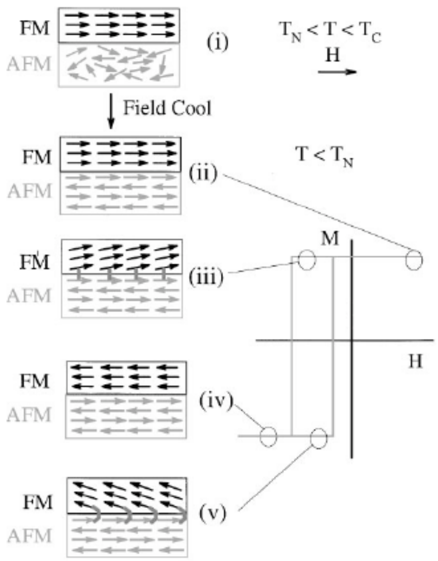

Figure 7: Spin configuration of FM and AFM bilayers exhibiting exchange bias [40].

Néel Coupling

Néel coupling (also referred to as "orange peel" coupling) occurs between sandwiched FM layers. As depicted in Figure 8, magnetostatic interactions between the free poles at the FM interfaces cause Néel coupling. This coupling results in minor loop shifts and a broadening of the hysteresis. Conformal roughness of the magnetic thin films results in higher Néel coupling [41-43].

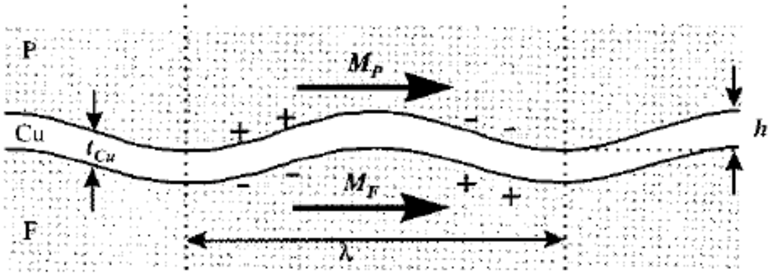

Figure 8: Néel coupling between two infinitely thick FM slabs [44].

Spin-Valves (SVs)

Spin-valves (SVs) are devices based on the GMR effect [37,45-46]. A SV consists of alternating FM and nonmagnetic layers separated by a metal spacer. When the layers are parallel, the spin-dependent scattering of the carriers is at a minimum and the resistance is low; when antiparallel, the scattering of the carriers is at a maximum and the resistance is high. The change in resistance is larger compared to the anisotropic magnetoresistance (AMR) effect, thus the preface “giant”. SVs are commonly used in high-density magnetic recording heads [47] and magnetic field sensors [48-49].

The structure and shape of the SV depends on the application. Digital SVs are composed of antiparallel or parallel alternating layers and are useful for storing bits (0s and 1s) or for this research, capturing (and storing) or releasing a SPB. Analog SVs are composed of perpendicular alternating layers and are used as sensors; the presence of an external magnetic field changes the resistance of the GMR sensor. The majority of SVs for SPB detection were analog.

The “simple” digital SVs fabricated for this research consist of two identical magnetic layers separated by a spacer layer (see Figure 9). An AFM IrMn thin film pins the magnetization of one FM layer in one direction, while the other FM layer remains free to rotate. A non-magnetic Cu spacer reduces Néel coupling between the two magnetic layers. The specific structure of our SVs is discussed in CHAPTER 3: FABRICATION and CHAPTER 6: SUPERPARAMAGNETIC BEAD (SPB) MANIPULATION.

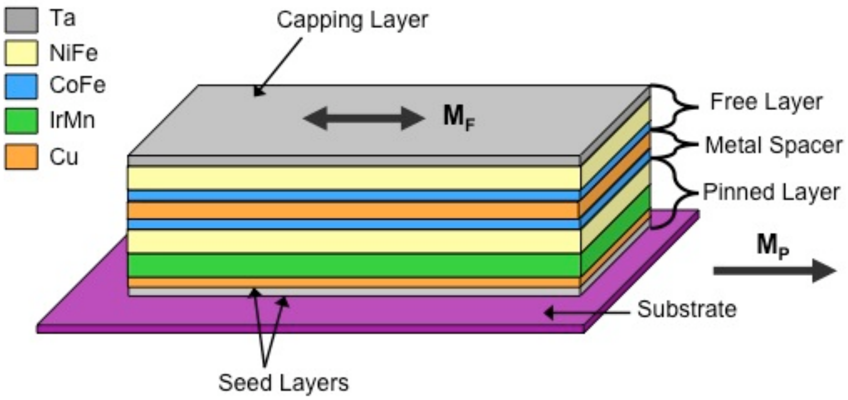

Figure 9: Anatomy of a SV illustrating the free, metal, and pinned layers. M_P and M_F represent the magnetic moments of the pinned and free layers.

In the digital conformation, the two layers prefer either the parallel (open flux) or antiparallel (closed flux) configuration. If both orientations are stable at zero applied field (bistable), then the SV can be used as a low power and programmable SPB trap. As shown in Figure 10 (a), with the SV in the parallel “ON” state, a SPB will be trapped near the high magnetic field gradient located on the SV’s blunt end. When in the antiparallel “OFF” state, the SPB will be released. In top-pin SVs, the pinned layer is on the top; in bottom-pin SVs, the pinned layer is on the bottom. Because no external magnetic field or current is required to maintain the state of the SV, this “switchable permanent magnet” is a low power and low heat alternative to other arrayed microfluidic transport devices [50-51].

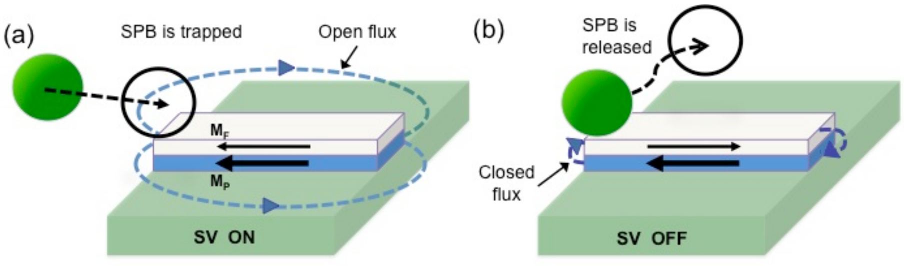

Figure 10: (a) SPB trapped by the ON SV with open flux (free layer moment M_F is parallel to pinned layer moment M_P), (b) SPB released or ignored by the OFF SV with closed flux (M_F antiparallel to M_P).

Figure 11 shows the typical GMR response from a digital SV device and the B-H loop for a typical digital SV thin film. The thick and thin arrows represent the moments of the pinned and free layers, respectively. In the GMR response shown in Figure 11 (a), the free layer switches from parallel to antiparallel at -2 mT, and from antiparallel to parallel at +8 mT. The pinned layer switches at -18 mT and -10 mT. In Figure 11 (b), the free layer switching (hysteresis centered on the y-axis) occurs at +0.5 and -1 mT. The biased pinned layer switches at -8 mT and -5 mT.

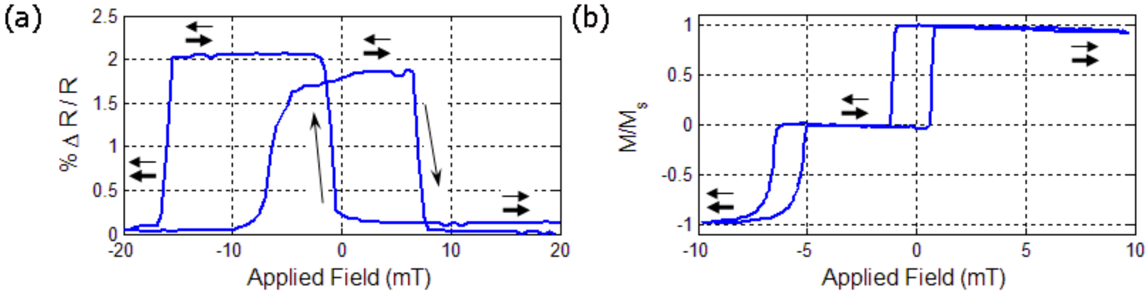

Figure 11: (a) GMR response of a digital SV, (b) B-H loop of a SV thin film. The thick and thin arrows represent the magnetic moment orientation of the pinned and free layers, respectively.

SV Layer Properties

The SV's exchange bias, GMR, diffusion, free- and pinned-layer coercivity, and Néel coupling are dependent on the layer material and thickness. For a summary of these findings, refer to Table 1.

Table 1: Summary of SV properties based on layers.

SV Property	**SV Layer Variables**
Exchange Bias Field	Inversely proportional to FM thickness. Proportional to surface roughness.
GMR	Dependent on FM thickness. Decreases with AFM thickness > 10 nm due to shunting. Inversely proportional to surface roughness caused by IrMn, thus bottom-pin SVs have lower GMR. Inversely proportional to spacer thickness.
Coercivity	Proportional to FM thickness and surface roughness.
Pull Force	Proportional to FM layer thickness.
Diffusion and Oxidation	Co reduces diffusion between Cu and Permalloy. Shorter annealing time reduces diffusion. Dependent on the thickness and type of material used to cap the stack.
Néel Coupling	Proportional to interface roughness and spacer thickness.

With magnetic thin films, seed and buffer layers are critical for controlling the structure, texture, and morphology of the magnetic medium [52]. A rougher seed layer leads to conformal roughness in all the other layers, which reduces the GMR and increases the exchange bias. Common buffer or seed layers are titanium (Ti), copper (Cu), and tantalum (Ta). The seed layer Ta greatly improves the <111> texture of Cu and IrMn [53-54]; the presence of a seed or buffer Ta layer enhances Cu and IrMn smoothness [55]. Nakagawa demonstrated that the presence of an ultra-thin Si buffer layer increased the exchange bias of their NiFe (10 nm)/FeMn (20 nm) thin film [56]. As shown in Figure 12, Nishioka's group observed an increase in the exchange coupling as the buffer layer and spacer layer increased [57]. Gong observed a maximum NiFe GMR with a 3 nm Ta buffer layer; Si and MgO could also be used a buffer layers [58].

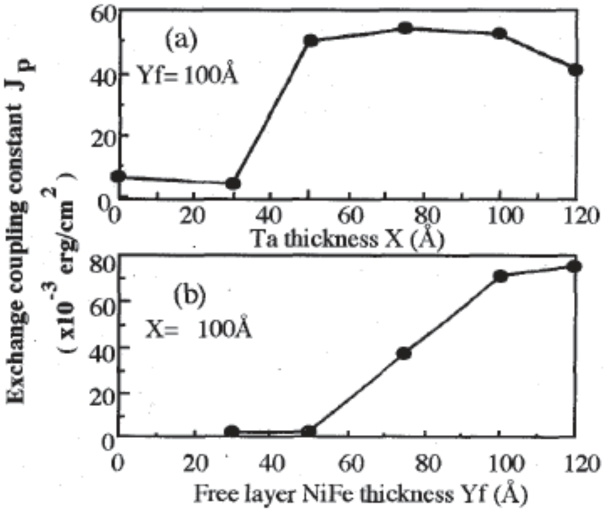

Figure 12: Ta and free-layer thickness dependence on exchange coupling [57].

AFM IrMn and PtMn are commonly used to exchange bias the FM layer. The exchange bias field is dependent on the quality of the IrMn structure [59-60]. The (111) IrMn texture greatly influences the exchange-bias field. For a SV with AFM IrMn and a free-layer Permalloy thickness of 15-20 nm, the exchange anisotropy ranges between 5-20 mT [61]. Anderson observed a critical IrMn (111) thickness of 3.5 nm and an optimal thickness of

5 nm in IrMn/CoFe systems [62]. An IrMn layer thickness above 10 nm increased current shunting resulting in reduced GMR and exchange bias [59,62]. Van Driel found a 580 K in-field anneal increased the exchange bias by 50% (see Figure 13).

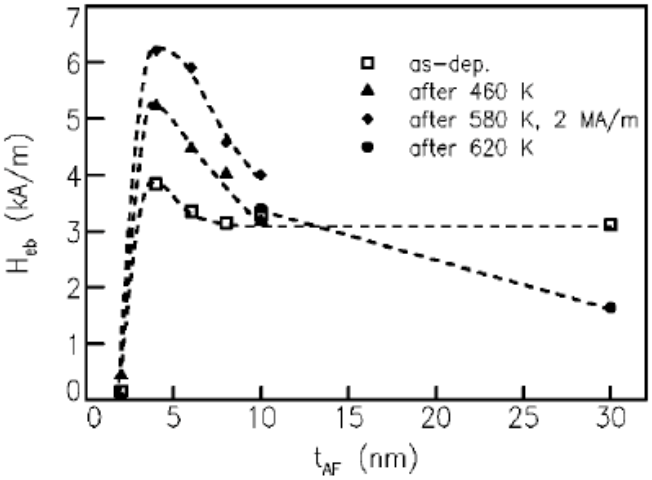

Figure 13: IrMn exchange bias as a function of thickness and anneal [60].

AFM IrMn has a face-centered-cubic (fcc) structure and good pinning profile, but a relatively low coercivity and blocking temperature [62]. The Mn in IrMn [63] and PtMn is prone to oxidation; oxidation will decrease GMR and increase Néel coupling between the layers. PtMn has better corrosion resistance and exchange coupling compared to IrMn, but it requires a higher temperature anneal after deposition to achieve the correct crystal structure [64]. This higher temperature could be detrimental to the other SV layers.

Devasahayam found that exchange bias increased with increasing DC-magnetron-sputtering pressure for the magnetic and buffer layers; a poor texture corresponded to a large exchange field [65].

For SPB trapping, a thicker FM layer will increase the magnetic pull force of the SV device. However, the desire for a high-force trap must be balanced with the other properties of the SV, such as exchange bias and coercivity. The exchange-bias field is inversely proportional to the thickness of the FM material [66-67]. Common FM layers are Co, $Co_{90}Fe_{10}$, and Permalloy ($Ni_{80}Fe_{20}$). As shown in Figure 14, Thanh observed that a Permalloy thickness greater than 6 nm led to a reduction of the exchange-bias field in a top IrMn SV [68]. Increasing the thickness of a FM Co90Fe10 layer reduced the GMR [69].

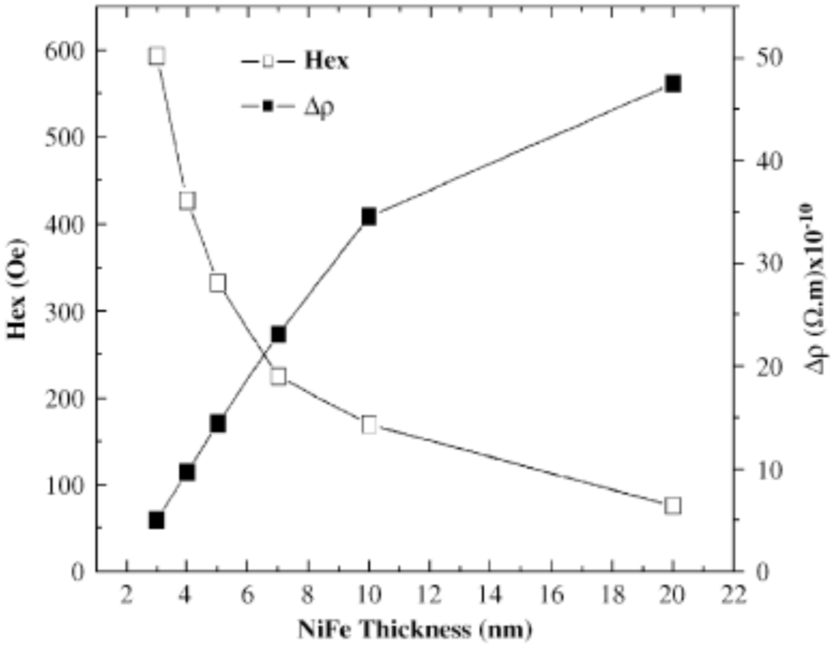

Figure 14: Exchange bias due to NiFe thickness in a NiFe/IrMn system [68].

The thickness of the spacer should be large enough to restrict FM exchange coupling via pinholes between the free and pinned layers; however, some coupling is necessary to maintain the SV's parallel and antiparallel states. The GMR ratios followed an exponential decay as the Cu spacer thickness increased [70-71]. This decrease was due to reduced magnetic coupling between the layers. Dieny found that GMR decreased exponentially with increasing spacer-layer thickness and an ~8 µm free-layer thickness was optimal [72]. Similarly, Hung observed a decrease in the MR for NiFe/IrMn Hall sensors as the thickness of the NiFe free layer increased [73]. Nishioka's group observed an increase in the exchange coupling as the spacer thickness increased [57].

CoFe has a high magnetization and is immiscible with Cu resulting in reduced interfacial diffusion and better thermal stability in SVs [74-77]. Additionally, Parkin demonstrated that Co greatly enhanced the MR [78]. However, the addition of Co also increased the coercivity and lowered the permeability [79].

The SV is capped to protect the magnetic layers from oxidation and corrosion. As shown in Figure 15, Hawraneck found that the GMR of SVs with a 5 nm Ta cap degraded over only 5 hours at 300°C due to oxidation [80]. Annealing sped up the GMR degradation due to interdiffusion between the layers; a 10 nm TaN cap preserved the GMR for the longest time. As expected, interdiffusion led to more surface roughness resulting in more Néel coupling between layers. With devices that switch at low fields, it is desirable to minimize the Néel coupling. An additional conductive capping layer of ruthidium (Ru) improved the GMR.

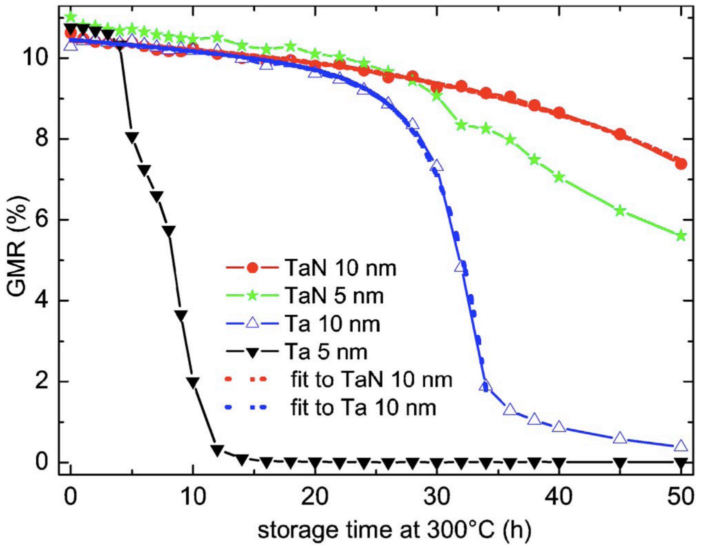

Figure 15: Degradation of SVs with different capping layers [80].

The sputtering conditions greatly influence the switching characteristic of the SV thin film. Hayashi demonstrated that deposition rates were linearly proportional and the saturation magnetization was inversely proportional to the sputtering gun power [81]. Additionally, they showed that the argon partial pressure affected the deposition rate and film composition. Li and Yang observed that a higher power and sputtering pressure resulted in larger NiFe grains and coercivity [82]. Chan and Tao found that a higher Cu sputtering power resulted in a higher deposition rate; low-power deposition resulted in poor microstructure [83]. Similarly, low argon pressures enhanced the Cu film crystallinity by forming larger grains [84]. Mao found that a low base pressure minimized impurities in the thin film [85].

Additionally, the sputtering and patterning of magnetic structures presented a challenge due to surface roughness and edge effects. Surface roughness produces unwanted high exchange bias, low GMR, and multi-domain magnetic structures. Edge effects can result in multi-domain devices.

Top-Pin and Bottom-Pin SVs

Anderson evaluated the differences between top-pin and bottom-pin CoFe/IrMn SVs [59]. Post-deposition annealing was necessary for good exchange bias and improved GMR in bottom-pin SVs, but detrimental to the GMR and exchange bias in top-pin SVs. In general, bottom-pin SVs show lower GMR and higher exchange bias compared to top-pin SVs. This difference is due to the rough AFM IrMn layer located at the base of the bottom-pin SV as well as current shunting in the Cu seed layer.

Shape Anisotropy

In SV films, the magnetic anisotropy dominates; however, shape anisotropy dominates after etching the excess material away. Patterned, exchange-biased SVs behave differently than thin-film SVs due to magnetostatic interactions in the SV; demagnetizing fields and layer interactions should be considered [86-87].

The width and aspect ratio are important parameters for SV traps [88]. For wider traps, the magnetic fields will be larger and more extended due to the increase in effective magnetic charges at the ends. This will promote SPB trapping from a greater distance. However, smaller widths and larger aspect ratios are required to maintain a single-domain structure and to minimize magnetostatic coupling at the ends, which promotes an antiparallel configuration. For active surfaces, the traps must have a high density;

however, they must not interact strongly and their minimum spacing is limited by the strength of the magnetostatic interaction between different elements.

For a rectangular SV with aspect ratio $A_R = L/w$, where L is the length, w is the width, and w << L, the energy barrier ΔE between the parallel and antiparallel states is proportional to the magnetization M, thickness t of the free layer, and the width w [88].

$$\Delta E \propto \frac{Mt}{w} \tag{2}$$

The coupling between the two FM layers causes a small free layer shift as shown in Figure 11 (b). The antiparallel (high-resistance) state is lower in energy than the parallel (low-resistance) state. Decreasing the width will result in a higher energy barrier due to the higher magnetostatic energy. Increasing the thickness or choosing a material with higher magnetization will also increase the switching fields.

The demagnetizing field H_d is inversely proportional to A_R and w.

$$H_d \propto \frac{1}{A^2 w} = \frac{w}{L^2} \tag{3}$$

Thus, a SV with a high aspect ratio will have a lower demagnetizing field. High demagnetizing fields can result in SVs not being bistable at zero applied field.

Cross evaluated rectangular NiFe/Cu/NiFe/FeMn analog SVs with a width-to-height ratio of 1:10 [86]. The authors found the GMR response became parabolic and less sensitive as the device size decreased, but the maximum GMR did not change. The interlayer magnetostatic fields and demagnetizing fields were similar to the pinning field as the device size decreased. In another study by the same group, Russek evaluated digital NiFe/Co/Cu/Co/NiFe/Fe/Mn SVs with varied widths and aspect ratios [88]. They found the switching fields and switch-field symmetry increased as the width decreased (Figure 16). Additionally, they found the MR decreased as the width decreased due to dead zones along the length of the device. The MR response was sharper and the free-layer switching fields increased as the width decreased. With a decrease in aspect ratio, Barkhausen noise (noise caused by domain-wall movement) and switching field asymmetry increased sharply. Lim confirmed these results by computer simulation [89].

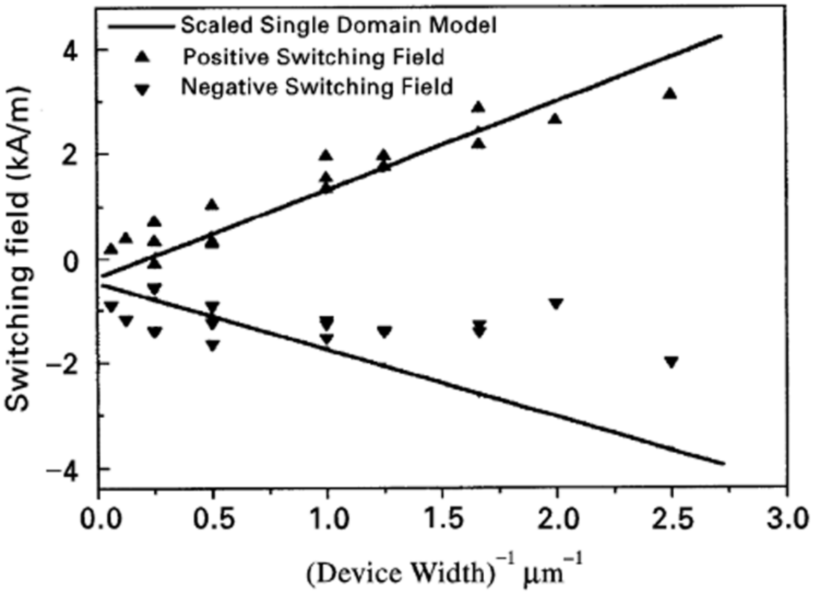

Figure 16: Effect of SV width on the free-layer switching field compared to scaled single domain model [88].

Mao evaluated analog SVs 30 µm in length with varied width (1 µm, 9 µm, and 19 µm) [90]. As shown in Figure 17, increasing the aspect ratio resulted in lower free-layer coercivity and a higher pinned-layer bias field.

The demagnetizing field caused a broadening of the MR curve as the width decreased. Devices with smaller aspect ratios exhibited more Barkhausen noise and devices with smaller widths exhibited more magnetostatic effects [87,91].

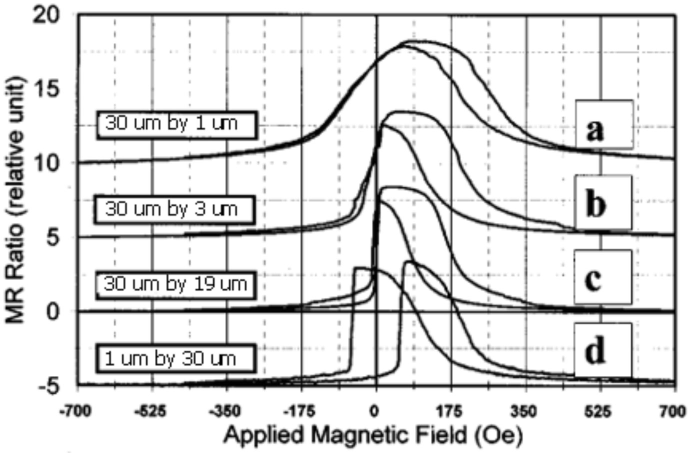

Figure 17: GMR response of perpendicular SVs with varied aspect ratios [90].

Johnson evaluated 20 nm and 30 nm thick elliptical Permalloy elements with aspect ratios ranging from 1.2 to 6.8 [92]. As the aspect ratio increased, the switching field decreased to a minimum. A 20 nm or 30 nm thick Permalloy element with an aspect ratio of 6 or 7 had a switching field of -20 mT and a demagnetizing field ranging from +3 to +6 mT. The nucleation energy was higher in the thinner samples. The authors hypothesized that this could be a result of a larger perpendicular demagnetizing field or the reversal mechanism for switching a thinner film.

Castano found that increasing the aspect ratio of their 70 nm wide pseudo-SVs resulted in higher low-field switching [66]. They concluded that an aspect ratio below 5.4 led to poor remnance because the layers favored the antiparallel state [66]; the magnetostatic coupling between layers and the demagnetizing field decreased as the aspect ratio increased. In higher aspect ratio devices, the exchange coupling energy was high enough to enable the SVs to favor the parallel state [66]. However, Castano found the magnetostatic coupling decreased as the spacer thickness increased leading to the SVs favoring the parallel state and higher remnance [66]. Similarly, Zhu observed the effect of aspect ratio on NiCoFe/Cu/NiCoFe SV switching fields and found an aspect ratio above 4 was desirable [93]. However, increasing the length of the SV led to larger coercivity [94].

Gadbois evaluated how the end shape affected coercivity and observed that tapered or elliptical SVs switch at lower fields compared to rectangular SVs [95]. Kirk also studied the effect of end shape on switching in closely packed Permalloy (26 nm) and Co (27 nm) nano-elements [96]. The length of their elements ranged from 1.6-3.5 μm with a width of 200 nm. The spacing ranged from 250 nm to 7 μm, center-to-center. Conversely, they found that elements with no flat ends switched at higher fields; the rectangular elements had a slightly lower coercivity compared to tapered elements. Closure domains at the ends nucleated the lower switching fields of blunt elements. For closely packed elements, the neighbors stabilized un-switched elements and lowered the applied switching field required for reversal. The magnetic state of the neighbor influenced the switching values [96].

Magnetoresistive Random Access Memory (MRAM)

Arraying SVs in an architecture analogous to magnetoresistive random access memory (MRAM) is needed to achieve the long-term goal of this research, which is to construct an array of individually-addressable SVs that can manipulate and detect individual or bulk SPBs on a two-dimensional (2D) surface. MRAM SV technology is nonvolatile and has unlimited read and write endurance [97]. The SV is written with an external magnet or a write line proximal to the SV and the GMR is read with a read line adjacent to the surface of the SV. Resistance uniformity, switching behavior, and integration with CMOS circuits are challenges.

Most recently, MRAM technology is based on a structure similar to the SV, the magnetic tunnel junction (MTJ). A MTJ stack consists of two magnetic layers separated by a dielectric barrier (Figure 18). One magnetic layer is polarized in a fixed (pinned) direction and retains its polarization when exposed to magnetic fields that switch the free layer. As shown in Figure 18, the current line (also referred to as an Ampere field) directly above and in contact with the MTJ is the bit line [97]. The bit line is parallel to the MTJ and it assists in both the MTJ read and write. The digit line is below the stack and oriented perpendicular to the MTJ. The bit line is electrically isolated from the MTJ. To switch the MTJ, current is passed through the orthogonal digit and bit lines. To read the MTJ or bit, the transistor is turned on to enable the sense current to flow through the stack.

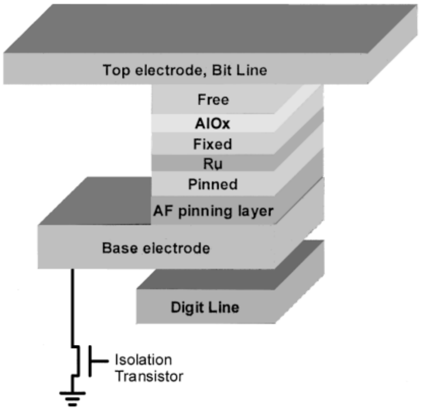

Figure 18: Illustration of 1-MTJ, 1-transistor MRAM cell [97].

Functionalized Carriers

Bioassays frequently employ functionalized carriers (also referred to as mobile substrates) to manipulate and/or detect biological targets, such as biomolecules and cells. Common carriers include superparamagnetic or polymeric nano- and micro-beads. More recently, nano-tubes are being explored as possible carriers or immobile substrates [98-99]. To functionalize or tag the surface of the carrier, the carrier surface is coated with phospholipids polyvinyl alcohol (PVA), dextran, proteins, or biotinylated DNA [23]. As shown in Figure 19, the type of functionality can be highly specialized by coating the carrier with specific antigens, antibodies, single stranded DNA (ssDNA) chains, or oligo DTs. When the functionalized carrier is introduced to a solution containing the target, the target biomolecules or cells will hybridize to the carrier and the unwanted solution containing other cells and biomolecules is eluted. Then the carrier (and the isolated target) can be maneuvered for isolation, purification, and detection.

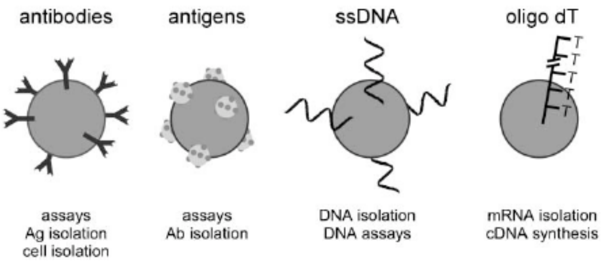

Figure 19: Illustration of surface functionalized particles utilized in biochemical reactions [100].

Functionalized micro- or nano-SPBs are used in bioassays as single or bulk “mobile substrates” [35]. Bioassays utilizing magnetic beads have many benefits including reduced reaction times due to the short diffusion lengths, increased mobility, high throughput, and high affinity. Figure 20 shows the scanning electron micrograph (SEM) of DNA attached to SPBs and a single SPB attached to a cell. The properties of the SPBs depend on the FM content and material, volume, and manufacturer. In a review of commercially available SPBs, Brzeska found the maximum magnetic moment per particle ranged from 2 to 50 fA m^2 [101]. Because micro-beads may spatially hinder biomolecule-biomolecule interactions, there is a push to use nano-beads, which are on the length scale of most biomolecules. As a magnetic particle is reduced in size, a larger magnetic field gradient (not a larger magnetic field) will be needed to manipulate that particle.

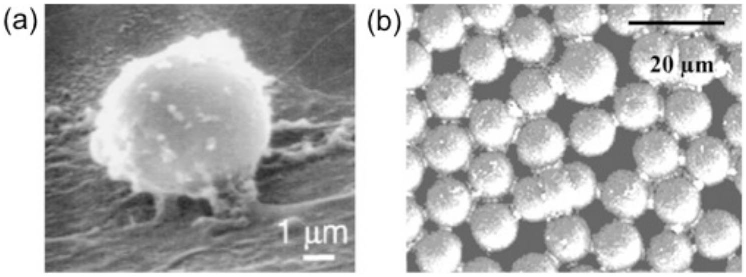

Figure 20: (a) Scanning electron micrograph (SEM) of a DNA-SPB assembly [102], (b) SEM of SPB bound to cell [103].

Magnetophoretic Manipulation Technology: A Review

There are a variety of MEMS platforms to manipulate biomaterials including optical, electrical, mechanical, and magnetic technologies; however, the focus of this review will be on magnetophoretic technologies. Optical tweezers, atomic-force microscopy (AFM) cantilevers, dielectrophoresis [104], electrophoresis [11], centrifugation, and filtration manipulation methods will not be discussed.

Magnetic devices offer many advantages because they typically are not hindered by surface charge, pH, ionic concentrations, and temperature [100]. Additionally, they provide a rapid method for separating particles from dilute suspensions [9]. With the exception of red blood cells, ferritin, and magnetobacteria, magnetic systems require the target sample to be attached to a magnetic bead, which can be a limitation of the method [100]. Compared to the more traditional optical detection systems, such as DNA microarrays, magnetic devices are more sensitive and can be more densely packed [2,25,105].

As mentioned previously (page 6), magnetic manipulation has been performed for centuries and the concept is quite simple. Materials with a magnetic moment experience a force when exposed to a magnetic field gradient. The magnitude and direction of the force depends on the gradient as well as the magnetic properties of the material. The following sections will review the current magnetic thin-film, electromagnetic, and domain-wall technologies used for SPB manipulation.

Magnetic Thin-Film Devices

Patterned magnetic thin films controlled with either an external or local magnetic field can trap, manipulate, and release beads in solution. The patterns can range from long stripes to complex shapes. Typical magnetic materials used are Permalloy ($Ni_{80}Fe_{20}$), cobalt (Co) or cobalt-iron ($Co_{90}Fe_{10}$), nickel (Ni), bismuth-substituted ferrite garnet, and neodymium-iron-boron (NdFeB).

Mirowski demonstrated that arrayed 1.2 μm × 3.6 μm × 30 nm Permalloy ($Ni_{80}Fe_{20}$) elements (Figure 21) could trap 2-3 μm diameter SPBs from up to 5 μm away in the presence of a +8 mT external field applied along the long axis of the traps. By observing the SPB Brownian motion, they calculated a trap force of 97 ±15 pN [106]. Also, they demonstrated the trap and semi-release of a SPB with an external applied magnetic field. The bead was not fully released from the trap due to remnance in the Permalloy when the applied field was removed.

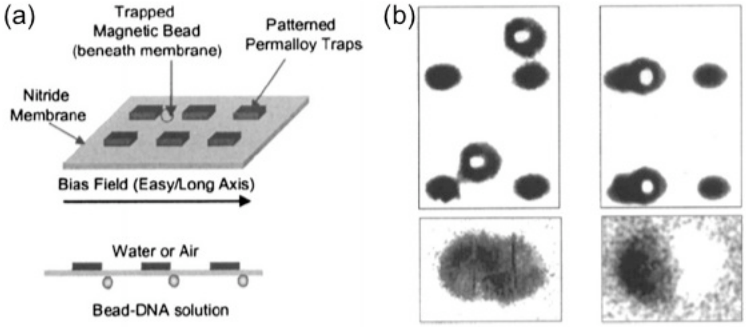

Figure 21: (a) Schematic of microfluidic platform with Permalloy traps to trap SPBs, (b) semi-release and trapping of 2-3 μm diameter SPBs [106].

Gunnarsson's group used thin-film magnetic elements to form one-way "transport lines" to manipulate 2.8 μm SPBs (Figure 22) [107]. The elliptical

(2 μm × 6 μm × 0.1 μm) Permalloy elements were arrayed in a staircase pattern and were actuated with an external, rotating magnet (6.3 kA/m). The size of the trap prevented more than one bead from attaching to the trap [108]. The path of the particle could be altered depending on the rotational direction of the applied field and by varying the element pattern.

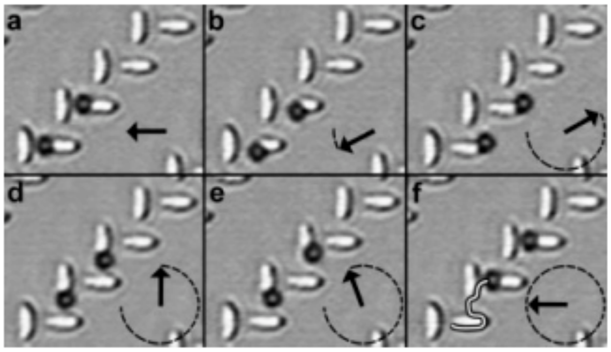

Figure 22: Elliptical Permalloy "transport lines" actuated with an external magnet to transport individual SPBs [107].

Conroy used magnetic field gradients generated by local radii of curvature on patterned structural edges (Figure 23 (a)) in combination with an external field to move 8 μm diameter magnetic beads coated with antibodies [109]. The magnetic pattern of 1 μm thick Ni was analogous to bubble memory. An external magnet saturated the patterned magnets and a maximum bead velocity of 10 μm/s and a force magnitude in the pico-Newtons were observed (Figure 23 (b)).

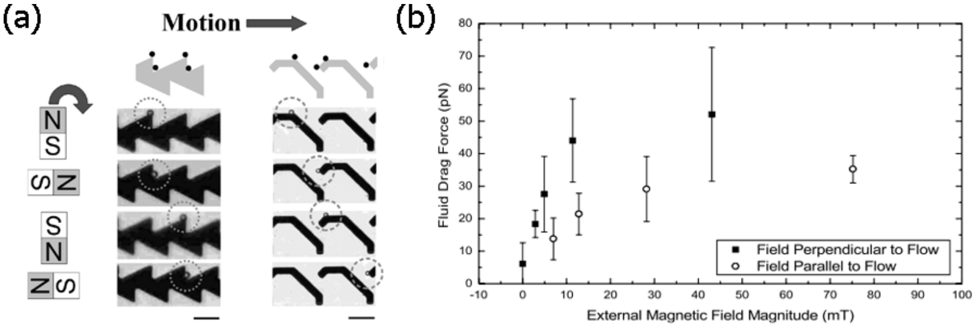

Figure 23: (a) Periodic zig-zag patterns to trap and transport 8 μm diameter magnetic beads, (b) pull forces required to detach the bead from the trap with fluid flow [109].

Similarly, Donolato demonstrated 1 μm and 2.8 μm functionalized SPB translation on patterned Permalloy via domain-wall movement induced by applying a 10 mT external field [110]. A 100 nm precision translation was demonstrated on the Permalloy zig-zag (Figure 24) and ring structures (not shown). The bead followed the domain-wall movement along the structures.

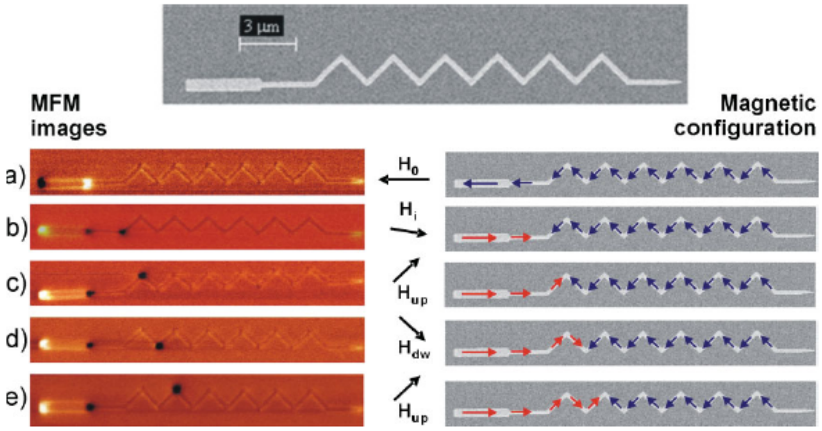

Figure 24: Manipulation of magnetic bead along Permalloy zig-zag lines actuated with an applied magnetic field [110].

Johansson demonstrated controlled transport of protein-functionalized 4 μm beads on lithographically patterned triangular Permalloy elements spaced 8 μm apart. Each equilateral triangle had a base length of 6 μm and a

Permalloy thickness of 70 nm. Prior to testing the chip with beads, the surface was coated with polyethylene glycol (PEG). Bead velocity averaged 20 μm/s.

Inglis used micro-fabricated magnetic nickel stripes to manipulate ensembles of SPB tagged cells (leukocytes) [111]. The bead diameters ranged from 20-100 nm. The stripes were 2 μm thick and 10 μm wide. With an applied field of 100 mT, the beads moved an average velocity of 100 μm/s. They calculated a pico-Newton force on the 10 μm diameter cells.

K. Smistrup used hydrodynamic focusing integrated with arrays of electroplated Permalloy elements (50 μm × 40 μm × 4.9 mm) to separate biotinylated 1 μm SPBs flowing through a 100 μm × 120 μm microfluidic channel [21]. The passive magnets produce a homogeneous magnetic-flux density of 21 mT across the channel. In another paper, the group demonstrated passive captures of 1.0 μm fluorescent SPBs flowing at a velocity of 5 mm/s with a similar design and an applied field of 50 mT [112].

Yellen and Friedman used a pattern of micromagnets to programmably assemble micro-SPBs in micro-wells [108]. The patterned cobalt micro-magnets were 100 nm thick, 20 μm long, and 4 μm wide. Analogous to thermomagnetic recording, a focused laser beam heated the micromagnetic elements to turn them "OFF". The temperature increase reduced the coercive switching fields of the selected elements, thus enabling them to be switched with a lower applied field. The bead was attracted to the trap when "ON" and repelled by the trap when "OFF". The authors reported issues with demagnetization.

Rong developed a magnetic bead separator with Permalloy magnetic tips as inductors as shown in Figure 25 [113]. SPB flow was directed to one of two outlets depending on the excitation applied to the inductors. They observed forces on the order of tens of pico-Newtons and a flow rate of 1 μm/s.

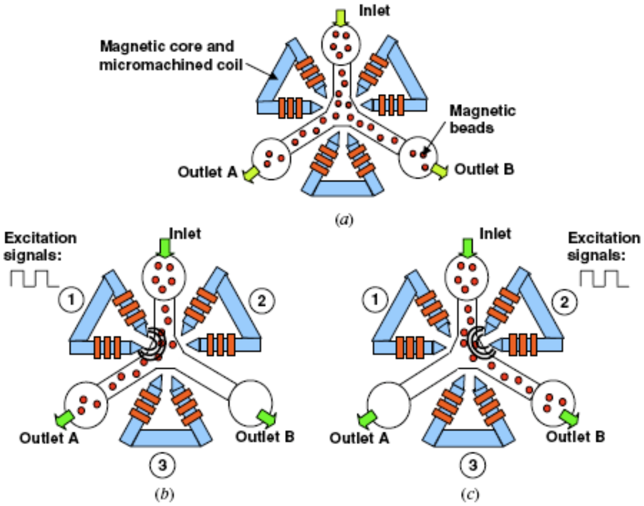

Figure 25: Illustration of the operational principle of the magnetic bead separator: (a) no excitation signal applied directs SPBs to both Outlet A and Outlet B, (b) signal applied to left inductor directs SPBs to Outlet A, and (c) signal applied to right conductor directs SPBs to Outlet B [113].

In 2007, Mirowski demonstrated the efficacy of using a SV element as a nonvolatile bistable magnetic structure to confine a SPB [114]. The SVs (5 nm Ta/15 nm $Ni_{80}Fe_{20}$/5 nm Co/10 nm Cu/5 nm Co/15 nm $Ni_{80}Fe_{20}$/5 nm IrMn/5 nm Ta) were deposited on a 200 nm thick nitride membrane that isolated the beads from the devices. The 1 μm × 4 μm SVs had a coercivity of 3.5 mT; an applied field of -1.5 mT turned the SV "OFF" and +2 mT turned the SV "ON". A rotational field of 1.2 mT and a field gradient of 3 mT/cm were applied to demonstrate the rotation of a bead chain on an "ON" SV (Figure 26).

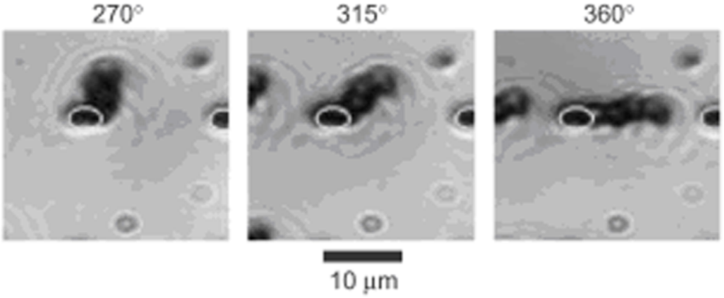

Figure 26: Rotation of a chain of SPBs trapped on an "ON" SV. A rotating field of 1.2 mT was too low to flip the SV free layer [114].

Henighan demonstrated programmed movement of bulk 2.8 μm SPBs around 40 nm thick 5-10 μm diameter circular Permalloy disks [115]. The beads, tethered to T-lymphocytes, had an average velocity of 20 μm/s around the outer circumference of the disc. They also demonstrated parallel bead-lymphocyte manipulation with an array of disks actuated with a 6 mT in-plane external magnetic fields rotated clockwise or counterclockwise. The beads "hopped" between disks by reversing the field.

Electromagnetic Devices

Electromagnetic devices use current to produce the magnetic field gradient necessary to move the SPBs in solution. If the SPB is polarized, the electromagnetic field generated by current running through a wire can induce attractive or repulsive forces. Current-line and coil electromagnetic devices are discussed in the following section.

As depicted in Figure 27, Tondra used 2 μm wide current lines and a 20 kA/m external field to sort SPBs as a function of magnetic moment [116]. The external field was needed to magnetize the 460 nm beads. A 10 mA current through one line pushed the beads to the opposite wall. A -10 mA current resulted in the polarized beads being attracted to the opposite wall nearest the active current line.

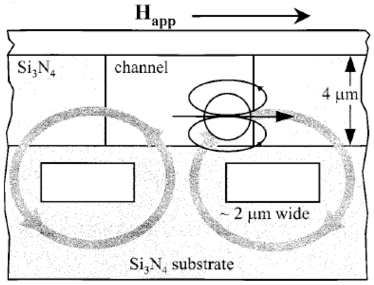

Figure 27: Cross-sectional schematic of SPB sorter with current lines to move beads polarized by an external applied field [116].

Lagae demonstrated mass 300 nm SPB concentration and transport with tapered current lines [6]. The tapered line, as shown in Figure 28, produced the electromagnetic gradient that propelled the SPBs towards the SV sensor at the center of the chip. The tapered gold lines were 150 nm thick and were passivated with 250 nm SiO_2. The width of the tapered conductor at the center of the chip was 5 μm. The generation of heat limited the experiments to only a few minutes.

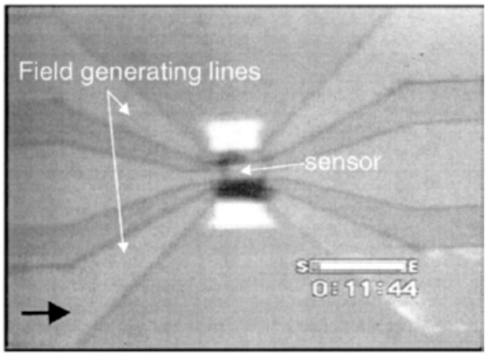

Figure 28: Movement of ensembles of SPBs along tapered current lines [6].

Similar to Tondra's results, Lagae evaluated the current-line polarity's effect on SPB movement; in this experiment, the SV sensor and the current lines polarized the bead (see Figure 29). In another paper, Graham used the same chip layout, but with aluminum current lines, to demonstrate 400 nm and 2 μm SPB transportation [117]. The tapered current line controlled the magnetically labeled biomolecules while the SV sensors detected the magnetic beads.

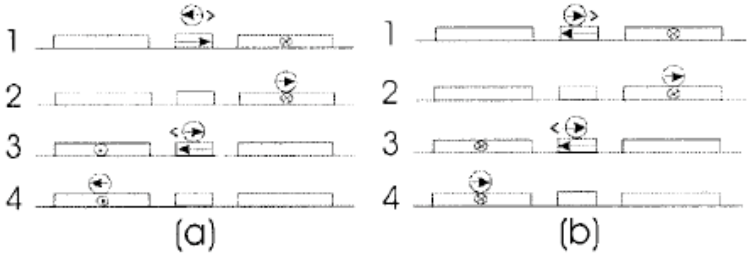

Figure 29: Schematic of current-line polarity's effect on SPB movement [6].

Similarly, Jiang integrated MR sensors with tapered current lines within a microfluidic cell to detect and sort 9 μm magnetic beads [118]. In this study, they used tapered lines to focus the beads into the center of the laminar flow microfluidic channel.

Alternatively, Pekas developed a particle diverter by means of an external field integrated and local current lines within the microfluidic channel [119]. The 0.96 μm SPBs were polarized with the external field and perturbed with the current lines. The current lines were 1.7 μm thick aluminum passivated with a 1.8 μm thick planarizing layer of benzocyclobuthene (BCB). A current of 50 mA deflected beads towards the preferred channel.

Deng employed zig-zag current lines (Figure 30), 50-100 μm wide and 10-20 μm tall, to manipulate SPBs [120]. The current lines created peak magnetic fields of hundreds of gauss (tens of mT). The serpentine current lines were π/3 out of phase to enable the SPBs to bounce from one line to the other.

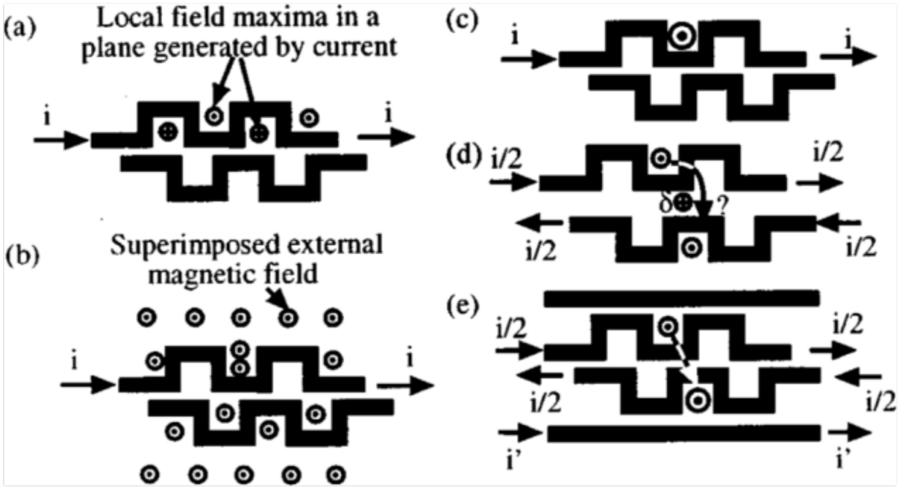

Figure 30: Illustration of serpentine current lines to transport SPBs [120].

Wirix-Speetjens and de Boeck used two saw-tooth shaped current conductors (Figure 31) to trap and guide a single 2 μm SPB along a defined track [121]. The two saw-tooth current lines were 180° out of phase and produced a maximum magnetic field gradient near the corners of the rectangular cross section. When a current flowed through one of the conductors, a SPB moved towards the narrow (local maximum magnetic field) part of the conductor. This field was oriented mostly perpendicular to edge of the tapered current line. To move the SPB to the next location on the track, a current flowed through the other conductor making a new local maximum field. By using low frequency non-overlapping clock pulses alternately through both the conductors, a SPB was translated along the conductors. They found 50 mA current at a frequency of 0.10 Hz was optimal.

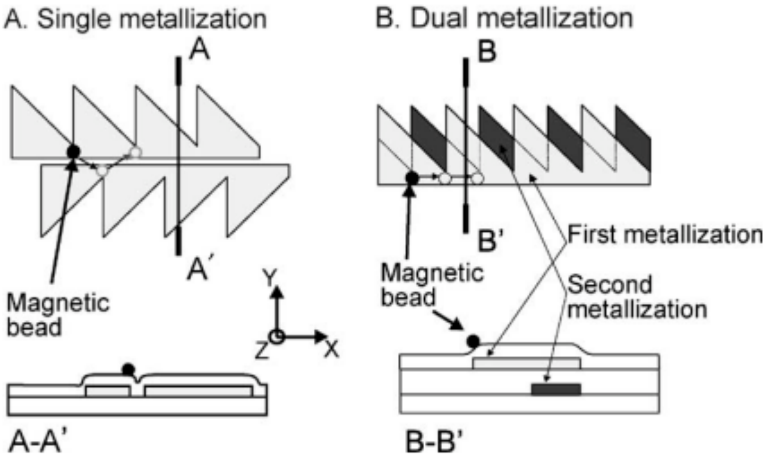

Figure 31: Illustration of single SPB movement device design with (a) single metallization and, (b) dual metallization devices [121].

C.S. Lee used a 7 × 7 matrix of current lines to demonstrate 2D manipulation of nano-SPB ensembles [51]. The chip consisted of two perpendicular layers of straight current carrying conductors separated by two insulating layers (Figure 32 (a) and (b)). The current lines were 10 μm wide, 3 μm tall, and spaced 20 μm apart. The matrix provided a noninvasive method for moving, rotating, and sorting yeast cells. Cooling prevented boiling. Thermal heating and power limited long-term use of the chip. In another paper, H. Lee demonstrated the movement of a yeast cell bonded to a 2.8 μm SPB on a 10 × 10 matrix [122]. They calculated the force on the bead to be ~40 pN. In a later publication by H. Lee, they used a 10 × 10 matrix to assemble magnetic nano-particles from magnetotactic bacteria (Figure 32 (c)) [123]. Interestingly, the bacteria synthesize the nano-particles within their bodies.

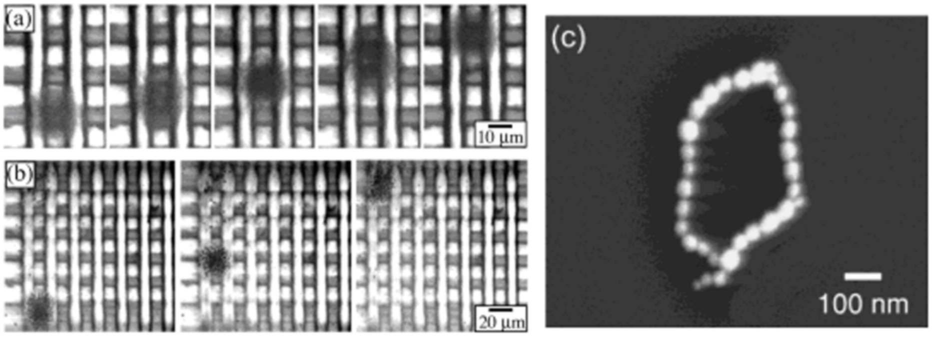

Figure 32: (a,b) Insulated current-line matrix (10 × 10) to transport beads [51], (c) the assembly of a SPB chain by means of the matrix and magnetobacteria [123].

In a similar arrayed current-line approach, Ishikawa developed a CMOS chip consisting of multiple parallel and perpendicular current lines (3 μm wide and spaced 3 μm apart) to manipulate a single 2.8 μm SPB [50]. This chip was fabricated by means of the standard 180 nm CMOS process. The current patterns to manipulate the bead are shown in Figure 33.

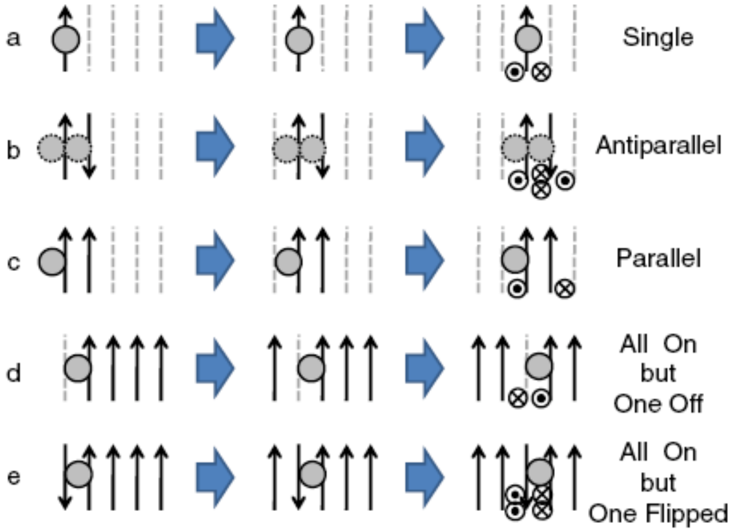

Figure 33: Illustration of SPB actuation movement correlated to current patterns [50].

Another arrayed approach used a 2D array of coils to manipulate bovine capillary endothelial cells tagged with 250 nm SPBs [124]. H. Lee developed a CMOS chip consisting of an 8 × 8 array of 20 μm × 20 μm coils spaced 1 μm apart as shown in Figure 34. A 20 mA current actuated each coil and temperature was monitored and controlled to prevent overheating.

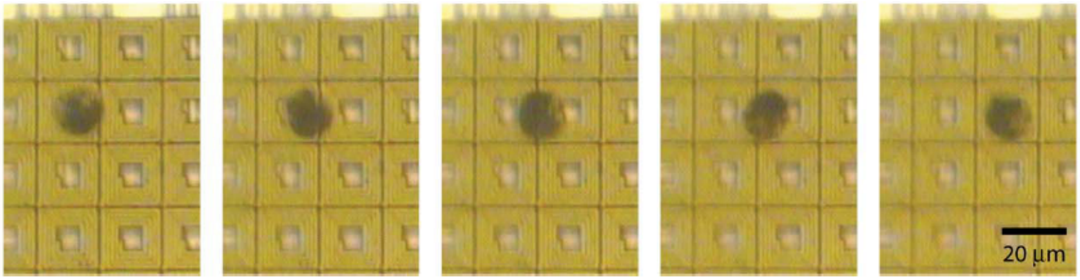

Figure 34: Micro-coil bead manipulator demonstrating transportation of a cell hybridized to a SPB [124].

Choi demonstrated bulk micro-SPB (0.8-1.3 μm) separation with 10 μm-wide serpentine conductors encapsulated in Permalloy [125]. In two other papers, Choi used the serpentine conductors to separate the beads, and then detect the beads with electrochemical immunosensors [126-127]. This device could separate ~18 million particles per second.

Similar to Choi, Rida demonstrated bulk transport of magnetic 1 μm SPBs with simple planar coils and permanent magnets [128]. The permanent magnets produced a uniform static magnetic field of 50 mT while the coils produced a small field of 1-4 mT. The beads traveled at a velocity on the order of 1 mm/s.

Ramadan integrated arrays of large micro-coils with asymmetrically shaped conductors and FM core pillars (NiCoP) to transport bulk 1 μm SPBs

[129-132]. The bead trapping efficiency was 84% and the coils could detect the presence of the SPBs.

Similarly, Ahn used micro-coils to achieve magnetic field gradients of 10^2 to 10^3 T/m to trap 1 μm SPBs from suspension (Figure 35) [133]. Their device consisted of thin-film electromagnets integrated with coils. They observed the bead travel at a speed of ~1 mm/s. To elute the particles, the electromagnet was simply turned off. They achieved a magnetic flux density of 30 mT with 500 mA of current through the coil conductors.

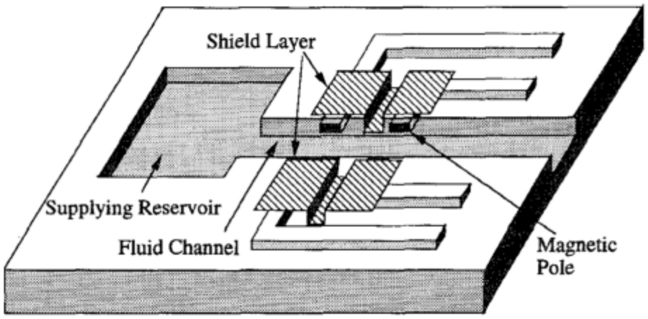

Figure 35: Schematic of fully integrated micro-coils and electromagnets to trap SPBs [133].

Liu developed a micro-device that used both magnetophoresis and dielectrophoresis to transport 4.5 μm Dynabeads (SPBs from Invitrogen) at a speed of 36 μm/s along current lines, as shown in Figure 36. The device consisted of two intertwining snake-like electrically insulated current lines (Figure 36). One line created an in-plane magnetic field to move the particle along the x-direction. The other line "levitated" the bead from the device surface to prevent the beads from sticking to the surface [134].

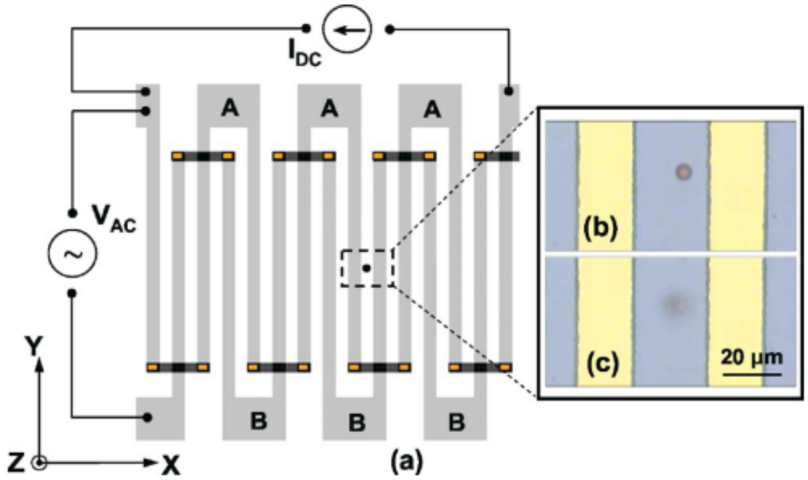

Figure 36: Chip layout for SPB magnetophoresis and dielectrophoresis levitation [134].

Likewise, Krishnan developed a microfluidic device that used dielectrophoresis and magnetophoresis to separate SPBs (1 µm, 2.8 µm, and 2.4 µm) based on size with ~90% efficiency [135]. Permanent neodymium-iron-boron (NdFeB) disk magnets (150 mT, 1 mm long, 1 mm diameter) are integrated into the microfluidic device to trap the beads.

Thin-Film Domain-Wall Devices

The movement of domain walls in unpatterned magnetic thin films can guide a magnetic bead along the surface of a chip. Helseth used domain-wall tips (Figure 37) to drag SPBs across the thin-film surface [136]. The magnetic domains were created by grains in the magnetic layers as well as by imperfections. They use 4 µm thick bismuth-substituted ferrite garnet films grown on gadolinium gallium garnet substrates to produce the domain walls. The maximum observed velocity of the 1.4 µm SPB was 30 µm/s.

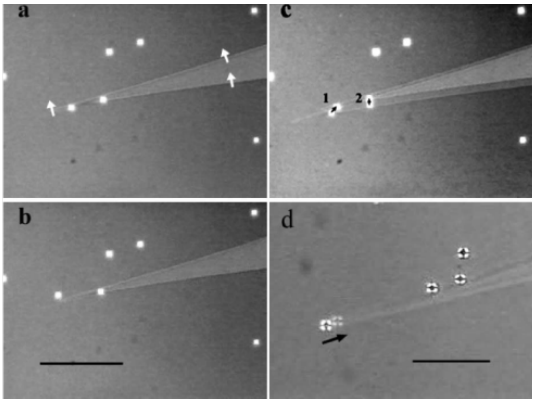

Figure 37: Domain-wall tips transporting SPBs [136].

In a paper by Bryan, manipulation of SPBs by propagation of domain walls within a magnetic thin film was modeled [137]. The walls were propagated with an applied magnetic field or spin-polarized currents. They determined that the drag force greatly limited the speed of a bead transported by a domain wall.

Magnetoresistive SPB Detection

On-chip detection of magnetic SPBs, and thus the biological sample of interest, may revolutionize POC diagnostics in the medical [3,23], veterinary, food, and national security [5,138] industries. MR sensors can eliminate the need for expensive optical systems, reduce processing time by simplifying the bioassay process (fewer steps), and may be integrated into handheld LOC or μ-TAS devices. Advantages of magnetic sensors include high sensitivity, fast response time, low-power consumption, corrosion resistance, low cost, and high signal-to-noise ratio. Additionally, magnetic labels offer more stability and less background noise compared to fluorescent labels, which are prone to bleaching when exposed to light. Magnetic beads can be sensed or detected with SVs, magnetic tunnel junctions (MTJs), Hall sensors, anisotropic magnetoresistive (AMR) sensors, FM resonance, or giant magnetoimpedance (GMI). For an excellent review on sensors, please refer to Graham or Megens [105,139].

With MR sensors, an electrical resistance change is measured when a polarized magnetic bead or carrier is on or near the MR sensor. As shown in Figure 38, the stray fields from the polarized magnetic bead induce a magnetic change in the MR sensor. As the sense current remains fixed, the voltage, thus resistance change, is measured.

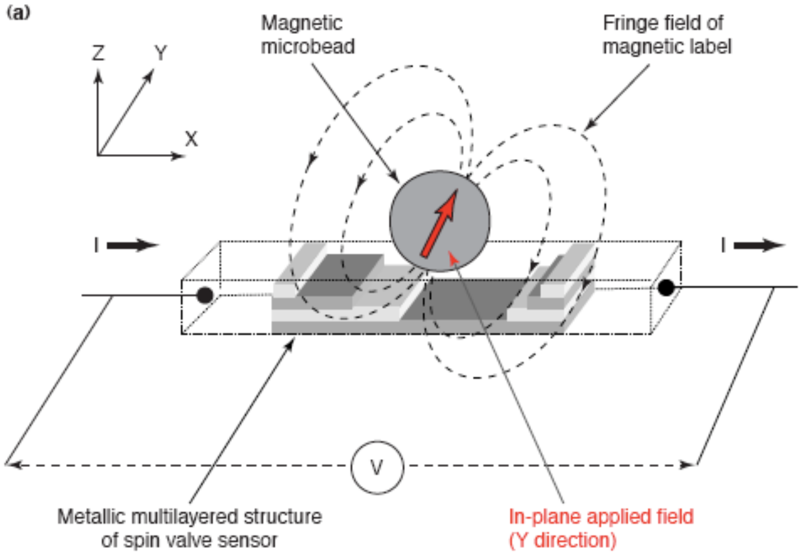

Figure 38: Schematic for magnetic label detection by means of a SV sensor [139].

In GMR sensors (i.e., SVs), a metal spacer separates two magnetic thin films. As shown in Figure 38, a current runs through the SV sensor and the voltage is measured. Any field can be used to polarize the bead; however, the SV is insensitive to an out-of-plane field, so the bead can be polarized with this field without altering the SV performance. The SV is most sensitive when the pinned and free layers are perpendicular (analog SV). Four detection modes are depicted in Figure 39. The bias field H_b can be generated with an exchange biased FM, shape anisotropy, or an external field. The applied field H_t is generated with a current line or an external magnetic field.

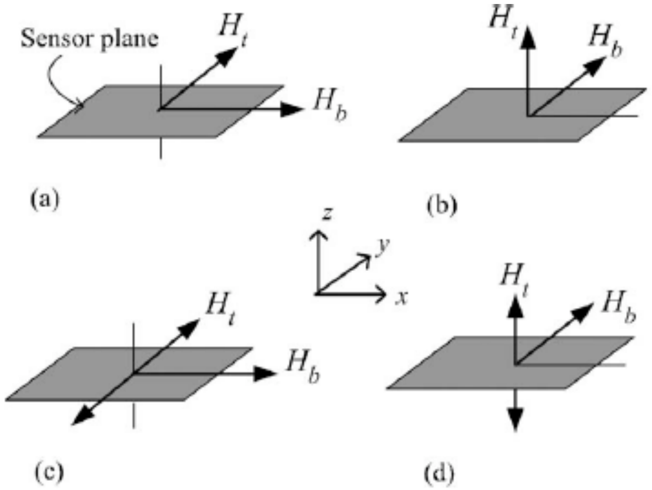

Figure 39: Four SV SPB detection modes. H_b is the bias field and H_t is the applied field [1].

MTJ sensors consist of two magnetic thin films separated by an insulator and they are more sensitive than GMR sensors [140]. The MTJ sensor shows great potential in carrier sensing; however, only a handful of groups are working on these biosensors [140-141]. Hall cross and ring sensors fall into the domain of AMR sensors. AMR sensors rely on shape anisotropy; similar to the other types of sensors, the fringe fields from a magnetized bead induce a voltage change across the sensor. AMR sensors are capable high micro- and nano-SPBs detection sensitivity [118,142-146].

GMR Sensor Technology: A Review

The scope of the review will be limited to GMR sensors due to their potential use in an MRAM-like architecture for both bead detection and manipulation.

Baselt's research group pioneered the MR SPB-sensing field when they developed a biosensor referred to as the Bead ARray Counter (BARC) [5,34,138,147]. In their first paper, the surface of the 100 nm thick GMR sensor was functionalized with the target molecule and magnetic beads with the complementary molecule selectively hybridized to the sensor surface. To remove unbound beads, an external force was applied and the remaining beads were optically and magnetically counted. A force of ~1 pN applied for 5-10 seconds removed 99 ± 1% of the unbound (non-hybridized) beads. They also demonstrated the detection of 2.8 μm SPBs with 80 μm × 5 μm and 100 nm thick GMR sensors.

Li demonstrated detection of a single 2.8 μm SPB with 3 μm × 12 μm (3 μm × 4.1 μm active area) as well as 2.5 μm × 10 μm (2.5 μm × 3.8 μm active area) analog SVs [49]. In a later paper, Li and Wang demonstrated detection of a monolayer of 16 nm Fe_3O_4 nano-particles on 300 nm wide × 4 μm long SV (10% GMR) sensors. SVs sensors detected magnetic nano-particles even when the particles were randomly distributed [148]. Similarly, Li developed a SV sensor (see Figure 40) that could detect as few as 23 monodisperse 16 nm SPBs polarized by an external field [1]. The analog SV (11.3% GMR) consisted of substrate/3 nm Ta/4 nm seed layer/15 nm /2 nm CoFe/0.85 nm Ru/2 nm CoFe /2.3 nm Cu/2 nm CoFe/1 nm Cu/4 nm Ta [49].

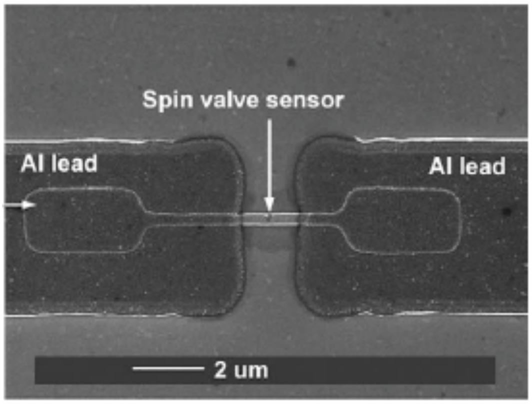

Figure 40: SV sensor with for the detection of micro- and nano-SPBs [1].

In research by the Biomedical Sensor Systems at Philips Research (Netherlands), De Boer developed a compact platform, which used disposable cartridges and an electronic reader to sense SPBs on a GMR sensor. As shown in Figure 41, a local current line polarizes the bead. No details on the sensor were given, but their results indicated that they could detect three 300 nm beads on a sensor area of 1500 μm^2. Koets used this chip in a later study to demonstrate rapid and sensitive detection of tagged PCR amplicons [149].

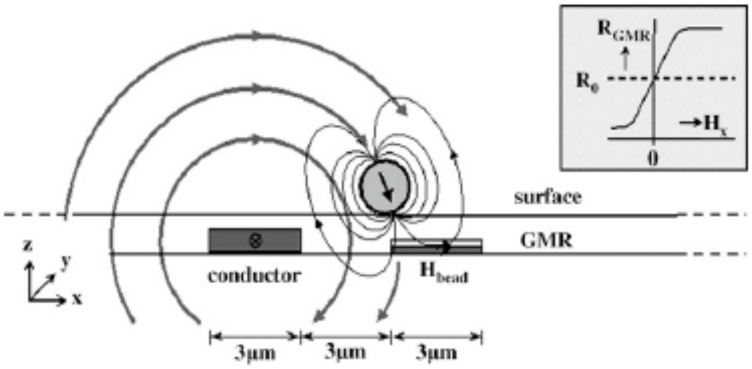

Figure 41: GMR sensor with SPB magnetized with local conductor [150].

Xu used a SV sensor array to detect human papillomavirus (HPV) hybridized to 10 nm SPBs within 10 minutes [151]. Their analog SVs (biased perpendicular to long axis) consisted of substrate/5 nm Ta/seed layer/8 nm IrMn/2 nm CoFe/0.8 nm Ru/2 nm CoFe/2.3 nm Cu/1.5 nm CoFe/3 nm Ta with an active area of 93 μm × 1.5 μm and a passivation layer of 40 nm $SiO_2/Si_3N_4/SiO_2$. An applied field of 5 mT along the long axis biased the SV into a single-domain regime and measurements were taken at 708 Hz.

Lagae used a 2 μm × 16 μm SVs (8% MR) to detect ensembles of 300 nm SPBs (Figure 28) [6]. Their SV consisted of 2 nm Ta/2 nm NiFe/1 nm CoFe/2.5 nm Cu/2.5 nm CoFe/1 minute nano-oxide layer (NOL)/1 nm CoFe/10 nm MnIr/2 nm Ta and had a high sensitivity of 2.2%/(kA/m). In another paper, Lagae used 1.4 μm × 4 μm and 2 μm × 6 μm rectangular analog SVs (5% MR) to detect single 2 μm SPBs as well as a small quantity of 250 nm SPBs [152]. The simple SV stack consisted of 5 nm Ta/3 nm NiFe/8 nm IrMn/5 nm NiFe/2.7 nm Cu/5 nm NiFe/2.5 nm Ta.

With a similar chip design, Graham and Ferreira used 2 μm × 6 μm SV sensors (actual SV area was 2 μm × 14 μm) with 5% MR to detect single 2 μm and bulk 400 nm SPBs [117,153]. In 2005, Graham used the same chip design to demonstrate rapid probe-target hybridization and sensing on 250 nm beads [154]. In 2005, Ferreira published a paper comparing experimental data from the 2 μm × 6 μm (7.5% MR) SV sensor to a theoretical model [155].

De Palma evaluated parameters other than the SV sensor such as dose, blocking procedure (where to allow beads to bond to sensor), the type of magnetic carrier, and the sensitivity to a specific marker protein [156]. Their SV consisted of substrate/1.5 nm Ta/4.5 nm $Ni_{80}Fe_{20}$/0.5 nm $Co_{90}Fe_{10}$/1.9 nm Cu/2.5 nm $Co_{90}Fe_{10}$/7 nm $Ir_{80}Mn_{20}$/2 nm Ta/5 nm TiW and could detect bulk

300 nm SPBs. They concluded that smaller particles were more sensitive and determined where to promote marker binding to increase detection.

Lui used a 2 µm × 4 µm SV to detect a single 2 µm SPB placed onto the sensor with optical tweezers [7]. The SV stack consisted of 3 nm Ta/2 nm NiFe/8 nm IrMn/2 nm CoFe/0.8 nm Ru/3 nm CoFe/2.3 nm Cu/2.6 nm CoFe/1 nm Cu/5 nm Ta and had a 4.5% MR. Kim demonstrated detection of bulk 2.8 µm beads on a 3 µm × 9 µm analog SV sensor with a 10 mA sense current [157]. The SV consists of 5 nm Ta/4.5 nm NiFe/15 nm CoFe/2.6 nm Cu/4 nm CoFe/15 nm IrMn/5 nm Ta and had a 5% MR.

In a break from the traditional rectangular SV, Gooneratne used a ring shaped SV sensor (5.9% MR), as shown in Figure 42, to detect multiple 1 µm SPBs [158].

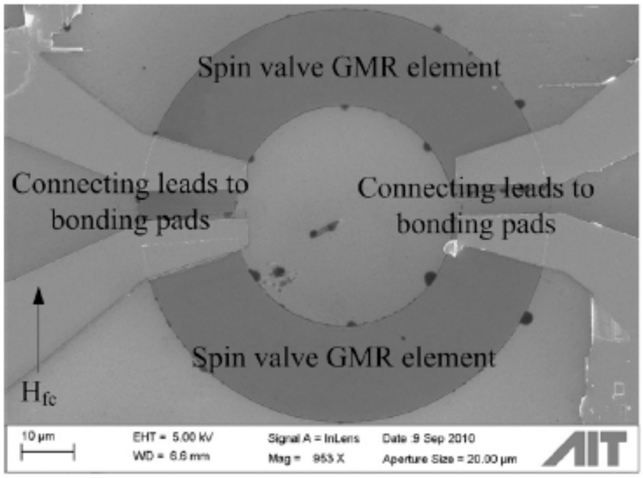

Figure 42: GMR ring sensor for detecting SPBs [158].

Shen detected individual 2.8 µm SPBs flowing through a microfluidic channel with elliptical 2 µm by 6 µm MTJ sensors consisting of 30 nm Pt/3 nm Permalloy/13 nm FeMn/6 nm Permalloy/0.7 nm Al_2O_3/12 nm

Permalloy/20 nm Pt [140]. Similarly, Grancharov demonstrated detection of bulk functionalized 12 nm SPBs on an MTJ field sensor from Micro Magnetics, Inc. [141].

Microfluidics

Advantages of performing bioassays within microfluidic systems include: (1) small sample and reagent volumes, (2) faster reaction times due to smaller diffusion lengths, (3) large surface-to-volume ratio for reactions, (4) portability, and (5) disposability [35,159]. A microfluidic system typically handles 10^{-9} to 10^{-18} L in channels tens to hundreds of micron (micro-meter) in width and depth [160]. Limitations include channel clogging, high pressures, and the difficulty of sample loading.

Fluids at the micro-scale behave differently than fluids at the macro-scale. Flow in microfluidic channels is typically laminar; fluids do not mix convectively. Mixing can occur through diffusion or by adding mixing elements like serpentine channels or micro-mixers. The fluid can undergo electro-osmotic flow if the sidewalls are charged and a potential is applied. Due to the short length scale, properties such as concentration, pH, temperature, magnetic field, and shear force tend to be uniform across the channel. Inertial effects can generally be neglected and viscous dissipation dominates mass transport [161].

Channels are commonly fabricated with SU-8 or polydimethylsiloxane (PDMS). SU-8 is an epoxy-based negative photoresist (PR) ideal for microchannels due to its superior aspect ratio, resist thickness, surface roughness of the side walls, and transparency [162]. It is clear and corrosion resistant, but can be difficult to work with. SU-8 is prone to unwanted swelling and non-specific binding of biomolecules. PDMS is a low-cost silicon-based polymer that is optically clear, inert, permeable to some gases, and non-toxic. Commonly, a mold is fabricated with SU-8 and the PDMS is cured over the mold, and then peeled off. Oxygen plasma helps to permanently attach PDMS to silicon nitride-based chips [135].

Surface Passivation

Passivation of the electromagnetic components prevents oxidation and corrosion, and protects the biological sample from any non-biocompatible materials within the MEMS device. For the microfluidic applications in this research, the surface should also be hydrophilic to decrease non-specific binding and to enable the bead solution to travel through the channels at lower pressures. Salt-based buffers are commonly used in bioassays, thus a coating will be needed to prevent device failure due to corrosion. Examples of passivation layers are shown in Table 2.

Table 2: Examples of passivation layers.

Material	**Thickness**
Silicon Dioxide (SiO_2)	120 nm [73], 75 nm [111,135], 250 nm [6], 300 nm [117], 1 μm [125]
Silicon Nitride (Si_3N_x)	500 nm [135], 200 nm [106,114]
SU-8	7 μm [109]
Tantalum (Ta)	4 nm [2]
Polyimide	Unknown thickness [121]
Glass	Unknown thickness [126]
Bisbenzocyclobutene (BCB)	Varied [122]
Gold (Au)	1.2 μm [134], 80 nm [5]
Polyethylene glycol (PEG)	Thickness not given [163]

The hydrophobic surface of silicon nitride and PDMS can be temporarily made hydrophilic with a plasma treatment [164,165]. Typically, this treatment should be done on the day of the experiment. A 5 minute 70 W plasma treatment renders the PDMS hydrophobic for more than 6 hours [165]. If the devices are stored in ionized water, the PDMS will remain hydrophobic for weeks.

Summary

The goal of this thesis is to demonstrate SPB capture, release, transport, and detection by means of low power and addressable SVs. SVs are devices based on the GMR effect. Background material on magnetism and magnetic materials, SVs, bead manipulation, bead sensing, microfluidics, magnetic carriers, and passivation was presented.

CHAPTER 2: GOVERNING EQUATIONS & MODELS

The following chapter will describe the governing equations for magnetophoresis as well as the modeling techniques used to evaluate the SVs.

Governing Equations for Bead Manipulation

A magnetic field gradient exerts a force on a magnetic particle. The gradient can be generated by means of permanent magnets or electromagnets; a uniform or homogeneous magnetic field can apply torque, but not translational movement. For the magnetic gradient to move the bead, the force induced by the gradient ($\mathbf{F_b}$) must be larger than the opposing drag force ($\mathbf{F_{drag}}$), Langevin force ($\mathbf{F_L}$) or Brownian motion, and gravitational forces ($\mathbf{F_g}$) exerted on the bead suspended in solution (Figure 43). The following section looks at the forces influencing the bead.

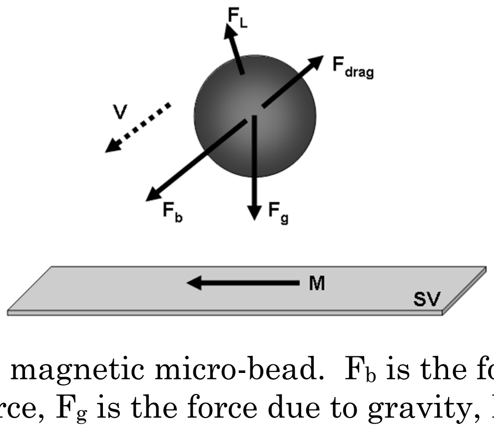

Figure 43: Forces on a magnetic micro-bead. F_b is the force from the SV trap, F_L is the Langevin force, F_g is the force due to gravity, F_{drag} is the drag force in a fluid medium with velocity V, and M is the magnetization of the SV.

We assume the magnetic beads (SPBs) are spherical and have a low density in suspension, thus we can neglect interparticle interactions. Also, we neglect the increased mass and drag force of the bead when bound to a biological sample.

The magnetic force (**F$_b$**) acting on a bead modeled as a point-like magnetic dipole (**m$_b$**) in the field gradient produced by the magnetic field (**B**) is,

$$\vec{\mathbf{F_b}} = (\vec{\mathbf{m_b}} \cdot \nabla)\vec{\mathbf{B}} \tag{4}$$

For our application, the ON SVs, current lines, and external magnetic fields generate the magnetic field gradients. The force generated by the magnetic field gradient is referred to as the "pull force". With a dense solution of SPBs, other polarized SPBs will also generate magnetic fields.

For a saturated magnetic bead suspended in water, a diamagnetic medium, the total moment will be $m_b = V_bM_b$, where V_b is the volume of the bead and Mb is the saturation magnetization [23]. The potential energy U_b of the bead is,

$$U_b = -\vec{\mathbf{m_b}} \cdot \vec{\mathbf{B}} \tag{5}$$

Because the energy of the applied field is much greater than the bead's Brownian motion energy (κT), where κ is the Boltzmann constant and T is the temperature in Kelvin, the energy can be simplified to,

$$U_b = -m_bB \tag{6}$$

Thus, we have,

$$F_b = -\nabla U_b = B\nabla m_b + m_b\nabla B \tag{7}$$

The first term can be neglected if we assume the bead is magnetically saturated and m is independent of B. When the bead is not in saturation, the force (**F$_b$)** is,

$$\vec{\mathbf{F}}_b = \frac{V_b \chi_{eff}}{2\mu_0} \nabla \vec{\mathbf{B}}^2 \tag{8}$$

where χ_{eff} is the effective susceptibility of the particle relative to the liquid medium and μ_0 is the permeability of free space ($\mu_0 = 4\pi \times 10^{-7}$ Vs/A/m) [23,125]. This force is proportional to the gradient of the magnetostatic field energy density, ½ **B·H,** where **H** is the strength of the magnetic field.

Stoke's law for the drag force (**F$_{drag}$**) on a sphere is,

$$\overrightarrow{\mathbf{F}}_{\mathbf{drag}} = -6\pi\eta R \overrightarrow{\mathbf{v}} \tag{9}$$

where η is the viscosity of the solution, R is the radius of the bead, and v is the velocity of the bead. Due to the size of the particle, the force due to gravity is negligible compared to the magnetic force, thus the velocity can be assumed to be in the direction of the field gradient.

In a fluid medium, beads also experience Langevin forces responsible for Brownian motion or random displacement. Observation of the Brownian motion can be used to determine the pull force from a magnetic trap [106]. Using the equipartition theorem, the spring constant (k_{trap}) of a magnetic trap is given by

$$k_{trap} = \frac{\kappa_B T}{\langle x^2 \rangle} \tag{10}$$

where κ_B is the Boltzmann constant, T is the temperature in Kelvin, an x is the displacement or the Brownian motion. At room temperature, $\kappa_B T = 4.0 \times 10^{-21}$ J and the superparamagnetic MyOne Dynabeads (diameter ~1 μm) will move an average distance of 0.7 µm/s [166]. A bacterium will experience 10 femto-Newtons of force every second [167].

The gravitational force (F_g) acting on a magnetic bead is given by,

$$\vec{\mathbf{F}}_{\mathbf{g}} = -m_b g \vec{\mathbf{e}_{\mathbf{z}}} \tag{11}$$

where m_b is the buoyant mass, g is the gravitational constant, and $\mathbf{e_z}$ is the unit vector in the z-direction. The MyOne Dynabeads have a gravitational force of 0.004 pN leading to a sinking speed of 0.5 µm/s [166]. Smaller beads will sink at a slower rate.

The Derjaguin-Lanau-Verwey-Overbeek (DLVO) force occurs when the particle or cells are charged in an electrolytic solution [168-171]. The DLVO force is caused by van der Waals and electrostatic forces on the surfaces of the beads and substrates. This force can become quite large when the beads are near the surface resulting in unwanted non-specific binding.

As shown in Figure 43, all these forces scale monotonously relative to the magnetic particle size [172]. Magnetic forces loose their dominance when the particle diameter drops below 200 nm.

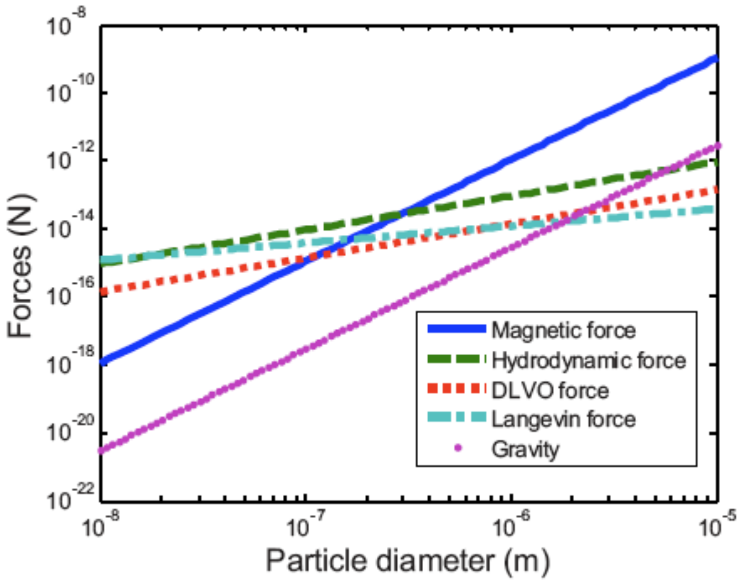

Figure 44: Plot of the strength of the magnetic force, hydrodynamic drag force, DLVO force, Langevin force, and gravity as a function of the particle size [172].

Magnetic Flux Density Equations

The magnetic field ($\mathbf{B_b}$) created by a magnetic particle approximated as a dipole field is:

$$\mathbf{B_b}(\mathbf{r}) = \frac{3\mu_0(\mathbf{m_b}\cdot\mathbf{r})\mathbf{r} - (\mathbf{r}\cdot\mathbf{r})\mathbf{m_b}}{4\pi r^5} \tag{12}$$

where **r** is the distance from the center of the bead, μ_0 is the permeability of free space, and **m** is the magnetic moment of the bead. This moment will depend on the external applied field as well as the field from the SV, write and read current lines, and other magnetized beads.

The magnetic field ($\mathbf{B}_i$) generated by a current line is calculated with the Biot-Savart Law for an infinite wire,

$$\mathbf{B_i}(r) = \frac{\mu_0 I}{2\pi r} \tag{13}$$

where **r** is the distance from the center of the wire and I is the current. For a flat current line, the maximum gradient occurs at the center of the line.

The magnitude of the B-field generated by a current line is limited by Ohmic heating [173]. For a normal wire with current I and width w on a planar substrate, the maximum current-to-width ratio is,

$$\frac{I}{w} \leq \left(\frac{\kappa \Delta T_{max}}{\rho}\right)^{1/2} \tag{14}$$

where κ is the thermal conductivity of the metal, ΔT_{max} is maximum temperature difference between the substrate and the wire, and ρ is the electrical resistivity. For gold, Drndic found $I/w \leq 1 \times 10^4$ A/cm.

The SV magnetic flux density was modeled with an equivalent-charge model. The external magnetic flux density **B** for a rectangular bipolar (bar) magnet with the saturation magnetization M_s along the z-axis is:

$$\overrightarrow{\mathbf{B}}(x,y,z) = \frac{\mu_0 M_s}{4\pi} \sum_{k=1}^{2} (-1)^k \int_{y_1}^{y_2} \int_{x_1}^{x_2} \frac{[(x-x')\hat{\mathbf{x}} + (y-y')\hat{\mathbf{y}} + (z-z')\hat{\mathbf{z}}]dx'dy'}{[(x-x')^2 + (y-y')^2 + (z-z')^2]^{3/2}} \tag{15}$$

where μ_0 is the permeability of free space. The flux density of multiple layers can be modeled by means of superposition:

$$\overrightarrow{\mathbf{B}}(x,y,z) = \sum^{n} \overrightarrow{\mathbf{B}_\mathbf{i}}(x,y,z) \tag{16}$$

where $\mathbf{B}_i$ is the field due to the *i*th block [31].

SV Pull Force Calculation

The effect of bead size, SV aspect ratio, and array lattice spacing on the pull force was evaluated with an equivalent-charge model. An equivalent-charge model reduces the three dimensional (3D) SV to an equivalent distribution of magnetic surface charges. In the case of the SV, the charges will be located on the blunt ends of the SV as shown in Figure 45.

MatLab (refer to Appendix B: MatLab Code) was programmed to calculate the 3D magnetic flux density and pull-force vectors generated by a multilayer SV in the ON and OFF orientations, as shown in Figure 45. The SV has length L and width W. H_{Py} is the thickness of the Permalloy ($Ni_{19}Fe_{81}$), H_{CoFe} is the thickness of the CoFe, H_{Cu} is the thickness of the copper spacer, and t is the thickness of the passivation layer. The SV depicted in Figure 45 is in the ON state; for the OFF state, the charges will be reversed on the top Permalloy/CoFe layer.

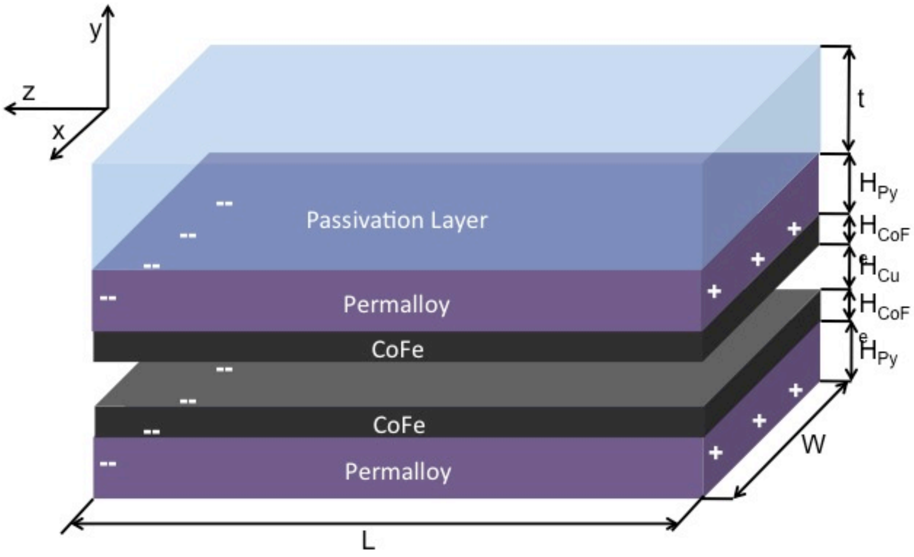

Figure 45: Equivalent-charge SV multilayer model for pull force calculations. H_{Py}, H_{CoFe}, H_{Cu}, and t represent the thickness of the Permalloy ,CoFe, Cu, and passivation layers, respectively. Image not to scale.

The properties of Dynabeads (Invitrogen) were used to evaluate the SVs due their commercial availability and common use in manipulation and sensing bioapplications. The effective magnetic susceptibilities chosen for the

1 μm, 2.8 μm, and 4.5 μm diameter Dynabeads were 1.458, 0.976, and 1.6, respectively [174]. The susceptibility of the beads is not proportional to their size due to different iron-content percentages.

SPB Size and Pull Force

The magnetic flux densities and pull forces for 1 μm, 2.8 μm, and 4.5 μm diameter Dynabeads on the passivation surface were calculated. For the model, W = 1 μm, L = 8 μm, H_{Py} = 15 nm, $M_{s,Py}$ = 800 kA/m, H_{CoFe} = 5 nm, $M_{s,CoFe}$ = 1400 kA/m, H_{Cu} = 10 nm, and t = 70 nm. For the model, we assumed the SV was saturated, so the field and pull forces calculated were best-case estimations.

The SV B-field magnitude and maximum pull-force contour plots for 1.0 μm, 2.8 μm, and 4.5 μm diameter Dynabeads located on the surface of the passivation layer are shown in Figure 46. Only the area around the SV's blunt end (shown in black) was meshed due to limitations in computer memory. For all these plots, the y-axis slice was in the plane where the SPB center would be located when on the surface of the passivation layer. For example, y = 1.52 μm for the 2.8 μm SPB (0.05 μm thick SV + 0.07 μm passivation layer + 1.4 μm bead radius). This height estimate is a conservative estimate; the bead could potentially be closer to the SV due to conformal coating of the gold, nitride, and SV layers during fabrication.

(a) 1.0 µm Dynabead on the passivation surface

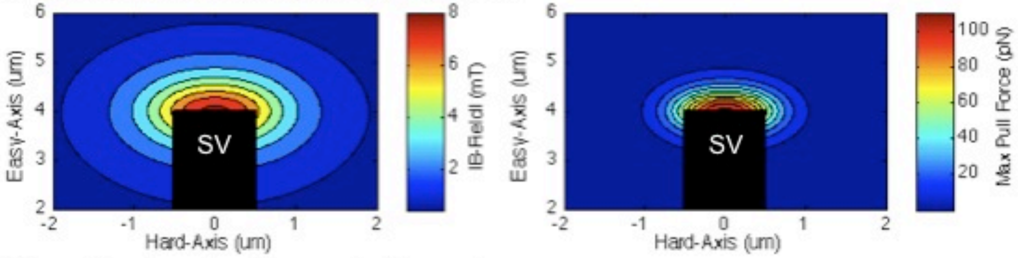

(b) 2.8 µm Dynabead on the passivation surface

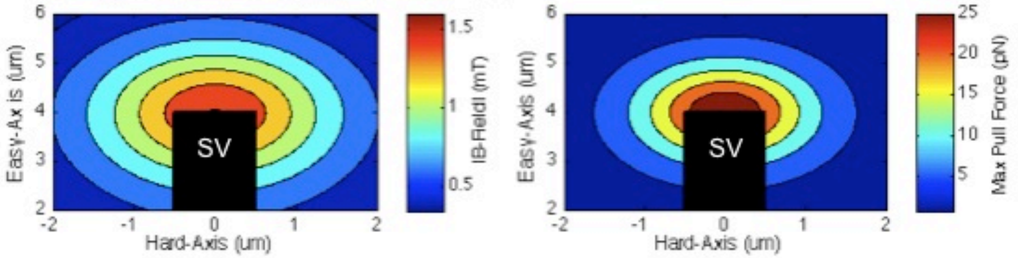

(c) 4.5 µm Dynabead on the passivation surface

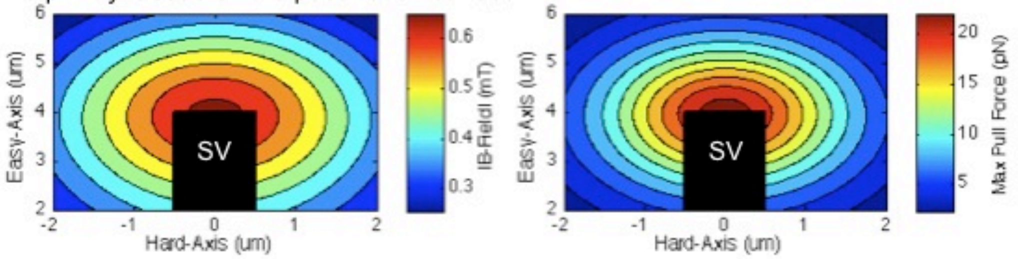

Figure 46: B-field magnitude and maximum pull force near the blunt end of the 1 μm × 8 μm SV (shown in black) for (a) 1.0 μm, (b) 2.8 μm, and (c) 4.5 μm diameter Dynabeads on the surface of the passivation layer.

As seen in Figure 46, a small bead will experience a larger pull force compared to a large bead on the same SV. The maximum calculated pull forces for the ON and OFF SVs are given in Table 3. A bead with a smaller diameter will be closer to the source of the magnetic field resulting in the bead being more magnetized (larger magnetic moment). Additionally, the curvature in the magnetic flux is greater near the source, which also results in a larger pull force. Ideally when the SV is OFF, there would be no pull force attracting the bead; however, some force is present due to asymmetry (bead is closer to one magnetic layer).

Table 3: Calculated maximum pull force on chip surface for Dynabeads (Invitrogen) with a diameter of 1.0 μm, 2.8 μm, and 4.5 μm on a 1 μm × 8 μm SV. The χ_{eff} values are for Dynabeads suspended in PBS [174].

Bead Diameter	**Fe Content**	**χ_{eff} (Unit Less)**	**Max Pull Force SV ON**	**Max Pull Force SV OFF**
1.0 μm	26%	1.458	112 pN	0.221 pN
2.8 μm	12%	0.976	29.6 pN	0.014 pN
4.5 μm	20%	1.6	22.9 pN	0.005 pN

To put these forces into perspective, the force of an adenosine triphosphate (ATP) molecular motor is on the order of 10 pN, while covalent bonds can be broken with nano-Newton forces [167]. Motor proteins generate 5-4500 pN of force and kilo-Newton of force when working together [175].

Figure 47 shows how quickly the pull force reduces as the bead is moved vertically away from the field source (blunt end of the SV); the blue curve represents a 2.8 μm SPB on the surface of the passivation layer. In order to maximize the strength of the SVs, the distance between the SV and SPB should be minimized; however, a passivation layer is necessary to prevent non-specific binding and to reduce SV corrosion. Promoting bead settling on the passivation surface will increase the probability of bead trapping due to the higher pull forces near the SV.

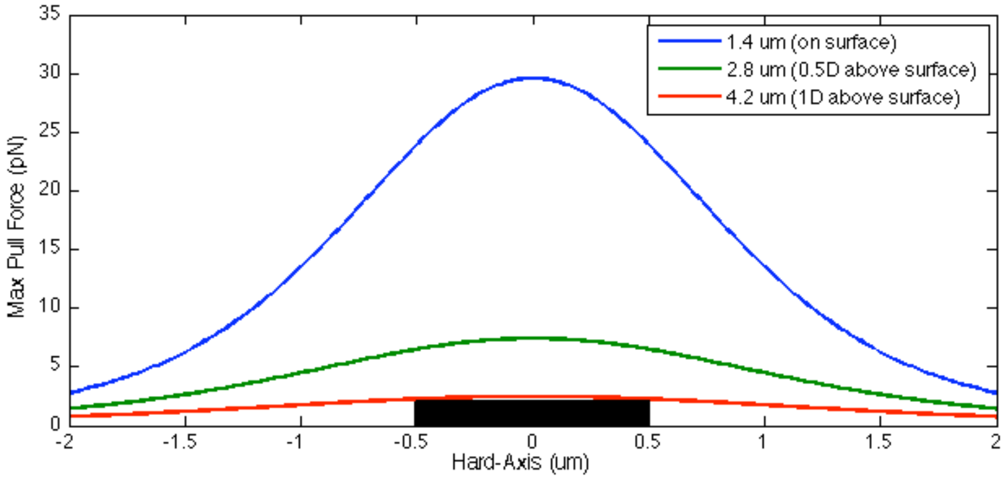

Figure 47: Maximum pull forces for the 2.8 μm bead along the blunt edge of the SV in relation to the distance between the bead and the SV. The blue line shows the pull force of a bead on the surface of the passivation layer.

In summary, as the bead is reduced in size and the SV dimensions are kept constant, the maximum pull force will increase; however, the force is also dependent on the effective susceptibility of the bead as well as the distance between the bead and the SV. The susceptibility will greatly depend on the composition of the bead. Higher pull forces can be achieved by increasing the bead's iron content.

SV Aspect Ratio and Pull Force

The effect of SV aspect ratio on the pull force was evaluated for the 1.0 μm, 2.8 μm, and 4.5 μm diameter Dynabeads. Figure 48 shows the pull force for 1.0 μm, 2.8 μm, and 4.5 μm Dynabeads corresponding to an 8 μm long SV with varying width (0.25-6.0 μm). When the width of the SV is smaller than the diameter of the bead, the forces will not be very large. As the width increases, the projection of the field along the z-axis (along the length axis) increases resulting in an increased pull force; however, the observation point of the bead also moves further from the field source as the width increases, thus reducing the pull force. The projection effect dominates for small SV widths and the observation effect dominates for large SV widths.

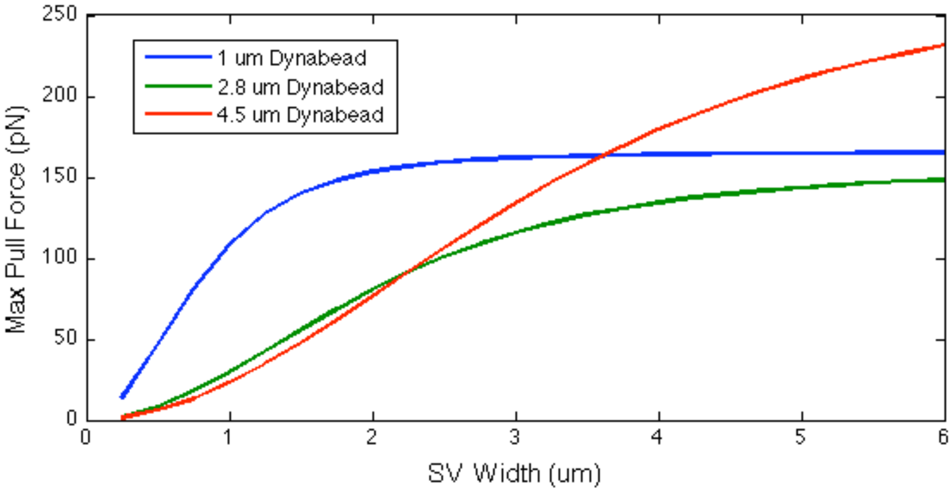

Figure 48: Maximum pull force for the 1 μm, 2.8 μm, and 4.5 μm Dynabeads as the width of the 8 μm wide SV is increased.

Figure 49 shows the pull force for 1.0 μm, 2.8 μm, and 4.5 μm Dynabeads corresponding to the 1 μm wide SV with varying length (2-10 μm). The length of the SV has little effect on the pull force; however, a high aspect ratio increases the AMR and lowers the potential for multi-domain SVs. A SV with high AMR is also more likely to be bistable.

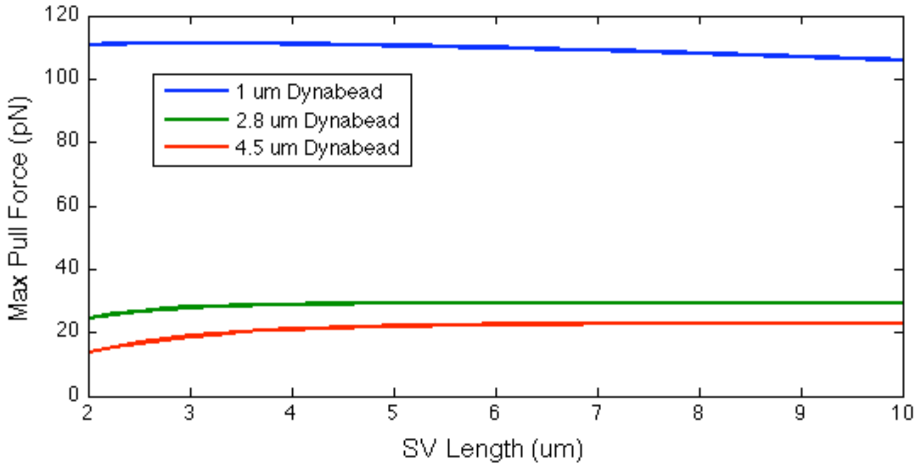

Figure 49: Maximum pull force for the 1 μm, 2.8 μm, and 4.5 μm Dynabeads as the length of the 1 μm wide SV is increased.

Array Lattice and SV State

The effect of the SV array lattice and state on the pull force was evaluated. Identical to the previous model, H_{Py} = 15 nm, $M_{s,Py}$ = 800 kA/m, H_{CoFe} = 5 nm, $M_{s,CoFe}$ = 1400 kA/m, H_{Cu} = 10 nm, and t = 70 nm. Unless otherwise noted, the SVs evaluated were 1 μm wide × 8 μm long and only the 2.8 μm Dynabeads were incorporated into these models.

Figure 50 shows the B-field and pull-force contour plots for a 3 × 3 array of ON SVs. The SVs are on a 3 μm × 10 μm lattice. When adjacent SVs were ON, the magnitude and gradient of the flux density around the adjacent blunt ends was distorted and reduced due to the proximity of the opposite polarities. This led to a 5 pN reduction in the pull force at those blunt ends.

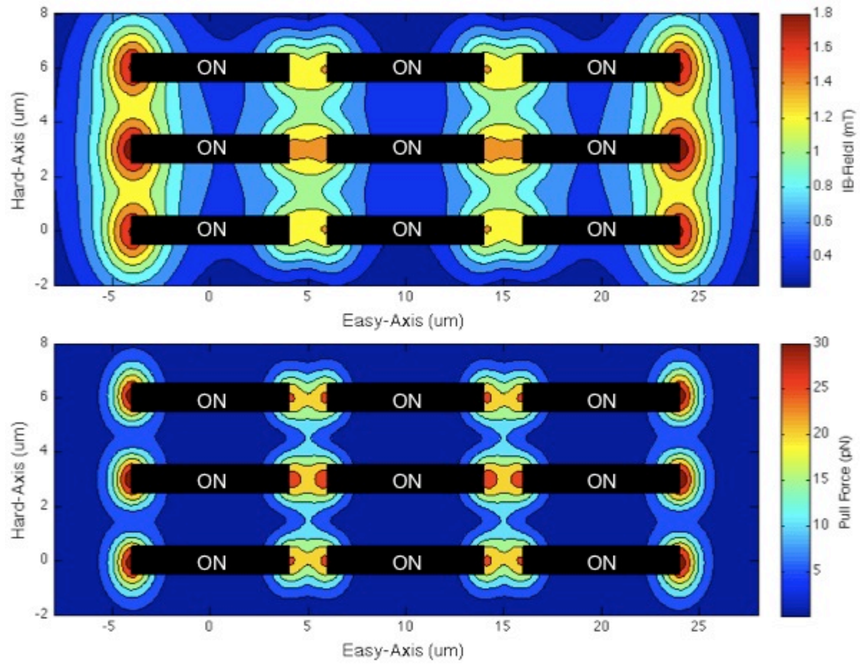

Figure 50: B-field and 2.8 μm Dynabead pull-force contour plots for a 3 × 3 array of ON SVs attracting a 2.8 μm Dynabeads.

Figure 51 shows the B-field and pull-force contour plots when all but the center SV were ON. The presence of the center OFF SV had little effect on the surrounding flux density and pull forces. As observed in Figure 50, the center ON SVs (bottom and top) distorted and reduced the pull forces of the nearest-neighbor SVs due to the proximity of the opposite polarities.

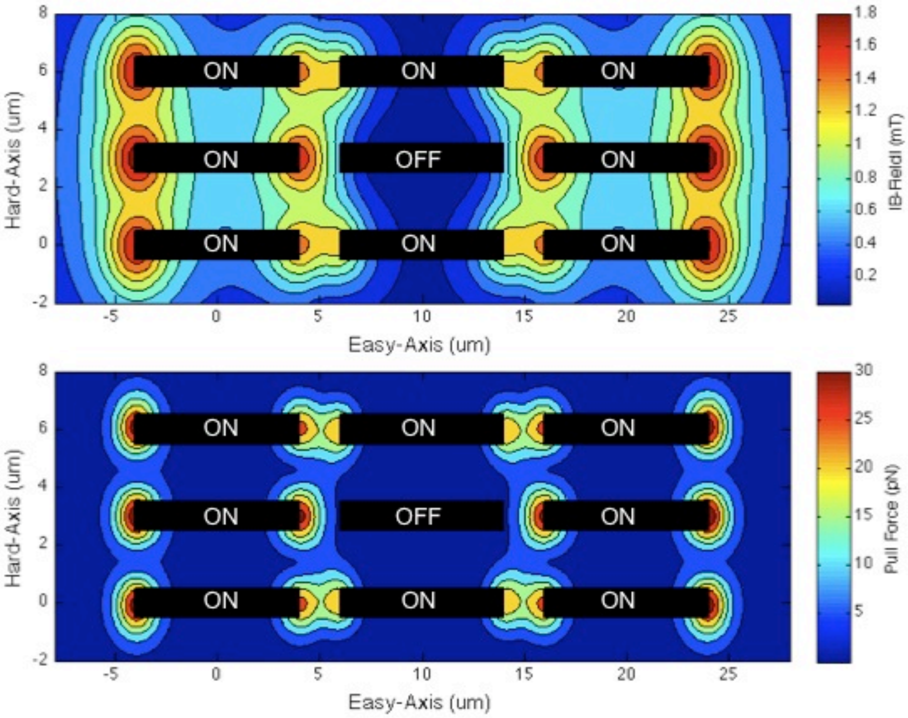

Figure 51: B-field and 2.8 μm Dynabead pull-force contour plots for a 3 × 3 array of SVs with all but the center SV ON.

Figure 52 shows the B-field and pull-force contour plots when all but the center column of SVs were ON. The presence of the OFF SVs broadened the B-field, but had negligible effect on the pull force of the SVs in the first and third column. Unlike the previous cases (Figure 50 and Figure 51), the pull forces on the blunt ends of the ON SVs were not distorted or reduced in magnitude.

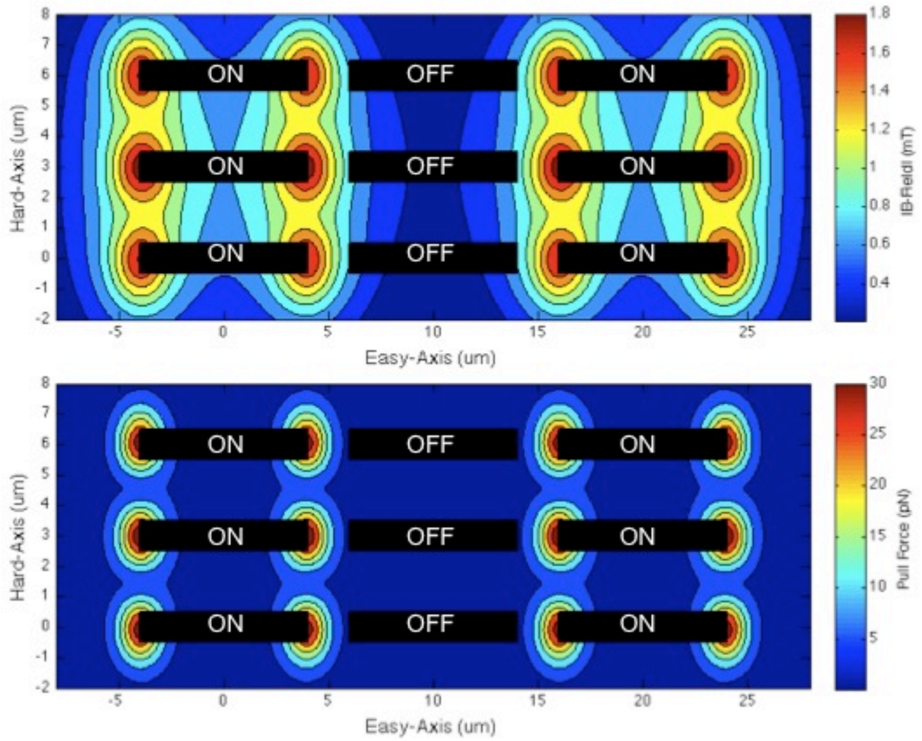

Figure 52: B-field and 2.8 μm Dynabead pull-force contour plots for a 3 × 3 array of SVs with all but the center column of SVs ON.

A symmetrically staggered array of 1 μm × 8 μm SVs was also evaluated. Figure 53 shows the B-field and pull-force contour plots for the staggered array of all ON SVs. To create the symmetrically staggered or rhombic array of SVs, the SVs were located at lattice points (0 μm, 0 μm), (0 μm, 3 μm), and (10 μm, 1.5 μm). The adjacent ON SVs distorted and reduced the magnitude and curvature of the flux density around the neighboring blunt ends due to the proximity of the opposite magnetic polarities, and this also led to a reduction in pull forces. Compared to the rectangular array of SVs, the staggered-array pull-force contours were less distorted.

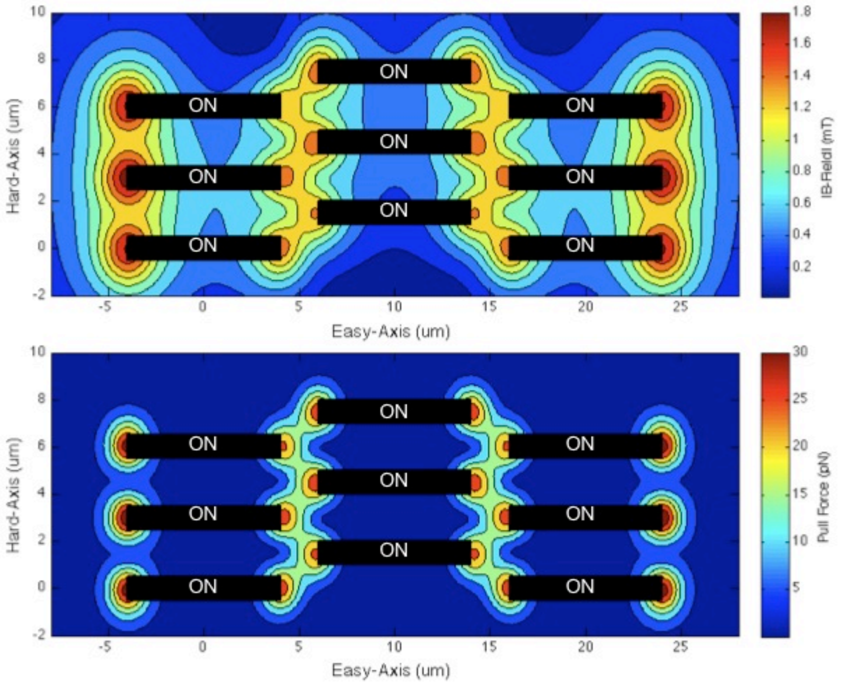

Figure 53: B-field and 2.8 μm Dynabead pull-force contour plots for a symmetrically staggered 3 × 3 array of SVs with all the SVs ON.

Figure 54 shows the B-field and pull-force contour plots for the staggered array of SVs with all but the center SV ON. The presence of the center OFF SV had little effect on the surrounding SV pull forces. The center ON SVs (bottom and top) reduced and distorted the pull force of the nearest-neighbor SVs due to the proximity of the opposite polarities.

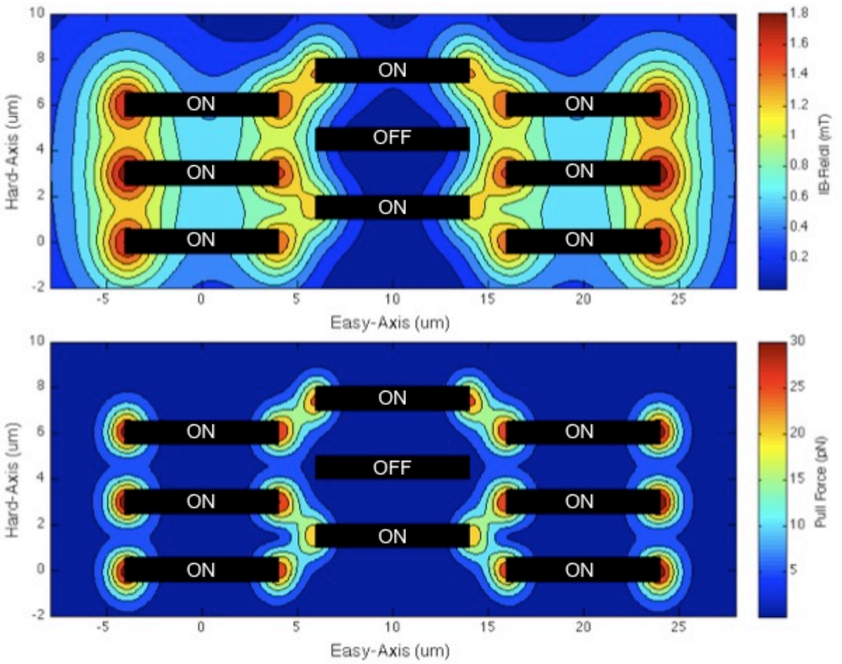

Figure 54: B-field and 2.8 μm Dynabead pull-force contour plots for a symmetrically staggered 3 × 3 array of SVs with all but the center SV ON.

Figure 55 shows the B-field and pull-force contour plots when all but the center column of SVs were ON. The presence of the OFF SVs broadens the B-field, but had negligible effect on the pull forces of the ON SVs.

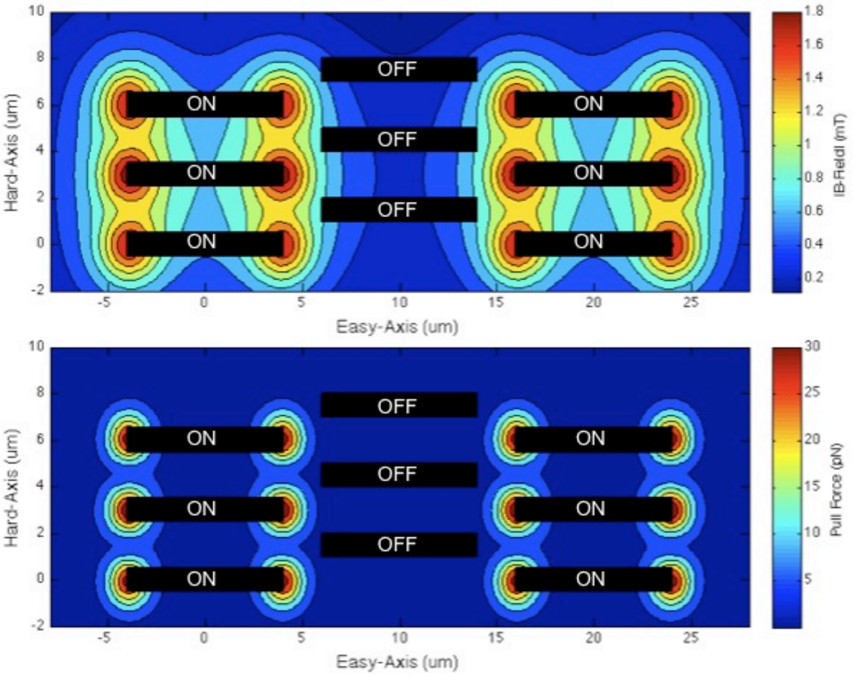

Figure 55: B-field and 2.8 μm Dynabead pull-force contour plots for a symmetrically staggered 3 × 3 array of SVs with all but the center column of SVs ON.

Next, the same SV array was evaluated for trapping 1 μm Dynabeads and the resulting pull-force contour plot is shown in Figure 56. In this array, all but the center SV were ON. Unlike the 2.8 μm bead pull-force contour plot for the same array dimension and SV states (Figure 54), the pull forces were not distorted or reduced due to the state of adjacent SVs. Additionally, the maximum pull force on the 1 μm Dynabead was over three times the maximum pull force on the 2.8 μm bead. A bead diameter equivalent to the SV width permits the bead center to be closer to the magnetic source resulting in a higher flux density (more magnetized bead) and higher field curvature (larger pull force).

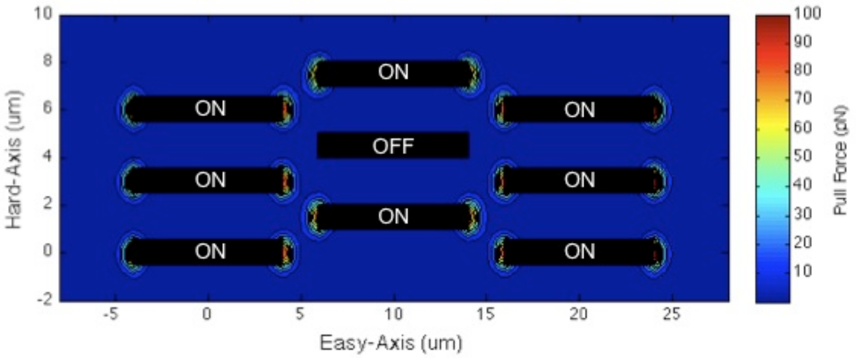

Figure 56: B-field and 1 μm Dynabead pull-force contour plot for a symmetrically-staggered 3 × 3 array of SVs with all but the center SV ON.

Figure 57 shows the pull-force contour for a 2.8 μm bead on 3 μm by 8 μm SVs with all but the center SV ON. The lattice was 9 μm × 28 μm with SVs located at coordinates (0 μm, 0 μm), (0 μm, 9 μm), and (14 μm, 4,5 μm). Matching the bead diameter and SV width, as well as increasing the lattice size generated high and isolated SV pull forces.

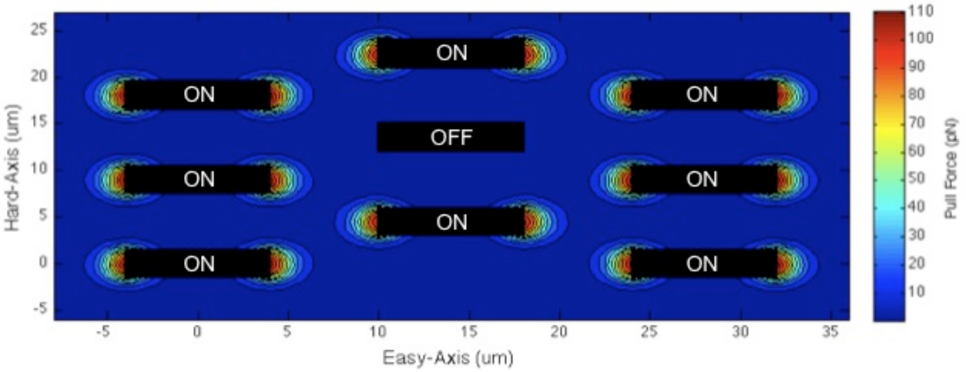

Figure 57: B-field and 2.8 μm Dynabead pull-force contour plot for a symmetrically-staggered 3 × 3 array of 3 μm × 8 μm SVs with all but the center SV ON.

In summary, the array and SV dimensions can be manipulated to achieve optimal trapping conditions for a specific sized bead. A larger bead will require larger SVs and array spacing to limit pull-force interference between adjacent SVs. Additionally, the state of adjacent SVs may impact array performance.

Landau-Lifshitz-Gilbert (LLG) Equation for SV Switching

The Landau-Lifshitz-Gilbert (LLG) equation was employed to estimate the magnetic switching fields of the SV free layer. Low switching fields are desirable due to current limitations in the write line. The LLG equation describes the response of a single-domain magnet with unit vector magnetization ($\hat{\mathbf{m}}$) to an effective magnetic field ($\mathbf{H_{eff}}$) [176-177]. The equation is,

$$\frac{d\hat{\mathbf{m}}}{dt} = |\gamma_g|\mu_0\hat{\mathbf{m}} \cdot \mathbf{H_{eff}} + \alpha\hat{\mathbf{m}} \cdot \frac{d\hat{\mathbf{m}}}{dt} - |\gamma_g|\frac{A}{M_s V}(\tau_{\parallel} + \tau_{\perp}) \tag{17}$$

where the γ_g is the gyromagnetic ratio, μ_0 is the magnetic vacuum permeability, $\hat{\mathbf{m}} = \mathbf{M}/M_s$, α is the damping parameter, M_s is the saturation magnetization, V is the volume, A is the sample area, and τ is the spin-transfer torque. The first term describes the processional motion of **M** around **H.** The second term applies damping to settle devices into the lowest energy configuration with **M**||**H**. For low-speed switching, we are mostly concerned with the second term [178].

A LLG model was used to evaluate the effect of SV width, length, aspect ratio, and thickness on the switching field. Because the SV will be toggled ON and OFF with a magnetic field generated by a current line, the switching fields should be small to avoid current line burnout: the maximum current density of gold is on the order of 10^8 A/cm^2. The LLG model assumed the entire SV free layer contained only one domain and incorporated a demagnetization field. For the simulation, the SV was assumed to be rectangular (Figure 58) and an average magnetic saturation M_s based on percent thickness represented the Permalloy (M_s = 800kA/m) and CoFe (M_s = 1400 kA/m) FM layers. With 15 nm Permalloy and 5 nm CoFe, the $M_{s,avg}$ = 950 kA/m. The gyromagnetic ratio γ_g was 2π × 28 GHz/T and the damping parameter α was 0.1. To compare these models to actual data, a bias field was applied to the model to account for the FM coupling and shape anisotropy biasing the actual SV free layer.

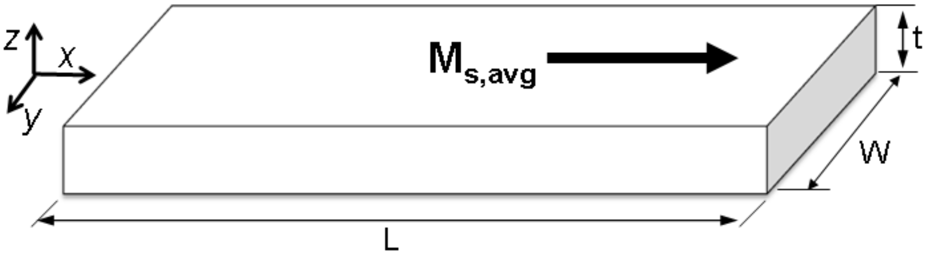

Figure 58: LLG single-domain rectangular free-layer model. M_s is averaged for the FM Permalloy and CoFe.

As shown in Figure 59, the averaged M_s (LLG Py & CoFe) model biased with 2.6 mT compared well with the experimental MR data for the 1 μm × 8 μm bottom-pin SV. Multiple domains in the SV cause the rounded switching seen in the MR data. Simply using Permalloy (LLG Py) under approximated the switching fields.

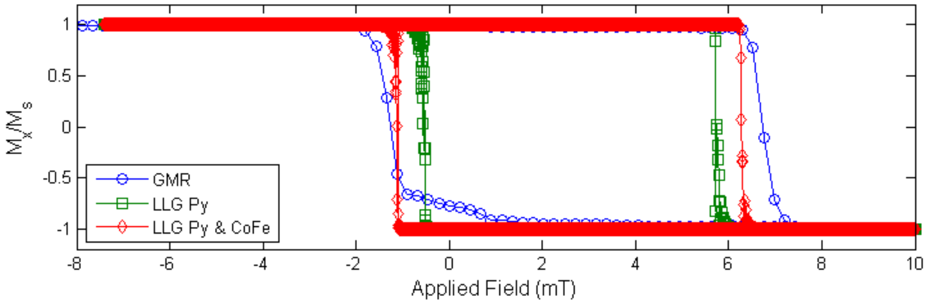

Figure 59: Comparison of biased LLG model to GMR data for a 1 μm × 8 μm bottom-pin SV.

Figure 60 demonstrates that varying the SV length does not have a significant effect on the coercivity compared to varying the SV width. As the free-layer length (aspect ratio) increased from 4 μm to 10 μm, the coercivity increased 9%. As the free-layer width increased from 0.5 μm to 2 μm, the coercivity increased 260%. However, the aspect ratio will affect the demagnetization field, which influences the rententivity; a lower aspect ratio device may not be bistable at zero applied field. Additionally, a wider SV may promote trapping of more than one bead, which may or may not be desirable.

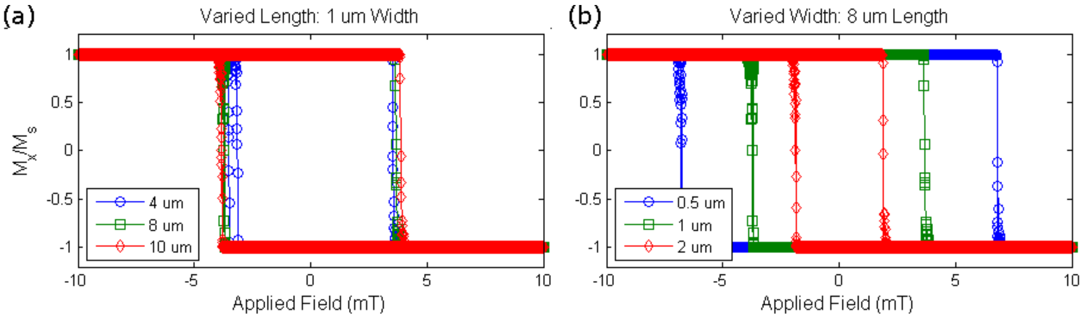

Figure 60: (a) Effect of SV length (1 μm width) on free-layer low-field switching, (b) effect of SV width (8 μm length) on free-layer low-field switching.

As predicted by Equation (2), increasing the thickness of the FM layer increases the coercivity (Figure 61). While keeping the Permalloy and CoFe thickness percentages constant, increasing the free layer thickness from 10 nm to 30 nm resulted in a 130% increase in the coercivity. Because CoFe has a higher saturation magnetization, if the CoFe layer thickness remains 5 nm and the Permalloy thickness increases to 25 nm ($M_{s,avg}$ = 900 kA/m), the coercivity will not increase as much due to the lower moment.

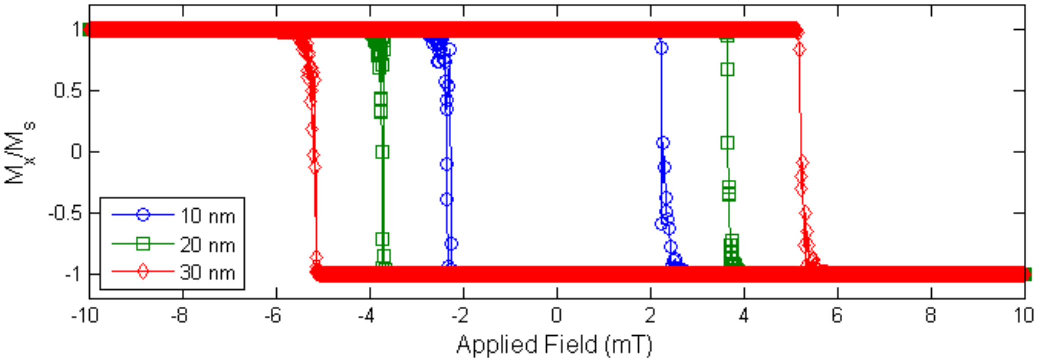

Figure 61: Free-layer coercivity dependence on free-layer thickness.

By controlling the width, aspect ratio, and thickness of the SV, the coercivity, B-field, pull force can be optimized for specific bead manipulation applications.

Object Oriented Micro-Magnetic Framework (OOMMF) for SV Switching

Object Oriented Micro-Magnetic Framework (OOMMF) software was used to evaluate a multi-domain 2D free layer model and 3D SV model. The complex MR response of the SV can be understood by evaluating the domain structure predicted by OOMMF.

OOMMF (http://math.nist.gov/oommf/) is a free modeling program that uses a Landau-Lifshitz ordinary differential equation (ODE) solver to relax 3D spins onto a 2D square mesh. The domain structure and switching characteristics of the SV were studied with this multi-domain modeling software. The solver incorporates the self-magnetostatic (demagnetizing) field, anisotropy, applied field, and initial magnetization.

OOMMF 2D Free Layer Model

The SV free layer was modeled as both a Permalloy (M_s = 800 kA/m) and a Permalloy/CoFe ($M_{s,avg}$ = 950 kA/m) rectangle 8 μm long, 1 μm wide, and 10 or 20 nm thick. One side of the cubic cell size is equivalent to the thickness of the free layer. The hysteresis curves are shown in Figure 62. For comparison, a bias field of +3 mT was applied to the OOMMF 2D model to compare to the MR data. The OOMMF 2D model overestimates the coercivity in all cases. Similar to results found by Russek, the actual switching fields are only 40-60 % of the ones predicted by the OOMMF model [88].

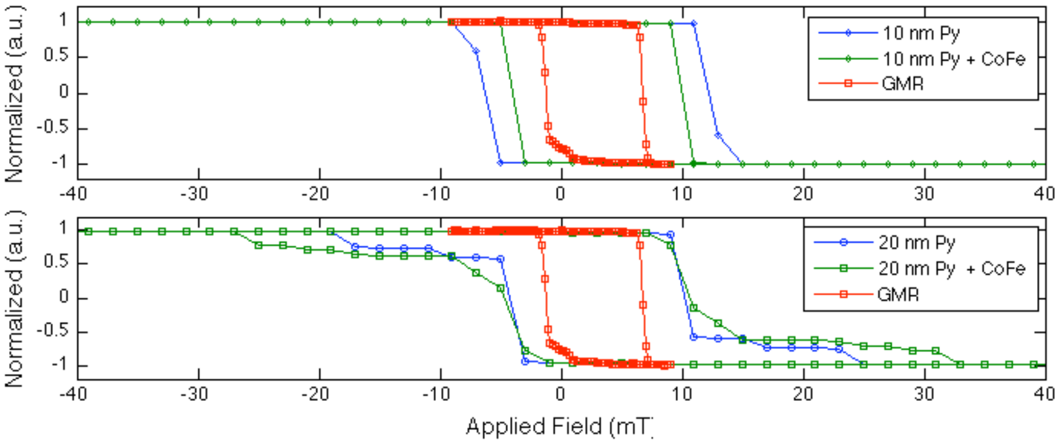

Figure 62: OOMMF 2D model with varied thickness and M_s values compared to the 1 μm × 8 μm top SV MR.

In the 20 nm thick free layer, OOMMF predicts edge domains (see Figure 63), which cause the “foots” seen at ± 20 mT in Figure 62. This feature is not seen in the free-layer MR switching data; however, it is seen in the pinned-layer MR switching.

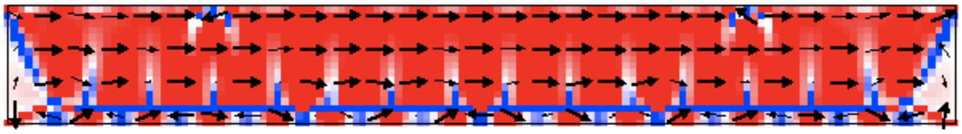

Figure 63: Edge domains seen in the OOMMF 2D 20 nm thick models. The edge domain impedes switching.

OOMMF 3D SV Model

With OOMMF Oxsii, a 3D model incorporating both the pinned-bottom and free-top magnetic layers was simulated. To view the .mif file, refer to Appendix C: OOMMF .mif File. The modeled SV was 8 μm long and 1 μm wide; both the free-layer and pinned-layer thicknesses were 20 nm, and the copper spacer was 10 nm thick. The cell size was 50 nm × 40 nm × 10 nm. The standard six-nearest-neighbor exchange energy was 13×10^{-12} J/m. AFM surface exchange coupling (Ruderman-Kittel-Kasuya-Yosida (RKKY)-style coupling) between the top and bottom layers was represented by σ and σ_2 and both were equal to -1×10^{-15} J/m^2. Due to the spacer being quite thick, it was assumed that there was not much RKKY interaction between the two magnetic layers. Higher σ and σ_2 energies result in a more slanted and biased free-layer hysteresis curves. A large bias field of 60 kA/m (75 mT) was applied to the bottom magnetic layer. The saturation magnetization for Permalloy is 800 kA/m. Uniaxial anisotropy was set along the long-axis of the SV. An applied field of 100 mT 2° off axis is applied along the long axis in 2 mT steps. The model result was compared to the 1 μm × 8 μm SV MR as seen in Figure 64. The coercivity of the OOMMF model was larger than what was measured with MR; this could be due to the model's large bias field or the estimated nearest-neighbor or RKKY energies. Remanent edge domains in the real device can lower the coercivity by providing nucleation for the switching. The extended switching at the ends is due do edge domains along the length of the SV as shown in Figure 63.

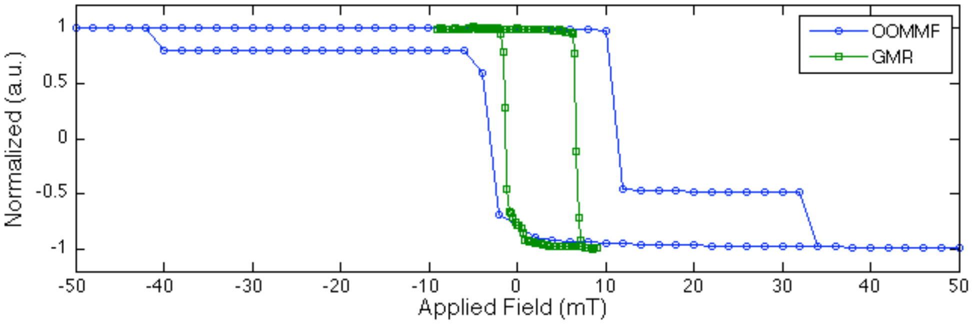

Figure 64: OOMMF 3D model compared to MR and MOKE data.

Summary

Magnetic field gradients exert a pull force on SPBs. The gradient can be generated with current lines, an external applied magnetic field, or SVs. In additional to magnetic pull forces, the bead will also experience gravitational, Langevin, drag, and DLVO forces. The magnetic pull force depends on the type of bead, the distance from the SV, the state of the SV, the dimensions of the SV, and the array density. The SV switching field depends on the SV dimensions and magnetic domains.

CHAPTER 3: FABRICATION

The following chapter will describe the generic fabrication process for all the samples. Numerous design modifications and mask revisions were completed to optimize the fabrication process and chip design, but this chapter will mostly focus on the most current wafer design. Detailed process charts for designs reported in this work can be found in Appendix D: Fabrication Process Charts. The bottom-to-top fabrication was completed within facilities on the National Institute of Standards and Technology (NIST) campus. These facilities included a state-of-the-art cleanroom.

Process Overview

The generalized process chart for the fabrication of all the SV chips is shown in Figure 65. First, write lines were evaporated onto a clean substrate, and then plasma-enhanced chemical vapor deposition (PECVD) silicon nitride was deposited to electrically insulate the write lines from both the SVs and read lines. The SV thin film was deposited in a DC-magnetron sputtering system, and then annealed with a magnetic annealer. Lithography and ion milling patterned the SV thin film into SV traps. Read line contact leads were evaporated on top of the SVs for direct electrical contact. Reactive ion etching (RIE) of the insulating silicon nitride exposed the write lines. The surface of the chip was passivated with PECVD silicon nitride. For the final step, a molded PDMS microfluidic channel was positioned over the SVs and sealed to the silicon nitride passivation layer.

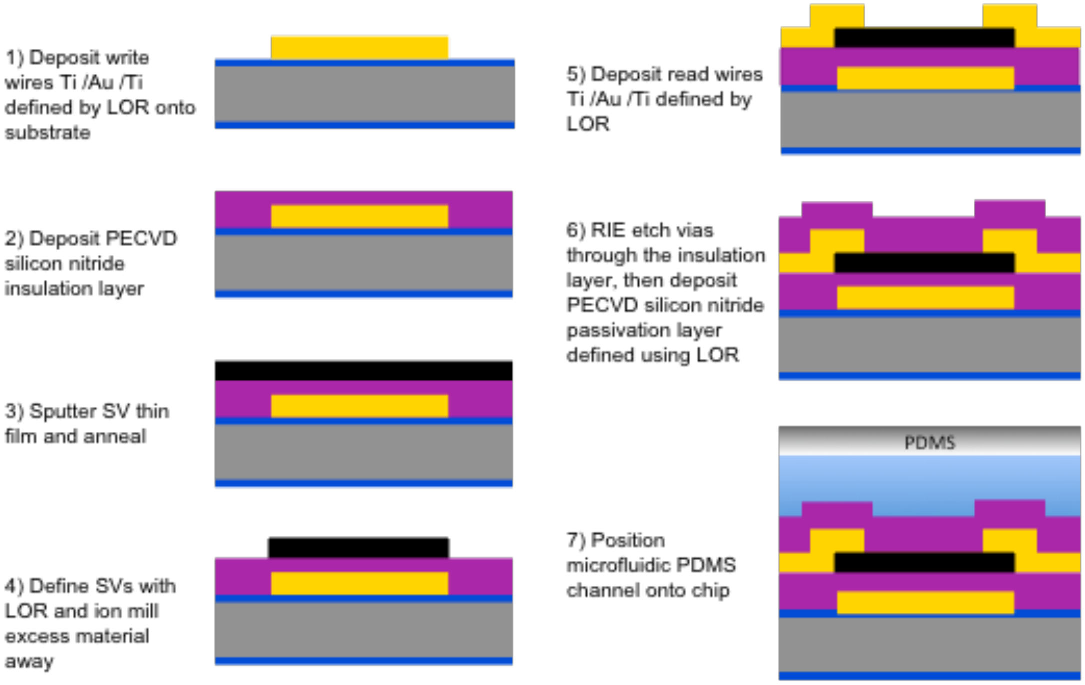

Figure 65: Generic fabrication process chart for the SV-microfluidic chips (not shown to scale).

When testing the DC-magnetron sputtering conditions, only the SV sputtering, ion milling, and read line deposition were completed (Steps 3 through 5). For magneto-optical Kerr effect (MOKE) testing, only the SV sputtering and ion milling were completed (Steps 3 and 4). For the initial microfluidic testing, an open SU-8 channel was used in lieu of the encapsulated PDMS channel. Detailed wafer designs are discussed in CHAPTER 6: SUPERPARAMAGNETIC BEAD (SPB) MANIPULATION.

Substrate

Excluding the samples for testing the magnetron sputtering system, the starting substrate was a 390 μm thick double-side-polished silicon <100> wafer coated with 200-400 nm of low-pressure chemical vapor deposition (LPCVD) silicon nitride. Prior to being placed in the Tystar furnace for deposition, the natural oxide on the silicon wafer was stripped with a 4% hydrofluoric acid (HF) wet etch. A 6:1 ratio of dichlorosilane and ammonia during deposition produced a nitride that was neither compressive, nor tensile. The oxide-stripped wafers were placed in the furnace for 1-2 hours at 835 °C with 12 sccm ammonia and 59 sccm dichlorosilane; the pressure was 250 mTorr. Silicon nitride is a hard ceramic with moderate thermal conductivity and high fracture toughness often used as an insulating layer. The surface of nitride is naturally hydrophobic.

Single-side-polished B-doped Czochralski (CZ) silicon <100> wafers with a native silicon oxide layer were the substrate of choice for testing the DC-magnetron sputtering conditions. The insulating oxide layer was not removed prior to sputtering the SV thin film.

Prior to depositing (evaporating) the write lines, alignment marks (AMs) were etched into the LPCVD silicon nitride using an 8 minute RIE etch. AMs enable the 5X ASML Reduction Stepper to align the mask layers with a precision of 200 nm. The AMs on the single-side-polished wafers were etched into the sputtered SV thin film with a 16.5 minute ion mill.

DC-Magnetron Sputtering

A DC magnetron sputtering system was utilized to deposit tantalum (Ta), Permalloy ($Ni_{80}Fe_{20}$), cobalt iron ($Co_{90}Fe_{10}$), copper (Cu), ruthenium (Ru), and iridium manganese ($Ir_{20}Mn_{80}$). The base pressure of the high-vacuum system ranged from 10^{-8} to 10^{-10} Torr. Purified argon was the sputtering gas. The wafer was rotated 20-30 revolutions per minute (rpm) during deposition and the sputtering rates averaged 1-2 Å/s; specific rates can be found in Appendix D: Fabrication Process Charts. The magnetic films were deposited in an applied field of 25 mT to create an easy axis along the long dimension of the SV (also along the wafer flat) and to set the pinning layer. Deposition pressures and powers were varied to determine their effect on the SV thin-film hysteresis (refer to page 108).

Both top-pin and bottom-pin SVs were fabricated. Nearly identical to the SV recipe used by Mirowski, the top-pin SV thin-film stack consisted of substrate-5 nm Ta/15 nm $Ni_{80}Fe_{20}$/5 nm $Co_{90}Fe_{10}$/10 mm Cu/5 nm $Co_{90}Fe_{10}$/15 nm $Ni_{80}Fe_{20}$/10 nm $Ir_{20}Mn_{80}$/ 5 nm Ta [114]. The bottom-pin SV stack consisted of substrate/3 or 5 nm Ta/3 or 5 nm Cu/10 nm $Ir_{20}Mn_{80}$/15 nm $Ni_{80}Fe_{20}$/5 nm $Co_{90}Fe_{10}$/10 nm Cu/5 nm $Co_{90}Fe_{10}$/15 nm $Ni_{80}Fe_{20}$/5 nm Ta/0 or 3 nm Ru. The magnetic layers are thicker than those typically used for SV sensors (refer to GMR Sensor Technology: A Review on page 48) because we required devices with large magnetic gradients to trap micro-beads. Due to availability, the $Co_{90}Fe_{10}$ has replaced the Co layer found in Mirowski's SVs. The $Co_{90}Fe_{10}$ layers limit diffusion between the Cu and $Ni_{80}Fe_{20}$ layers, reduce intercoupling, and increase GMR [76,78]. The bottom Ta layer serves as a seed layer while the top layer protects the SVs from corrosion. The bottom Cu buffer layer reduces the roughness of the $Ir_{20}Mn_{80}$ layer. The large thickness of the Cu spacer could result in lower MR [71]. The maximum MR of the thin-film SV stacks ranged from $\Delta R/R = 2.0\%$ to 3.6%.

Ion Milling SV Thin Film

SV thin films were sputtered, and then ion milled to reduce the formation of unwanted domains and edge effects. Traditional lift-off-resist (LOR) processing for metal layers will result in unwanted magnetic edge effects. Additionally, Co, Cu, and NiFe are nonvolatile, so they do not reactively etch in plasmas [179]. During ion milling, ionized argon particles bombard the wafer surface blasting unprotected material away (Figure 66). The wafer is continuously rotated at a 15° angle to produce a more even etch and to reduce redeposition of the blasted material.

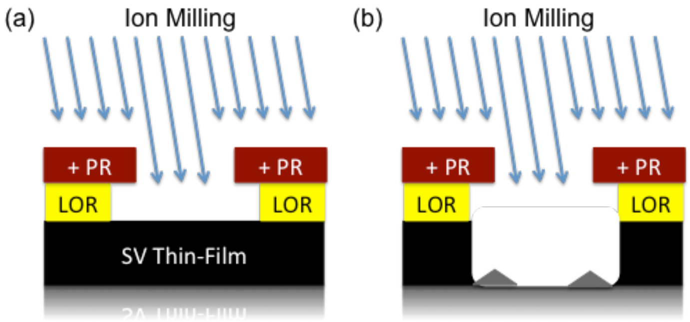

Figure 66: (a) Ion milling to define SV structure, (b) unwanted redepostion during ion milling.

The wafer chuck was water cooled to prevent overheating of the substrate and photoresist (PR). Burnt on PR (see Figure 67) was impossible to remove resulting in the wafer being scrapped. Ion milling also introduces heat, which increases diffusion, thus Néel coupling, between the layers, so care was taken to limit thermal damage. High Néel coupling can result in non-bistable devices. The thermal damage can also cause the SVs to delaminate due to either mismatches in layer stresses or due to increased oxidation of the IrMn (Figure 68 (a)). Similarly, care was taken to completely mill the SV thin film (Figure 68 (b)); failure to completely mill the film resulted in shunting and magnetostatic interaction. If the SV thin film was not entirely etched after removing the PR, the wafer was scrapped.

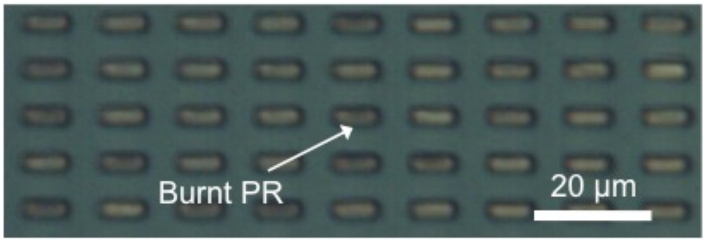

Figure 67: Burnt on PR that cannot be removed from 2 μm × 6 μm SVs on silicon nitride.

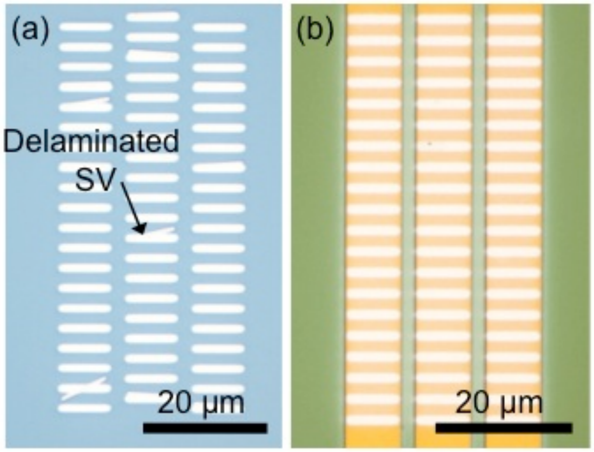

Figure 68: (a) Delaminated 1 μm × 8 μm SVs on silicon oxide, (b) Incomplete ion mill of 1 μm × 8 μm SVs on gold write lines.

Another problem caused by ion milling was redeposition (Figure 66(b) and Figure 69). Redeposition led to undesirable SV debris coating the sidewalls leading to shunting between the layers. A thin masking layer was desirable to increase the ability of sputtered substrate material to escape.

LOR inhibits the sputtered substrate material from coating the sidewalls of the SVs.

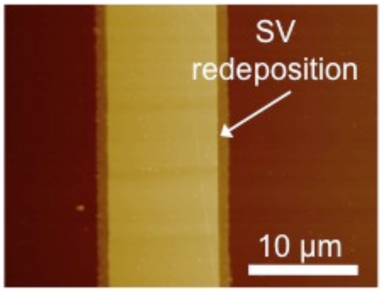

Figure 69: Atomic-force microscopy (AFM) image taken with a high-field magnetic-force microscopy (MFM) tip showing redepostion along the sidewalls of the 10 µm wide SV line defined without LOR.

Well-defined and ion milled SVs are shown in Figure 70. Rounding of the edges was observed due to the photolithography and shadowing effects in the ion mill.

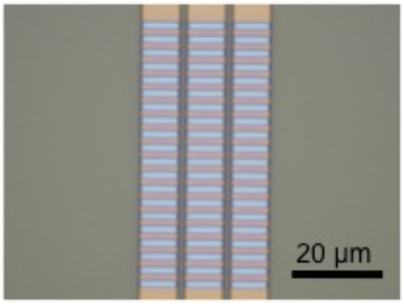

Figure 70: Well defined and ion milled 1 µm × 8 µm SVs on 8 µm write line.

Photolithography

Positive PR, negative PR, and lift-off resist were utilized during fabrication. The following section describes the techniques used.

Positive Photoresist (PR)

High-resolution positive PR Megoposit SPR 660L was used for masking most steps. After dehydrating a clean wafer on a 95°C hotplate for 60 seconds, an automated spinner (Solitec) was used to dispense and spin the PR at a speed of 2200 rpm for 40 seconds. Then the wafer was pre-baked on a 95 °C hotplate for 60 seconds. This produced a ~1.2 μm thick PR film across the wafer. A 5X reduction stepper (ASML PAS 5000/55) with 5 inch soda lime reticle masks exposed the PR with 165 mJ/cm^2 dose of UV (optimized specifically for this work). Next, the wafer was post-baked at 110°C for 60 seconds and spray developed with MF701 in the automated Solitec spray developer. The length of development depended on the application. If just SPR660L was being developed, the PR was spray developed for 60 seconds.

Lift-Off Resist (LOR)

Thin-film gold read and write lines were defined by means of traditional LOR technique for metals. LOR is a soluble coating (not photosensitive) spun onto the clean wafer prior to spinning on SPR660L PR. Upon development of the PR, the LOR provides an undercut, which prevents conformal coating of the metal thin film during deposition. This discontinuity allows the clean removal of unwanted metal from the PR covered parts of the wafer. Additionally, LOR and PR masking were used to prevent redeposition of the SV thin film during ion milling (refer to Figure 66). Depending on availability, either LOR 3A or 5A (MicroChem) was used.

Before spinning, the surface of the wafer was cleaned with acetone, isoproponal, and dried with N_2 or cleaned in the automated dryer (ProSonic).

The wafer was ashed in a 60 Watt O_2 plasma for 1-3 minutes to remove any organic matter and to promote a hydrophilic surface. The hydrophilic surface enabled the LOR to spread more evenly during the spin-on step. The ash was skipped if SV devices were exposed due to issues with oxidation of the IrMn. The wafer was dehydrated on a 150°C hotplate for five minutes to promote adhesion. LOR was poured onto the wafer and spun at 300 rpm (500 rpm/sec ramp) for 5 seconds, then at 2500 rpm (1500 rpm /sec ramp) for 45 seconds. The LOR underwent a pre-exposure bake at 150°C for 5 minutes. Next, PR SPR660 was poured on and spun at 2200 rpm (600 rpm/s ramp) for 40 seconds with an automated spinner followed by a 60 second pre-exposure bake at 95°C. Then, the wafer was loaded into the stepper and exposed. The exposure energy at the time of this thesis was optimized to 165 mJ/cm^2; however, as the lamp ages, this setting may change. After exposure, the wafer was baked for 60 seconds at 110°C and developed in MF701 developer (Shipley Company) with the automated spray developer (Solitec). The optimal development time for the SV lithography was 50 seconds (produces 200 nm undercut), while all other LOR steps were spray developed for 55 seconds. Over development of the SV lithography resulted in the photoresist washing off due to a large LOR undercut.

Negative PR SU-8

Negative PR SU-8 was used to fabricate non-encapsulated 75 μm thick microfluidic channels (Figure 71) and 40 μm thick PDMS molds for encapsulated microfluidic channels (Figure 72). A clean single-side polished wafer was dehydrated on a 65°C hotplate for 10 minutes. The process parameters used for SU-8 2025 (MicroChem) are shown in Table 4. All temperature changes were done gradually to prevent cracking due to a high SU-8 thermal expansion coefficient. Unlike all the other masks, a 4 inch by 4 inch soda lime mask was used for the SU-8 UV exposure; the ASML Stepper would not accept a wafer with thick SU-8.

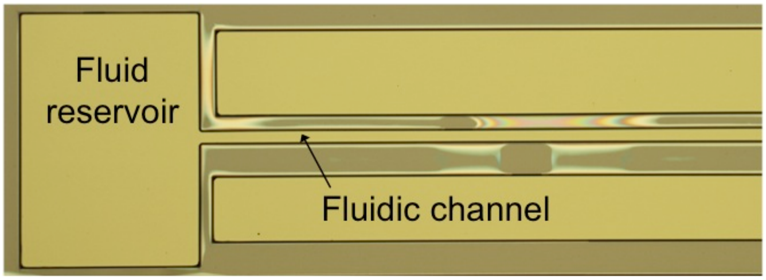

Figure 71: Capillary 75 μm thick SU-8 microfluidic channels. The reservoirs are 1000 μm × 1400 μm.

Table 4: SU-8 process parameters.

Thickness	**40 μm**	**75 μm**
Spin Speed	100 rpm/s ramp for 5 sec 2000 rpm for 30 sec	100 rpm/s ramp for 5 sec 1000 rpm for
Pre-Exposure Bake	2 min at 65 °C 20 min ramp to 90 °C 5 min at 90°C	5 min at 65 °C 20 min ramp to 90 °C 9 min at 90°C
Exposure	Karl Suss MJB3 Aligner 50 seconds	Karl Suss MJB3 Aligner 60 seconds
Post-Exposure Bake	1 min at 65 °C 20 min ramp to 90 °C 3 min at 90°C 15 minute cool down on hotplate	1 min at 65 °C 20 min ramp to 90 °C 5 min at 90°C 15 minute cool down on hotplate

Figure 72 shows part of the PDMS SU-8 mold with the 1 mm diameter inlet leading to the 80 μm wide channel. The four boxes are gross AMs, which are complementary to patterns on the SVWIRE wafers. The dark area is the 40 μm thick SU-8 and the light area is the silicon oxide.

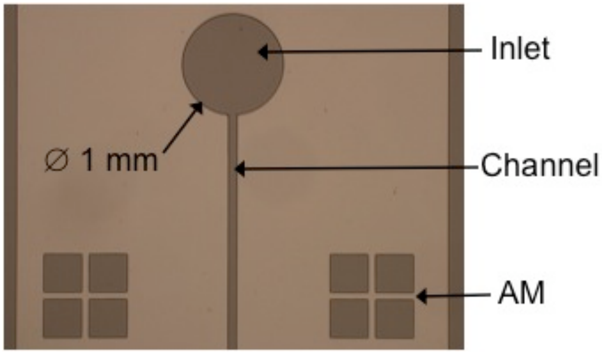

Figure 72: SU-8 PDMS mold for encapsulated microfluidic channels. The SU-8 is the darker material and the bare Si is the lighter material.

Polydimethylsiloxane (PDMS) Microfluidic Channel

Polydimethylsiloxane (PDMS) is a commonly used silicon-based organic polymer for microfluidics channels. PDMS is optically clear, non-toxic, and generally inert. The PDMS (Sylgard 184 Silicone Elastomer Kit) was gently mixed with a 1:10 base to curing agent ratio. Prior to pouring the mixture onto the SU-8/Si wafer mold, the PDMS was allowed to sit for 20 minutes to allow the bubbles to dissipate. The viscous PDMS was poured onto the SU-8 mold and cured on a 60°C hotplate for 4 hours in the chemical hood to prevent dirt from accumulating on the PDMS. In the cleanroom, the PDMS was peeled off the Si/SU-8 wafer mold and sliced along the division lines with a razor blade. With the diced PDMS piece sitting on a clean glass microscope slide, a blunt 14 gauge × ½ inch long needle with a luer hub was used to punch inlet and outlet holes into the PDMS. A completed PDMS 5 mm wide and 22.5 mm long slab containing the 17 mm long, 40 μm deep, and 80 μm wide microfluidic channel is shown in Figure 73.

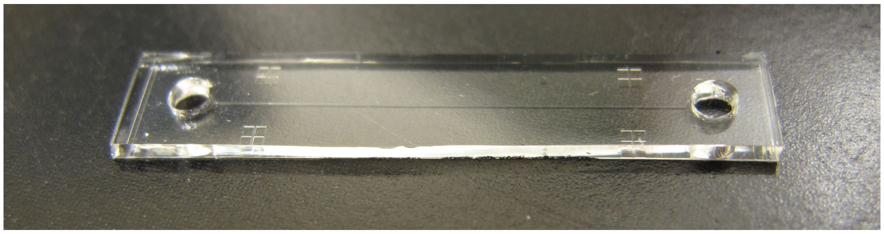

Figure 73: PDMS microfluidic channel. The channel is 40 μm deep and is 80 μm wide. For scale, inlet and outlet holes are 1 mm in diameter.

The PDMS was cleaned with acetone, isoproponal, methanol and nitrogen. Scotch tape was used to remove any remaining dust. During the bonding process, the PDMS was placed in a 100 watt oxygen-plasma ash for 60 seconds to clean the surface of any residual organic material. With the aid of AMs on both the SVWIRE wafers and the PDMS, the channel was aligned onto the SV chip by hand. A microscope helped to verify placement. Next, the wafer-bonded PDMS was placed in a 100 Watt oxygen-plasma ash for another 60 seconds. To further seal the channel, the bonded wafer was placed on a 60°C hotplate for at least 5 minutes.

The wafer-bonded PDMS was pulled off once each set of bead manipulation and detection experiments was completed. If removed after the experiment, the PDMS cleanly peeled off and a 30 minute ultrasound, auto spin dry, and a 3 minute oxygen-plasma ash completely cleaned the wafer. If the PDMS was left on the wafer for an extended time (over two weeks), some residual PDMS (Figure 74) remained on the wafer even after extensive cleaning.

Figure 74: Residual PDMS near the outlet holes and AMs due to the wafer not being promptly cleaned after a SPB experiment.

Magnetic Thin-Film Annealing

After deposition of the SV thin film, the wafer was annealed at 180-200°C in argon with a pressure of 667 Pa in a field of 1.0 T along the long axis of the SVs for 2 hours in an Magnetic Solutions custom Annealer. The wafer was cooled at a rate of -10°C per minute in the 1.0 T field. Annealing the SV thin film improved its switching characteristics.

E-Beam Evaporation of Read and Write Lines

An E-Beam evaporator (Kurt J. Lesker) deposited the gold write and read lines. The titanium (Ti) seed layer promoted the growth of gold on the LPCVD silicon nitride surface, while the Ti cap promoted the future growth of PECVD nitride on the surface of the lines. Without the Ti cap, the gold peeled off. Gold was deposited at a rate of 10 Å/s and Ti at a rate of 2 Å/s. Unless otherwise noted, the gold thickness was 150-200 nm and all Ti layers were 5 nm thick.

PECVD Silicon Nitride

A PECVD chamber (Kurt J. Lesker or IntelVac) deposited the silicon nitride, which electrically insulated the read/write lines and passivated the surface of the chip. Prior to deposition, the wafer was cleaned with isoproponal, acetone, and N_2. The deposition rate of both systems averaged 3.0 nm/min. For more details, refer to the process charts in Appendix D: Fabrication Process Charts.

Reactive Ion Etching (RIE) of Silicon Nitride

Reactive-ion etching (RIE) removed the excess silicon nitride to expose the gold write-line pads and to create the 5X reduction stepper AMs. The Axic RIE parameters were 2 sccm O_2 and 42 sccm CF_4, 150 watt RF power, -100 volts RF DC bias, and a 35×10^{-3} Torr process pressure. The base pressure of the chamber was 5×10^{-5} Torr. Laser interferometry and a designated bare “flood” die were used to detect the end of the etch.

Masking

All the masks were designed and fabricated in the cleanroom at NIST. The chips were designed with L-edit layout software (Tanner Research, Inc.) and the masks were UV exposed by means of an in-house pattern generator (Interserv). The L-edit .td file was converted to a GDS II (.gds) file before being fractured by Xic Graphical Editor (Whiteley Research, Inc.). The soda lime mask PR was developed in CD-30 and the chrome was etched with CR-7. The 5 in masks were exposed in the 5X Reduction Stepper (see Appendix D: Fabrication Process Charts for Stepper parameters) and the 4 inch masks for the SU-8 were exposed by the Karl Suss mask aligner.

Summary

The fabrication process for constructing the SV and microfluidic chips was presented. Fabrication included lithography, evaporation, magnetron sputtering, RIE, PECVD, LPCVD, annealing, and ion milling. Detailed fabrication charts can be found in Appendix D: Fabrication Process Charts.

CHAPTER 4: MEASUREMENT TECHNIQUES

The following chapter will discuss the SV thin-film and device measurement techniques.

B-H Loop Tracer

Immediately after sputtering the SV, the thin-film hysteresis loop was measured with the B-H loop tracer (Figure 75). The tracer is composed of two sets of Helmholtz coils. A solenoid coil applies an AC magnetic field (maximum field of ±15 mT) and the pickup or sense coil measures the induced electromagnetic field (e.m.f.). The induced e.m.f. is integrated to calculate the magnetic flux density. The wafer is located at the center of the coils. All measurements were taken at 50 Hz, with a gain of 20, and at room temperature.

Figure 75: B-H loop tracer for measuring the SV hysteresis curve. The loop tracer consists of a solenoid coil and a pickup coil.

Magneto-Optical Kerr Effect (MOKE)

The surface magnetization of SV thin-films was measured by means of the magneto-optical Kerr effect (MOKE). Light reflected off a magnetized surface undergoes a change in polarization (rotation) and reflectivity. The reflected beam will consist of two orthogonal vectors represented by the big Fresnel amplitude reflection coefficient *r* and the small Kerr coefficient *k*. The light intensity measured is proportional to the Kerr rotation or ellipticity, both of which are proportional to the magnetization of the surface. As shown in Figure 76, a diode detector measured the intensity of the rotated, polarized light from a laser reflected off the thin-film surface. Visible light can only penetrate ~20 nm into typical metals, thus MOKE is limited when measuring thick multi-layered magnetic structures. For this research, only longitudinal micro-MOKE (p-plane) was used to measure the hysteresis loops of the patterned thin films SVs.

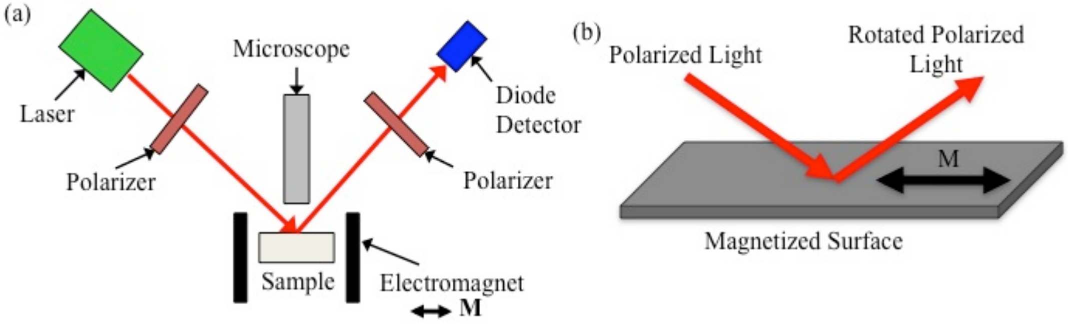

Figure 76: (a) Longitudinal MOKE setup on an anti-vibration table, (b) laser reflected on the surface of the magnetized material.

For the MOKE measurements, both the polarizer and the analyzer were set to 23.5°. The laser (Coherent) was controlled by a PEM-90 Photoelastic Modulator set to a 635 nm wavelength and 90° phase. The voltage from the diode detector was measured with a multimeter (Keithley 2001) as well as a lock-in amplifier (Stanford Research Systems, Model SR830 DSP). A computer-controlled bipolar operational power supply/amplifier ran the water-cooled electromagnetic. Figure 77 shows a photograph of the MOKE platform set up for micro-MOKE measurements

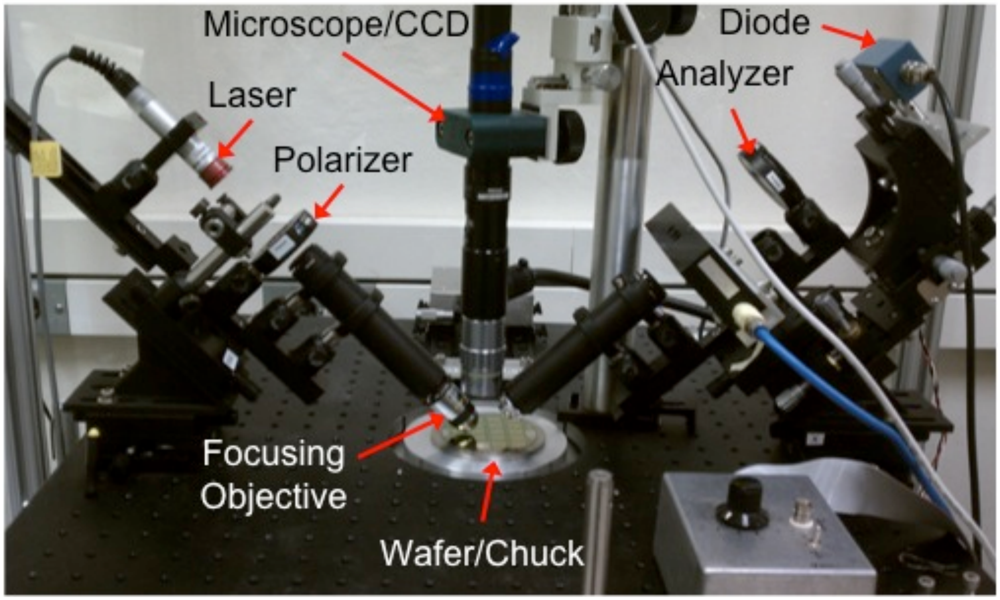

Figure 77: Micro-MOKE measurement setup located on an anti-vibration table. The water-cooled electromagnet resides under the chuck.

MOKE measures the hysteresis curve of the un-patterned SV films, while the micro-MOKE measured the hysteresis of patterned SV films. For micro-MOKE, the laser beam was focused to a diameter of 20-50 μm with a lens.

Thin-Film Magnetoresistance

The MR of the magnetic thin films was measured by means of a four-point probe measurement, as shown in Figure 78. The four probes are aligned parallel and spaced equally; the inner two probes apply a current, while the outer two probes sense the current change due to GMR. A water-cooled electromagnet swept a magnetic field across the wafer (usually along the easy axis) as the probe resistance was measured with a multimeter (Keithley 2001) set to 4Ω with all filtering off. The H-R curve was used to calculate the GMR of the SV thin film.

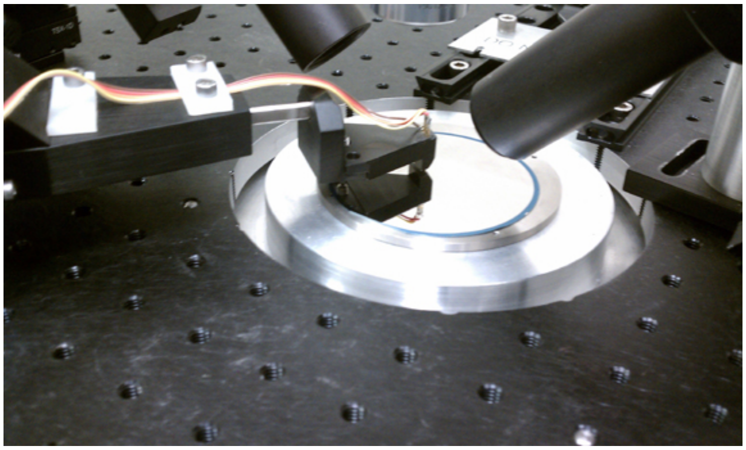

Figure 78: Four-point probe measurement of SV thin film on a 3-in wafer.

GMR is intrinsically anisotropic, so the probes can be placed at any angle or on any spot on the wafer; however, the probe should be near the center of the electromagnet for an accurate applied field measurement. A slightly lower GMR will be measured if the probes are not aligned perpendicular to the easy axis of the thin film [180].

Read-Line Magnetoresistance (MR)

The MR of an individual SV was measured by depositing gold read contact leads (5 nm Ti/ 150-200 nm Au/ 5 nm Ti) onto the blunt ends of the SVs. An example of 1 μm wide and 2 μm wide contact leads on a 1 μm × 8 μm SV is shown in Figure 79.

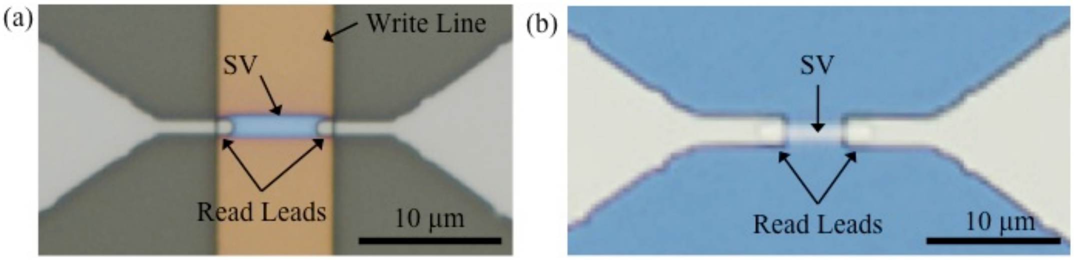

Figure 79: Single 1 µm x 8 µm SV trap with (a) 1 µm wide and 200 nm thick gold read-line contact leads, and (b) 2 µm wide and 200 nm thick gold contact leads.

Both 1 µm and 2 µm wide read line contact leads were evaluated. The 2 µm wide leads were less prone to static electrical charge burnout compared to the 1 µm leads; however, care had to be taken to not accidently burnout the read lines and SVs even with the 2 µm wide leads, as shown in Figure 80.

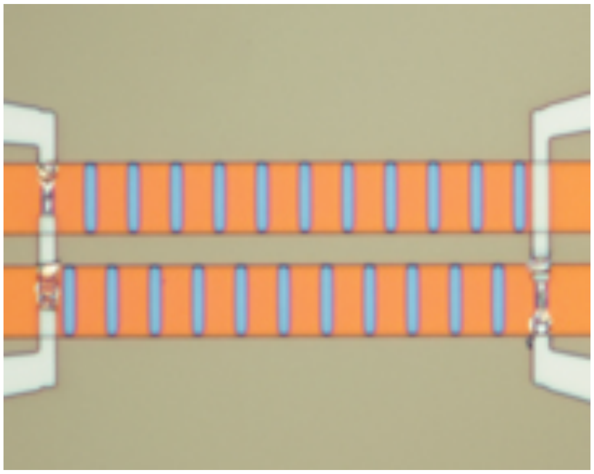

Figure 80: Static burnout of 2 µm wide read line contact leads.

The gold read line expanded out to 500 µm × 500 µm contact pads. Beryllium copper low resistance probes connected the pads to the current source (Valhalla Scientific) and lock-in amplifier (Stanford Research Systems) (see Figure 81). A 100 µA, 100 Hz sense current was applied to the read line with an AC-DC current calibrator. Two rectifier diodes were placed back-to-back on the current source to prevent current spikes from blowing the SVs and read lines. A lock-in amplifier measured the voltage.

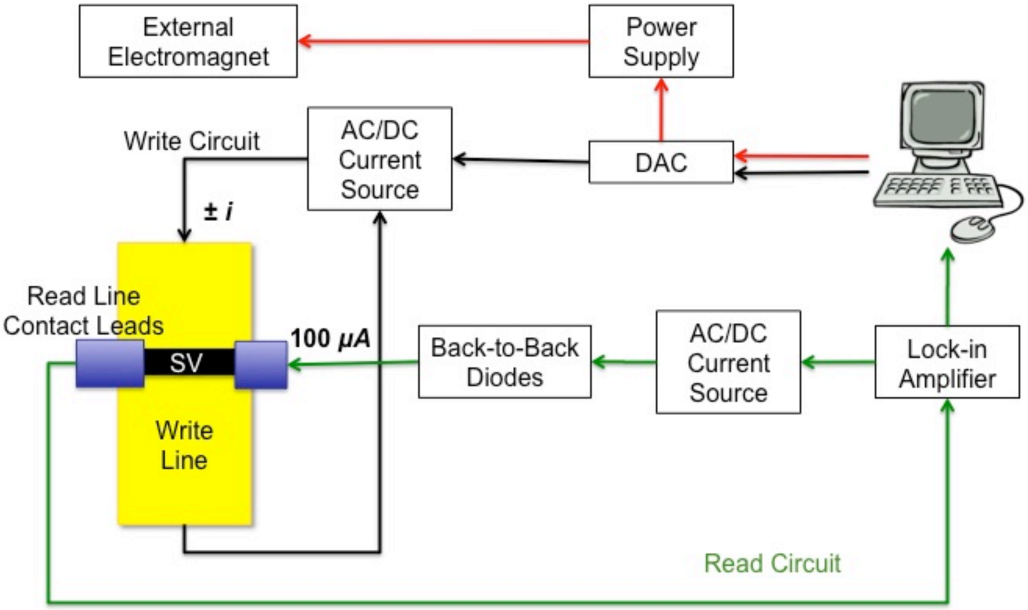

Figure 81: Measurement circuit to write and read the SVs for SPB manipulation and detection.

A magnetic field was applied in two different ways: (1) a water-cooled electromagnet under the platform or, (2) a write line deposited under and electrically insulated from the SV (discussed in next section).

SV Write Line

A 150-250 nm thick gold write line (5 nm Ti seed and cap layers) under the SV (Figure 82) locally switched the SV between the parallel ON and antiparallel OFF states. An 80-150 nm thick PECVD silicon nitride layer electrically insulated the write line from the SVs. Each write line was connected via 500 μm by 500 μm contact pads to manipulator probes connected to an AC-DC current calibrator (set to a maximum of 200 mA) as shown in Figure 81. When the current calibrator was set to 1 A, the write line overheated due to noise from the DAC and resulted in write-line burnout and bubbles forming in the microfluidic channel (Figure 83). A custom Microsoft Basic Visual 6.0 program (MBC.exe) controlled the manually rotatable in-plane external electromagnet and the write lines. The program also displayed the read-line MRs.

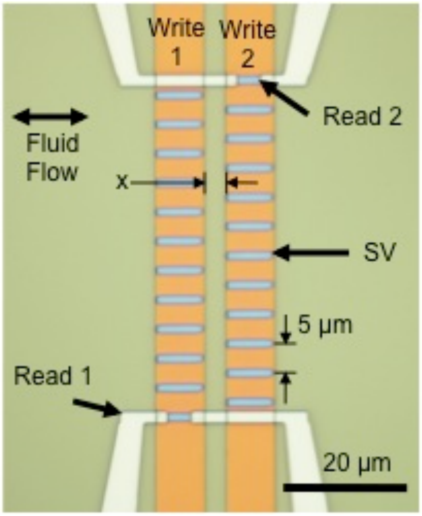

Figure 82: SVs with two write lines and a common ground. One read line on each write line is also shown.

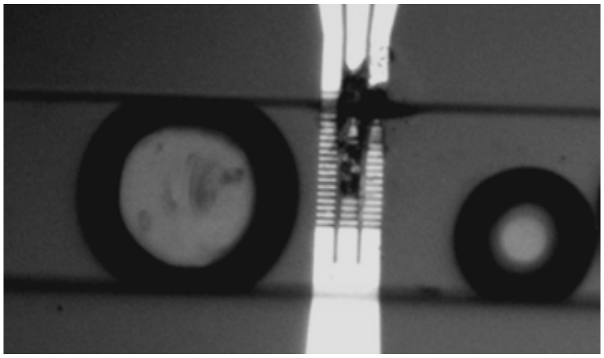

Figure 83: Bubbles formed in the microfluidic channel by wire burnout from continuous 11 mA DAC noise with the AC/DC Current Generator set to 1 A.

Summary

The tools for characterizing the SV thin films, devices, and arrays were discussed. These tools include a B-H looper, MOKE, and read and write lines.

CHAPTER 5: SV CHARACTERIZATION

Characterizations of the SV thin-film and patterned SV structures are described in this chapter. Characterization included evaluating whether the SVs were bistable, determining the GMR, and measuring the switching curves of the SV thin films and individual SV devices.

Thin-Film Characterization

The quality of the SV thin film was evaluated at least twice with a B-H loop tracer, four-point probe, or MOKE measurement: once after sputtering and again after annealing. The effect of SV structure, annealing, and sputtering conditions are discussed in the following sections.

Bottom-pin and Top-Pin

A comparison of bottom-pin and top-pin SV thin-film B-H loop tracer curves demonstrated that the coercivity and exchange bias field were lower in top-pin SV thin films (Figure 84). Anderson found this to be a result of increased surface roughness caused by IrMn being sputtered on the bottom of the stack [59]. The bottom-pin SV stack consisted of substrate/buffer and seed layers/10 nm IrMn/15 nm NiFe/5 nm CoFe/10 nm Cu/5 nm CoFe/15 nm NiFe/5 nm Ta and the top-pin SV stack consisted of substrate/15 nm NiFe/5 nm CoFe/10 nm Cu/5 nm CoFe/15 nm NiFe/10 nm IrMn/5 nm Ta. The top-pin SV thin films were deposited and etched prior to installation of the 3-inch wafer annealing system (Magnetic Solutions), so no annealed data is available for them. Unlike the top-pin SV thin films, the bottom-pin SV thin films required annealing to distinguish the high- and low-field switching loops. The exchange-bias field of the non-annealed top-pin SV thin films ranged from -4 mT to -6 mT. Prior to installation of the new sputtering guns, the annealed bottom-pin SV exchange-bias field varied from -7 mT to -9 mT. After installation of the new guns, the exchange bias field ranged from -4 mT to -7 mT.

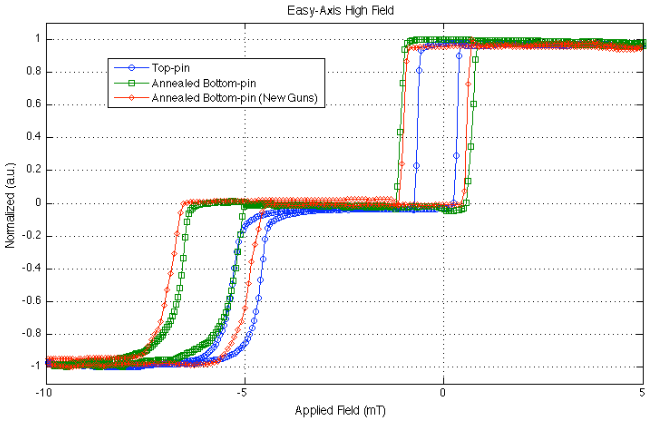

Figure 84: Comparison of top-pin and bottom-pin SV thin-film easy-axis hysteresis. Bottom-pin SVs must be annealed to create distinct high-field and low-field loops.

Annealing

Annealing greatly improved the switching characteristics of the SV thin film, as shown in Figure 85. After SV deposition, the wafer was annealed at 180-200°C in argon with a pressure of 667 Pa in a field of 1.0 T along the long axis of the SVs for 2 hours, then allowed to slowly cool to room temperature. Annealing sharpened the curve and further distinguished the low- and high-field loops. The effect of annealing on the exchange bias was inconsistent. Generally, the coercivity of the pinned layer decreased.

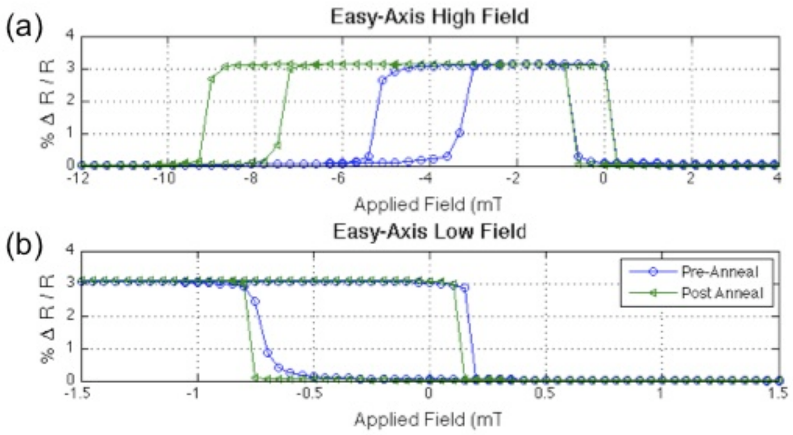

Figure 85: (a) High-field and, (b) low-field bottom-pin SV thin-film easy-axis hysteresis curves before and after annealing.

DC-Magnetron Sputtering Conditions

The DC-magnetron sputtering conditions were varied to optimize the SV thin-film stack. Due to high variability and low sample numbers, more testing and characterization is needed to optimize the sputtering conditions; however, a few observed trends are discussed in this section.

Reproducibility of the SV thin-film curves was an issue. Figure 86 shows the GMR curves for two samples deposited with identical power and flow settings, but with different sputtering rates (Table 5), exchange bias and coercivity. During the sputtering of sample 8, the IrMn had a power supply error (a common error), while sample 6 ran without errors. The difference in deposition rates was most likely due to a difference in the base pressure or the chamber temperature. The difference in the exchange bias could be due to the difference in sputtering rates, base pressure, temperature, or the introduction of contaminants through the load-lock chamber. Logging the chamber temperature, base pressure, and running a longer load-lock pump down (> 30 minutes) may reduce contamination and improve reproducibility.

For all the samples shown in this section, once the load-lock turbo pump reached its target speed and the load-lock pressure was ~10^{-6} mTorr (approximately 5-10 minutes), the load-lock gate was opened and the wafer was moved into the main chamber.

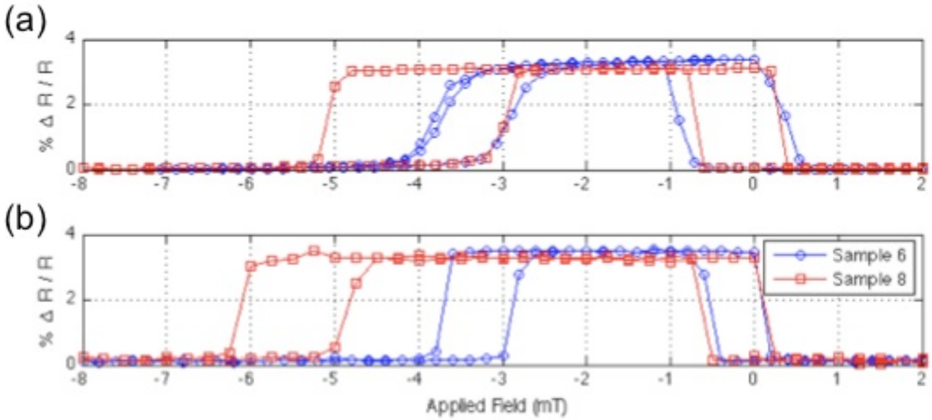

Figure 86: (a) Pre-anneal and, (b) post-anneal sample 6 and 8 hysteresis curves sputtered under similar power and argon conditions.

Table 5: DC-magnetron sputtering conditions for sample 6 and 8.

Target	**Ar Flow (sccm)**	**Sputter Rate (Å/s)**		**Power (Watts)**
		Sample 6	**Sample 8**	
Ta	15	0.83	0.66	150
Cu	15	1.33	1.12	100
IrMn	20	0.91	0.71	100
NiFe	15	1.10	1.38	250
CoFe	15	0.38	0.44	100

The argon pressure and power for all the targets were varied, but no consistent trend was observed once the samples were annealed. For example, the effects of changing the CoFe gun power, while maintaining a 15 sccm argon flow rate on the thin-film switching curves are shown in Figure 87. The deposition rates for sample 10 and 11 are shown in Table 6. The coercivity of the free layer was not altered by the increase in CoFe gun power;

however, the coercivity and exchange bias of the pinned layer differed for the two samples. Both the coercivity and exchange bias of the sample sputtered at the higher power were larger than those measured at the lower power. Interestingly, after annealing, this trend was reversed. This could be explained by grain size, but atomic-force microscopy (AFM) was not performed to measure roughness. Future studies to optimize the sputtering conditions should include AFM roughness measurements in order to interpret the hysteresis curves when the sputtering conditions are varied.

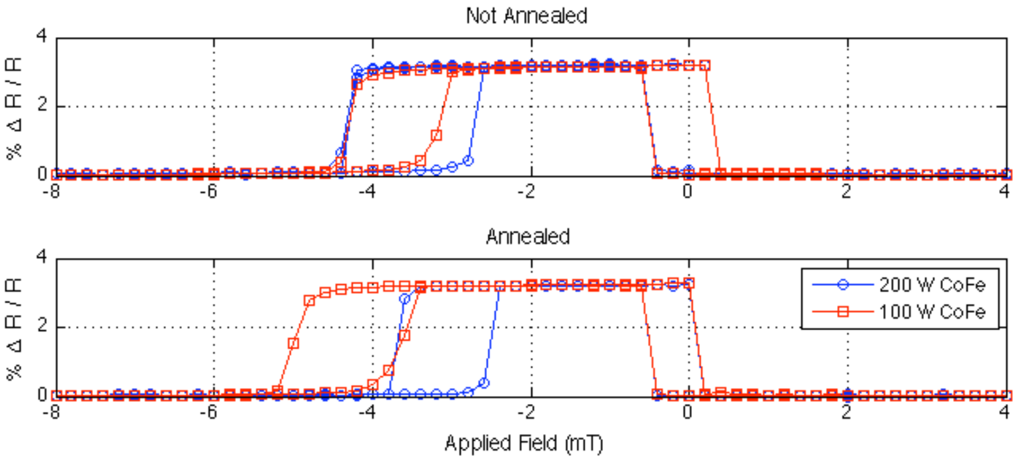

Figure 87: Comparison of 100 W and 200 W CoFe sputtering.

Table 6: DC-magnetron sputtering conditions for sample 10 and 11.

Target	**Ar Flow (sccm)**	**Deposition Rate (Å/s)**		**Power (Watts)**	
		S10	**S11**	**S10**	**S11**
Ta	15	0.93	0.93	200	200
Cu	16	1.31	1.31	125	125
IrMn	20	1.09	1.05	150	150
NiFe	15	1.06	1.06	200	200
CoFe	15	0.81	0.43	200	100

Further evaluation of the sputtering conditions is needed. As the scale of the SVs is reduced, grain size and roughness may have a more profound effect on the switching characteristics of the thin film as well as the etched devices.

SV Array Characterization

Using longitudinal MOKE with an external field applied along the SV easy axis, the switching characteristics of arrayed SVs with varied array density and sizing were studied. The MOKE measurements were only sensitive to the top-magnetic-layer switching, but still useful for determining the magnitude and distribution of the fields required to turn the traps ON and OFF, and for evaluating whether the SVs were interacting with each other in the array. Because the MOKE measured the switching curves of multiple devices, the MOKE curve is not as sharp as the MR curve due to averaging over many SVs in the array. The arrays were fabricated (wafer = TESTBED4) in a variety of sizes and lattice dimensions as listed in Table 7.

Table 7: Varied SV sizes and array lattices tested with MOKE.

Width W (μm)	**Length L (μm)**	**Lattice Spacing (μm × μm): % Surface Coverage**
1	3, 4, 5, 6, 8, and 10	2L × 2W: 25%, 2L × 3W: 17% 2L × 4W: 13%, 2.5L × 3W: 13%, 2.5L × 4W: 10%, and 2.5L × 5W: 8%
2	5, 6, 7, 8, 9, and 10	
3	5, 6, 7, 8, 9, and 12	

As shown in Figure 88, the SV arrays covered a 50 μm × 50 μm footprint to match the diameter of the focused MOKE laser spot. The width and aspect ratios are important parameters for SV traps due to the demagnetizing field [88]. Because of lithography limitations, SVs with widths and array spacing smaller than 1 μm could not be fabricated. Figure 88 shows fabricated 1 μm × 8 μm bottom SV arrays with different lattice spacing.

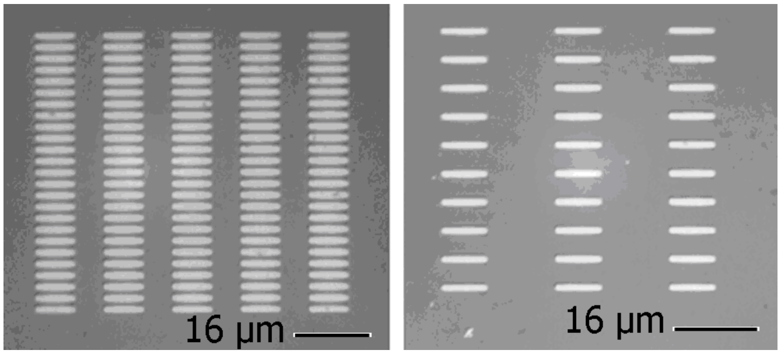

Figure 88: Array of 1 μm × 8 μm bottom SVs on a 2 μm × 16 μm and a 4 μm × 20 μm lattice.

Top-pin and Bottom-pin SV Arrays

As shown in Figure 89, the free-layer switching of arrayed 1 μm × 4 μm top-pin SVs on a 2 μm × 8 μm lattice was difficult to distinguish with MOKE measurements. To continue to use MOKE to analyze the SV arrays, Mirowski's top-pin SV recipe [114] was adapted into a bottom-pin SV recipe; bottom-pin SVs are more sensitive to MOKE due to the layer of interest, the free layer, being on top of the stack. MOKE utilizes a laser to detect the surface magnetization of the sample (see page 99 for more details on MOKE), so it cannot penetrate deep enough into the sample to clearly detect the bottom layer's magnetic switching.

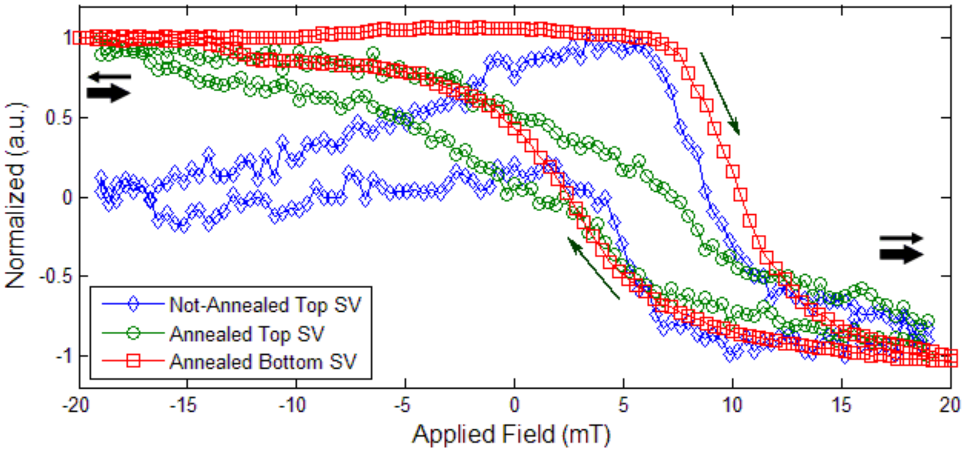

Figure 89: Comparison of 1 µm × 4 µm top-pin and bottom-pin SVs on a 2 µm × 8 µm lattice. The thin and thick arrows represent the moment of the free and pinned layers, respectively.

Aspect Ratio and Width

As demonstrated in the LLG modeling section (refer to page 76), the width and aspect ratio of the device impacted the low-field switching. This is expected because the magnetostatic energy required for free-layer reversal increases as the width decreases. Additionally, a higher aspect ratio results in higher AMR and a lower demagnetizing field. Figure 90 demonstrates the effect of increasing the SV width as well as increasing the aspect ratio on the MOKE free layer switching response. When the width was increased, the coercivity decreased and the curve became more symmetric. According to the MOKE response, the 1 µm × 4 µm and 3 µm × 12 µm SVs appear to not be bistable (the curve is not at -1 when it crosses 0 mT). For the 1 µm, 2 µm, and 3 µm wide SVs, an aspect ratio of 1:6 was needed to see a semi-bistable MOKE response. Increasing the aspect ratio reduced the free-layer switching and resulted in a more symmetric hysteresis curve. After evaluating the MOKE results, the 1 μm × 8 μm SV was found to have optimal switching characteristics.

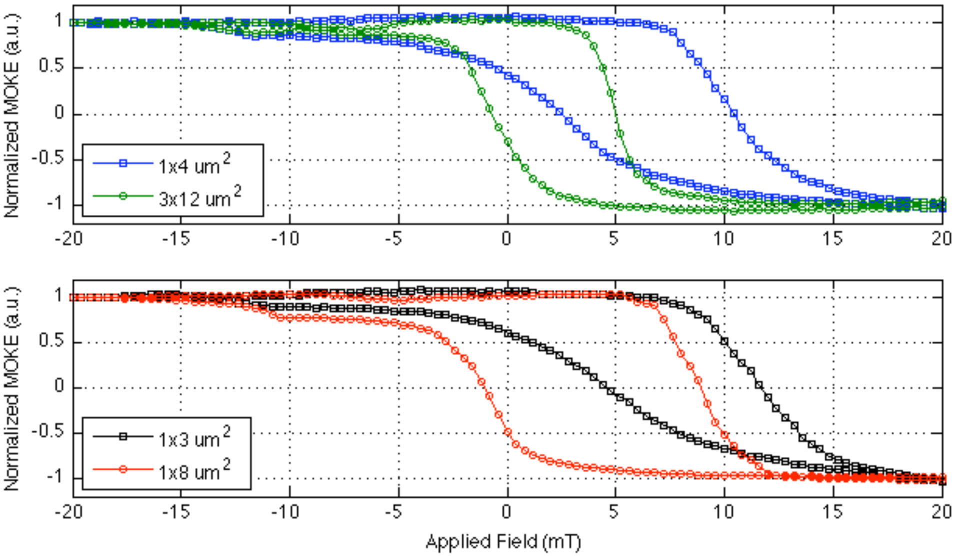

Figure 90: Effect of SV width (top plot) and aspect ratio (bottom plot) on free-layer switching measured with MOKE.

Array Spacing

As the spacing between SVs was decreased, there was only a small change in the switching transitions as seen in Figure 91. The small differences in the data show that the magnetostatic interaction within the SV array is minimal. MOKE 25%, 13%, and 8% represent the percent surface area covered by the arrayed 1 μm × 8 μm SVs on a 2 μm × 16 μm lattice, 4 μm × 16 μm lattice, and 5 μm × 20 μm lattice, respectively. For the lattice spacing tested, neither the switching fields nor the hysteresis shape significantly differ. The closely packed MOKE 25% SVs have a sharper curve, which may be caused by minor magnetostatic interaction from neighboring SVs in the array. Overall, this small magnetostatic interaction should not have a significant impact on our bead manipulation application.

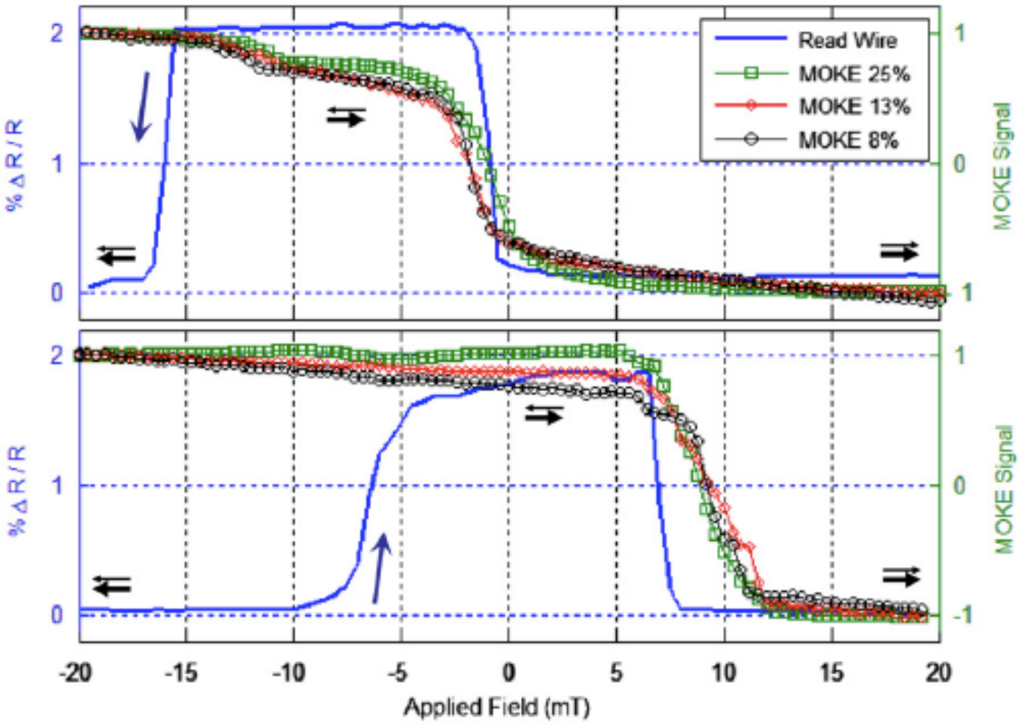

Figure 91: MOKE switching characteristics of SV arrays with different array densities represented by percent surface area coverage compared to the MR of one SV. The 25%, 13%, and 8% surface coverage data represent 1 μm × 8 μm SVs on a 2 μm × 16 μm, 2 μm × 24 μm, and 2 μm × 32 μm lattice, respectively. The top plot shows the positive-to-negative field sweep and the bottom plot shows negative-to-positive field sweep. The free- and pinned-layers are depicted as thin and thick black arrows, respectively.

Individual SV Characterization

The shape and switching characteristics of individual SVs were evaluated by means of MR measurements (refer to page 101 for more details on the read line). The GMR for a 1 μm × 8 μm bottom SV is shown in Figure 92. With an applied field of ±4 mT, the free layer does not completely flip to antiparallel resulting in a minor loop with some zero field retention (~1.3 % GMR). With an applied field of ±9 mT, the SV free layer flips completely from parallel to antiparallel at -2 mT and from antiparallel to parallel at +8 mT. This SV is bistable (~2 % GMR). With an applied field of ±20 mT, both the free and pinned layers switch. During the positive-to-negative sweep, the free layer switches at -3 mT and the pinned layer at -18 mT. A mix of free- and pinned-layer switching begins around -7 mT, but does not finish until +17 mT. This foot-like shape in the curve is most likely due to edge domains in the SV. Additionally, the SV never regains the full antiparallel state GMR during the negative sweep after having the pinned layer switched. Thus, flipping the pinned layer resulted in a SV not completely balanced or OFF. The 1 μm × 8 μm SV will turn OFF with an applied field of –2 mT after being in the ON state. An applied field greater than +8 mT will turn the SV ON after being in the OFF state. If the pinned layer was previously switched, a field greater than +18 mT will be needed to definitively return the SV to the parallel ON state.

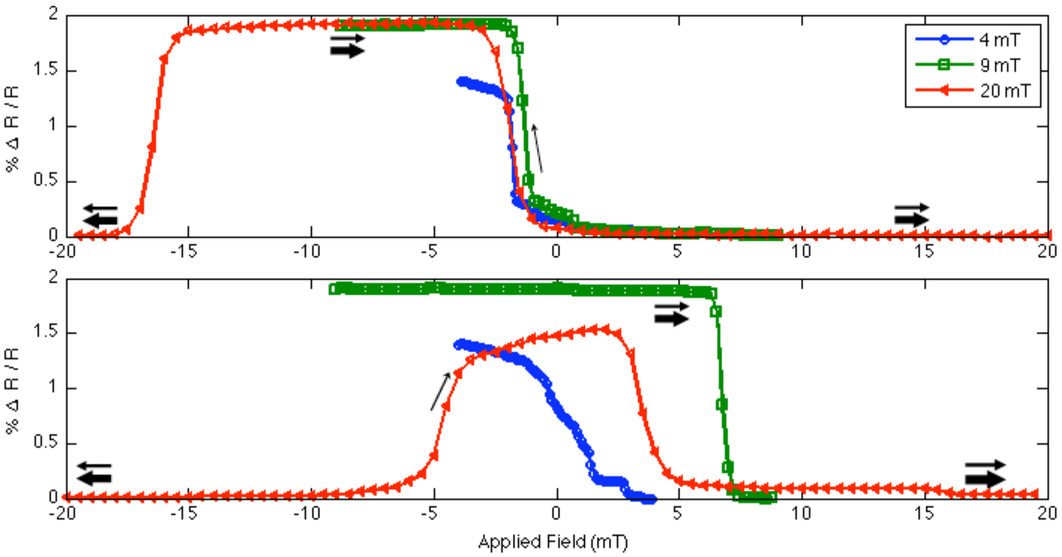

Figure 92: %ΔR/R of 1 μm × 8 μm SV. The top and bottom plots show the negative and positive sweeps, respectively. The thin and thick arrows represent the moment of the free and pinned layers, respectively.

Figure 93 demonstrates the variability of individual device switching across one wafer (SVWIRE6.1). Device 1 has a larger ΔR due to a lower resistance in the read line (fewer squares); read line designs should minimize the read-line resistance to maximize the sensitivity of the SV. All the devices have low- and high-field switching at different applied fields; however, a +12 mT field will turn all the SVs ON and a field between -3 and -9 mT will turn all the SVs OFF. A field < -17 mT will switch the SV to the non-stable parallel state. Differences in the actual switching values could be due to domain walls, SV shape (rounding of the edges due to lithography), impurities, or shunting.

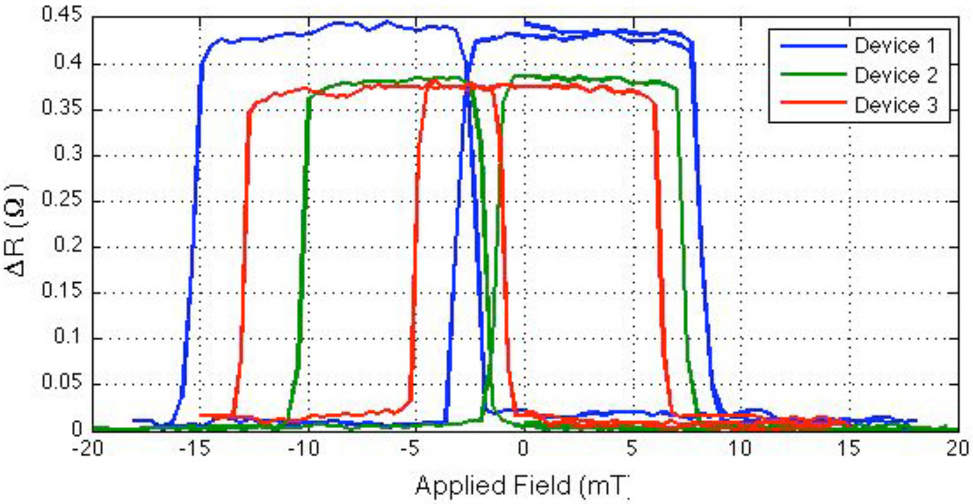

Figure 93: Switching variability of individual SV devices on the same wafer (SVWIRE6.1). The 1 μm × 8 μm SVs were switched with an external field.

Figure 94 shows the variability in SV switching between two different wafers with nearly identical sputtering conditions (see Table 5). Similar to the devices in Figure 93, the low- and high-field switching occurs at different applied fields, but a +12 mT field will turn the SVs ON and a field between -3 and -9 mT will turn the SVs OFF.

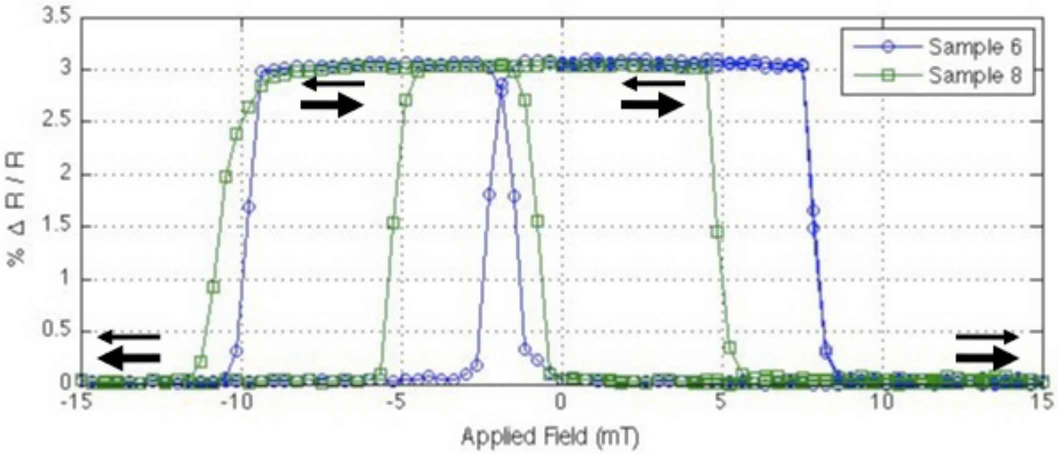

Figure 94: Switching variability of individual SV devices on the different wafers (sample 6 and 8). The 1 μm × 8 μm SVs were switched with an external field.

Next, toggling the SV ON and OFF was demonstrated with a field pulse instead of a sweep, as shown in Figure 95. The SV begins in the high-resistance OFF state, then a t = 10 s, a 10 ms, +12 mT square wave pulse turns the SV to the low-resistance ON state. At t = 20 s, a 10 ms, -8 mT square wave pulse turns the SV OFF. Sinusoidal waves (±12 mT amplitude) with frequencies up to 2.5 Hz successfully toggled the SV between the ON and OFF states. Faster SV switching was not possible with the lock-in amplifiers and DAQ hardware used to control the read and write lines.

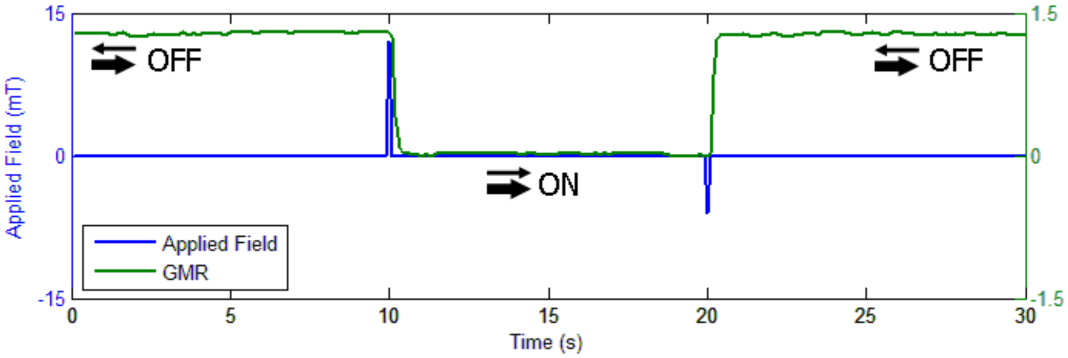

Figure 95: Toggling SV ON and OFF with 10 ms square wave pulses.

Figure 96 demonstrates the toggling of the SV with a 1 s square pulse. An initial pulse of +22 mT at t = 2 s ensures the SV is in the ON state, and then the SV is turned OFF and ON five times. At t = 24 s, a -22 mT pulse wave flips the pinned layer and results in a GMR between the ON and OFF GMR. This state would trap the bead, but without as much force as the ON state shown at t = 0 s.

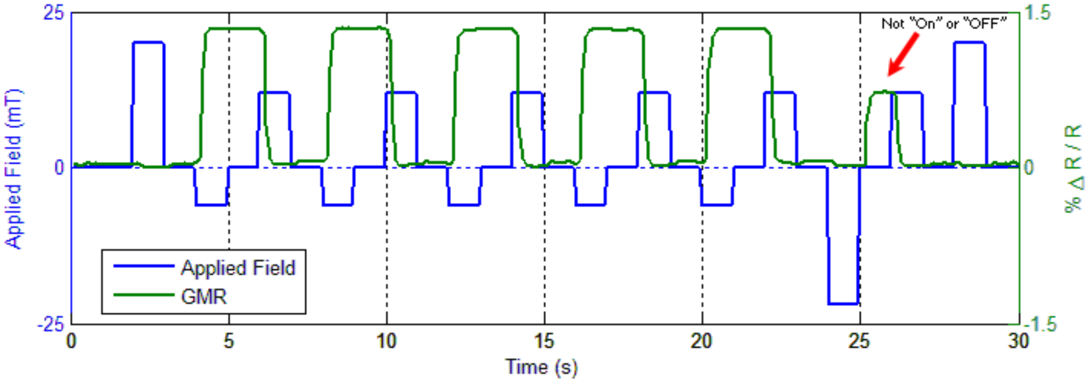

Figure 96: Toggling SV ON and OFF with square-wave field pulses.

Next, the SV was toggled ON and OFF with a local write line under the SV (Figure 82). Figure 97 shows the write-line current sweeps toggling two different SV devices (Read 1 and Read 2) ON and OFF. The ON parallel resistance (minimum resistance) of Read 1 and Read 2 was 31.0 Ω and 29.2 Ω, respectively. The two read lines have different minimum resistances because they are not identical; Read 1 has more surface area or squares (□s).

The free- and pinned-layer switching occurs at different currents for the two SVs. Joule heating in the write line causes the parabolic shape of resistance curves. Pulsing minimizes Joule heating when manipulating SPBs; however, Joule heating could be useful when it is desirable to heat the fluid medium. A current greater than +90 mA (7.5×10^6 A/cm^2) turned both

SVs ON and a current between -140 mA (1.2×10^7 A/cm^2) and -25 mA (2.1×10^6 A/cm^2) turned the SV OFF. A current less than -170 mA (1.4×10^7 A/cm^2) turned the SV to the non-stable parallel state.

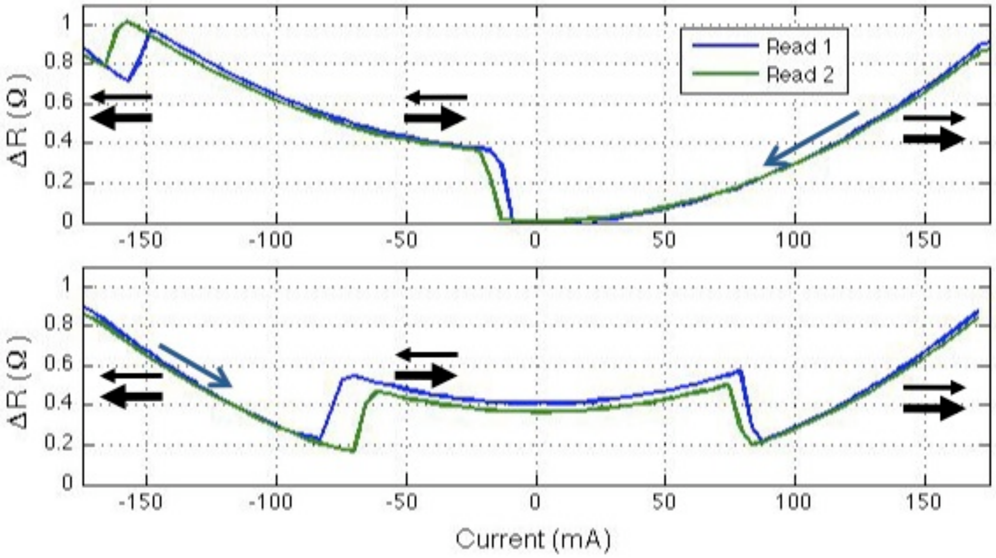

Figure 97: SV switching with a local write-line current sweep. The top and bottom plots show the negative and positive sweeps, respectively.

Figure 98 demonstrates both the write and read of two SVs with 10 ms write-line pulses. A 10 ms, 150 mA current pulse turned the SV ON and a 10 ms, -100 mA current pulse turned the SV OFF. The peaks in the GMR that occur at the switching events are due to momentary heating from the write currents. The observed lag between the switching event and the write pulse was due to artifacts (long time constants) in the measurement circuit, and was not due to an intrinsic delay in the SV switching process. Due to the close proximity of the write lines and the fact that the read lines cross over the adjacent write lines, a current pulse through one write line transiently affects the resistance of neighboring read lines. Future designs should seek to limit this cross talk or interference between lines.

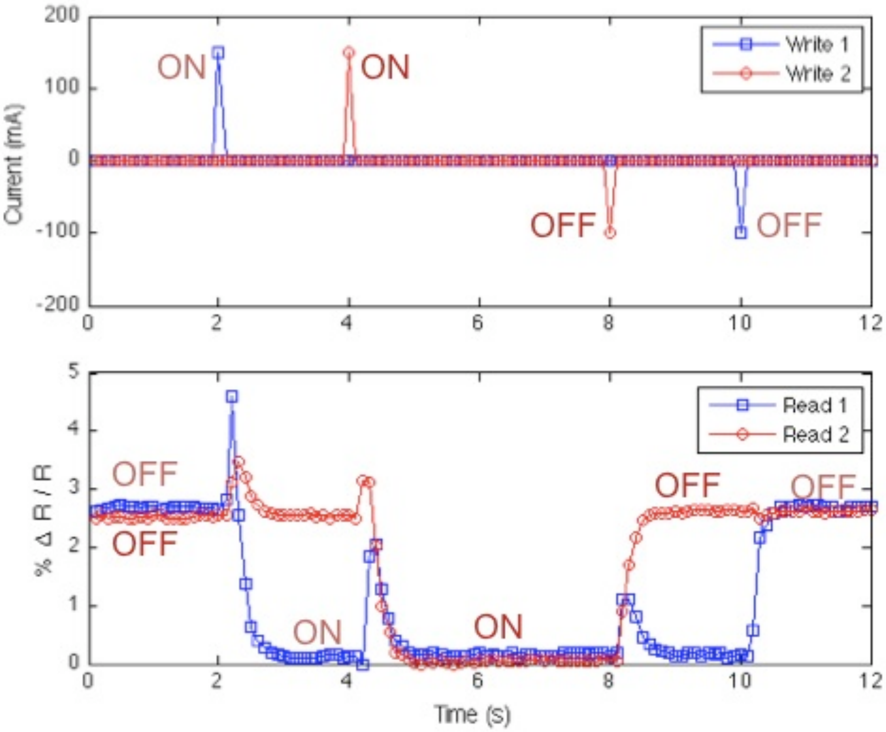

Figure 98: Write-line current pulses to turn the SVs ON and OFF and the ΔR/R of a proximal SV on each write line being turned ON and OFF.

MOKE Compared to MR Measurement

The MOKE response for an array of 1 µm × 8 µm SVs is compared to the MR of one 1 µm × 8 µm SV, as shown in Figure 99. The high-field switching cannot be resolved with MOKE; however, it can be used for approximation of the low-field switching. Device averaging and magnetostatic interaction amongst the arrayed SVs soften the switching curve. In general, MOKE over estimates the coercivity and should not be used to evaluate whether the SVs are bistable.

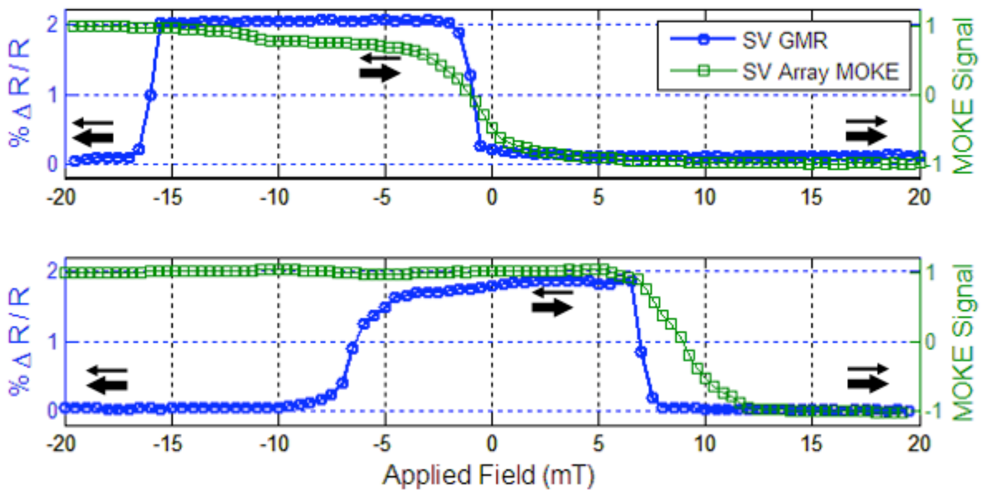

Figure 99: MOKE Results compared to GMR for 1 μm × 8 μm SVs. The top and bottom plots show the negative and positive sweeps, respectively.

Summary

The SV thin film, devices, and arrays were characterized to determine the quality of the stack as well as the switching fields. The magnetic properties of the SVs depend on the SV microstructure, multi-layers, and dimensions. Determination of the maximum switching speed could not be determined with the current hardware setup. For the 1 μm × 8 μm SVs, a 150 mA, 10ms current pulse or +12 mT in-plane parallel field turned ON the SV and a -100 mA, 10ms current pulse or -8mT in-plane parallel field turned OFF the SV.

CHAPTER 6: SUPERPARAMAGNETIC BEAD (SPB) MANIPULATION

Superparamagnetic bead (SPB) capture, release, and transport by SVs are described in this chapter. This chapter is split into three sections; each section describes a different wafer design and SPB manipulation experiment. The three wafers described are TESTBED4, SVWIRE3, and SVWIRE6. Both capture and quasi-release of micro-SPBs were demonstrated with wafer TESTBED4. Both capture and release of SPBs were demonstrated with wafer SVWIRE3. Precise SPB capture, transport, and release were demonstrated with wafer SVWIRE6.

SPB Capture and Quasi-Release

Permanent capture or trapping of 1 μm diameter SPBs was accomplished on arrays of 1 μm × 8 μm and 2 μm × 10 μm SVs toggled ON and OFF with an in-plane external magnetic field. Capture and quasi-release of beads, bead clusters, and bead chains were demonstrated on 1 μm × 8 μm and 2 μm × 8 μm SVs. The following sections will detail the experimental setup and results.

Experimental Setup

TESTBED4 wafer design was used to demonstrate bead trapping and quasi-release. The SVs on this wafer were characterized with MOKE (refer to Aspect Ratio and Width *and* Array Spacing sections), so precise switching fields were not available. Arrays of 1 μm × 8 μm SVs on a 4 μm × 16 μm lattice and 2 μm × 10 μm SVs on a 6 μm × 20 μm lattice were tested. The thin-film stack consisted of 5 nm Ta/5 nm Cu/10 nm IrMn/15 nm NiFe/5 nm CoFe/10 nm Cu/5 nm CoFe/15 nm NiFe/5 nm Ta. SU-8 microfluidic reservoirs and channels (Figure 71) were fabricated onto the surface of the wafer. A glass cover slip slowed evaporation and improved imaging. Only SV arrays located in the SU-8 reservoir were observed; flow was too variable within the capillary microfluidic channel to observe SPB movement. Initially, no passivation layer separated the SVs and the fluid medium.

SPB MyOne Dynabeads (Invitrogen) coated with silane and suspended in de-ionized (DI) water were used to test the trapping capabilities of the SVs. Each 1 μm diameter SPB contains approximately 105 iron-oxide grains (8-15 nm) embedded in a polystyrene matrix. A low concentration of beads (4 μg/μL) was used to reduce SPB clustering. With a pipette, 5 μL of the bead solution was deposited into the SU-8 reservoir, and then the reservoir was covered with a glass cover slip. For experiments with SPB clusters and chains, a higher concentration of SPB (400 μg/μL) was deposited into the reservoir. A 5 mega-pixel (MP) CCD camera (DCM 510) recorded the SPB trapping; frame rates were estimated to be 2-3 frames per second. For these experiments, it was assumed that there was negligible fluid flow in the reservoirs.

The video frames were extracted from the .avi video file with either *DivX Converter* (www.divx.com) or *ImTOO Video to Picture* (imtoo.com) software. Once converted to a .bmp or .tiff picture file, *Adobe Photoshop* (www.adobe.com) was used to extract the region of interest.

Results

Figure 100 shows a 1 μm diameter SPB trapped by a 1 μm × 8 μm SV from over 20 μm away and Figure 101 shows a SPB trapped by a 2 μm × 10 μm SV from 15 μm away. Prior to being trapped, Brownian motion of the SPBs was observed, but not quantified. An in-plane ±15 mT magnetic field sweep appeared to turn OFF the SVs; however, the state of the SV cannot be verified without a MR measurement. The field sweep had to be symmetric due to software limitations. The other SPBs were previously trapped by the SVs.

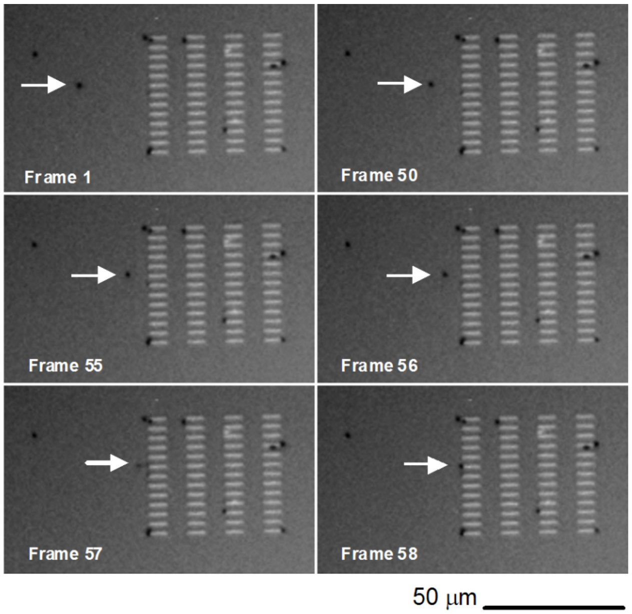

Figure 100: 1 μm SPB (shown by the arrow) trapped by an array of ON 1 μm × 8 μm SVs. Some SPB were previously trapped by the SV array.

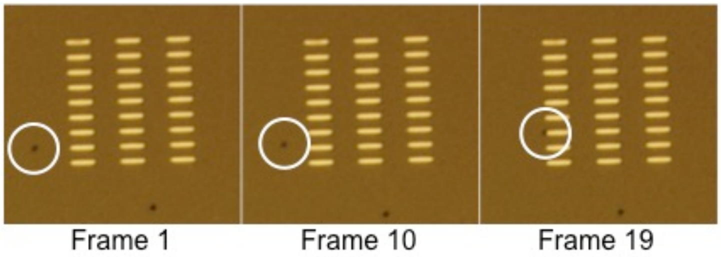

Figure 101: 1 µm SPB (shown in the white circle) trapped by an array of ON 2 µm × 10 µm SVs. Video rate is 2-3 frames/sec.

When the arrayed SVs were ON, the SPBs were attracted to and trapped by the SVs. The SPBs always moved towards the blunt ends of the SV where the magnetic field gradients were maximized. When the SVs were OFF, no additional SPBs were trapped; however, the previously trapped SPBs were rarely released from the OFF SVs. Figure 102 shows the rare movement of a 1 µm SPB from one 2 µm × 10 µm SV to another, where it permanently remained trapped. It should be noted that the SPB never appeared completely trapped (on the blunt end) by the first SV. Once trapped on the second 2 µm wide SV, the SPB was observed to rotate around one blunt end of the SV when a ±15 mT magnetic field sweep was applied. The SPB followed the free-layer moment, but was not released when the SV array was toggled OFF. Introducing a random magnetic field gradient by moving a permanent magnet close to the chip successfully removed some of the trapped SPBs, but the majority remained permanently trapped.

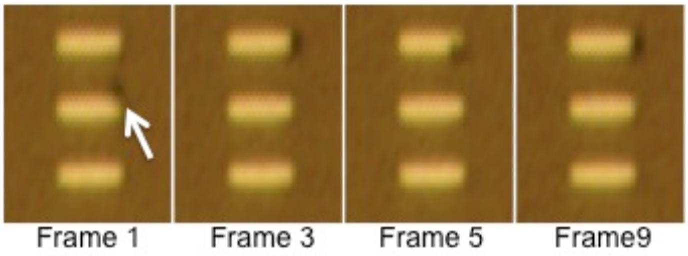

Figure 102: 1 μm SPB transported from one 2 μm × 10 μm SV to another in Frame 1 and 3. Once trapped on the 2nd SV, the OFF field resulted in the SPB rotating around one blunt end of the SV, but was not released.

To determine if the lack of a passivation layer hindered SPB release, 200 nano-meters of silicon nitride was deposited onto the surface of the wafer (conformal coating of silicon nitride was also on the SU-8 channel walls) and the wafer was retested. Immediately after the deposition, repeatable SPB capture and release was observed on arrayed 2 μm × 8 μm SVs toggled ON and OFF with a ±10 mT in-plane magnetic field sweep. Due to camera errors, this quick test was not documented with video stills. A week later, the broken camera was replaced and the experiment was repeated, but the trapped SPBs failed to consistently release. It was observed that the substrate surface had become more hydrophobic since the previous experiment.

Figure 103 shows the capture and quasi-release of 1 μm SPB chains and clusters on the 1 μm × 8 μm SV array a week after being passivated with silicon nitride. The SV array was turned ON and OFF with a ±15 mT field sweep. Frame 1 shows the SV traps before turning them ON. Frame 18 shows the ON SV array as it began to attract and trap SPBs and SPB clusters from the surrounding static fluid medium. Frame 43 shows SPB chains forming and aligning with the applied field as well as being trapped by the SV array. Frame 57 shows the trapped- and chained-SPB ensembles. Frame 78 shows the SPB chains and large ensembles released when the SVs were toggled OFF. Even though the large SPB chains appeared to be released, the “anchor” beads remained close to or trapped by the SVs. A few beads have moved towards the center of the SVs and some remain trapped on the blunt SV ends. Some SPBs go out of focus (different focal plane) when the SVs were toggled OFF due to being released and moving vertically away from the trap. Frame 99 shows the recapture of the SPBs, SPB clusters, and SPB chains. Non-specific binding of beads led to a few SPBs remaining trapped on the substrate surface or SVs. Frame 157 shows the capture of more SPBs and the formation of longer chains with the constant applied field. Frame 168 shows the release of the SPB chains and small SPB ensembles. Like before, anchor SPBs remain trapped by or near the SVs. Some SPBs appear to be released and some appear to be permanently trapped. Frame 174 shows the recapture of the SPB ensembles and chains.

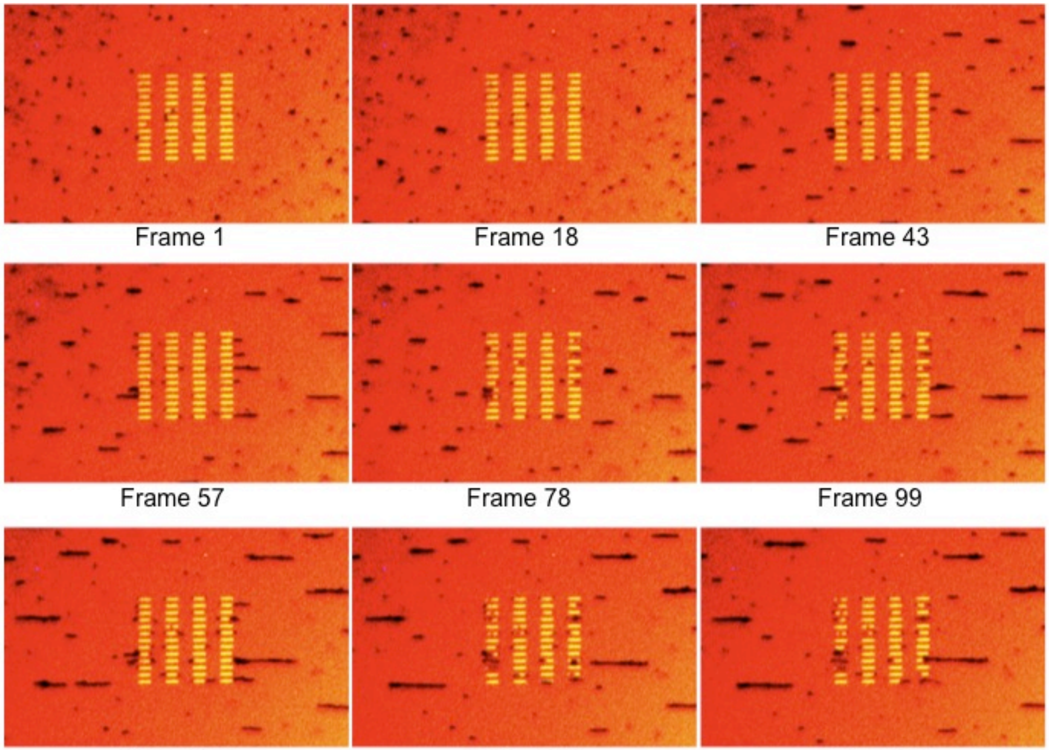
Frame 1
Frame 18
Frame 43
Frame 57
Frame 78
Frame 99
Frame 157
Frame 168
Frame 174

Figure 103: Capture and quasi-release of 1 μm SPB ensembles and chains with ± 15 mT field sweep.

Discussion

Successful capture of 1 μm SPBs, SPB clusters, and SPB chains was demonstrated with the 1 μm × 8 μm, 2 μm × 8 μm, and 2 μm × 10 μm SV arrays. Once the SV surface was passivated with silicon nitride, the release of SPBs, SPB ensembles, and chains was observed; however, the SVs ability to release SPBs decreased over time due to the nitride surface becoming more hydrophobic. SPB capture was enhanced when the applied field was ON, thus magnetically saturating the SVs and SPBs. Additionally, having an array of SVs all ON may enhance SPB trapping due to the additive nature of the SV array magnetic flux density, thus the pull force. The capture of the SPBs appeared to be permanent when there was no passivation layer or surface treatment; SPBs failed to release when the SVs were turned OFF. Permanent trapping may be caused by non-specific binding of the SPB to the substrate, stiction, or edge domains. Alternatively, the OFF field may not have been sufficient to toggle the SV into the antiparallel state. More accurate switching measurements were needed.

Silicon nitride is naturally hydrophobic, which can promote non-specific binding. An oxygen plasma treatment of the silicon nitride and PDMS renders the surface hydrophilic for a couple of hours or for weeks if in a solution [181]. Unfortunately, the bare SV traps could not withstand the oxygen plasma to render the silicon nitride, which electrically insulated the SVs from the write lines, hydrophilic due to oxidation of the IrMn; the SVs delaminated when oxidized. Depositing a thin silicon nitride passivation layer protected the SVs during plasma treatment, which temporarily rendered the nitride surface hydrophilic.

The lack of controlled fluid flow, high-resolution optics, frame time stamps, local addressability, and precise SV actuation control hindered observation and documentation of SPB capture and release. Bead aggregation and non-specific binding were major issues. Additionally, evaporation limited the observation time to less than 10 minutes.

SPB Capture and Release

Repeatable 1 μm and 2.8 μm diameter SPB capture and release on an array of 1 μm × 8 μm SVs was accomplished with wafer design SVWIRE3. The following section will detail the experimental setup and results.

Experimental Setup

Wafer design SVWIRE3 was used to demonstrate SPB capture and release. The SVs were toggled ON and OFF with an in-plane external magnetic field or local write lines, as shown in Figure 104. The linear addressable arrays consisted of three write lines, with each write line actuating twenty 1 μm × 8 μm SVs. Two array lattices were evaluated: a rectangular lattice, as shown in Figure 104 (a), and a symmetrically-staggered lattice, as shown in Figure 104 (b). The wafer also contained numerous test SVs, as shown in Figure 104 (c) to measure the switching characteristics of the 1 μm × 8 μm SVs by MR.

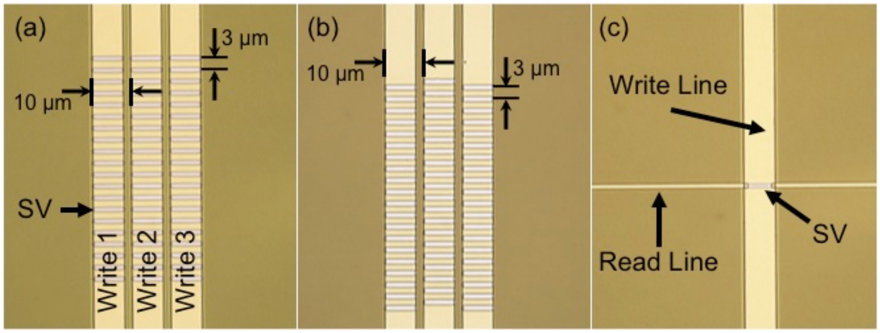

Figure 104: The SVWIRE3 chip design contains a 3 × 20 array of 1 μm × 8 μm SVs on a (a) rectangular lattice and, (b) symmetrically-staggered lattice. (c) Test SV with read and write line to determine switching fields and currents.

The mask layout for one 12 mm × 19 mm SVWIRE3 die is shown in Figure 105. Fabrication involved six masks (read, write, spinvalve, pass, via, and fluidchannel) plus two generic masks (align and flood). Details on the fabrication can be found in CHAPTER 3: FABRICATION and Appendix D: Fabrication Process Charts: SVWIRE 3.1. The SV stack consisted of 5 nm Ta/5 nm Cu/10 nm IrMn/15 nm NiFe/5 nm CoFe/10 nm Cu/5 nm CoFe/15 nm NiFe/5 nm Ta/5 nm Ru. The Ru was added to improve electrical conductivity and GMR, but no significant improvement was observed. The surface was passivated with 100 nano-meters of silicon nitride. The die contained numerous test SVs located on the top and bottom of the die. The SV arrays (3 rectangular, 2 staggered) for SPB capture and release were located in the middle of the die and the write lines taper towards them. The three write lines per array have a common ground.

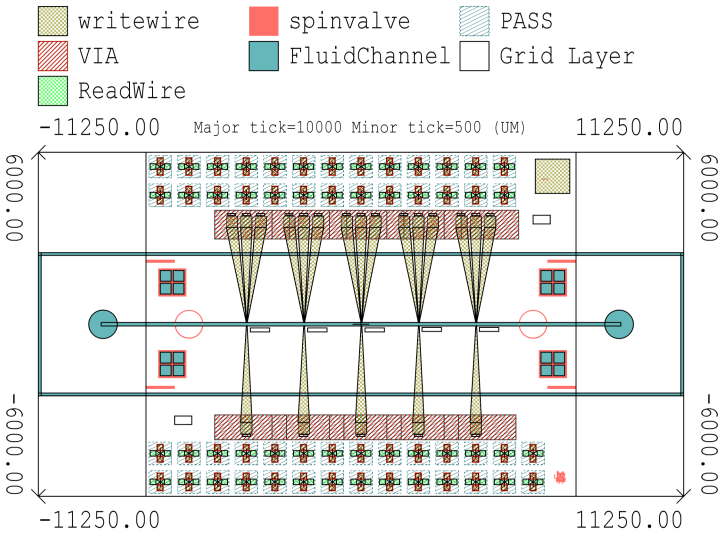

Figure 105: SVWIRE3 mask layout.

Figure 106 shows the fabricated wafer without the PDMS-microfluidic channel. The wafer contains two stepper AMs and a flood mark. The flood mark is a ¼ inch square helpful for detecting the completion of the RIE silicon nitride *via* etches. The wafer contains 15 full dies; one die has been boxed for perspective. During oxygen-plasma cleaning of the wafer, the wafer shattered into small pieces, but some dies remained usable. Most likely, residual water leftover from an auto-wash rapidly evaporated and generated a pressure pulse, which impacted the wafer. All wafers should be dehydrated for 1 minute at 95°C before being placed in a plasma to prevent this from happening again.

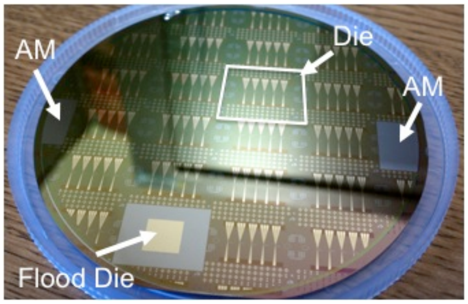

Figure 106: Completed SVWIRE3 wafer showing the dies, AMs, and flood die. One full die has been boxed.

To reduce evaporation and control fluid flow, a PDMS-encapsulated microfluidic channel was designed and fabricated (Figure 73). As shown in the mask layout (Figure 105: FluidChannel), the PDMS microfluidic channel was positioned in the middle of the die and did not cover the contact pads or the test SVs. Square and circle AMs aid in positioning the fluidic channel over the arrays. The 22.5 mm × 6 mm PDMS chip extended beyond the SV die because of spatial limitations on the measurement platform. The microfluidic port (MFP, Cascade MicroTech) and microscope objective could not be used simultaneously if the PDMS inlet and outlets were spaced closer. Because the PDMS microfluidic chip is longer than one SVWIRE die, individual dies should not be diced from the wafer. The size of the SV die was restricted by the 5X reduction stepper mask requirements.

Both 1 μm and 2.8 μm diameter SPBs were captured and released. Initially, 1 μm diameter MyOne™ Dynabeads (Invitrogen) coated with silane were tested. However, imaging of the 1 μm SPBs was hindered by the microscope's limited magnification and the bead aggregation, thus 2.8 μm diameter M-280 Dynabeads (Invitrogen) coated with streptavidin were tested. The protein streptavidin is extensively used in biomolecule purification and detection assays due to its high affinity for biotin, which can be specifically bound to biotinylated biomolecules of interest. A 1:20 dilution of SPBs was loaded into the syringe tubing. This equates to ~3.5-6 × 10^7 1 μm SPBs and ~3-4 × 10^6 2.8 μm SPBs per loading. To reduce unwanted non-specific binding between the SPBs and substrate, the SPBs were suspended in phosphate-buffered saline (PBS) (pH 7.4), 0.01% (v/v) TWEEN 20, and 0.1% (w/v) bovine serum albumin (BSA), per the manufacturers recommendation.

As shown in Figure 107, the SPB solution was injected into the PDMS microfluidic channel with a 1 mL glass syringe connected to a MFP. The flow was controlled with a syringe pump (KD Scientific). Refer to APPENDIX E: Microfluidics Standard Operating Procedure (SOP) for detailed instructions on loading the SPBs into the microfluidic channel.

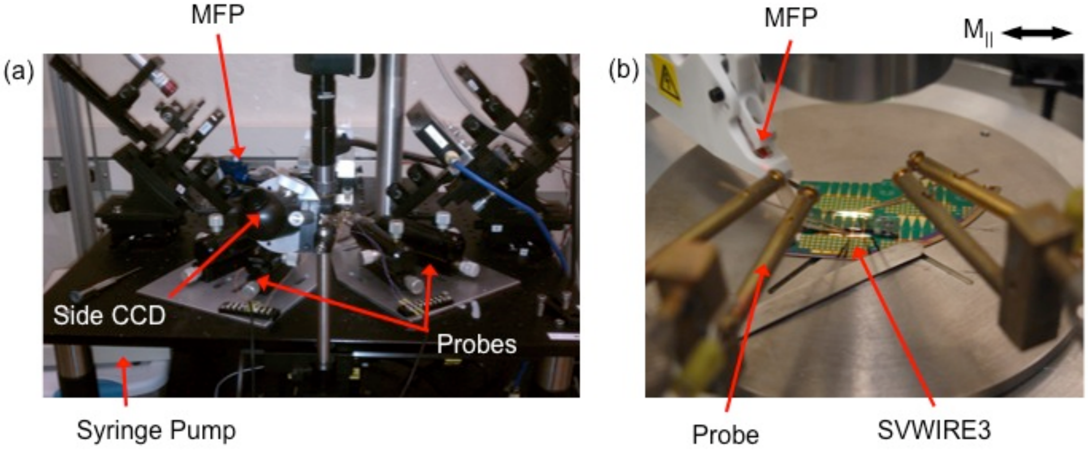

Figure 107: (a) Platform setup showing the location of the syringe pump, side CCD, MFP and probes, (b) SVWIRE3 is located at the center of the platform; a MFP injects the SPB solution and probes connect the current lines to the hardware and software.

A good seal between the PDMS inlet and MFP was important to prevent leakage. Figure 108 (a) and (b) shows the approach of the MFP to the inlet, and (c) shows a sealed inlet. For the 1 μm SPBs, the surfaced was rendered hydrophilic with an oxygen-plasma ash the day before the experiments, but non-specific binding and bead aggregation were still a major problem. For the 2.8 μm SPBs, the surface was rendered hydrophilic on the day of the experiment and less non-specific binding and bead aggregation were observed.

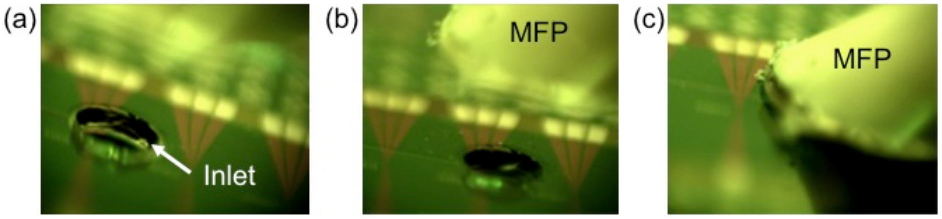

Figure 108: (a) Photo image of PDMS inlet taken from side CCD camera, (b) approach of MFP to the PDMS inlet, and (c) MFP sealed to PDMS inlet.

The SVs were toggled ON and OFF with an external in-plane parallel magnetic field or the write lines controlled by a specially designed Microsoft Visual Basic 6.0 program (MBC.exe). Refer to Figure 81 for the measurement circuit. Unless otherwise noted, a +12 mT or 150 mA 10 ms pulse turned the SVs ON and the -8 mT or -100 mA 10 ms pulse turned the SVs OFF.

The frame rates were dependent on the camera's exposure settings, thus each frame was time stamped to determine accurate frame rates and SPB velocities. The .tiff photo frames were extracted from the large .avi video files with *Im TOO Video to Picture* software. As shown in Figure 109, the .tiff photo frames were then processed with *Adobe Photoshop* software to move the time stamp closer to the channel image, rotate the image if necessary, and to reduce the image to the region of interest. Bead velocities were determined by measuring the bead displacement with the Adobe *Photoshop* ruler tool between the time-stamped frames. The resolution of the frames averaged 20 pixels/μm.

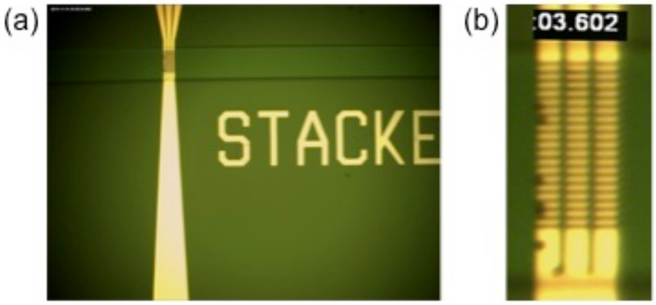

Figure 109: (a) Large 14 MB frame extracted from .avi video file before processing and, (b) processed frame showing only the array. Processing included relocating the time stamp, rotating the image, and cropping.

Results

Figure 110 (a) shows the movement of 1 μm SPB and SPB ensembles on and between the 1 μm × 8 μm SVs without the aid of fluid flow. Many SPBs on Write 1, Write 2, and Write 3 were permanently trapped and did not respond to SV and write-line actuation. Due to hardware limitations (only one current source), only current-line Write 2 was active. Figure 110 (b) shows the pulse sequence associated with the video stills. At 43 s, all the SVs in the array were toggle ON with a +15 mT in-plane parallel external field. At 45 s, Write 2 was pulsed with 100 mA for 10 ms, which resulted in a few SPBs (SPB movement is shown with red arrows) on Write 1 SVs moving towards Write 2. The current pulse generated a field gradient highest near the center of Write 2, which attracted the SPBs trapped on the Write 1 SVs.

At 48 s, a -100 mA 10 ms current pulse turned Write 2 SVs OFF; however, without a read line, the state of all the SVs could not be verified. The pulse resulted in a few SPBs moving from Write 1 towards Write 2. Also, some of the SPBs on Write 2 appeared to release from the blunt ends of the SVs, but they remained near the SVs. At this time, SVs on Write 1 and Write 3 should have been ON and attracting SPBs; however, none of the SPBs moved from SVs on Write 2 to SVs on Write 1 or 3. At 49 s, a 100 mA 10 ms pulse turned the Write 2 SVs ON, which resulted in a SPB ensemble moving from a Write 1 SV to Write 2 SV. Also, the SPB ensemble that appeared to be released at 49 s appeared to be trapped again. When Write 2 was pulsed again with 100 mA, a large SPB ensemble clearly moved toward the center of the SV on Write 2.

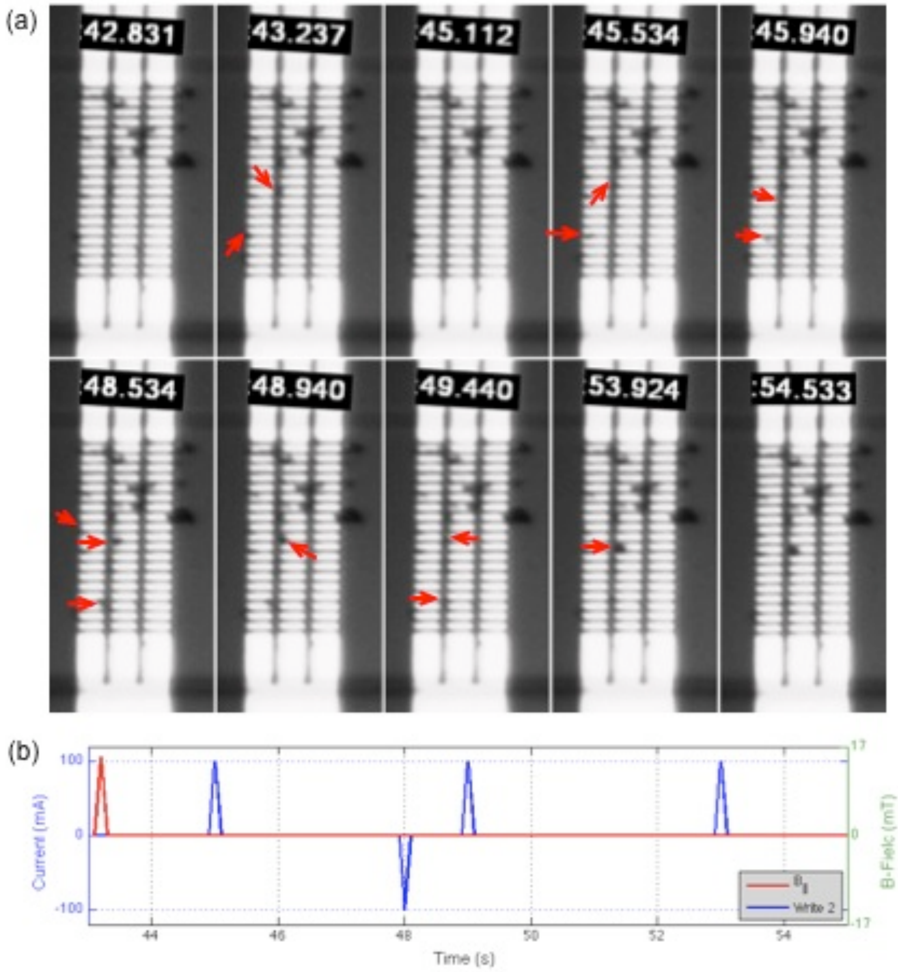

Figure 110: (a) Video stills showing 1 μm SPB movement associated with, (b) $B_{||}$, Write 1, and Write 2.

Due to difficulty observing and manipulating the aggregated 1 μm diameter SPBs, 2.8 μm SPBs were evaluated. Figure 111 shows the capture and release of 2.8 μm SPBs traveling 175-230 μm/s. At t = 0 s, a +12 mT external in-plane field saturates the ON SVs and SPBs resulting in the capture of SPBs and formation of SPB chains aligned with the applied field. At t = 0.6 s, an -8 mT pulse turns OFF the SV traps and the SPBs were released.

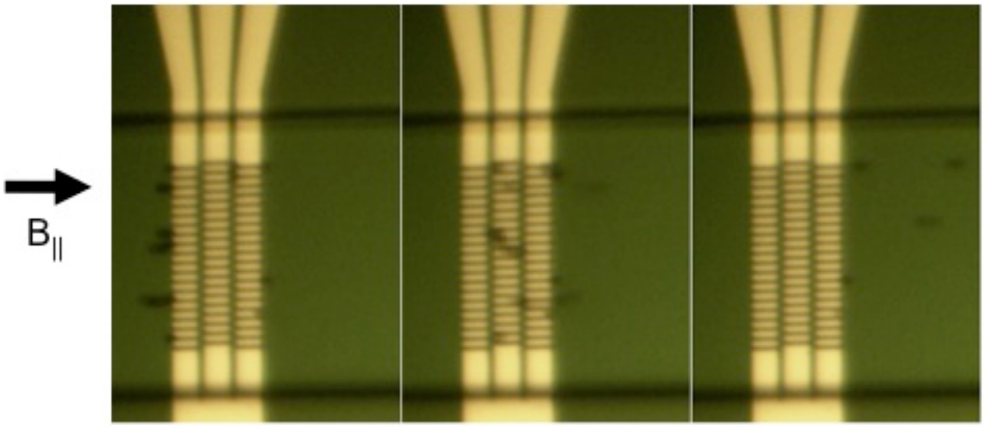

t = 0 s
$B_{||}$ = 1.2 mT

t = 0.6 s
$B_{||}$ = -8 mT Pulse

t = 1.2 s
$B_{||}$ = 0 mT

Figure 111: Video stills of 2.8 μm SPB captured and released on SVs toggled with $B_{||}$. At t = 0, the polarized SPBs are trapped on the saturated ON SVs. The -8 mT field pulse switches the SVs OFF and the SPBs are released at t = 0.6 s.

Figure 112 demonstrates SPB capture and release as well as unwanted interaction between the adjacent write lines and SVs. Only Write 1 was active during this experiment. The SVs on Write 2 and Write 3 were switched ON with a +15 mT in-plane external field pulse. Between 0.880 s and 1.490 s, the Write 1 SVs were switched OFF and the SPB near the top of the array on Write 1 was released; the SPB moved toward Write 2 and changed focal planes. The SPB trapped between SVs on Write 1 and Write 2 was pushed away from Write 1 and hovered between two SVs on Write 2. As shown at 2.084 s, the upper SPB continued to shift right towards Write 2 and the lower SPB was captured by another SV on Write 2. At 24.865 s, the upper SPB was trapped between SVs on Write 1 and Write 2 and the lower SPB remained trapped.

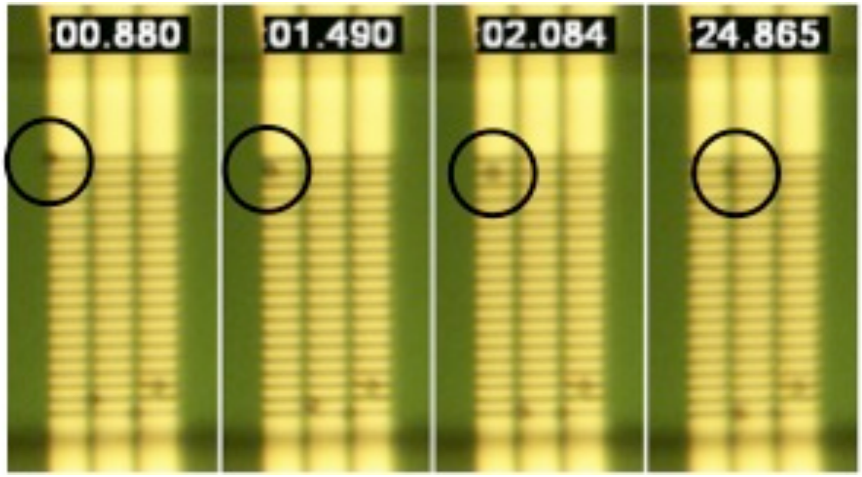

Figure 112: Video stills showing a 2.8 μm SPB released from Write 1 SV and captured by a Write 2 SV.

Figure 113 demonstrates a 2.8 μm SPB being captured and released on the staggered SV array. Both Write 1 and Write 2 were connected to current sources to locally toggle the SVs ON and OFF. A +150 mA current pulse turned the SV trap ON and the -100 mA current pulse turned the SV OFF. The SVs on Write 3 were turned ON with a +15 mT external field pulse. At 38.844 s, the SPB is trapped on the left side of an ON Write 1 SV. At 39.453 s, the Write 1 SVs are OFF and the SPB was released and trapped by an ON Write 2 SV. At 43.047 s, the Write 2 SVs are OFF and the SPB was released and trapped by an ON Write 3 SV. At 44.250 s, the SVs on Write 2 are ON and the SPB moved back to a Write 2 SV; however, the SPB did not appear to be securely trapped (different focal plane). This could be due to the Write 3 SVs still being ON and the small gap between the SVs allowing both SVs to attract the bead. At 44.844 s, the Write 2 SVs are OFF and the SPB was released, and then trapped on the right side of Write 3. The flow rate in the channel was 60 -70 μm/s.

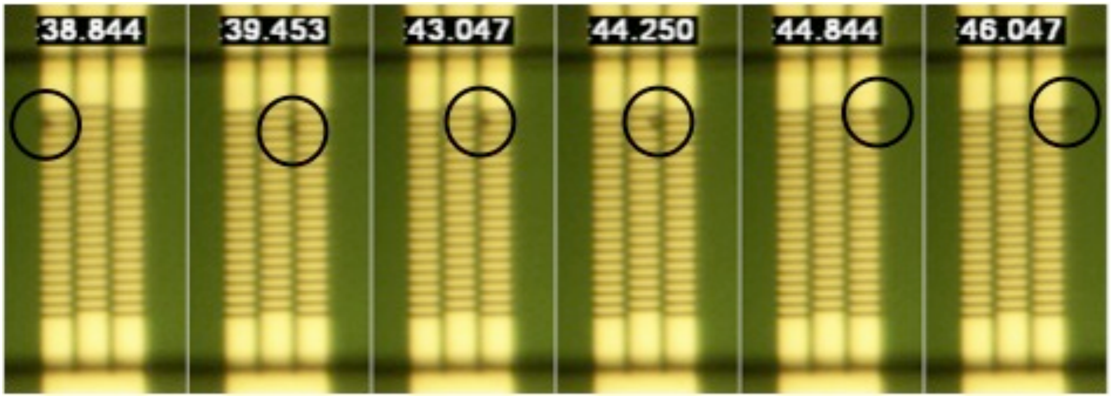

Figure 113: Video stills showing a 2.8 μm SPB moving from SVs on Write 1, to Write 2, to Write 3, back to Write 2, then back to Write 3.

Discussion

Capture and release of 2.8 μm SPBs were successfully demonstrated on both the rectangular and symmetric-staggered SV arrays actuated with either the external in-plane magnetic field or the local write lines. The velocity of captured SPBs varied greatly; the state of the SVs, thickness of the passivation layer, the surface treatment, whether the channel previously dried out, and the time elapsed since the plasma surface treatment affected both the SV pull force and non-specific binding. For example, with all the SVs ON and biased with a +12 mT in-plane magnetic field, SPBs traveling 175-230 μm/s were trapped and released. With all the SVs ON without a bias field, SPBs traveling ~40-60 μm/s were trapped.

The 1 μm SPB experiments failed to clearly demonstrate SPB capture and release; however, the findings influenced the design and setup of future chips and experiments. The movement and location of the 1 μm SPB was difficult to observe with the optical system; either larger SPBs or a better optical system was needed. Without read lines, the state of the SVs on each line could not be verified, thus the SPB movement could not be precisely interpreted. At least one read line on each write line would verify the state of the SVs and the viability of the current lines.

As shown in both the 1 μm the 2.8 μm SPB experiments, the arrayed SVs were packed too closely and the write lines influenced SPB movement on adjacent lines; more spacing between SV traps and write lines would reduce these unwanted interactions. Due to hardware limitations, only two write lines could be actuated. A third line was not needed. And finally, the channel should be prepped on the day of the experiment to reduce non-specific binding.

SPB Capture, Transport, and Release

Precise capture, transport and release of 2.8 μm SPBs with an addressable linear array of staggered SVs will be described in this section.

Experimental Setup

Wafer SVWIRE6 was designed and fabricated with both read and write lines. Figure 114 (a) shows the cross-sectional schematic of the chip and microfluidics. A 170 nm thick silicon nitride layer insulated the 1 μm × 8 μm SV from the 150 nm thick and 8 μm wide gold write lines. As shown in Figure 114 (b) and (c), there are two write lines, Write 1 and Write 2, spaced 2 μm or 4 μm apart. Each write line contains twelve SVs and the SVs were symmetrically staggered. The SVs were spaced 5 μm apart along each line. Spacing between the SVs and write lines was increased in order to clearly see SPB movement between the SVs and to minimize SV and write-line interactions. Additionally, if the SV blunt ends are too close together, they can lower the pull force of adjacent SVs (refer to Array Lattice and SV State on page 68). One SV on each write line was connected to a read line, Read 1 or Read 2, via 2 μm wide contact leads evaporated onto the blunt end of the SV.

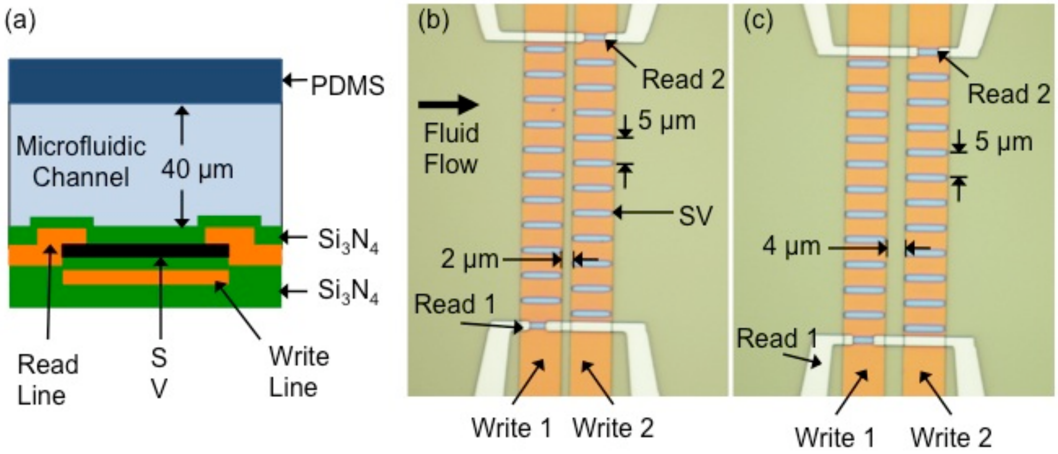

Figure 114: (a) Cross-sectional schematic of the microfluidic chip. The silicon nitride layers separate the SVs from the write line and microfluidic channel. (b) Optical image of the chip containing two read-line leads (Read 1 and Read 2) and two addressable write lines (Write 1 and Write 2) spaced 2 μm apart and, (c) 4 μm apart.

Each SVWIRE6 die also contains numerous test SVs with both read and write lines. Some of the test structures have more than one SV on the write line or are in the middle of a SV array. Future studies could evaluate how the state of neighboring SVs effects the SV's switching characteristics.

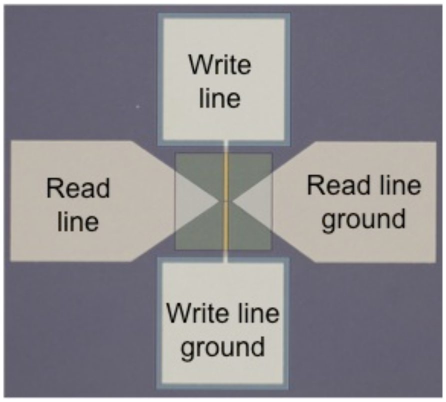

Figure 115: Test SV addressable with both read and write lines.

The mask layout for one SVWIRE6 die is shown in Figure 116. Five new masks (read, write, spinvalve, pass, and via) as well as the “align” and “flood” masks were used to fabricate the SVWIRE6 wafer. The SV stack consisted of 3 nm Ta/3 nm Cu/10 nm IrMn/15 nm NiFe/5 nm CoFe/10 nm Cu/5 nm CoFe/15 nm NiFe/5 nm Ta. The seed and buffer layers were thinned due to concerns about surface roughness. A detailed fabrication process chart can be viewed in Appendix D: Fabrication Process Charts.

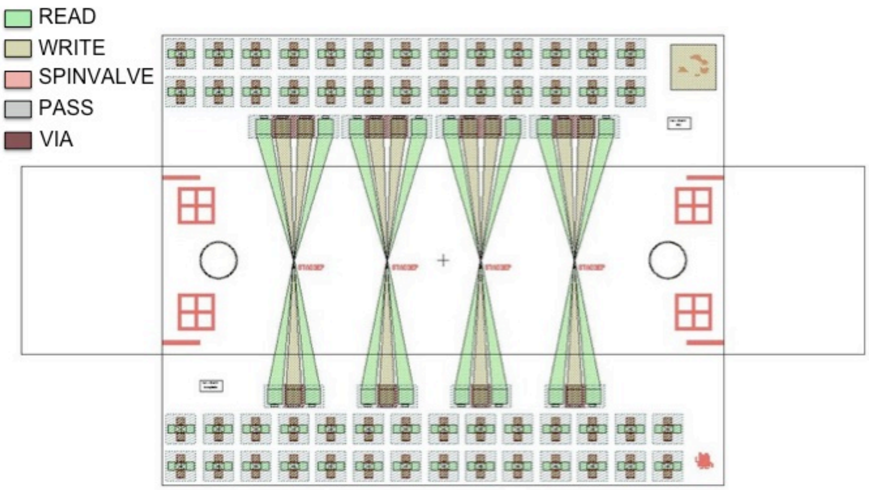

Figure 116: SVWIRE6 die layout. Each die is 12 mm × 19 mm.

SVWIRE6 was designed to use the same disposable PDMS microfluidic chip design (Figure 73) fabricated for SVWIRE3. The PDMS microfluidic chip was positioned in the center of the die, which left the contact pads and test SVs exposed. AMs and circles on the wafer and PDMS assisted alignment.

Figure 117 shows the completed wafer with a PDMS-microfluidic chip bonded to one of the thirteen full dies. The wafer was not diced to simplify the cleaning process after each experiment was completed. Before cleaning the wafer, the PDMS microfluidic chip was removed and discarded. The PDMS-microfluidic chip was not reused due to crystallized PBS and SPBs clogging the channels after 2-3 days of use. One die has been boxed for perspective. The flood die was used during fabrication to determine when the silicon nitride *via* RIE was complete. The two AMs were necessary for stepper mask alignment.

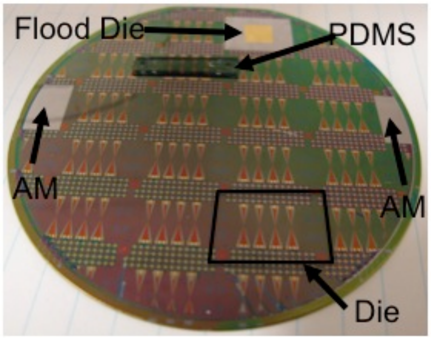

Figure 117: Completed SVWIRE6 wafer showing the dies, AMs, and flood mark. One full die has been boxed.

Figure 118 shows the platform setup for the bead manipulation experiments. A MFP injects the SPB solution stored in the 1 mL glass syringe into the microfluidic channel. A syringe pump, shown in Figure 118 (c), controls the channel flow rate (0.001-2.0 μL/min). Due to the flexibility of the PDMS, the flow rate does not always correlate to the SPB velocity. Seven probes (P1-7) connect the write and read lines to two lock-in amplifiers and four current sources (see Figure 81 for the measurement circuit). Figure 118 (b) shows the probe layout and (d) shows which probe controls each line. Both write lines have a common ground, thus P6 was listed twice.

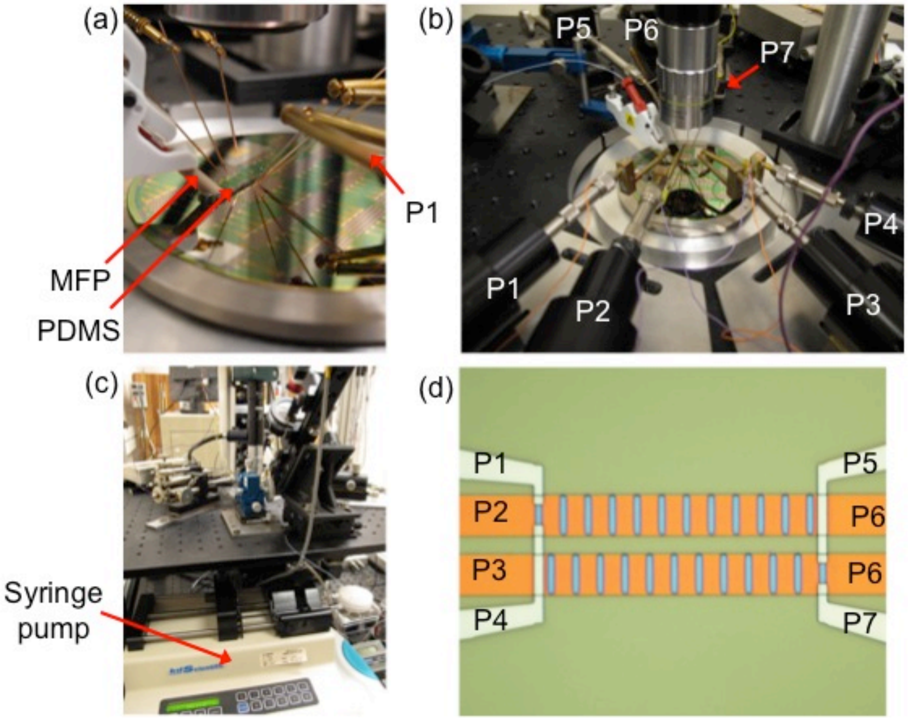

Figure 118: (a) Close-up of PDMS microfluidic channel, MFP, and probes, (b) layout of the seven probes: Read 1 (P1), Write 1 (P2), Write 2 (P3), Read 1 (P4), Read 2 (P5), Write common ground (P6), and Read 2 (P7), (c) location of the syringe pump and back probes, and (d) probe connections to the read and write lines.

The frame rates were dependent on the camera's exposure settings, thus each frame was time stamped to determine accurate frame rates and SPB velocity. The .tiff photo frames were extracted from the large .avi video files with *Im TOO Video to Picture* software. The .tiff photo frames were then processed with *Adobe Photoshop* to move the time stamp closer to the channel image and to reduce the image to the region of interest. SPB velocities were determined with the time-stamped video frames and *Adobe Photoshop* ruler tool.

Results

Capture of 2.8 μm SPBs on an array of ON SVs is shown in Figure 119. All the SVs were switched ON with an in-plane +15 mT external field pulse. Average bead velocity was 160 μm/s. The SPBs collected on both blunt ends of the SV. On a few SVs, multiple SPBs have collected along the length of the SV.

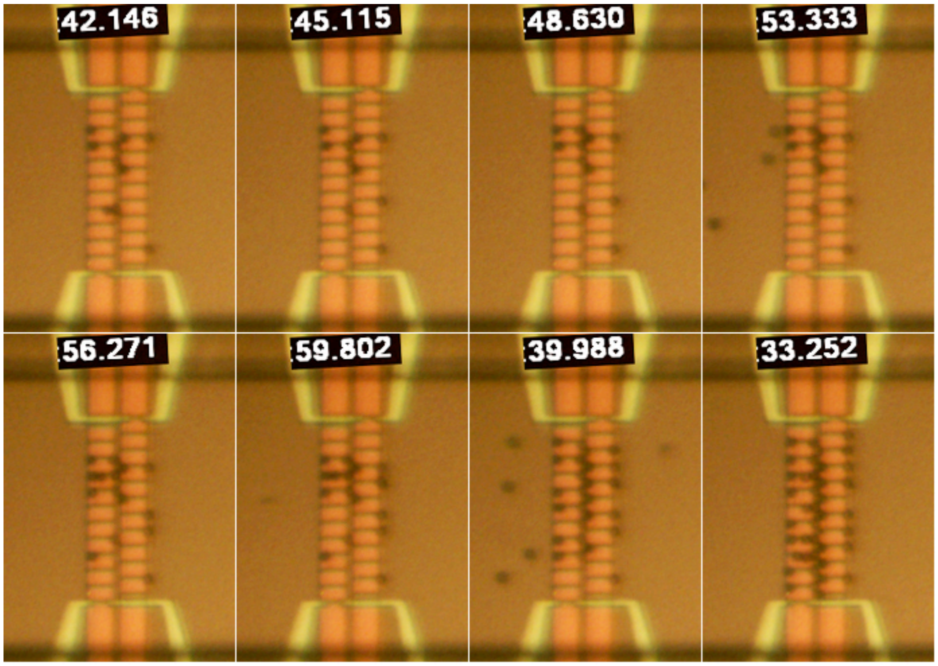

Figure 119: ON SVs trapping 2.8 μm SPBs.

Figure 120 shows a SPB not trapped by the ON SVs either due to a high velocity (~120-130 μm/s) or bead-bead interaction. At 42.640 s, the bead traveled between one vacant ON SV and one occupied ON SV without being trapped. At 42.968 s, the bead abuts two beads trapped on an ON Write 2 SV, but is not trapped. Instead, it is pushed above and to the side of the beads and continues to flow down the channel.

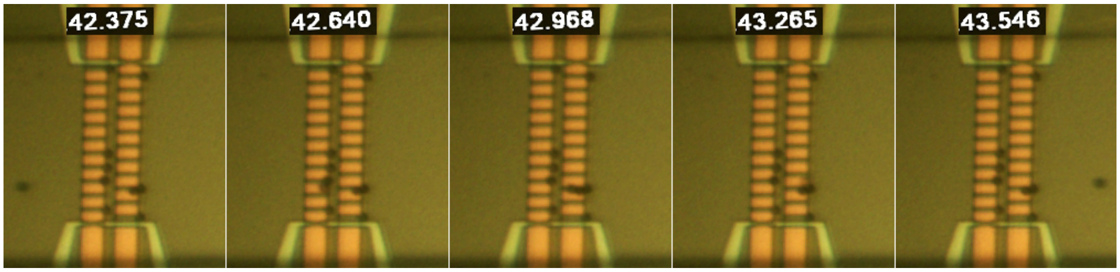

Figure 120: SPB traveling ~120-130 μm/s not trapped by ON SVs.

Figure 121 demonstrates 2.8 μm SPB capture and release with the write lines toggling each SV line ON and OFF. At 12.928 s, beads are trapped on the Write 1 and 2 SVs. Bead velocities were observed to range from 45 μm/s to 65 μm/s. Between 12.928 s and 13.537 s, Write 1 was toggled OFF with a -100 mT 10 ms pulse and ON with a 150 mT 10 ms pulse. Beads on Write 1 were released; however, the current through Write 1 interfered with the trapped Write 2 SVs and two beads were accidentally released. At 14.147 s, another bead approached the Write 1 SV traps and the released beads moved between Write 1 and Write 2. At 14.741 s, the beads released from Write 1 SVs were trapped on the right side of the Write 2 SVs and a Write 1 SV trapped another bead. With a flow rate of 45-65 μm/s, the beads on the right side of Write 2 can be released with a current pulse through Write 1 or by toggling OFF the SVs on Write 2. One Write 1 SV bead was permanently bound to the substrate and did not respond to the write-line current pulses.

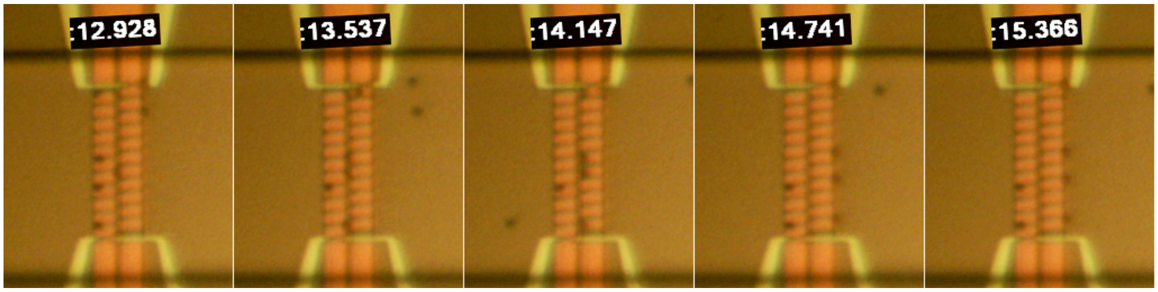

Figure 121: SPB release and capture by write-line actuated SVs.

Figure 122 shows the “Back and Forth” pulse sequence, corresponding read-line GMR, and video stills to transport 2.8 μm SPBs back and forth between the two SV write lines. The velocity of beads in the channel was 1-2 μm/s. The beads were transported from Write 1 to Write 2 SVs by turning the Write 1 SVs OFF with a -100 mA 10 ms pulse, then turning the Write 2 SVs ON with a +150 mA 10 ms pulse. To transport the beads back to Write 1 SVs, the Write 2 SVs were toggled OFF, and then the Write 1 SVs were toggled ON. Two beads appeared to be permanently bound to the SV traps and did not respond to current-line or SV actuation. The observed lag between the read-line switching event and the write-line current pulse was due to artifacts (long time constants) in the measurement circuit and was not due to any intrinsic delay in the SV switching process. The peaks in the GMR that occur at each switching event were due to momentary write current Joule heating.

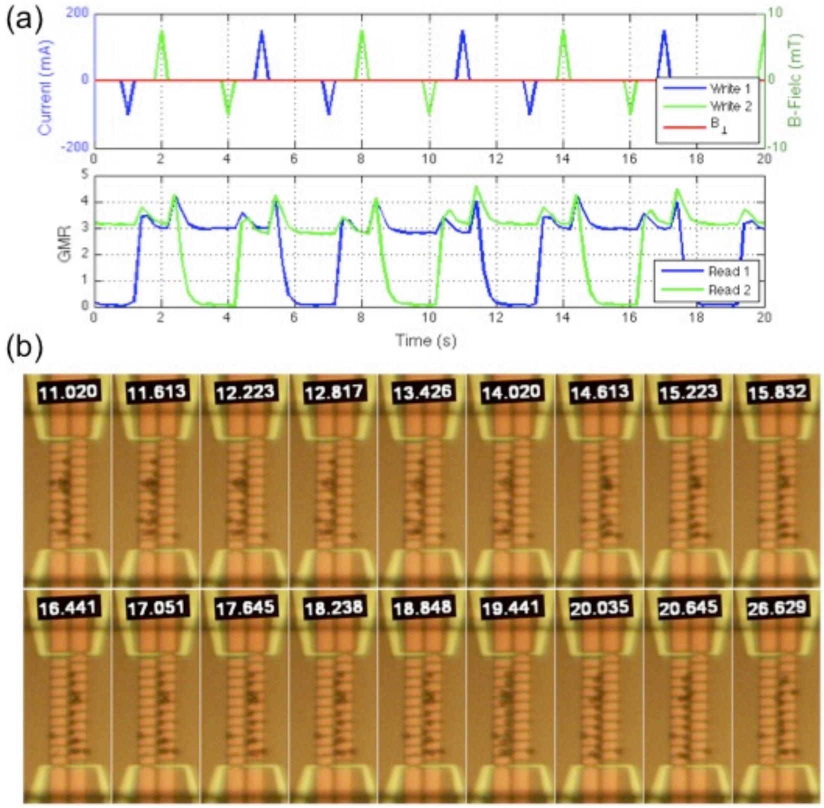

Figure 122: (a) Pulse sequence to transport 2.8 μm SPBs "Back and Forth" between Write 1 and 2 SVs. (b) Video stills demonstrating beads transported between Write 1 and 2.

With the "Back and Forth" SV pulse sequence, as shown in Figure 122 (a), a high concentration of 2.8 μm beads were transported back and forth between the Write 1 and 2 SVs as shown in Figure 123. Bead velocities in the channel averaged 20 μm/s. Beads were easily transported from Write 1 to Write 2 SVs with the aid of fluid flow; however, when the beads were transported against the fluid flow from Write 2 to Write 1 SVs, some beads were not recaptured and were swept away with the flow. Eventually, the majority of the beads were released due to the strong fluid flow and bead-bead interactions. Less delay between switching Write 2 SVs OFF and Write 1 SVs ON or a slower cross flow may reduce unwanted SPB release.

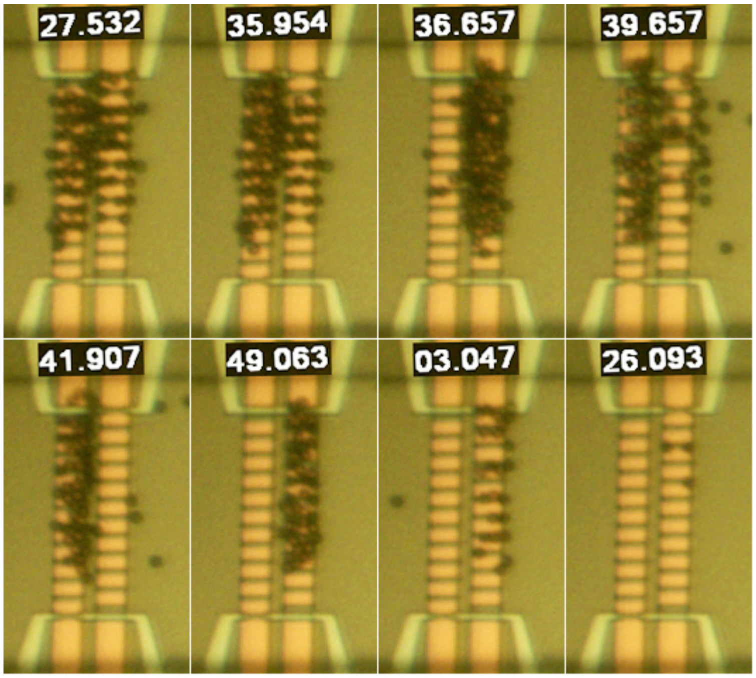

Figure 123: Transport of numerous SPBs “Back and Forth” between Write 1 and 2 SVs.

Figure 124 shows the pulse sequence to transport the 2.8 μm SPBs back and forth between Write 1 and 2 SVs biased with a +1 mT in-plane magnetic field. Average bead velocity was 1-2 μm/s. With the bias field, the beads align along the length of the SV instead of collecting at the blunt end of the SV. This low-bias field increased the bead capacity of each SV.

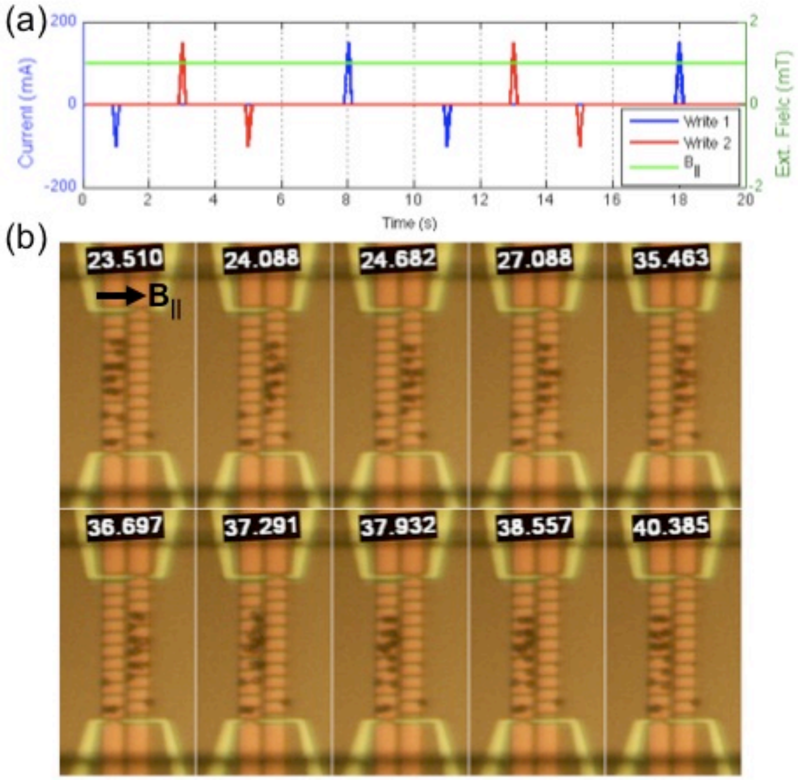

Figure 124: (a) “Biased Back and Forth” pulse sequence to transport 2.8 μm SPBs back and forth between Write 1 and 2 SVs biased with an in-plane +1 mT field. (b) Video stills demonstrating beads transported between Write 1 and 2.

Figure 125 (a) shows the pulse sequence, “Down Ladder”, to transport the SPBs between and down the SVs and, (b) shows SPBs transported between and down SVs on Write 1 and Write 2. Fluid flow in the channel was 1-2 μm/s (syringe pump set to 0.001 μL/min). To transport the beads down the SV “ladder” and perpendicular to the fluid flow, an external in-plane field (**B**$_{\perp}$) perpendicular to the SV easy axis, in addition to the write lines was applied. The ±1 mT perpendicular field orients the free layer moment off axis without toggling the SV ON or OFF. The polarized SPB follows the free layer moment and moves to the corner of the SV as shown at 46.045 s, 46.639 s, 49.029 s, and 49.623 s. As depicted in the schematic, when the SPB, trapped on the corner of the perpendicularly biased ON SV, is released, it will be attracted to and trapped by the nearest ON SV, which happens to be down the ladder on the other write line. When the external perpendicular bias field was removed, the SPBs returned to the blunt end of the SV, as seen at 47.248 s, 50.232 s, and 35.387 s.

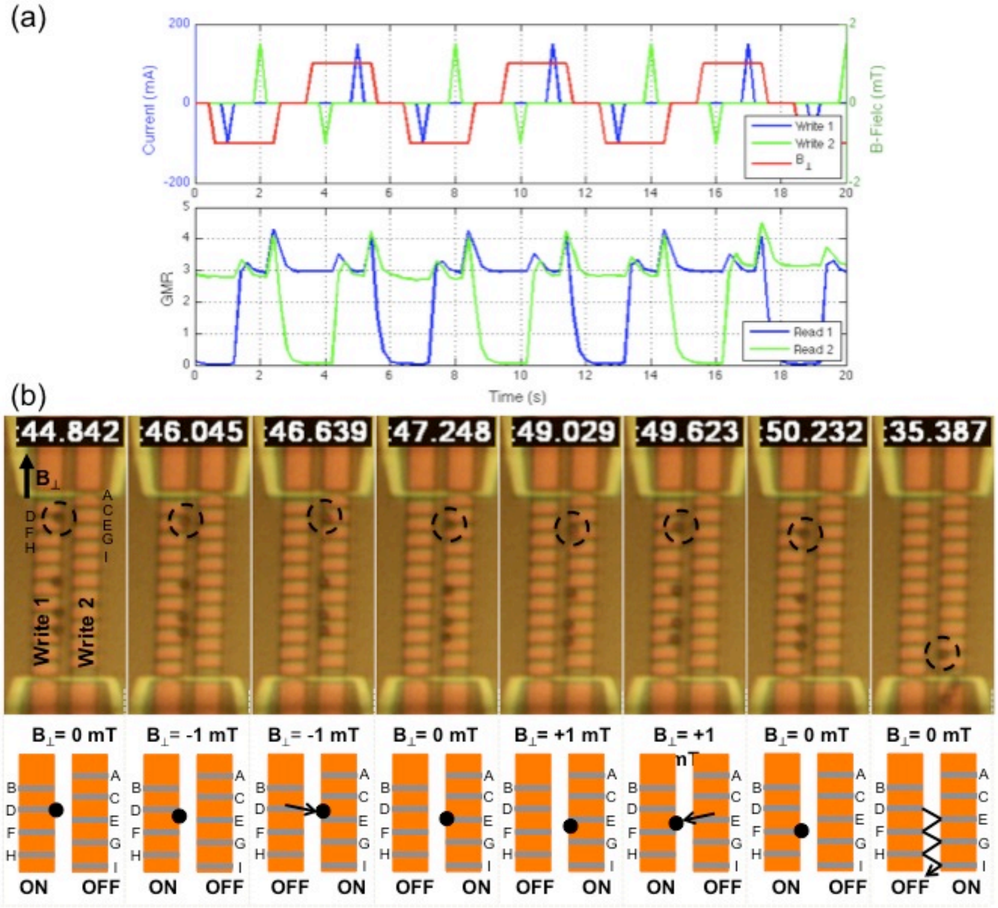

Figure 125: (a) "Down Ladder" pulse sequence to transport SPBs down the SV ladder and the associated read line GMR. (b) Video stills and schematics illustrating transportation of four 2.8 μm SPBs down the SV ladder.

As shown in Figure 126, the SPBs were transported up the SV ladder by reversing the polarity of $\mathbf{B}_\perp$. The pulse sequence to move the SPB up the ladder was called, "Up Ladder". The average bead velocity was 1-2 μm/s. In addition to moving the beads up the ladder, a bead trapped on the right side of a Write 2 SV was transported to the left side of the Write 2 SV (see 37.914 s frame), then transported to the right side of a Write 1 SV (see 39.711 s frame), and then transported up the ladder.

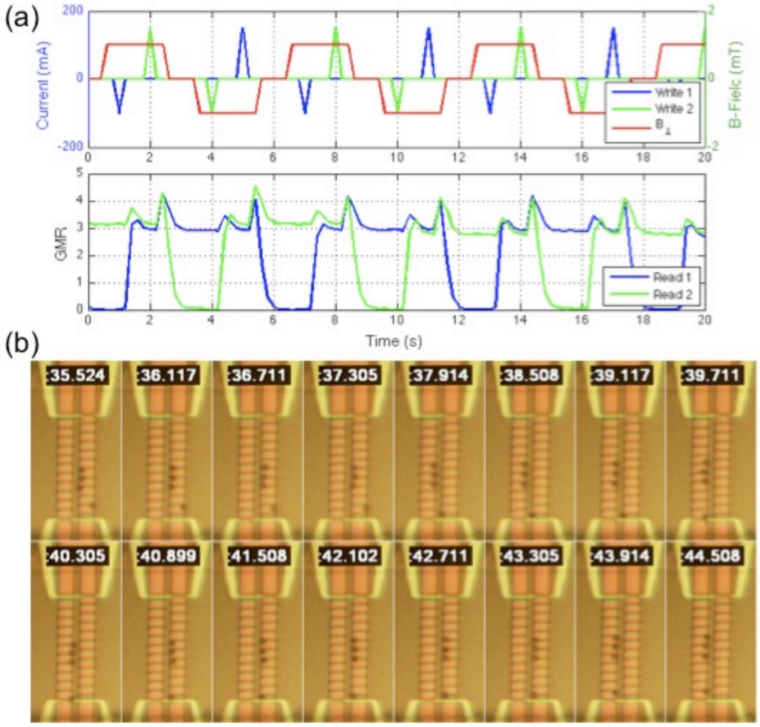

Figure 126: (a) "Up Ladder" pulse sequence to transport beads up the SV ladder and the associated read line GMR. (b) Video stills and schematics illustrating transportation of four 2.8 µm SPBs up the SV ladder.

Figure 127 demonstrates the capture, transport, and collection of 2.8 µm SPBs. The write lines and external perpendicular in-plane magnetic bias field were actuated with the pulse sequence, "Up Ladder". Between 45.479 s and 45.792 s, a SPB traveling 6 µm/s was trapped on the right side of an ON Write 1 SV (shown in the dotted black circle). When Write 1 SVs were turned OFF, the released SPB moved towards and was trapped by an ON Write 2 SV (see frame at 48.323 s). Once trapped on the left side of the ON Write 2 SV, the SPB climbed up the ladder. One bead was permanently bound to a lower SV on Write 1.

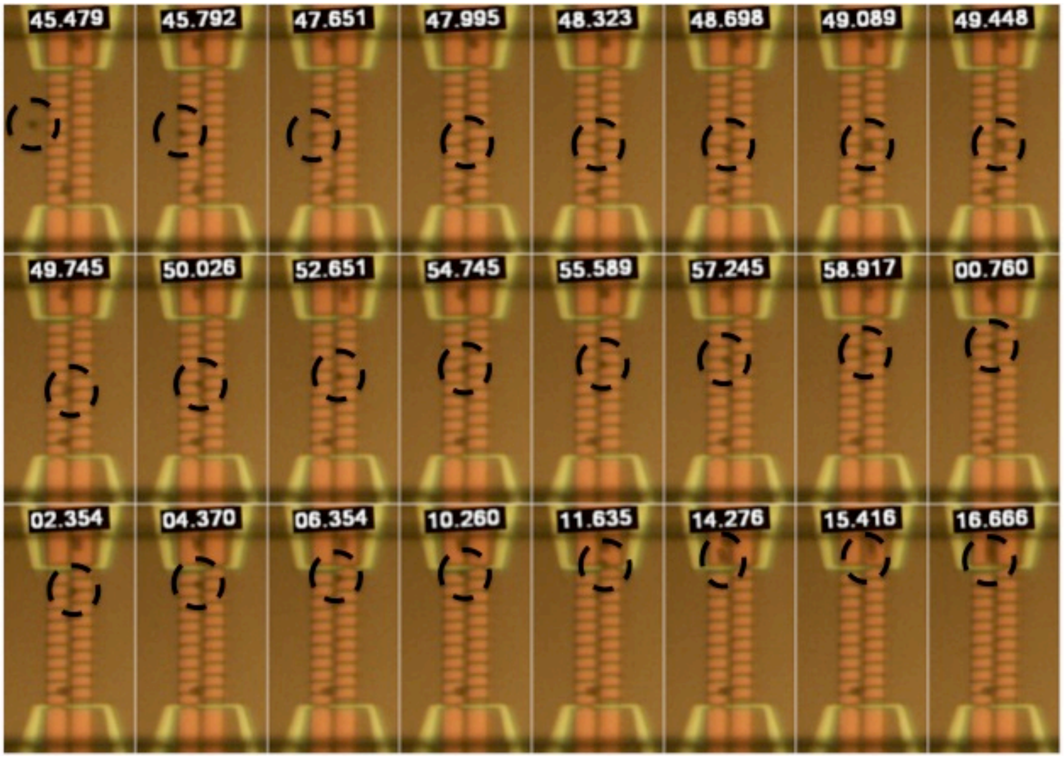

Figure 127: SPB capture, transport, and collection on SV array with the "Up Ladder" pulse sequence and read line sense current.

When the bead reached the top of the SV ladder, it was released into the Read 2 "well", where two other previously released SPBs had collected. The 100 μA 100 Hz current running through Read 2 (and Read 1) generates a magnetic flux gradient, which prevents the beads from leaving the Read 2 "well" during low flow (6 μm/s). Additionally, these trapped beads aligned with the external perpendicular field and bounced between Write 1 and Write 2 as they followed the high gradient generated by the ON and OFF current-line pulses. Due to cross flow, the beads trapped in the Read 2 well hovered on the right side of Write 1 when the Write 1 SVs were pulsed and hovered near the center of Write 2 when Write 2 SVs were pulsed.

Figure 128 shows the attempted bulk bead transport by means of the “Up Ladder” pulse sequence. The high concentration of beads and 20-30 μm/s flow velocity hindered bead movement up the SV ladder. When the beads were released from the Write 2 SVs, not all the beads were captured by the Write 1 SVs, as shown in the frames at 2.300 s and 4.112 s. Either the opposing fluid flow was too fast and the delay between turning OFF Write 2 SVs and ON Write 1 SVs was too long, or bead-bead interactions hindered recapture and transport up the SV ladder. Additionally, the short ladder increased bead-bead interactions.

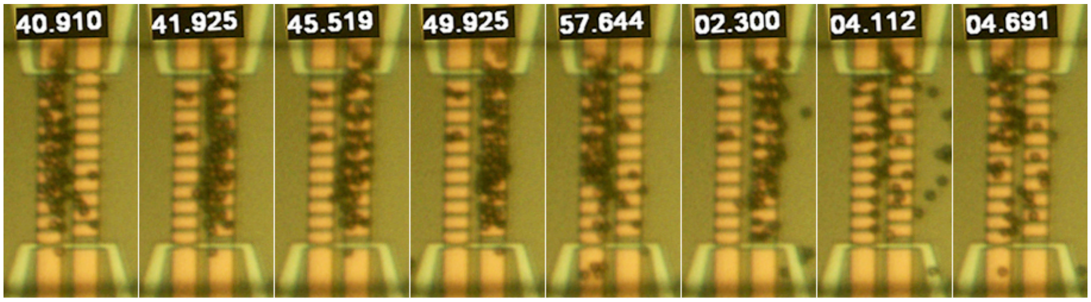

Figure 128: “Up Ladder” pulse sequence with high bead concentration and high fluid flow (20-30 μm/s).

The “Up Ladder” and “Down Ladder” pulse sequences were combined, as shown in Figure 129 (a) and (b). Both a two-bead complex and a single bead are transported up the SV ladder, then down the SV ladder. Due to the size of the two-bead complex, it failed to go down the ladder at 31.192 s, but the single bead was transported up and down the SV ladder without error. The average bead velocity was 10-14 μm/s.

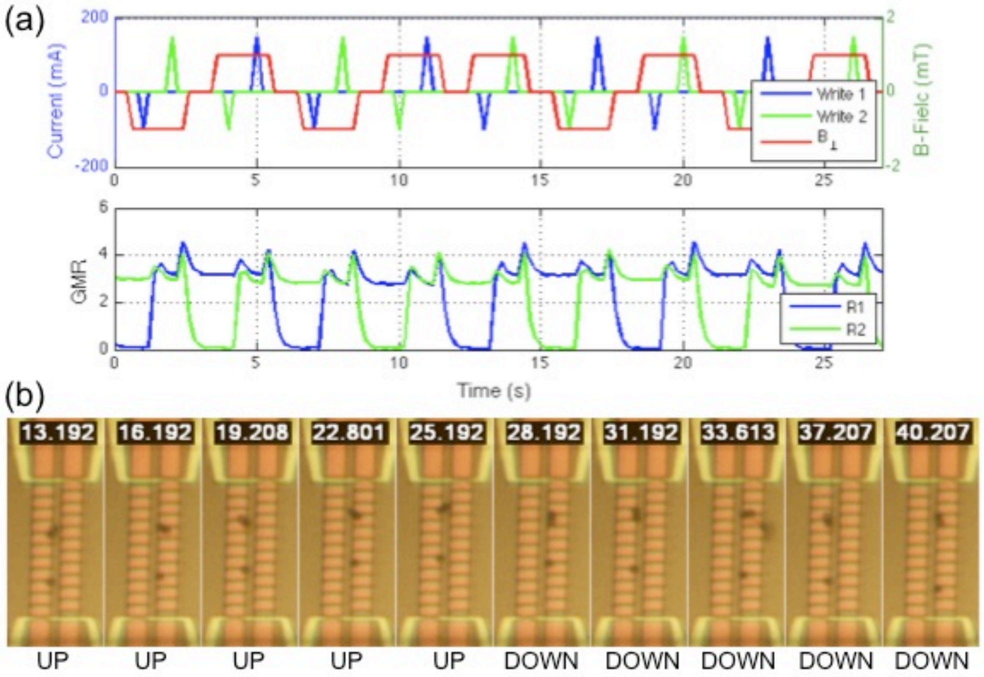

Figure 129: (a) Combined "Up Ladder" and "Down Ladder" pulse sequence transporting a, (b) two-bead complex and a single SPB.

Discussion

With bistable SVs actuated locally by write lines, 2.8 μm SPB capture, transport, and release were demonstrated. The velocity of beads prior to being captured varied greatly depending on the array and fluid flow conditions. With all the SVs ON, beads traveling up to 160 μm/s were captured and released. With this high flow rate, the first line of the SVs acted like a break and beads were trapped on the second line. With a flow velocity < 65 μm/s, some SPBs could be captured by the ON Write 1 SVs. With a flow velocity < 30 μm/s, very few capture errors occurred with low SPB concentrations. Additionally, with the aid of an in-plane ±1 mT perpendicular magnetic field, precise SPB transport perpendicular to low fluid flow (≤ 14 μm/s) was accomplished.

When transporting SPBs against fluid flow from Write 2 to Write 1 SVs, a low flow, low SPB concentration, or a high switching speed was required. Few transport errors occurred with flow velocities of ≤ 14 μm/s and low bead concentrations. Transport errors moving the beads between Write 2 and 1 SVs occurred with flow velocities ≥ 20 μm/s and when there was a high concentration of beads. This could be due to a low SV pull force, limited SV bead capacity, or the 2-3 second delay between turning SVs OFF and ON. The SV switching speed was limited by the measurement circuit hardware. A higher switching rate and higher flow rate may be possible, but not with the current hardware setup.

In lieu of directing the SPB path with the global bias field, altering the direction of fluid flow (e.g., flow perpendicular to SV easy axis), redesigning the SV array pattern, applying write-line current pulse below the SV switching thresholds, or implementing a fully addressable array of SVs, analogous to magnetic random access memory (MRAM), may be used to direct the bead along a desired path.

Summary

In this chapter, we have demonstrated a programmable and reusable SV platform to trap, release, and precisely transport functionalized SPBs. Although the motion of the bead was limited by the simple linear array of SVs used in these experiments, it demonstrates a technology that can be useful for complex bead manipulation. A programmable array of SVs can be used for simultaneously controlling the individual motions of a large number of beads, and their attached payloads, for sorting and programmed chemical synthesis applications.

CHAPTER 7: SPB DETECTION

The detection of a single 2.8 µm SPB by means of read lines, in tandem with a large applied in-plane perpendicular magnetic field, was accomplished and will be discussed in this chapter.

Experimental Setup

Wafer SVWIRE6 (Figure 114 on page 143) containing two write lines and two read lines was used to demonstrate single-bead detection. For a detailed description of SVWIRE6 and the experimental setup, please refer to the SPB Capture, Transport, and Release Experimental Setup section on page 142.

The "Up Ladder" and "Down Ladder" pulse sequences were used to position the SPB on either the Read 1 SV or Read 2 SV, as shown in Figure 130. To detect whether the read-line SVs were occupied by a bead or not (vacant), a large external in-plane field ($B_{\perp}$) perpendicular to the SV easy axis was applied and the read-line resistances were measured with a 100 µA 100 Hz sense current.

For all the detection measurements, the resistance of the ON SV was measured for ten seconds before applying a positive $B_{\perp}$ for ten seconds. Once removing the positive applied field, the resistance of the SV was measured for another ten seconds without an applied field before a negative $B_{\perp}$ was applied for ten seconds. The slow switching was due to hardware and microscopy limitations and not due to any intrinsic SV limitation. Figure 130 shows the response of SPBs trapped on Read 1 and Read 2 SVs to a ±9 mT applied field. A SPB trapped on the Read 1 SV moved toward the channel wall when the positive field was applied and away from the wall when the negative field was applied. Similarly, a SPB trapped on the Read 2 SV moved toward the wall in response to a positive applied field and away from the wall with a negative applied field. The opposite movement of the beads on the Read 1 and 2 SVs in response to the positive or negative field was due to the beads being trapped on opposite blunt ends (opposite polarities) of the ON SVs.

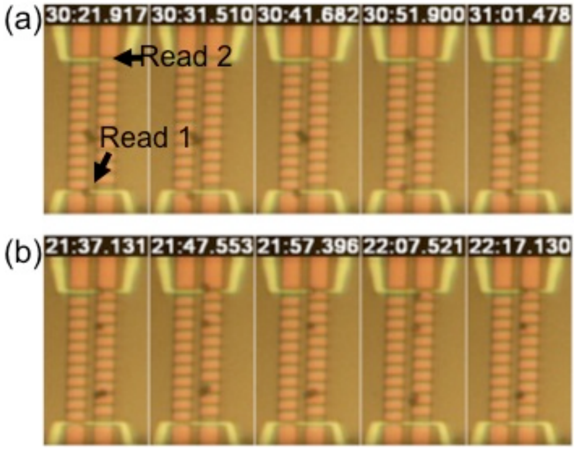

Figure 130: (a) SPB trapped on Read 1 SV, (b) SPB trapped on Read 2 SV.

Results

Figure 131 shows the occupied and vacant Read 1 SV resistance response to various $B_\perp$. No consistent or significant difference in the resistance data was observed between occupied and vacant SVs with an applied perpendicular bias field of ±4 mT, ±6 mT, and ±8mT. If the ON SV was occupied, the resistance of the SV either remained constant or increased when the bias field was positive. The resistance of the occupied ON SV always decreased when the bias field was negative. The small decrease in SV resistance from the low resistance parallel ON state was most likely due to the SV having a multi-domain structure. Similarly, The variation in the parallel resistance states between the different measurements was most likely due to different magnetic domain configurations or thermal heating. Once the bias field was removed, the resistance returned to its nominal ON state resistance.

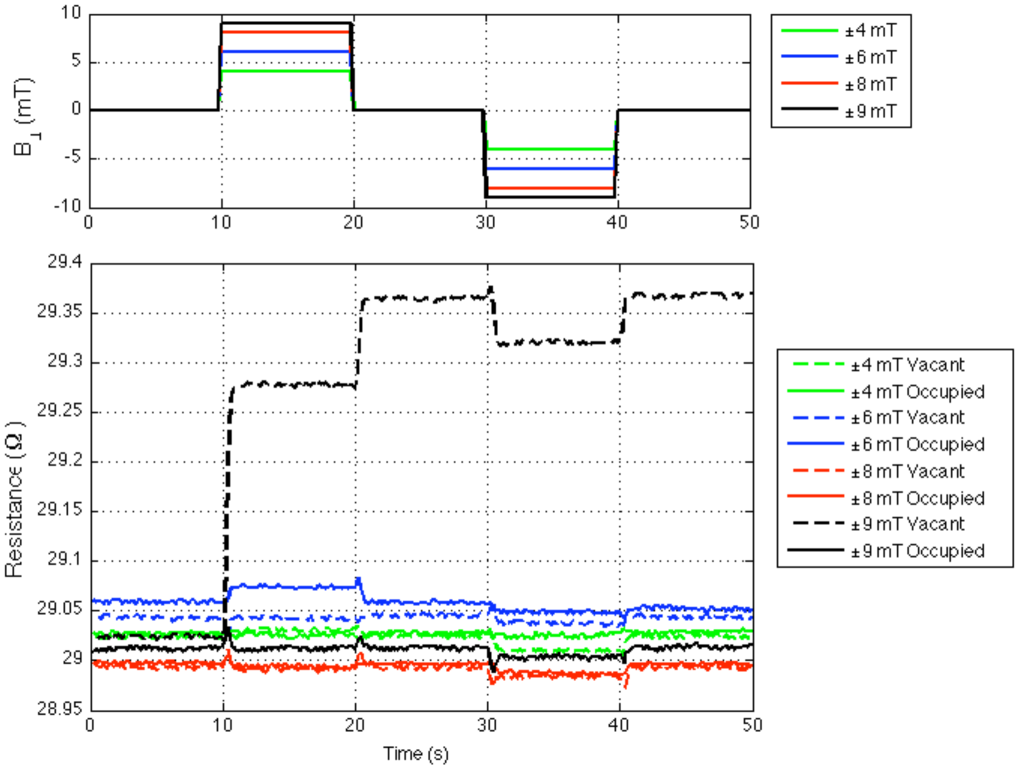

Figure 131: Occupied and vacant SV resistance response to $\mathbf{B}_\perp$.

As shown in both Figure 131 and Figure 132, a difference between the occupied and vacant SV resistance was observed with an applied bias field of +9 mT. When the ON SV was vacant, the bias field toggled the SV OFF. If the SV was occupied by a SPB, the SV did not toggle OFF. In Figure 132, the dotted red line represents the antiparallel OFF resistance and the dotted black line represents the parallel ON resistance. These findings were verified on both the Read 1 and Read 2 SVs, as shown in Figure 132. The actual beads detected in Figure 132's plots are shown in Figure 130.

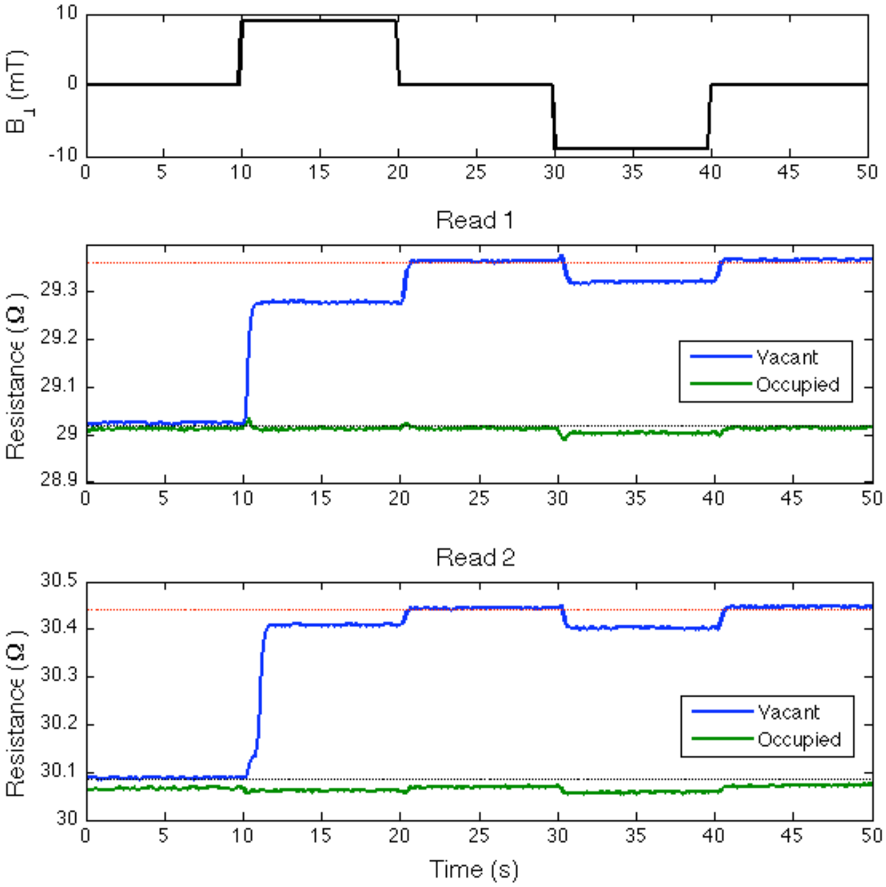

Figure 132: Detection of vacant or occupied (2.8 µm SPB) SV with a ±9 mT external in-plane perpendicular field.

Figure 133 shows the inconsistent resistance response from occupied and vacant Read 1 and 2 SVs biased with a ±8 mT perpendicular field. Some SVs that were occupied (trapped bead visually verified) incorrectly appeared to be vacant when the SV toggled OFF in response to the bias field; toggling the SV OFF led to the unwanted release of the bead. When the SV was vacant, the SV did not toggle OFF in response to the ±8 mT applied field.

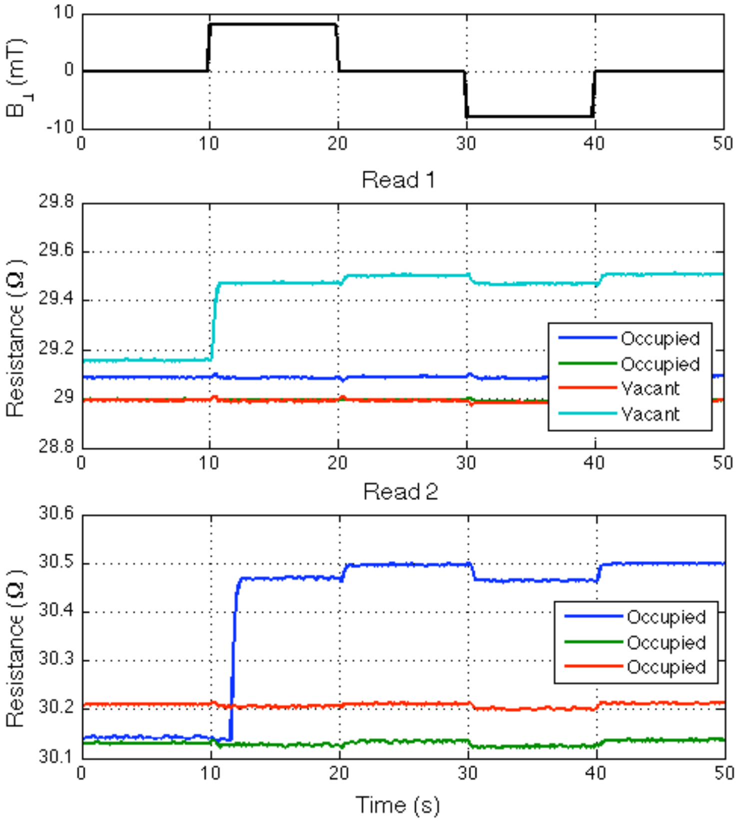

Figure 133: Inconsistent occupied and vacant SV response to ±8 mT in-plane perpendicular field.

Figure 134 shows multiple detections of a 2.8 μm SPBs trapped on the Read 1 SV. Each occupied read represents the detection of a different and single SPB. The figure also demonstrates ON occupied, ON vacant, and OFF (vacant) Read 1 SV resistance variability. The variability may be due to drift in the measurement circuit or reconfiguration of domain walls during and in-between tests. Additionally, the state of adjacent SVs or nearby beads may affect the resistance measurement.

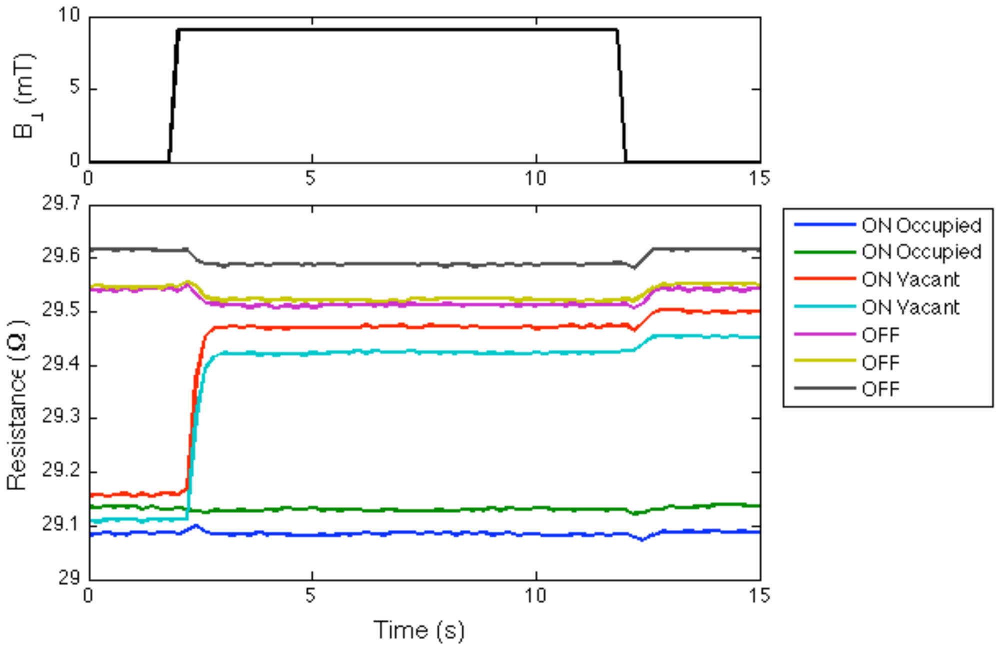

Figure 134: Read-1 MR variability during successful detection of individual 2.8 μm beads.

Discussion

A single 2.8 μm SPB was detected by a fully addressable 1 μm × 8 μm SV biased with an external 9 mT in-plane perpendicular field. The SV remained ON and the 2.8 μm SPB remained trapped after the +9 mT bias field was removed. As depicted in Figure 135, the stray fields from the magnetized SPB counter the applied field. The vacant ON SV will toggle OFF in response to the applied field; however, the SV should be toggled ON to reorient the domain configuration into the parallel state if more bead manipulation and detection is desired. The vacant OFF SV will remain OFF in response to the applied field.

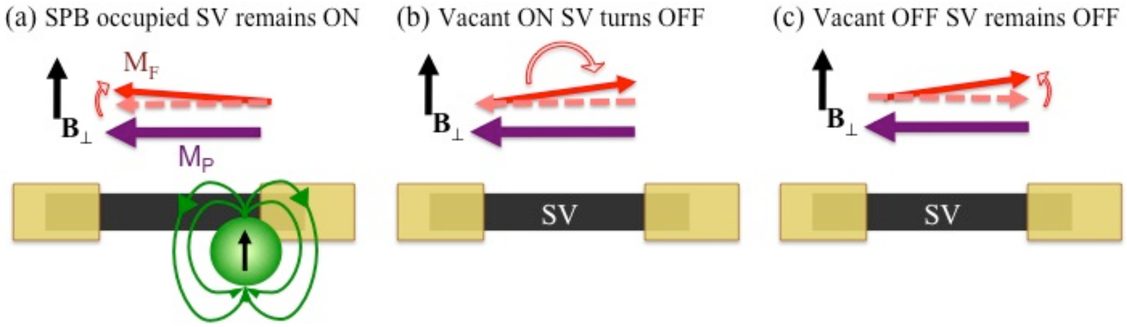

Figure 135: (a) Stray magnetic fields from the polarized SPB counter the +9 mT applied field and the SV remains ON, (b) the vacant ON SV turns OFF in response to the +9 mT applied field, and (c) the vacant OFF SV remains OFF.

The ±4 mT, ±6 mT, and ±8 mT applied bias fields did not aid in the detection of the SPB or SPB vacancy. The energy provided by the ±8 mT bias field appeared to either be on the threshold for toggling the SV OFF when vacant or the stray fields from the polarized SPBs may not be strong enough, or positioned correctly, to counter the bias field.

The need for the large applied field may not be necessary with a more sensitive measurement circuit. Additionally, a current line, rather than the global bias field, may locally magnetize a bead to enable detection.

Summary

A single 2.8 µm SPB was detected on 1 µm × 8 µm SVs addressed locally by read/write lines and biased with a +9 mT perpendicular in-plane field. If the ON SV was vacant, a change in resistance was measured after the bias field was applied. If a trapped bead occupied the ON SV, the resistance did not change in response to applying and removing the field.

CHAPTER 8 - DISCUSSION AND CONCLUSIONS

The following chapter will highlight accomplishments, publications, presentations, grants, and recommendations for future work.

Accomplishments

In this work, individual SPB capture, release, transport, and detection within an integrated microfluidic and MEMS package were accomplished. The capture, release, and transport of individual, and ensembles of, 2.8 µm SPBs functionalized with streptavidin were demonstrated on an addressable linear array of 1 µm × 8 µm bottom-pin SVs actuated with either a global in-plane magnetic field or locally with write-line current pulses. In addition to SPB manipulation, SVs with both a read and write line successfully detected the presence of a trapped SPB when biased with a +9 mT perpendicular field.

To evaluate the potential of SV technology for SPB manipulation and detection, a microfluidic, magnetic, and electronic platform was developed. This platform included a disposable and encapsulated PDMS microfluidic chip, which enabled controlled bead injection and fluid flow. A measurement circuit and software were developed to control the SV actuation and to document the experiment with both video and electrical data. The design and fabrication of the wafer were completed in-house and involved numerous lithography, deposition, and etching steps. Multiple mask revisions and process adjustments were completed to optimize the design and the fabrication steps.

The feasibility of low-power SPB storage, handling, and detection within a novel SV platform was demonstrated. In so doing, we have expanded the technology options for automated magnetic-based bioassay systems.

Publications

Peer-reviewed Journal Publications

W.R. Altman, J. Moreland, S.E. Russek, B.W. Han, and V.M. Bright. "Microfluidic Transport of Superparamagnetic Beads with Spin-Valve Traps." Manuscript submission in progress.

W.R. Altman, J. Moreland, S.E. Russek, and V.M. Bright. "Optimization of Spin-Valve Parameters for Magnetic Bead Trapping and Manipulation." *Journal of Magnetism and Magnetic Materials*, vol. 322, no. 21, pp.3236-3239, 2010.

Papers and Presentations at Professional Meetings

W.R. Altman, J. Moreland, S.E. Russek, B.W. Han, and V.M. Bright. "Microfluidic Transport and Sensing of Functionalized Superparamagnetic Beads using Integrated Spin-Valves." *Abstract accepted for 2011 Micro-TAS*, October 2-6, 2011, Seattle, WA (Poster).

W.R. Krauser[2], J. Moreland, S.E. Russek, V.M. Bright, "Magnetic Switching Characteristics of Spin-Valve designed for Bead Trapping and Manipulation", 11th Joint MMM-Intermag Conference, Jan. 16-22, 2010, Washington, D.C., USA (Talk).

W.R. Krauser, S.E. Russek, V.M. Bright, and J. Moreland, "Switching Characteristics of Magnetic Spin-Valve Traps for Magnetic Bead Manipulation in Microfluidics," 7th Int. Conf. on the Scientific and Clinical Applications of Magnetic Carriers, May 21-24, 2008, Vancouver, Canada, (Poster).

J. Moreland, D. Porpora, W.R. Krauser, and V.M. Bright, "Magnetic Templates for Nanometer Scale Manipulation and Assembly," MMM2007: The 10th Magnetism & Magnetic Materials Conference, Jan. 7-11, 2007, Baltimore, MD (Invited Talk).

Grants

CU/NIST seed grant, "Nanometer-scale Manipulation and Assembly of Biomolecules using a Microfabricated Magnetic Transducer Platform," 8/1/07-7/31/08; V.M. Bright (PI) and J. Moreland (Co-PI).

Recommendations for Future Work

Recommendations for future work include SV optimization, nano-SPB manipulation and detection (scaling potential), measurement setup improvements, and a bioassay demonstration.

---

[2] Prior to marriage in 2010, Wendy R. Altman was legally Wendy R. Krauser.

SV Optimization

The SV layer thicknesses and configuration will impact the SV's ability to manipulate and detect SPBs. Future studies should evaluate top-pin SVs because they exhibit higher GMR due to less surface roughness induced by the IrMn layer. With a higher GMR, the top-pin SVs would be more sensitive to trapped SPBs compared to bottom-pin SVs. Similarly, MTJs and analog SVs (pinned layer is perpendicular to free layer) should be evaluated to determine whether they could transport SPBs. Both MTJs and analog SVs exhibit high GMR, thus they would be able to detect nano-SPBs. However, the pinned and free layers may never be balanced enough, even with the aid of a bias field, to release a SPB.

The thickness of the magnetic layers should be optimized per application. Halving the thickness of the FM layer would reduce the maximum pull force by half. The size, FM content, and velocity of the beads to be manipulated or detected should be considered when choosing the FM thickness. Furthermore, thinner magnetic layers would introduce fewer topographical features into the microfluidic channel, which may be beneficial when manipulating nano-sized beads and molecules.

The exchange bias and stability of the SV may be improved by replacing the AFM IrMn layer with PtMn. AFM PtMn requires a high anneal temperature (> 270°C) to attain the necessary face center tetragonal (FCT) crystal structure; however, Peng found that annealing patterned MTJs at temperatures > 275°C resulted in device degradation [64]. Diffusion between the layers due to the high anneal temperature may be an issue.

Non-specific bonding of the beads to the chip surface, PDMS, and tubing must be reduced to prevent manipulation and detection errors. Alternative passivation layer materials and thicknesses, surface treatments, and SPB solutions should be explored. A stable hydrophilic coating would reduce non-specific binding and extend the shelf life of the chip.

Nano-SPB Manipulation and Detection: Scaling Potential

Ultimately, the SV-microfluidic platform will need to be scaled down to manipulate and detect nano-sized SPBs. Nano-systems can generate the same fields as micro- and macro-systems; however, the gradients and curvatures will be larger leading to larger pull forces. This is because the magnetic field, magnetic field gradient, and magnetic field curvature proportionally scale to the size (x) of the system. For example, the magnetic field curvature is inversely proportional to x^2. The following section will discuss how scaling may affect SV SPB manipulation and detection.

Smaller SPBs can get closer to the biological target, which is important when isolating or detecting biomolecule-biomolecule interactions. A biomolecule immobilized on a micro-SPB will be more spatially hindered than the same biomolecule on a nano-SPB. When proteins bind, they undergo nano-scale mechanical movement and these mechanical conformational changes are critical to their function. Also, a nano-SPB may improve bioassay sensitivities or throughputs due to their larger surface area to volume ratio. Nano-particles composed of a single crystal display less hysteresis, which will reduce particle aggregation as observed with the micro-SPBs. Due to projection and observation effects (see page 66), the diameter of the SPB should be equivalent to the SV width to maximize the pull force. Fluorescent microscopy and biomolecules tagged with fluorescent proteins will be necessary if visual verification is desired.

The width (W) and length (L) of the SV should be reduced for optimal nano-SPB manipulation; a micro-sized SV width cannot be used to isolate a single nano-SPB. A minimum 1:6 (W:L) aspect ratio will increase AMR and decrease the demagnetization field; a high demagnetization field will promote the antiparallel SV configuration, thus the SV may not be bistable. With W << L, the length of the SV does not affect the switching fields or the pull force. Reducing the width while maintaining the same SPB size will greatly decrease the SV's pull force. However, when the width is similar in size to the diameter of the SPB, a high pull force can be achieved. The width is inversely proportional to the free-layer switching fields, thus higher fields will be necessary to toggle the less wide SV ON and OFF. High switching fields produced by current lines may inhibit SV bead manipulation by directly manipulating the nano-SPBs and may introduce unwanted Joule heating.

The thickness of the FM free and pinned layers is proportional to the pull force and the free-layer switching fields. Thinner FM layers will switch at lower fields, thus less current will be required to toggle the SV ON and OFF. The thickness of these layers should be equal to produce a balanced SV. If the SV is not balanced, the flux of the OFF SV may be too large to release the SPB. If the width of the SV is reduced, the thickness of the FM layers can be reduced to maintain a low switching field, but this may reduce the SVs pull force.

The read and write lines may be scaled down, but Joule heating and burnout are two major concerns. The write lines must be thick enough to handle the high current pulses required to toggle the SV OFF and ON. For the read line, the resistance, thus the number of squares (□s), should be minimized to maximize the SV sensitivity (ΔR) and to reduce the signal to noise ratio.

Measurement Setup Improvements

Limitations in the measurement setup hindered characterization of the SV manipulation and detection platform. Future work should include the development of a faster control system with more write and read capabilities, installment of a faster camera with higher magnification or better imaging software, integration of the video and electronic data (e.g., current data), and wafer packaging to eliminate the need for so many probe tips. The addition of an out-of-plane magnetic field may improve bead detection capabilities.

Due to hardware and camera limitations, the maximum SPB transport rate could not be determined. The maximum verified SV switch frequency was 2.5 Hz; however, nano-second switching rates should be achievable. The drag force on the SPB within the fluid medium, not the rate at which the SV can be toggled ON and OFF, should be the limiting speed factor. Furthermore, the frame rate of the video was limited to three frames per second due to the required exposure settings and software. Installation of a camera that allows a region of interest to be designated will speed up the frame rate. With the current imaging system, the large 14 MB video frame included a lot of unnecessary data, which slowed down video capture and increased the post-experiment video processing. The size of each .avi video file was 1.5-10 gigabytes; data storage was also a concern. Furthermore, the magnification of the optical system should be increased to observe beads smaller than 1 μm.

Bioassay Demonstration

In collaboration with biophysicists or molecular biologists, a simple bioassay could be demonstrated. Possible bioassay demonstrations include biomolecule isolation or cell manipulation. Fluorescence microscopy will be needed if biomolecules are manipulated. Large cells like yeast would not need fluorescence. Mammalian cell manipulation and detection studies would require additional thermal controls within the system.

Concluding Remarks

Addressable arrays of low-power SVs have the potential to enable rapid biomolecule manipulation and detection on a 2D surface. Advantages of the multipurpose SV trap and sensor include: (1) SPBs are not permanently immobilized (SPB can be trapped, detected, then released), (2) multiple or individual SPBs can be manipulated, (3) low-power requirement (no power in the "quiescent" state), (4) low-heat production due to short current pulses, (5) customizable to SPB size/content and bioapplications, (6) CMOS compatible, (7) individually addressable on a 2D surface if an MRAM-like architecture is applied, and (8) one device both captures and detects the bead. SV technology can be used for simultaneously controlling and detecting the individual motions of a large number of SPBs, as well as their attached payloads, for automated chemical synthesis applications at molecular and cellular levels.

BIBLIOGRAPHY

[1] G. Li, S. Sun, R. J. Wilson, R. L. White, N. Pourmand, and S. X. Wang, "Spin valve sensors for ultrasensitive detection of superparamagnetic nanoparticles for biological applications," *Sensors and Actuators A: Physical*, vol. 126, no. 1, pp. 98-106, 2006.

[2] V. Joshi, G. Li, S. X. Wang, and S. Sun, "Biochemical Stability of Components for Use in a DNA Detection System," *IEEE Transactions on Magnetics*, vol. 40, no. 4, pp. 3012-3014, 2004.

[3] B. Srinivasan et al., "A Detection System Based on Giant Magnetoresistive Sensors and High-Moment Magnetic Nanoparticles Demonstrates Zeptomole Sensitivity: Potential for Personalized Medicine," *Angewandte Chemie*, vol. 48, no. 15, pp. 2764-2767, 2009.

[4] J. W. Roh, O.-T. Son, Y. T. Lee, K.-il Lee, H.-I. Jung, and W. Lee, "Highly sensitive spin-valve devices for chip-cytometers," *Physica Status Solidi A*, vol. 206, no. 7, pp. 1636 –1640, 2009.

[5] M. M. Miller et al., "A DNA array sensor utilizing magnetic microbeads and magnetoelectronic detection," *Journal of Magnetism and Magnetic Materials*, vol. 225, no. 1-2, pp. 138-144, 2001.

[6] L. Lagae et al., "On-chip manipulation and magnetization assessment of magnetic bead ensembles by integrated spin-valve sensors," *Journal of Applied Physics*, vol. 91, no. 10, pp. 7445-7447, 2002.

[7] L. W. Y. Lui, K. B. Li, S. J. O'Shea, and C. H. Sow, "Optical manipulation of paramagnetic particles with on-chip detection using spin valve sensors," *Applied Physics Letters*, vol. 92, no. 1, p. 3, 2008.

[8] N. T. Thanh, B. P. Rao, N. H. Duc, and C. Kim, "Planar Hall resistance sensor for biochip application," *Physica Status Solidi A*, vol. 204, no. 12, pp. 4053-4057, 2007.

[9] G. M. Whitesides, R. J. Kazlauskas, and L. Josephson, "Magnetic separations in biotechnology," *Trends in Biotechnology*, vol. 1, no. 5, pp. 144-148, 1983.

[10] C. T. Yavuz, A. Prakash, J. T. Mayo, and V. L. Colvin, "Magnetic separations: From steel plants to biotechnology," *Chemical Engineering Science*, vol. 64, pp. 2510-2521, 2009.

[11] H. Andersson and A. van den Berg, "Microfluidic devices for cellomics: a review," *Sensors and Actuators B: Chemical*, vol. 92, no. 3, pp. 315-325, 2003.

[12] V. Y. Rawe, H. U. Boudri, C. A. Sedo, M. Carro, S. Papier, and F. Nodar, “Healthy baby born after reduction of sperm DNA fragmentation using cell sorting before ICSI,” *Reproductive BioMedicine Online*, vol. 20, no. 3, pp. 320-323, 2010.

[13] T. M. Said, S. Grunewald, U. Paasch, M. Rasch, A. Agarwal, and H.-J. Glander, “Effects of magnetic-activated cell sorting on sperm motility and cyrosurvival rates,” *Fertility and Sterility*, vol. 83, no. 5, pp. 1442-1446, 2005.

[14] J. J. Gooding, “Biosensor technology for detecting biological warfare agents: Recent progress and future trends,” *Analytica Chimica Acta*, vol. 559, no. 2, pp. 137-151, 2006.

[15] A. Ashkin, J. M. Dziedzic, J. E. Bjorkholm, and S. Chu, “Observation of a single-beam gradient force optical trap for dielectric particles,” *Optics Letters*, vol. 11, no. 5, pp. 288-290, 1986.

[16] A. Ashkin and J. M. Dziedzic, “Optical trapping and manipulation of viruses and bacteria,” *Science*, vol. 235, no. 4795, pp. 1517-1520, 1987.

[17] T. N. Buican, M. J. Smyth, H. A. Crissman, G. C. Salzman, C. C. Steward, and J. C. Martin, “Automated single-cell manipulation and sorting by light trapping,” *Applied Optics*, vol. 26, no. 24, pp. 5311-5316, 1987.

[18] R. W. Steubing, S. Cheng, W. H. Wright, Y. Numajiri, and M. W. Berns, “Laser induced cell fusion in combination with optical tweezers: The laser cell fusion trap,” *Cytometry*, vol. 12, no. 6, pp. 505-510, 1991.

[19] H. Liang, W. H. Wright, W. He, and M. W. Berns, “Micromanipulation of mitotic chromosomes in PTK2 cells using laser-induced optical forces (‘optical tweezers’),” *Experimental Cell Research*, vol. 197, no. 1, pp. 21-35, 1991.

[20] D. Melville, F. Paul, and S. Roath, “Direct magnetic separation of red cells from whole blood,” *Nature*, vol. 255, p. 706, 1975.

[21] K. Smistrup, B. G. Kjeldsen, J. L. Reimers, M. Dufva, J. Petersen, and M. F. Hansen, “On-chip magnetic bead microarray using hydrodynamic focusing in a passive magnetic separator,” *Lab on a Chip*, vol. 5, pp. 1315-1319, 2005.

[22] R. J. S. Derks, A. Dietzel, R. Wimberger-Friedl, and M. W. J. Prins, “Magnetic bead manipulation in a sub-microliter fluid volume applicable for biosensing,” *Microfluidics and Nanofluidics*, vol. 3, no. 2, pp. 141-149, 2007.

[23] Q. A. Pankhurst, J. Connolly, S. K. Jones, and J. Dobson, “Applications of magnetic nanoparticles in biomedicine,” *Journal of Physics D: Applied Physics*, vol. 36, no. 13, p. R167–R181, 2003.

[24] G. Reiss et al., “Magnetoresistive sensors and magnetic nanoparticles for biotechnology,” *Journal of Materials Research*, vol. 20, no. 12, pp. 3294-3302, 2005.

[25] R. S. Gaster et al., “Matrix-insensitive protein assays push the limits of biosensors in medicine,” *Nature Medicine*, vol. 15, no. 11, pp. 1327-1332, 2009.

[26] C. G. Gunther, *Electro-Magnetic Ore Separation*. New York: Hill Publishing Company, 1909.

[27] S. Trindade and H. Kolm, “Magnetic desulferization of coal,” *IEEE Transactions on Magnetics*, vol. 9, no. 3, pp. 310-313, 1973.

[28] D. Kelland, “High gradient magnetic separation applied to mineral beneficiation,” *IEEE Transactions on Magnetics*, vol. 9, no. 3, pp. 307-310, 1973.

[29] C. de Latour, “Magnetic separation in water pollution control,” *IEEE Transactions on Magnetics*, vol. 9, no. 3, pp. 314-316, 1973.

[30] B. D. Cullity and C. D. Graham, *Introduction to Magnetic Materials*, 2nd ed. Piscataway: IEEE Press, 2009.

[31] E. P. Furlani, *Permanent Magnet and Electromechanical Devices: Materials, Analysis, and Applications*. San Diego: Academic Press, 2001.

[32] W. H. Meiklejohn and C. P. Bean, “New Magnetic Anisotropy,” *Physical Review*, vol. 105, no. 3, pp. 904-913, 1957.

[33] W. H. Meiklejohn and C. P. Bean, “New Magnetic Anisotropy,” *Physical Review*, vol. 105, pp. 904-913, 1957.

[34] D. R. Baselt, G. U. Lee, M. Natesan, S. W. Metzger, P. E. Sheehan, and R. J. Colton, “A biosensor based on magnetoresistance technology,” *Biosensors and Bioelectronics*, vol. 13, no. 7-8, pp. 731-739, 1998.

[35] M. A. M. Gijs, “Magnetic bead handling on-chip: new opportunities for analytical applications,” *Microfluidics and Nanofluidics*, vol. 1, no. 1, pp. 22-40, 2004.

[36] “Magnetic Recording,” *McGraw-Hill Encyclopedia of Science and Technology*. McGraw-Hill Companies, Inc., 2010.

[37] M. N. Baibich et al., “Giant Magnetoresistance of (001)Fe/(001)Cr Magnetic Superlattices,” *Physical Review Letters*, vol. 61, no. 21, pp. 2472-2475, 1988.

[38] P. Grünberg, R. Schreiber, Y. Pang, M. B. Brodsky, and H. Sowers, “Layered Magnetic Structures: Evidence for Antiferromagnetic Coupling of Fe Layers across Cr Interlayers,” *Physical Review Letters*, vol. 57, no. 19, pp. 2442-2445, 1986.

[39] J. C. S. Kools, “Exchanged-Biased Spin-Valves for Magnetic Storage,” *IEEE Transactions on Magnetics*, vol. 32, no. 4, pp. 3165-3184, 1996.

[40] J. Nogues and I. K. Schuller, “Exchange bias,” *Journal of Magnetism and Magnetic Materials*, vol. 192, pp. 203-232, 1999.

[41] C.-M. Park, K.-I. Min, and K. H. Shin, “Effects of surface topology and texture on exchange anisotropy in NiFe/Cu/NiFe/FeMn spin valves,” *Journal of Applied Physics*, vol. 79, no. 8, pp. 6228-6230, 1996.

[42] D.-H. Han, J.-G. Zhu, J. H. Judy, and J. M. Sivertsen, “Effects of surface/interface morphology on giant magnetoresistance and magnetic field sensitivity of NiO-based spin-valves,” *IEEE Transactions on Magnetics*, vol. 33, no. 5, pp. 3550-3552, 1997.

[43] J. Clarke, C. H. Marrows, F. E. Stanley, R. J. T. Bunyan, B. K. Tanner, and B. J. Hickey, “The effect of conformal roughness on spin-valves,” *Journal of Physics D: Applied Physics*, vol. 32, no. 10, pp. 1169-1174, 1999.

[44] J. C. S. Kools, W. Kula, D. Mauri, and T. Lin, “Effect of finite magnetic film thickness on Neel coupling in spin valves,” *Journal of Applied Physics*, vol. 85, no. 8, pp. 4466-4468, 1999.

[45] B. Dieny, V. S. Speriosu, S. S. P. Parkin, B. A. Gurney, D. R. Wilhoit, and D. Mauri, “Giant magnetoresistive in soft ferromagnetic multilayers,” *Physical Review B*, vol. 43, no. 1, pp. 1297-1300, 1991.

[46] G. Binasch, P. Grünberg, F. Saurenbach, and W. Zinn, “Enhanced magnetoresistance in layered magnetic structures with antiferromagnetic interlayer exchange,” *Physical Review B*, vol. 39, no. 7, pp. 4828-4830, 1989.

[47] C. Tsang et al., “Design, Fabrication & Testing of Spin-Valve Read Heads for High Density Recording,” *IEEE Transactions on Magnetics*, vol. 30, no. 6, pp. 3801-3806, 1994.

[48] J. Pelegri, J. B. Ejea, D. Ramirez, and P. P. Freitas, “Spin-valve current sensor for industrial applications,” *Sensors and Actuators A*, vol. 105, no. 2, pp. 132-136, 2003.

[49] G. Li et al., “Detection of single micron-sized magnetic bead and magnetic nanoparticles using spin valve sensors for biological applications,” *Journal of Applied Physics*, vol. 93, no. 10, p. 3, 2003.

[50] T. Ishikawa, F. Kaneko, and K. Johguchi, “Actuation of Magnetic Beads on a Complementary Metal–Oxide–Semiconductor Chip for Biological Applications,” *Japanese Journal of Applied Physics*, vol. 49, p. 04DL08, 2010.

[51] C. S. Lee, H. Lee, and R. M. Westervelt, “Microelectromagnets for the control of magnetic nanoparticles,” *Applied Physics Letters*, vol. 79, no. 20, pp. 3308-3310, 2001.

[52] A. G. Roy and D. E. Laughlin, “Effect of seed layers in improving the crystallographic texture of CoCrPt perpendicular recording media,” *Journal of Applied Physics*, vol. 91, no. 10, pp. 8076-8078, 2002.

[53] P. Wisniowski, T. Stobiecki, J. Kanak, G. Reiss, and H. Bruckl, “Influence of buffer layer texture on magnetic and electrical properties of IrMn spin valve magnetic tunnel junctions,” *Journal of Applied Physics*, vol. 100, no. 1, p. 013906, 2006.

[54] J. Kanak, T. Stobiecki, O. Schebaum, G. Reiss, and H. Bruckl, “Microstructure and exchange coupling parameters of MTJ with CoFeB

bottom electrode," *Physica Status Solidi B*, vol. 243, no. 1, pp. 197-201, 2006.

[55] J. Kanak, T. Stobiecki, V. Drewello, J. Schmalhorst, and G. Reiss, "The influence of the texture on properties of IrMn spin valve magnetic tunnel junctions with MgO barrier and CoFeB electrodes," *Physica Status Solidi A*, vol. 204, no. 12, pp. 3942-3945, 2007.

[56] S. Nakagawa, K. Nishimura, Y. Shimizu, and M. Naoe, "Ultrathin Si buffer layers to improve the exchange bias between Ni-Fe and FeMn layers," *Journal of Applied Physics*, vol. 85, no. 8, pp. 4934-4936, 1999.

[57] K. Nishioka, S. Gangopadhyay, H. Fujiwara, and M. Parker, "Hysteresis and Interaction between the Magnetic Layers in Spin Valves," *IEEE Transactions on Magnetics*, vol. 31, no. 6, pp. 3949-3951, 1995.

[58] H. Gong, D. Litvinov, T. J. Klemmer, D. N. Lambeth, and J. K. Howard, "Seed Layer Effects on the Magnetoresistive Properties of NiFe Films," *IEEE Transactions on Magnetics*, vol. 36, no. 5, pp. 2963-2965, 2000.

[59] G. Anderson, Y. Huai, and L. Miloslawsky, "CoFe/IrMn exchange biased top, bottom, and dual spin valves," *Journal of Applied Physics*, vol. 87, no. 9, pp. 6989-6991, 2000.

[60] J. van Driel, F. R. de Boer, K.-M. H. Lenssen, and R. Coehoorn, "Exchange biasing by Ir19Mn81: Dependence on temperature, microstructure and antiferromagnetic layer thickness," *Journal of Applied Physics*, vol. 88, no. 2, pp. 975-982, 2000.

[61] Y. K. Kim, K. Ha, and L. L. Rea, "Unidirectional Anisotropy in Exchange Coupled NiFe/FeMn System for Thin NiFe Films," *IEEE Transactions on Magnetics*, vol. 31, no. 6, p. 3, 1995.

[62] G. W. Anderson and Y. Huai, "Spin valves exchange biased by IrMn/PtMn laminated antiferromagnets," *Journal of Applied Physics*, vol. 87, no. 9, pp. 4924 - 4926, 2000.

[63] J. R. Childress, M. M. Schwickert, R. E. Fontana, M. K. Ho, P. M. Rice, and B. A. Gurney, "Low-resistance IrMn and PtMn tunnel valves for recording head applications," *Journal of Applied Physics*, vol. 89, no. 11, pp. 7353-7355.

[64] T. Y. Peng et al., "Study of annealing and exchange bias effects in PtMn based magnetic tunnel junction system," *physica status solidi (c)*, vol. 1, no. 12, pp. 3628-3631, 2004.

[65] A. J. Devasahayam, P. J. Sides, and M. H. Kryder, "Magnetic, temperature, and corrosion properties of the NiFe/IrMn exchange couple," *Journal of Applied Physics*, vol. 83, no. 11, pp. 7216-7218, 1998.

[66] F. J. Castano, Y. Hao, C. A. Ross, B. Vogeli, H. I. Smith, and S. Haratani, "Switching field trends in pseudo spin valve nanoelement arrays," *Journal of Applied Physics*, vol. 91, no. 10, pp. 7317-7319, 2002.

[67] A. E. Berkowitz and K. Takano, “Exchange anisotropy - a review,” *Journal of Magnetism and Magnetic Materials*, vol. 200, no. 1-3, pp. 552-570, 1999.

[68] N. T. Thanh, M. G. Chun, N. D. Ha, K. Y. Kim, C. O. Kim, and C. G. Kim, “Thickness dependence of exchange anisotropy in NiFe/IrMn bilayers studied by Planar Hall Effect,” *Journal of Magnetism and Magnetic Materials*, vol. 305, no. 2, pp. 432-435, 2006.

[69] B. J. Qu, T. L. Ren, H. R. Liu, L. T. Liu, and Z. J. Li, “Dependence of GMR on NiFe Layer Thickness in High Sensitive Simple Spin Valve,” *IEEE Sensors Journal*, vol. 5, no. 5, pp. 905-908, 2005.

[70] L. Wang, G. Han, and Y. Wu, “Thickness Dependence of Giant Magnetoresistance in Spin Valves: Influence of Interface and Bulk Scattering,” *IEEE Transactions on Magnetics*, vol. 43, no. 2, pp. 506-509, 2007.

[71] T. C. Anthony, J. A. Brug, and S. Zhang, “Magnetoresistance of symmetric spin valve structures,” *IEEE Transactions on Magnetics*, vol. 30, no. 6, pp. 3819-3821, 1994.

[72] B. Dieny et al., “Magnetotransport properties of magnetically soft spin-valve structures,” *Journal of Applied Physics*, vol. 69, no. 8, pp. 4774-4779, 1991.

[73] T. Q. Hung et al., “Sensitivity Dependence of the Planar Hall Effect Sensor on the Free Layer of the Spin-Valve Structure,” *IEEE Transactions on Magnetics*, vol. 45, no. 6, p. 4, 2009.

[74] T.-N. Fang and J.-G. Zhu, “Effect of Crystalline Microstructure in Patterned Co and Permalloy/Co Film Elements,” *IEEE Transactions on Magnetics*, vol. 36, no. 5, pp. 2623-2625, 2000.

[75] W. F. Egelhoff Jr et al., “Magnetoresistance values exceeding 21% in symmetric spin valves,” *Journal of Applied Physics*, vol. 78, no. 1, pp. 273-277, 1995.

[76] D. Wang, J. Anderson, and J. M. Daughton, “Thermally stable, low saturation field, low hysteresis, high GMR CoFe/Cu multilayers,” *IEEE Transactions on Magnetics*, vol. 33, no. 5, pp. 3520-3522, 1997.

[77] C. S. Yoon, J. H. Lee, H. D. Jeong, C. K. Kim, J. H. Yuh, and R. Haasch, “Diffusion study of the exchange biased NiFe/MnIr/CoFe electrode in magnetic tunnel junctions,” *Applied Physics Letters*, vol. 80, no. 21, pp. 3976-3978, 2002.

[78] S. S. P. Parkin, “Dramatic enhancement of interlayer exchange coupling and giant magnetoresistance in Ni81Fe19/Cu multilayers by addition of thin Co interface layers,” *Applied Physics Letters*, vol. 61, no. 11, pp. 1358-1360, 1992.

[79] P. Lubitz et al., “Structures with improved magnetic characteristics for giant magnetoresistance applications,” *Journal of Applied Physics*, vol. 85, no. 8, pp. 5027-5030, 1999.

[80] M. Hawraneck et al., “Diffusion based degradation mechanisms in giant magnetoresistive spin valves,” *Applied Physics Letters*, vol. 93, no. 1, p. 012504, 2008.
[81] K. Hayashi et al., “Magnetic and other properties and sputtering behavior of Co-base amorphous alloy films,” *Journal of Applied Physics*, vol. 61, no. 8, p. 2983, 1987.
[82] X. H. Li and Z. Yang, “Effects of sputtering conditions on the structure and magnetic properties of Ni-Fe films,” *Materials Science and Engineering B*, vol. 106, no. 1, pp. 41-45, 2004.
[83] K.-Y. Chan and B.-S. Teo, “Sputtering power and deposition pressure effects on the electrical and structural properties of copper thin films,” *Journal of Materials Science*, vol. 40, no. 22, pp. 5971-5981, 2005.
[84] K. Y. Chan and B. S. Teo, “Effect of Ar pressure on grain size of magnetron sputter-deposited Cu thin films,” *IET Science Measurement Technology*, vol. 1, no. 2, pp. 87-90, 2007.
[85] M. Mao, C. Cerjan, B. Law, F. Grabner, and S. Vaidya, “Influence of Base Pressure on FeMn Exchange Biased Spin-valve Films,” presented at the 44th Annual Conference on Magnetism and Magnetic Materials, San Jose, CA, 1999, p. AS-08.
[86] R. W. Cross, Y. K. Kim, J. O. Oti, and S. E. Russek, “Magnetostatic effects in giant magnetoresistive spin-valve devices,” *Applied Physics Letters*, vol. 69, no. 25, pp. 3935-3937, 1996.
[87] J. O. Oti and S. E. Russek, “Micromagnetic Simulations of Magnetoresistive Behavior of Sub-Micrometer Spin-valve MRAM Devices,” *IEEE Transactions on Magnetics*, vol. 33, no. 5, pp. 3298-3300, 1997.
[88] S. E. Russek, J. O. Oti, and Y. K. Kim, “Switching characteristics of spin valve devices designed for MRAM applications,” *Journal of Magnetism and Magnetic Materials*, vol. 198, no. 1-3, pp. 6-8, 1999.
[89] S. H. Lim, S. H. Han, K. H. Shin, and H. J. Kim, “Size effects on characteristic magnetic fields of a spin-valve multilayer by computer simulation,” *Journal of Magnetism and Magnetic Materials*, vol. 223, no. 2, pp. 192-198, 2001.
[90] S. Mao, J. Giusti, N. Amin, Van ekJohannes, and E. Murdock, “Giant magnetoresistance properties of patterned IrMn exchange biased spin valves,” *Journal of Applied Physics*, vol. 85, no. 8, pp. 6112-6114, 1999.
[91] S. E. Russek, R. W. Cross, S. C. Sanders, and J. O. Oti, “Size Effects in Submicron NiFe/Ag GMR Devices,” *IEEE Transactions on Magnetics*, vol. 31, no. 6, pp. 3939-3942, 1995.
[92] J. A. Johnson et al., “Magneto-optic Kerr effect investigation of cobalt and permalloy nanoscale dot arrays: Shape effects on magnetization reversal,” *Applied Physics Letters*, vol. 77, no. 26, pp. 4410-4412, 2000.

[93] T. Zhu et al., "Switching characteristics of submicron dimension Permalloy sandwich films," *IEEE Transactions on Magnetics*, vol. 33, pp. 3601-3603, 1997.
[94] V. Kuncser et al., "Exchange bias and spin valve systems with Fe–Mn antiferromagnetic pinning layers, obtained by the thermo-ionic vacuum arc method," *Journal of Magnetism and Magnetic Materials*, vol. 320, no. 14, p. 4, 2008.
[95] J. Gadbois, J.-G. Zhu, W. Vavra, and A. Hurst, "The Effect of End and Edge Shape on the Performance of Pseudo-Spin Valve Memories," *IEEE Transactions on Magnetics*, vol. 34, no. 4, pp. 1066-1068, 1998.
[96] K. J. Kirk, J. N. Chapman, and C. D. W. Wilkinson, "Switching fields and magnetostatic interactions of thin film magnetic nanoelements," *Applied Physics Letters*, vol. 71, no. 4, p. 3, 1997.
[97] J. M. Slaughter et al., "Fundamentals of MRAM Technology," *Journal of Superconductivity*, vol. 15, no. 1, pp. 19-25, 2002.
[98] X. Tang, S. Bansaruntip, N. Nakayama, E. Yenilmez, Y.-lan Chang, and Q. Wang, "Carbon Nanotube DNA Sensor and Sensing Mechanism," *Nano Letters*, vol. 6, no. 8, pp. 1632-1636, 2006.
[99] M. Zheng et al., "Structure-Based Carbon Nanotube Sorting by Sequence-Dependent DNA Assembly," *Science*, vol. 302, no. 5650, pp. 1545 -1548, 2003.
[100] N. Pamme, "Magnetism and microfluidics," *Lab on a Chip*, vol. 6, pp. 24-38, 2006.
[101] M. Brzeska et al., "Detection and manipulation of biomolecules by magnetic carriers," *Journal of Biotechnology*, vol. 112, no. 1-2, pp. 25-33, 2004.
[102] J. Wang, R. Polsky, A. Merkoci, and K. L. Turner, "'Electroactive Beads' for Ultrasensitive DNA Detection," *Langmuir*, vol. 19, pp. 989-991, 2003.
[103] B. Fabry, G. N. Maksym, J. P. Butler, M. Glogauer, D. Navajas, and J. J. Fredberg, "Scaling the Microrheology of Living Cells," *Physical Review Letters*, vol. 87, no. 14, p. 148102, 2001.
[104] C. Zhang, K. Khoshmanesh, A. Mitchell, and K. Kalantar-zadeh, "Dielectrophoresis for manipulation of micro/nano particles in microfluidic systems," *Analytical and Bioanalytical Chemistry*, vol. 396, no. 1, pp. 401-420, 2010.
[105] M. Megens and M. Prins, "Magnetic biochips: a new option for sensitive diagnostics," *Journal of Magnetism and Magnetic Materials*, vol. 293, no. 1, pp. 702-708, 2005.
[106] E. Mirowski, J. Moreland, S. E. Russek, and M. J. Donahue, "Integrated microfluidic isolation platform for magnetic particle manipulation in biological systems," *Applied Physics Letters*, vol. 84, no. 10, pp. 1786-1788, 2004.

[107] K. Gunnarsson et al., “Programmable Motion and Separation of Single Particles on Patterned Magnetic Surfaces,” *Advanced Materials*, vol. 17, no. 14, p. 5, 2005.

[108] B. B. Yellen and G. Friedman, “Programmable Assembly of Heterogeneous Colloidal Particle Arrays,” *Advanced Materials*, vol. 16, no. 2, pp. 111-115, 2004.

[109] R. S. Conroy, G. Zabow, J. Moreland, and A. P. Korestsky, “Controlled transport of magnetic particles using soft magnetic patterns,” *Applied Physics Letters*, vol. 93, no. 20, p. 203901, 2008.

[110] M. Donolato et al., “On-Chip Manipulation of Protein-Coated Magnetic Beads via Domain-Wall Conduits,” *Advanced Materials*, vol. 22, no. 24, pp. 2706-2710, 2010.

[111] D. W. Inglis, R. Riehn, R. H. Austin, and J. C. Sturm, “Continuous microfluidic immunomagnetic cell separation,” *Applied Physics Letters*, vol. 85, p. 5093, 2004.

[112] K. Smistrup, T. Lund-Olesen, M. F. Hansen, and P. T. Tang, “Microfluidic magnetic separator using an array of soft magnetic elements,” *Journal of Applied Physics*, vol. 99, p. 08P102, 2006.

[113] R. Rong, J.-W. Choi, and C. H. Ahn, “An on-chip magnetic bead separator for biocell sorting,” *Journal of Micromechanics and Microengineering*, vol. 16, no. 12, pp. 2783-2790, 2006.

[114] E. Mirowski, J. Moreland, S. Russek, M. Donahue, and K. Hsieh, “Manipulation of magnetic particles by patterned arrays of magnetic spin-valve traps,” *Journal of Magnetism and Magnetic Materials*, vol. 311, no. 1, pp. 401-404, 2007.

[115] T. Henighan et al., “Manipulation of Magnetically Labeled and Unlabeled Cells with Mobile Magnetic Traps,” *Biophysical Journal*, vol. 98, no. 3, pp. 412-417, 2010.

[116] M. Tondra et al., “Design of integrated microfluidic device for sorting magnetic beads in biological assays,” *Magnetics, IEEE Transactions on*, vol. 37, no. 4, pp. 2621-2623, 2001.

[117] D. L. Graham, H. Ferreira, and J. Bernardo, “Single magnetic microsphere placement and detection on-chip using current line designs with integrated spin valve sensors: Biotechnological applications,” *Journal of Applied Physics*, vol. 91, no. 10, p. 3, 2002.

[118] Z. Jiang, J. Llandro, T. Mitrelias, and J. A. C. Bland, “An integrated microfluidic cell for detection, manipulation, and sorting of single micron-sized magnetic beads,” *Journal of Applied Physics*, vol. 99, no. 8, p. 08S105, 2006.

[119] N. Pekas, M. Granger, M. Tondra, A. Popple, and M. D. Porter, “Magnetic particle diverter in an integrated microfluidic format,” *Journal of Magnetism and Magnetic Materials*, vol. 293, no. 1, pp. 584-588, 2005.

[120] T. Deng, G. M. Whitesides, M. Radhakrishnan, G. Zabow, and M. Prentiss, "Manipulation of magnetic microbeads in suspension using micromagnetic systems fabricated with soft lithography," *Applied Physics Letters*, vol. 78, no. 12, pp. 1775-1777, 2001.

[121] R. Wirix-Speetjens and J. de Boeck, "On-chip magnetic particle transport by alternating magnetic field gradients," *IEEE Transactions on Magnetics*, vol. 40, no. 4, pp. 1944-1946, 2004.

[122] H. Lee, A. M. Purdon, and R. M. Westervelt, "Manipulation of biological cells using a microelectromagnet matrix," *Applied Physics Letters*, vol. 85, no. 6, pp. 1063-1065, 2004.

[123] H. Lee, A. M. Purdon, V. Chu, and R. M. Westervelt, "Controlled Assembly of Magnetic Nanoparticles from Magnetotactic Bacteria Using Microelectromagnets Arrays," *Nano Letters*, vol. 4, no. 5, pp. 995-998, 2004.

[124] H. Lee, Y. Liu, D. Ham, and R. M. Westervelt, "Integrated cell manipulation system - CMOS/microfluidic hybrid," *Lab on a Chip*, vol. 7, no. 3, pp. 331-337, 2007.

[125] J.-W. Choi, C. H. Ahn, S. Bhansali, and H. T. Henderson, "A new magnetic bead-based, filterless bio-separator with planar electromagnet surfaces for integrated bio-detection systems," *Sensors and Actuators B: Chemical*, vol. 68, no. 1-3, pp. 34-39, 2000.

[126] J.-W. Choi, T. M. Liakopoulos, and C. H. Ahn, "An on-chip magnetic bead separator using spiral electromagnets with semi-encapsulated permalloy," *Biosensors and Bioelectronics*, vol. 16, no. 6, pp. 409-416, 2001.

[127] J.-W. Choi et al., "An integrated microfluidic biochemical detection system for protein analysis with magnetic bead-based sampling capabilities," *Lab on a Chip*, vol. 2, no. 1, pp. 27-30, 2002.

[128] A. Rida, V. Fernandez, and M. A. M. Gijs, "Planar coil-based microsystem for the long-range transport of magnetic beads," in *TRANSDUCERS, Solid-State Sensors, Actuators and Microsystems, 12th International Conference on*, Boston, 2003, vol. 1, pp. 292-295.

[129] Q. Ramadan, V. Samper, D. P. Poenar, and C. Yu, "On-chip micro-electromagnets for magnetic-based bio-molecules separation," *Journal of Magnetism and Magnetic Materials*, vol. 281, no. 2-3, pp. 150-172, 2004.

[130] Q. Ramadan, C. Yu, V. Samper, and D. P. Poenar, "Microcoils for transport of magnetic beads," *Applied Physics Letters*, vol. 88, no. 3, p. 032501, 2006.

[131] Q. Ramadan, V. Samper, D. P. Poenar, and C. Yu, "Magnetic-based microfluidic platform for biomolecular separation," *Biomedical Microdevices*, vol. 8, no. 2, pp. 151-158, 2006.

[132] Q. Ramadan, V. Samper, D. P. Poenar, and C. Yu, "An integrated microfluidic platform for magnetic microbeads separation and confinement," *Biosensors & Bioelectronics*, vol. 21, no. 9, pp. 1693-1702, 2006.

[133] C. H. Ahn, M. G. Allen, W. Trimmer, Y.-N. Jun, and S. Erramilli, "A Fully Integrated Micromachined Magnetic Particle Separator," *Journal of Microelectromechanical Systems*, vol. 5, no. 3, pp. 151-158, 1996.

[134] C. Liu, L. Lagae, and G. Borghs, "Manipulation of magnetic particles on chip by magnetophoretic actuation and dielectrophoretic levitation," *Applied Physics Letters*, vol. 90, no. 18, p. 184109, 2007.

[135] J. N. Krishnan, C. Kim, H. J. Park, J. Y. Kang, T. S. Kim, and S. K. Kim, "Rapid microfluidic separation of magnetic beads through dielectrophoresis and magnetophoresis," *Electrophoresis*, vol. 30, no. 9, pp. 1457-1463, 2009.

[136] L. E. Helseth, T. M. Fischer, and T. H. Johansen, "Domain Wall Tip for Manipulation of Magnetic Particles," *Physical Review Letters*, vol. 91, no. 20, p. 208302, 2003.

[137] M. T. Bryan, J. Dean, T. Schrefl, F. E. Thompson, J. Haycock, and D. A. Allwood, "The effect of trapping superparamagnetic beads on domain wall motion," *Applied Physics Letters*, vol. 96, no. 19, p. 192503, 2010.

[138] R. L. Edelstein et al., "The BARC biosensor applied to the detection of biological warfare agents," *Biosensors & Bioelectronics*, vol. 14, no. 10-11, pp. 805-813, 2000.

[139] D. L. Graham, H. A. Ferreira, and P. P. Freitas, "Magnetoresistive-based biosensors and biochips," *Trends in Biotechnology*, vol. 22, no. 9, pp. 455-462, 2004.

[140] W. Shen, X. Liu, D. Mazumdar, and G. Xiao, "In situ detection of single micron-sized magnetic beads using magnetic tunnel junction sensors," *Applied Physics Letters*, vol. 86, no. 25, p. 253901, 2005.

[141] S. G. Grancharov et al., "Bio-functionalization of Monodisperse Magnetic Nanoparticles and Their Use as Biomolecular Labels in a Magnetic Tunnel Junction Based Sensor," *The Journal of Physical Chemistry B*, vol. 109, no. 26, pp. 13030-13035, 2005.

[142] P.-A. Besse, G. Boero, M. Demierre, V. Pott, and R. Popovic, "Detection of a single magnetic microbead using a miniaturized silicon Hall sensor," *Applied Physics Letters*, vol. 80, no. 22, p. 4199, 2002.

[143] F. W. Osterberg, B. T. Dalslet, C. D. Damsgaard, S. C. Freitas, P. P. Freitas, and M. F. Hansen, "Bead Capture on Magnetic Sensors in a Microfluidic System," *Sensors Journal, IEEE*, vol. 9, no. 6, pp. 682-688, 2009.

[144] L. Ejsing, M. F. Hansen, A. K. Menon, H. A. Ferreira, D. L. Graham, and P. P. Freitas, "Planar Hall effect sensor for magnetic micro- and

nanobead detection," *Applied Physics Letters*, vol. 84, no. 23, pp. 4729-4781, 2004.

[145] T. Q. Hung, S. Oh, J.-R. Jeong, and C. Kim, "Spin-valve planar Hall sensor for single bead detection," *Sensors and Actuators A*, vol. 157, no. 1, pp. 42-46, 2010.

[146] M. M. Miller, G. A. Prinz, S.-F. Cheng, and S. Bounnak, "Detection of a micron-sized magnetic sphere using a ring-shaped anisotropic magnetoresistance-based sensor: A model for a magnetoresistance-based biosensor," *Applied Physics Letters*, vol. 81, no. 12, pp. 2211-2213, 2002.

[147] J. C. Rife, M. M. Miller, P. E. Sheehan, C. R. Tamanaha, M. Tondra, and L. J. Whitman, "Design and performance of GMR sensors for the detection of magnetic microbeads in biosensors," *Sensors and Actuators A: Physical*, vol. 107, no. 3, pp. 209-218, 2003.

[148] G. Li, S. X. Wang, and S. Sun, "Model and experiment of detecting multiple magnetic nanoparticles as biomolecular labels by spin valve sensors," *Magnetics, IEEE Transactions on*, vol. 40, no. 4, pp. 3000-3002, 2004.

[149] M. Koets, T. van der Wijk, J. T. W. M. van Eemeren, A. van Amerongen, and M. W. J. Prins, "Rapid DNA multi-analyte immunoassay on a magneto-resistance biosensor," *Biosensors and Bioelectronics*, vol. 24, no. 7, pp. 1893-1898, 2009.

[150] B. M. de Boer, J. A. H. M. Kahlman, T. P. G. H. Jansen, H. Duric, and J. Veen, "An integrated and sensitive detection platform for magneto-resistive biosensors," *Biosensors and Bioelectronics*, vol. 22, no. 9-10, pp. 2366-2370, 2007.

[151] L. Xu et al., "Giant magnetoresistive biochip for DNA detection and HPV genotyping," *Biosensors and Bioelectronics*, vol. 24, no. 1, pp. 99-103, 2008.

[152] L. Lagae et al., "Magnetic biosensors for genetic screening of cystic fibrosis," *IEE Proceedings - Circuits, Devices and Systems*, vol. 152, no. 4, pp. 393-400, 2005.

[153] H. A. Ferreira, D. L. Graham, P. P. Freitas, and J. M. S. Cabral, "Biodetection using magnetically labeled biomolecules and arrays of spin valve sensors," *Journal of Applied Physics*, vol. 93, no. 10, p. 15444449, 2003.

[154] D. L. Graham, H. A. Ferreira, N. Feliciano, P. P. Freitas, L. A. Clarke, and M. D. Amaral, "Magnetic field-assisted DNA hybridization and simultaneous detection using micron-sized spin-valve sensors and magnetic nanoparticles," *Sensors and Actuators B: Chemical*, vol. 107, no. 2, pp. 936-944, 2005.

[155] H. A. Ferreira, N. Feliciano, D. L. Graham, and P. P. Freitas, "Effect of spin-valve sensor magnetostatic fields on nanobead detection for biochip

applications," *Journal of Applied Physics*, vol. 97, no. 10, p. 10Q904, 2005.

[156] R. De Palma et al., "Magnetic Bead Sensing Platform for the Detection of Proteins," *Analytical Chemistry*, vol. 79, no. 22, pp. 8669-8677, 2007.

[157] H. J. Kim, S. H. Jang, K. H. Oh, T. S. Kim, and K. Y. Kim, "The fabrication of high sensitive spin-valve sensor for magnetic bead detection," *Physica Status Solidi A*, vol. 201, no. 8, pp. 1961-1964, 2004.

[158] C. P. Gooneratne, I. Giouroudi, C. Liang, and J. Kosel, "A giant magnetoresistance ring-sensor based microsystem for magnetic bead manipulation and detection," *Journal of Applied Physics*, vol. 109, no. 7, p. 07E517, 2011.

[159] K. Jo, M. L. Heien, L. B. Thompson, M. Zhong, R. G. Nuzzo, and J. V. Sweedler, "Mass spectrometric imaging of peptide release from neuronal cells within microfluidic devices," *Lab on a Chip*, vol. 7, pp. 1454-1460, 2007.

[160] G. Whitesides, "The origins and the future of microfluidics," *Nature*, vol. 442, no. 7101, pp. 368-373, 2006.

[161] T. M. Squires and S. R. Quake, "Microfluidics: Fluid physics at the nanoliter scale," *Review of Modern Physics*, vol. 77, no. 3, pp. 977-1026, 2005.

[162] H. Lorenz, M. Despont, N. Fahrni, N. LaBianca, P. Renaud, and P. Vettiger, "SU-8: a low-cost negative resist for MEMS," *Journal of Micromechanics and Microengineering*, vol. 7, no. 3, pp. 121-124, 1997.

[163] L. Johansson et al., "A magnetic microchip for controlled transport of attomole levels of proteins," *Lab on a Chip*, vol. 10, pp. 654-661, 2010.

[164] T. Murakami, S. I. Kuroda, and Z. Osawa, "Dynamics of Polymeric Solid Surfaces Treated with Oxygen Plasma: Effect of Aging Media after Plasma Treatment," *Journal of Colloid and Interface Science*, vol. 202, no. 1, pp. 37-44, 1998.

[165] S. H. Tan, N.-T. Nguyen, Y. C. Chua, and Tae Goo Kang, "Oxygen plasma treatment for reducing hydrophobicity of a sealed polydimethylsiloxane microchannel," *Biomicrofluidics*, vol. 4, no. 3, p. 32204, 2010.

[166] M. A. M. Gijs, F. Lacharme, and U. Lehmann, "Microfluidic Applications of Magnetic Particles for Biological Analysis and Catalysis," *Chemical Reviews*, vol. 110, no. 3, pp. 1518-1563, 2010.

[167] T. Strick, J.-F. Allemand, V. Croquette, and D. Bensimon, "The Manipulation of Single Biomolecules," *Physics Today*, vol. 54, no. 10, pp. 46-51, 2001.

[168] P. Debye and E. Huckel, "The theory of electrolytes: Lowering of freezing point and related phenomena," *Physikalische Zeitschrift*, vol. 24, pp. 185-206, 1923.

[169] S. Levine and G. P. Dube, "Interaction between two hydrophobic colloidal particles using the approximate Debye-Huckel theory: General properties," *Transactions of the Faraday Society*, vol. 35, pp. 1125-1141, 1940.
[170] B. Derjaguin and L. Landau, "Theory of the stability of strongly charged lyophobic sols and the adhesion of strongly charged particles in solutions of electrolytes," *Acta Physico Chemica URSS*, vol. 14, p. 633, 1948.
[171] E. J. W. Verwey and J. T. G. Overbeek, *Theory of the stability of lyophobic collods*. Amsterdam: Elsevier, 1948.
[172] C. Liu, T. Stakenborg, S. Peeters, and L. Lagae, "Cell manipulation with magnetic particles toward microfluidic cytometry," *Journal of Applied Physics*, vol. 105, no. 10, p. 102014, 2009.
[173] M. Drndic, K. S. Johnson, J. H. Thywissen, M. Prentiss, and R. M. Westervelt, "Micro-electromagnets for atom manipulation," *Applied Physics Letters*, vol. 72, no. 22, pp. 2906-2908, 1998.
[174] B. Drogoff, L. Clime, and T. Veres, "The influence of magnetic carrier size on the performance of microfluidic integrated micro-electromagnetic traps," *Microfluidics and Nanofluidics*, vol. 5, no. 3, pp. 373-381, 2008.
[175] D. Spetzler et al., "Recent developments of bio-molecular motors as on-chip devices using single molecule techniques," *Lab on a Chip*, vol. 7, pp. 1633-1643, 2007.
[176] T. L. Gilbert, "A Lagrangian formulation of the gyromagnetic equation of the magnetic field," *Physical Review*, vol. 100, p. 1243, 1955.
[177] M. Gmitra, D. Horvath, M. Wawrzyniak, and J. Barnas, "Current-induced spin dynamics in spin-valve structures," *Physica Status Solidi B*, vol. 243, no. 1, pp. 219-222, 2006.
[178] S. Kaka and S. E. Russek, "Precessional switching of submicrometer spin valves," *Applied Physics Letters*, vol. 80, no. 16, pp. 2958-2960, 2002.
[179] M. E. Walsch, Y. Hao, C. A. Ross, and H. I. Smith, "Optimization of a lithographic and ion beam etching process for nanostructuring magnetoresistive thin film stacks," *Journal of Vacuum Science and Technology B*, vol. 18, no. 6, pp. 3539-3543, 2000.
[180] B. Dieny et al., "Spin-valve effect in soft ferromagnetic sandwiches," *Journal of Magnetism and Magnetic Materials*, vol. 93, pp. 101-104, 1991.
[181] S. Hu, X. Ren, M. Bachman, C. E. Sims, G. P. Li, and N. Allbritton, "Surface Modification of Poly(dimethylsiloxane) Microfluidic Devices by Ultraviolet Polymer Grafting," *Analytical Chemistry*, vol. 74, no. 16, pp. 4117-4123, 2002.

Appendix A: Acronyms

AC	Alternating current
AFM	Antiferromagnetic
AFM	Atomic force microscopy
AM	Alignment mark
AMR	Anisotropic MR
ATP	Adenosine triphosphate
BARC	Bead array counter
BCB	Bisbenzocyclobutene
BSA	Bovine serum albumin
CMOS	Complementary metal–oxide–semiconductor
CVD	Chemical vapor deposition
CZ	Czochralski
DAC	Digital-to-analog converter
DC	Direct current
DI	De-ionized
DNA	Deoxyribonucleic acid
FCC	Face-centered cubic
FM	Ferromagnetic
GMI	Giant magntoimpedance
GMR	Giant magnetoresistance
HF	Hydrofluoric Acid
HPV	Human papillomavirus
LLG	Landau-Lifshitz-Gilbert
LOC	Lab-on-a-chip
LOR	Lift-off resist
LPCVD	Low pressure CVD
MEMS	Microelectromechanical systems
MFM	Magnetic force microscopy
MFP	Micro-fluidic port
MOKE	Magneto-optical Kerr effect
MR	Magnetoresistance
MRAM	Magnetic random access memory
MTJ	Magnetic tunnel junction
N	Newton
NIST	National Institute of Standards and Technology
NOL	Nano-oxide layer
ODE	Ordinary differential equation
OOMMF	Object Oriented Micro-Magnetic Framework
PBS	Phosphate-buffered saline
PDMS	Polydimethylsiloxane
PECVD	Plasma enhanced CVD
PEG	Polyethylene Glycol
POC	Point-of-care
PR	Photoresist
Py	Permalloy
RF	Radio frequency
RIE	Reactive ion etch
RKKY	Ruderman-Kittel-Kasuya-Yosida
rpm	Revolutions per minute

SEM	Scanning electron microscopy
SPB	Superparamagnetic bead
SV	Spin-valve
T	Tesla
μ-TAS	Micro-total analysis system

Appendix B: MatLab Code

B-Field Calculation (Bcalculate.m)

```
function [B_x, B_y, B_z] = Bcalculate(X,Y,Z,state,x1,x2,z1,z2,HPy,HCo,space)
 % Subfunction to calulate B-Field

yPyp1 = 0;          % Thickness along the y-axis               %
yPyp2 = HPy;
yCop1 = yPyp2;
yCop2 = yCop1 + HCo;
yCof1 = yCop2 + space;
yCof2 = yCof1 + HCo;
yPyf1 = yCof2;
yPyf2 = yCof2 + HPy;

mu_0 = pi*4e-7;          % Permitivity, SI
M_sPy= 8.0e5;            % Magnetization of Permalloy A/m
M_sCo = 1400e3;           % Magnetization of CoFe

F11 =((Y-yPyp1)+((X-x1).^2+(Y-yPyp1).^2+(Z-z1).^2).^.5)./((Y-yPyp2)+((X-
x1).^2+(Y-yPyp2).^2+(Z-z1).^2).^(1/2));
F12= ((Y-yPyp1)+((X-x2).^2+(Y-yPyp1).^2+(Z-z1).^2).^.5)./((Y-yPyp2)+((X-
x2).^2+(Y-yPyp2).^2+(Z-z1).^2).^(1/2));
F22= ((Y-yPyp1)+((X-x2).^2+(Y-yPyp1).^2+(Z-z2).^2).^.5)./((Y-yPyp2)+((X-
x2).^2+(Y-yPyp2).^2+(Z-z2).^2).^(1/2));
F21= ((Y-yPyp1)+((X-x1).^2+(Y-yPyp1).^2+(Z-z2).^2).^.5)./((Y-yPyp2)+((X-
x1).^2+(Y-yPyp2).^2+(Z-z2).^2).^(1/2));

H11 =((X-x1)+((X-x1).^2+(Y-yPyp1).^2+(Z-z1).^2).^.5)./((X-x2)+((X-x2).^2+(Y-
yPyp1).^2+(Z-z1).^2).^.5);
H12= ((X-x1)+((X-x1).^2+(Y-yPyp2).^2+(Z-z1).^2).^.5)./((X-x2)+((X-x2).^2+(Y-
yPyp2).^2+(Z-z1).^2).^.5);
H22= ((X-x1)+((X-x1).^2+(Y-yPyp2).^2+(Z-z2).^2).^.5)./((X-x2)+((X-x2).^2+(Y-
yPyp2).^2+(Z-z2).^2).^.5);
H21= ((X-x1)+((X-x1).^2+(Y-yPyp1).^2+(Z-z2).^2).^.5)./((X-x2)+((X-x2).^2+(Y-
yPyp1).^2+(Z-z2).^2).^.5);
```

```
G111=((X-x1).^2+(Y-yPyp1).^2+(Z-z1).^2).^(-.5);
G112=((X-x1).^2+(Y-yPyp1).^2+(Z-z2).^2).^(-.5);
G122=((X-x1).^2+(Y-yPyp2).^2+(Z-z2).^2).^(-.5);
G222=((X-x2).^2+(Y-yPyp2).^2+(Z-z2).^2).^(-.5);
G211=((X-x2).^2+(Y-yPyp1).^2+(Z-z1).^2).^(-.5);
G221=((X-x2).^2+(Y-yPyp2).^2+(Z-z1).^2).^(-.5);
G212=((X-x2).^2+(Y-yPyp1).^2+(Z-z2).^2).^(-.5);
G121=((X-x1).^2+(Y-yPyp2).^2+(Z-z1).^2).^(-.5);

B_x = mu_0*M_sPy/4/pi*((reallog(F11)-reallog(F12)-reallog(F21)+reallog(F22)));
B_y = mu_0*M_sPy/4/pi*((reallog(H11)-reallog(H12)-reallog(H21)+reallog(H22)));
B_z =(mu_0*M_sPy/4/pi*(-atan((X-x1).*(Y-yPyp1)./(Z-z1).*G111)+atan((X-x1).*(Y-
yPyp1)./(Z-z2).*G112)-atan((X-x1).*(Y-yPyp2)./(Z-z2).*G122)+atan((X-x2).*(Y-
yPyp2)./(Z-z2).*G222)+atan((X-x2).*(Y-yPyp1)./(Z-z1).*G211)-atan((X-x2).*(Y-
yPyp2)./(Z-z1).*G221)-atan((X-x2).*(Y-yPyp1)./(Z-z2).*G212)+atan((X-x1).*(Y-
yPyp2)./(Z-z1).*G121)));

 % Round 2: Pinned CoFe layer
F11 =((Y-yCop1)+((X-x1).^2+(Y-yCop1).^2+(Z-z1).^2).^.5)./((Y-yCop2)+((X-
x1).^2+(Y-yCop2).^2+(Z-z1).^2).^(1/2));
F12= ((Y-yCop1)+((X-x2).^2+(Y-yCop1).^2+(Z-z1).^2).^.5)./((Y-yCop2)+((X-
x2).^2+(Y-yCop2).^2+(Z-z1).^2).^(1/2));
F22= ((Y-yCop1)+((X-x2).^2+(Y-yCop1).^2+(Z-z2).^2).^.5)./((Y-yCop2)+((X-
x2).^2+(Y-yCop2).^2+(Z-z2).^2).^(1/2));
F21= ((Y-yCop1)+((X-x1).^2+(Y-yCop1).^2+(Z-z2).^2).^.5)./((Y-yCop2)+((X-
x1).^2+(Y-yCop2).^2+(Z-z2).^2).^(1/2));

H11 =((X-x1)+((X-x1).^2+(Y-yCop1).^2+(Z-z1).^2).^.5)./((X-x2)+((X-x2).^2+(Y-
yCop1).^2+(Z-z1).^2).^.5);
H12= ((X-x1)+((X-x1).^2+(Y-yCop2).^2+(Z-z1).^2).^.5)./((X-x2)+((X-x2).^2+(Y-
yCop2).^2+(Z-z1).^2).^.5);
H22= ((X-x1)+((X-x1).^2+(Y-yCop2).^2+(Z-z2).^2).^.5)./((X-x2)+((X-x2).^2+(Y-
yCop2).^2+(Z-z2).^2).^.5);
H21= ((X-x1)+((X-x1).^2+(Y-yCop1).^2+(Z-z2).^2).^.5)./((X-x2)+((X-x2).^2+(Y-
yCop1).^2+(Z-z2).^2).^.5);

G111=((X-x1).^2+(Y-yCop1).^2+(Z-z1).^2).^(-.5);
G112=((X-x1).^2+(Y-yCop1).^2+(Z-z2).^2).^(-.5);
G122=((X-x1).^2+(Y-yCop2).^2+(Z-z2).^2).^(-.5);
G222=((X-x2).^2+(Y-yCop2).^2+(Z-z2).^2).^(-.5);
G211=((X-x2).^2+(Y-yCop1).^2+(Z-z1).^2).^(-.5);
G221=((X-x2).^2+(Y-yCop2).^2+(Z-z1).^2).^(-.5);
G212=((X-x2).^2+(Y-yCop1).^2+(Z-z2).^2).^(-.5);
G121=((X-x1).^2+(Y-yCop2).^2+(Z-z1).^2).^(-.5);
```

```
Bx=Bx + mu_0*M_sCo/4/pi*((reallog(F11)-reallog(F12)-reallog(F21)+reallog(F22)));
By=By + mu_0*M_sCo/4/pi*((reallog(H11)-reallog(H12)-reallog(H21)+reallog(H22)));
Bz=Bz + (mu_0*M_sCo/4/pi*(-atan((X-x1).*(Y-yCop1)./(Z-z1).*G111)+atan((X-
x1).*(Y-yCop1)./(Z-z2).*G112)-atan((X-x1).*(Y-yCop2)./(Z-z2).*G122)+atan((X-
x2).*(Y-yCop2)./(Z-z2).*G222)+atan((X-x2).*(Y-yCop1)./(Z-z1).*G211)-atan((X-
x2).*(Y-yCop2)./(Z-z1).*G221)-atan((X-x2).*(Y-yCop1)./(Z-z2).*G212)+atan((X-
x1).*(Y-yCop2)./(Z-z1).*G121)));

 % Round 3: Free CoFe layer
F11 =((Y-yCof1)+((X-x1).^2+(Y-yCof1).^2+(Z-z1).^2).^.5)./((Y-yCof2)+((X-x1).^2+(Y-
yCof2).^2+(Z-z1).^2).^(1/2));
F12= ((Y-yCof1)+((X-x2).^2+(Y-yCof1).^2+(Z-z1).^2).^.5)./((Y-yCof2)+((X-x2).^2+(Y-
yCof2).^2+(Z-z1).^2).^(1/2));
F22= ((Y-yCof1)+((X-x2).^2+(Y-yCof1).^2+(Z-z2).^2).^.5)./((Y-yCof2)+((X-x2).^2+(Y-
yCof2).^2+(Z-z2).^2).^(1/2));
F21= ((Y-yCof1)+((X-x1).^2+(Y-yCof1).^2+(Z-z2).^2).^.5)./((Y-yCof2)+((X-x1).^2+(Y-
yCof2).^2+(Z-z2).^2).^(1/2));

H11 =((X-x1)+((X-x1).^2+(Y-yCof1).^2+(Z-z1).^2).^.5)./((X-x2)+((X-x2).^2+(Y-
yCof1).^2+(Z-z1).^2).^.5);
H12= ((X-x1)+((X-x1).^2+(Y-yCof2).^2+(Z-z1).^2).^.5)./((X-x2)+((X-x2).^2+(Y-
yCof2).^2+(Z-z1).^2).^.5);
H22= ((X-x1)+((X-x1).^2+(Y-yCof2).^2+(Z-z2).^2).^.5)./((X-x2)+((X-x2).^2+(Y-
yCof2).^2+(Z-z2).^2).^.5);
H21= ((X-x1)+((X-x1).^2+(Y-yCof1).^2+(Z-z2).^2).^.5)./((X-x2)+((X-x2).^2+(Y-
yCof1).^2+(Z-z2).^2).^.5);

G111=((X-x1).^2+(Y-yCof1).^2+(Z-z1).^2).^(-.5);
G112=((X-x1).^2+(Y-yCof1).^2+(Z-z2).^2).^(-.5);
G122=((X-x1).^2+(Y-yCof2).^2+(Z-z2).^2).^(-.5);
G222=((X-x2).^2+(Y-yCof2).^2+(Z-z2).^2).^(-.5);
G211=((X-x2).^2+(Y-yCof1).^2+(Z-z1).^2).^(-.5);
G221=((X-x2).^2+(Y-yCof2).^2+(Z-z1).^2).^(-.5);
G212=((X-x2).^2+(Y-yCof1).^2+(Z-z2).^2).^(-.5);
G121=((X-x1).^2+(Y-yCof2).^2+(Z-z1).^2).^(-.5);

Bx=Bx + state*mu_0*M_sCo/4/pi*((reallog(F11)-reallog(F12)-
reallog(F21)+reallog(F22)));
By=By + state*mu_0*M_sCo/4/pi*((reallog(H11)-reallog(H12)-
reallog(H21)+reallog(H22)));
Bz=Bz + state*(mu_0*M_sCo/4/pi*(-atan((X-x1).*(Y-yCof1)./(Z-z1).*G111)+atan((X-
x1).*(Y-yCof1)./(Z-z2).*G112)-atan((X-x1).*(Y-yCof2)./(Z-z2).*G122)+atan((X-x2).*(Y-
yCof2)./(Z-z2).*G222)+atan((X-x2).*(Y-yCof1)./(Z-z1).*G211)-atan((X-x2).*(Y-
```

```
yCof2)./(Z-z1).*G221)-atan((X-x2).*(Y-yCof1)./(Z-z2).*G212)+atan((X-x1).*(Y-yCof2)./(Z-z1).*G121)));

 % Round 4: Free Py layer
F11 =((Y-yPyf1)+((X-x1).^2+(Y-yPyf1).^2+(Z-z1).^2).^.5)./((Y-yPyf2)+((X-x1).^2+(Y-yPyf2).^2+(Z-z1).^2).^(1/2));
F12= ((Y-yPyf1)+((X-x2).^2+(Y-yPyf1).^2+(Z-z1).^2).^.5)./((Y-yPyf2)+((X-x2).^2+(Y-yPyf2).^2+(Z-z1).^2).^(1/2));
F22= ((Y-yPyf1)+((X-x2).^2+(Y-yPyf1).^2+(Z-z2).^2).^.5)./((Y-yPyf2)+((X-x2).^2+(Y-yPyf2).^2+(Z-z2).^2).^(1/2));
F21= ((Y-yPyf1)+((X-x1).^2+(Y-yPyf1).^2+(Z-z2).^2).^.5)./((Y-yPyf2)+((X-x1).^2+(Y-yPyf2).^2+(Z-z2).^2).^(1/2));

H11 =((X-x1)+((X-x1).^2+(Y-yPyf1).^2+(Z-z1).^2).^.5)./((X-x2)+((X-x2).^2+(Y-yPyf1).^2+(Z-z1).^2).^.5);
H12= ((X-x1)+((X-x1).^2+(Y-yPyf2).^2+(Z-z1).^2).^.5)./((X-x2)+((X-x2).^2+(Y-yPyf2).^2+(Z-z1).^2).^.5);
H22= ((X-x1)+((X-x1).^2+(Y-yPyf2).^2+(Z-z2).^2).^.5)./((X-x2)+((X-x2).^2+(Y-yPyf2).^2+(Z-z2).^2).^.5);
H21= ((X-x1)+((X-x1).^2+(Y-yPyf1).^2+(Z-z2).^2).^.5)./((X-x2)+((X-x2).^2+(Y-yPyf1).^2+(Z-z2).^2).^.5);

G111=((X-x1).^2+(Y-yPyf1).^2+(Z-z1).^2).^(-.5);
G112=((X-x1).^2+(Y-yPyf1).^2+(Z-z2).^2).^(-.5);
G122=((X-x1).^2+(Y-yPyf2).^2+(Z-z2).^2).^(-.5);
G222=((X-x2).^2+(Y-yPyf2).^2+(Z-z2).^2).^(-.5);
G211=((X-x2).^2+(Y-yPyf1).^2+(Z-z1).^2).^(-.5);
G221=((X-x2).^2+(Y-yPyf2).^2+(Z-z1).^2).^(-.5);
G212=((X-x2).^2+(Y-yPyf1).^2+(Z-z2).^2).^(-.5);
G121=((X-x1).^2+(Y-yPyf2).^2+(Z-z1).^2).^(-.5);

B_x=Bx + state*mu_0*M_sPy/4/pi*((reallog(F11)-reallog(F12)-reallog(F21)+reallog(F22)));
B_y=By + state*mu_0*M_sPy/4/pi*((reallog(H11)-reallog(H12)-reallog(H21)+reallog(H22)));
B_z=Bz + state*(mu_0*M_sPy/4/pi*(-atan((X-x1).*(Y-yPyf1)./(Z-z1).*G111)+atan((X-x1).*(Y-yPyf1)./(Z-z2).*G112)-atan((X-x1).*(Y-yPyf2)./(Z-z2).*G122)+atan((X-x2).*(Y-yPyf2)./(Z-z2).*G222)+atan((X-x2).*(Y-yPyf1)./(Z-z1).*G211)-atan((X-x2).*(Y-yPyf2)./(Z-z1).*G221)-atan((X-x2).*(Y-yPyf1)./(Z-z2).*G212)+atan((X-x1).*(Y-yPyf2)./(Z-z1).*G121)));
```

Single SV (ChargeModelSigleSV.m)

```
% Equivalent Charge Model for the SV: This is an equivalent surface charge
% model of the SV CoFe and Permalloy layers.

clear all; % Clear and close all
clc;
close all;

plot2DGraphs = 1;       % Enter a 1 for all B-feld/Forceplots (must be Outside SV)
VariedWidth = 0;        % Enter a 1 to plot varied widths
VariedLength = 0;       % Enter a 1 to plot varied lengths
InsideSV = 0;           % Enter a 1 to look at B-field within SV
OutsideSV = 1;          % Enter a 1 to look at B/F outside of SV
PlaneSlice = 0;         % Enter a 1 to evaluate force as bead moves away from surface
state = 1;              % Enter a 1 for SV "ON"; -1 is "OFF"

%=======CONSTANTS=========================================
mu_0 = pi*4e-7;             % Permitivity, SI
M_sPy= 8.0e5;               % Magnetization of Permalloy A/m
M_sCo = 1400e3;             % Magnetization of CoFe
% SV dimensions
HPy = 15e-9;                % Thickness of one Permalloy section
HCo = 5e-9;                 % Thickness of one CoFe layer
space = 10e-9;              % Thickness of Cu spacer
nitride = 70e-9;            % Passivation nitride thickness

% Three different Dynabeads (Invitrogen) were evaluated.
bead = zeros(3,2);
bead(1,:) = [1.0e-6, 1.458];    % 1 micron diameter
bead(2,:) = [2.8e-6, 0.976];    % 2.8 micron diameter
bead(3,:) = [4.5e-6, 1.6];      % 4.5 micron diamter

 if plot2DGraphs == 1;         % Sets 2 by 6 figure
  figure;
 end

  for beadcount = 1; 1:1:3;          % Choose bead
  diam = bead(beadcount,1);       % Sets diameter and suscep
  suscep = bead(beadcount,2);
  V = 4/3*pi*(diam/2)^3;          % Volume of the bead (m^3)
  nonsat = suscep*V/2/mu_0;       % For the non-saturated force
  viscocity = 1.002e-3;           % Ns/m^2, viscocity of water at 20C
```

```
   velocity = 100e-6;          % um/s Bead velocity (estimated from video)
   drag = -6*pi*viscocity*diam/2*velocity*1e12; % Drag force on the bead in pN

%=======GRID/MESH==========================================
   points = 20;                  % X and Z mesh size
   Force = zeros(8,2*points+1);    % Sets up the arrays
   Field = zeros(8,2*points+1);
   Xhh = zeros(8,2*points+1);
   ForceD = zeros(8,2*points+1);
   ZdD = zeros(8,2*points+1);
   count = 1;                    % Width count
   count1 = 1;                    % Length count

%=======B-FIELD CALCULATION================================
for W=.5e-6:.5e-6:1e-6;          % Enter width(s) to eval
      width(count) = W*1e6;
      for L = 8e-6:.25e-6:8e-6;  % Enger length(s) to eval
         length(count1) = L*1e6;
         x1=-W/2;              % Width along the X-axis
         x2=-x1;
         z1=-L/2;              % Length along the z-axis
         z2=-z1;
         passivation = space+2*HPy+2*HCo+nitride;  % Where fluid channel starts
         upper = passivation + 4*1e-6;   % Upper passivaton limit

         if InsideSV ==1;
            step = 0.05e-9;     % Choose for inside SV
         end
         if OutsideSV ==1;
            step = 0.05e-6;     % Choose for outside SV
         end
         BeadCenter(beadcount) = ceil(diam/2/step+1); % Bead on surface
         HalfMicronAbove(beadcount) = ceil((diam/2+0.5e-6)/step+1); % Bead 0.5D
above surface
         MicronAbove(beadcount) = ceil((diam/2+1e-6)/step+1); % Bead 1D above
surface

         % Boundaries for calculation  (Just looking at blunt ends)
         xlimit = W;
         zlimitMin = .25*L;
         zlimitMax = .75*L;
         xlimitMin = -2*W;
         xlimitMax = 2*W;
```

```
        if OutsideSV ==1;
            [X,Y,Z] = meshgrid(xlimitMin:(xlimitMax-
xlimitMin)/points:xlimitMax,passivation:step:upper,zlimitMin:(zlimitMax-
zlimitMin)/points:zlimitMax);
        end

        if InsideSV ==1;
            [X,Y,Z] = meshgrid(-3*xlimit:6*xlimit/points:3*xlimit,yPyp1:step:yPyf2,-
L:2*L/points:L);
        end

        [t u v] = size(X);
        Bx = zeros(t,u,v);
        By = zeros(t,u,v);
        Bz = zeros(t,u,v);

        [B_x, B_y, B_z] = Bcalculate(X,Y,Z,state,x1,x2,z1,z2,HPy,HCo,space);
        Bx = Bx+B_x;
        By = By+B_y;
        Bz = Bz+B_z;
        BBx(beadcount,count,count1,:,:,:) = Bx;
        BBy(beadcount,count,count1,:,:,:) = By;
        BBz(beadcount,count,count1,:,:,:) = Bz;
        B = sqrt(Bx.^2+By.^2+Bz.^2); % Magnitude of Bfield Vector
        BB(beadcount,count,count1,:,:,:) = B;
        [px,py,pz] = gradient(B.^2,(xlimitMax-xlimitMin)/points,step,(zlimitMax-
zlimitMin)/points);
        F = 1e12*nonsat*sqrt(px.^2+py.^2+ pz.^2);
        FF(beadcount,count,count1,:,:,:) = F;
        XX(beadcount,count,count1,:,:,:) = X;
        YY(beadcount,count,count1,:,:,:) = Y;
        ZZ(beadcount,count,count1,:,:,:) = Z;

        if OutsideSV == 1;
            plane = BeadCenter(beadcount);     % Bead on surface
            Y(plane,plane,plane)
            Xplane(:,:) = X(plane,:,:).*1e6;  %Convert to micron
            Yplane(:,:) = Y(plane,:,:).*1e6;
            Zplane(:,:) = Z(plane,:,:).*1e6;
            Bxplane(:,:) = 1e3*Bx(plane,:,:);   % mT
            Byplane(:,:) = 1e3*By(plane,:,:);   % mT
            Bzplane(:,:) = 1e3*Bz(plane,:,:);   % mT
            Bplane(:,:) = 1e3*B(plane,:,:);
            Fplane(:,:) = F(plane,:,:);
```

```
            Bplot(beadcount,count, count1) = max(Bplane(:,points/2))
            Fplot(beadcount,count, count1) = max(Fplane(:,points/2))

        if PlaneSlice == 1;
            plane = HalfMicronAbove(beadcount);% Bead 1/2 micron abover surface
            Xplane1(:,:) = X(plane,:,:).*1e6;  %Convert to micron
            Yplane1(:,:) = Y(plane,:,:).*1e6;  %Convert to micron (along height)
            Zplane1(:,:) = Z(plane,:,:).*1e6;
            Bxplane1(:,:) = 1e3*Bx(plane,:,:);   % mT
            Byplane1(:,:) = 1e3*By(plane,:,:);   % mT
            Bzplane1(:,:) = 1e3*Bz(plane,:,:);   % mT
            Bplane1(:,:) = 1e3*B(plane,:,:);
            Fplane1(:,:) = F(plane,:,:);
            Fplot1(beadcount,count, count1) = max(Fplane1(:,points/2));
            plane = MicronAbove(beadcount); % Bead 1 micron above surface
            Xplane2(:,:) = X(plane,:,:).*1e6;
            Yplane2(:,:) = Y(plane,:,:).*1e6;
            Zplane2(:,:) = Z(plane,:,:).*1e6;
            Bxplane2(:,:) = 1e3*Bx(plane,:,:);   % mT
            Byplane2(:,:) = 1e3*By(plane,:,:);
            Bzplane2(:,:) = 1e3*Bz(plane,:,:);
            Bplane2(:,:) = 1e3*B(plane,:,:);
            Fplane2(:,:) = F(plane,:,:);
            Fplot2(beadcount,count, count1) = max(Fplane2(:,points/2));

            figure ('Name','Force above surface');
            plot(Xplane(:,points/2),Fplane(:,points/2),
Xplane(:,points/2),Fplane1(:,points/2),Xplane(:,points/2),Fplane2(:,points/2),'linewidt
h',2);
            ylabel ('Max Pull force (pN)','FontSize',11);
            xlabel ('Hard-Axis (um)','FontSize',11);
            rectangle('Position',[-.5,0,1,2],'LineWidth',2, 'FaceColor','k');
            legend('1.4 um (on surface)','2.8 um (0.5D above surface)','4.2 um (1D
above surface)');
        end

        if plot2DGraphs == 1;
            figure('Name','Magnetic Flux Density and Pull-force for bead on surface');
            subplot(2,1,1);
            surf(Xplane,Zplane,Bplane);
            hold on;
            xlim([-xlimit*1e6 xlimit*1e6]);
            title ('Magnetic Flux Density (mT) ', 'FontSize', 12);
            xlabel ('Hard Axis (micron)','FontSize',11);
```

```
        ylabel ('Easy Axis (micron)','FontSize',11);
        zlabel ('Magnetic Field (mT)','FontSize',11);
        colorbar('location','EastOutside');
        hold off
        subplot(2,1,2);
        surf(Xplane,Zplane,Fplane);
        hold on;
        xlim([-xlimit*1e6 xlimit*1e6]);
        title ('Pull-force (pN) ', 'FontSize', 12);
        xlabel ('Hard Axis (micron)','FontSize',11);
        ylabel ('Easy Axis (micron)','FontSize',11);
        zlabel ('Pull-force (pN)','FontSize',11);
        colorbar('location','EastOutside');
        hold off
        %figure('Name','Magnetic Flux Density and Pull-force for bead on
surface');
        subplot(3,2,2*beadcount-1);
        contourf(Xplane,Zplane,Bplane);
        hold on;
        xlabel ('Hard-Axis (um)','FontSize',11);
        ylabel ('Easy-Axis (um)','FontSize',11);
        zlabel ('Magnetic Field (mT)','FontSize',11);
        colorbar('location','EastOutside');
        h=colorbar;
        ylabel(h,'|B-Field|  (mT)');
        rectangle('Position',[-.5,2,1,2],'LineWidth',2, 'FaceColor','k');
        hold off
        subplot(3,2,2*beadcount);
        contourf(Xplane,Zplane,Fplane);
        hold on;
        xlabel ('Hard-Axis (um)','FontSize',11);
        ylabel ('Easy-Axis (um)','FontSize',11);
        zlabel ('Pull-force (pN)','FontSize',11);
        colorbar('location','EastOutside');
        h=colorbar;
        ylabel(h,'Max Pull-force (pN)');
        rectangle('Position',[-.5,2,1,2],'LineWidth',2, 'FaceColor','k');
        hold off
      end
      end
      count1 = count1+1;
    end
```

```
        count1 =1;
        count = count+1;
    end
    end

    if InsideSV ==1;
    figure('Name','In-plane field');
    for count = 1:1:2;
        for count1 = 1:1:2;
        BBxz(beadcount,count,count1,:,:,:) =
sqrt(BBx(beadcount,count,count1,:,:,:).^2+BBz(beadcount,count,count1,:,:,:).^2); %
Magnitude of Bfield Vector
        n = 10; % number of sections in fcontour
        plane = points+1;          % Midway through SV
        Xplane(:,:) = XX(beadcount,count,count1,plane,:,:).*1e6;  %Convert to micron
        Yplane(:,:) = YY(beadcount,count,count1,plane,:,:).*1e6;
        Zplane(:,:) = ZZ(beadcount,count,count1,plane,:,:).*1e6;
        Bxplane(:,:) = 1e3*BBx(beadcount,count,count1,plane,:,:);   % mT
        Byplane(:,:) = 1e3*BBy(beadcount,count,count1,plane,:,:);
        Bzplane(:,:) = 1e3*BBz(beadcount,count,count1,plane,:,:);
        Bplane(:,:) = 1e3*BB(beadcount,count,count1,plane,:,:);
        Bxzplane(:,:) = 1e3*BBxz(beadcount,count,count1,plane,:,:);
        Fplane(:,:) = FF(beadcount,count,count1,plane,:,:);
        Fplot(count) = max(Fplane(:,points/2));
        subplot(2,1,count);
        contourf(Zplane,Xplane,Bxzplane,n);
        ylabel('Hard-Axis (um)');
        xlabel('Easy-Axis (um)');
        xlim([-6 6]);
        ylim([-1.5 1.5]);
        caxis([0 40]);
        h=colorbar;
        ylabel(h,'|B-Field|  (mT)');
        rectangle('Position',[-length(count1)/2*1e6,-
width(count)/2,length(count1)*1e6,width(count)],'LineWidth',2, 'FaceColor','k');
        end
    end
end

 if VariedWidth == 1;
    figure;
    plot(width,transpose(Fplot),'LineWidth',2);
    xlabel ('SV Width (um)','Fontsize',12);
    ylabel ('Max Pull-force (pN)','Fontsize',12);
```

```
   legend ('1 um Dynabead','2.8 um Dynabead','4.5 um Dynabead');
end

if VariedLength == 1;
   [t u v] = size(Fplot);
   for blue = 1:1:t;
      temp1(:,blue) = Fplot(blue,1,:);
   end

   figure;
   plot(length,temp1,'LineWidth',2);
   xlabel ('SV Length (um)','Fontsize',12);
   ylabel ('Max Pull-force (pN)','Fontsize',12);
   legend ('1 um Dynabead','2.8 um Dynabead','4.5 um Dynabead');
end
```

Arrayed SVs (ChargeModelArrayed.m)

```
% Equivalent Charge Model for the SV: This is an equivalent surface charge
% model of the SV CoFe and Permalloy layers.

 clear all; clc; close all;

 % Enter a 1 for SV "ON"; -1 is "OFF"
SV1 = 1;
SV2 = 1;
SV3 = 1;
SV4 = 1;
SV5 = -1;
SV6 = 1;
SV7 = 1;
SV8 = 1;
SV9 = 1;

Array = 1; % Enter a 1 to look at the array
Staggered = 1; % Enter a 1 to stagger the SVs

%=======CONSTANTS==========================================
mu_0 = pi*4e-7;             % Permitivity, SI
M_sPy= 8.0e5;               % Magnetization of Permalloy A/m
M_sCo = 1400e3;              % Magnetization of CoFe
bead(1,:) = [1.0e-6, 1.458];    % 1 micron diameter
bead(2,:) = [2.8e-6, 0.976];    % 2.8 micron diameter
bead(3,:) = [4.5e-6, 1.6];      % 4.5 micron diamter
```

```
beadcount = 2;          % Choose bead
diam = bead(beadcount,1);       % Sets diameter and suscep
suscep = bead(beadcount,2);
V = 4/3*pi*(diam/2)^3;          % Volume of the bead (m^3)
nonsat = suscep*V/2/mu_0;       % For the non-saturated force
% SV dimensions
HPy = 15e-9;               % Thickness of one Permalloy section
HCo = 5e-9;                % Thickness of one CoFe layer
space = 10e-9;             % Thickness of Cu spacer
nitride = 70e-9;           % Passivation nitride thickness
beadcenter = 2*HPy+2*HCo+space+nitride+diam/2;
W = 3e-6;
L = 8e-6;
XLattice = 9e-6;
ZLattice = 14e-6;
stagger = 0;

if Staggered == 1;
   stagger = XLattice/2;
end

points = 200;                  % X and Z mesh size
step = .02e-6;

zlimitMin = -L;
zlimitMax = 3*ZLattice;
xlimitMin = -2*W;
xlimitMax = 3*XLattice;
ylimitMin = 1e-6;
ylimitMax = 2e-6;
plane = 1+ceil((beadcenter - ylimitMin)/step);

if Array == 0;
   zlimitMin = -.75*L;
   zlimitMax = .75*L;
   xlimitMin = -.75*W;
   xlimitMax = .75*W;
   ylimitMin = 0;
   ylimitMax = 0.1e-6;
end

[X,Y,Z] = meshgrid(xlimitMin:(xlimitMax-
xlimitMin)/points:xlimitMax,ylimitMin:step:ylimitMax,zlimitMin:(zlimitMax-
zlimitMin)/points:zlimitMax);
```

```
[t u v] = size(X);
Bx = zeros(t,u,v);
By = zeros(t,u,v);
Bz = zeros(t,u,v);

state = SV1;
p=0; n=0;
x1=-W/2+p*XLattice;              % Width along the X-axis
x2=W/2+p*XLattice;
z1=-L/2+n*ZLattice;              % Length along the z-axis
z2=L/2+n*ZLattice;
[B_x, B_y, B_z] = Bcalculate(X,Y,Z,state,x1,x2,z1,z2,HPy,HCo,space);
Bx = Bx+B_x;
By = By+B_y;
Bz = Bz+B_z;

if Array == 1;
state = SV2;
p=1;n=0;
x1=-W/2+p*XLattice;              % Width along the X-axis
x2=W/2+p*XLattice;
z1=-L/2+n*ZLattice;              % Length along the z-axis
z2=L/2+n*ZLattice;
[B_x, B_y, B_z] = Bcalculate(X,Y,Z,state,x1,x2,z1,z2,HPy,HCo,space);
Bx = Bx+B_x;
By = By+B_y;
Bz = Bz+B_z;

state = SV3;
p=2;n=0;
x1=-W/2+p*XLattice;              % Width along the X-axis
x2=W/2+p*XLattice;
z1=-L/2+n*ZLattice;              % Length along the z-axis
z2=L/2+n*ZLattice;
[B_x, B_y, B_z] = Bcalculate(X,Y,Z,state,x1,x2,z1,z2,HPy,HCo,space);
Bx = Bx+B_x;
By = By+B_y;
Bz = Bz+B_z;

state = SV4;
p=0;n=1;
x1=-W/2+p*XLattice+stagger;              % Width along the X-axis
x2=W/2+p*XLattice+stagger;
z1=-L/2+n*ZLattice;              % Length along the z-axis
```

```
z2=L/2+n*ZLattice;
[B_x, B_y, B_z] = Bcalculate(X,Y,Z,state,x1,x2,z1,z2,HPy,HCo,space);
Bx = Bx+B_x;
By = By+B_y;
Bz = Bz+B_z;

state = SV5;
p=1;n=1;
x1=-W/2+p*XLattice+stagger;              % Width along the X-axis
x2=W/2+p*XLattice+stagger;
z1=-L/2+n*ZLattice;              % Length along the z-axis
z2=L/2+n*ZLattice;
[B_x, B_y, B_z] = Bcalculate(X,Y,Z,state,x1,x2,z1,z2,HPy,HCo,space);
Bx = Bx+B_x;
By = By+B_y;
Bz = Bz+B_z;

state = SV6;
p=2;n=1;
x1=-W/2+p*XLattice+stagger;              % Width along the X-axis
x2=W/2+p*XLattice+stagger;
z1=-L/2+n*ZLattice;              % Length along the z-axis
z2=L/2+n*ZLattice;
[B_x, B_y, B_z] = Bcalculate(X,Y,Z,state,x1,x2,z1,z2,HPy,HCo,space);
Bx = Bx+B_x;
By = By+B_y;
Bz = Bz+B_z;

state = SV7;
p=0;n=2;
x1=-W/2+p*XLattice;               % Width along the X-axis
x2=W/2+p*XLattice;
z1=-L/2+n*ZLattice;              % Length along the z-axis
z2=L/2+n*ZLattice;
[B_x, B_y, B_z] = Bcalculate(X,Y,Z,state,x1,x2,z1,z2,HPy,HCo,space);
Bx = Bx+B_x;
By = By+B_y;
Bz = Bz+B_z;

state = SV8;
p=1;n=2;
x1=-W/2+p*XLattice;               % Width along the X-axis
x2=W/2+p*XLattice;
z1=-L/2+n*ZLattice;              % Length along the z-axis
```

```
z2=L/2+n*ZLattice;
[B_x, B_y, B_z] = Bcalculate(X,Y,Z,state,x1,x2,z1,z2,HPy,HCo,space);
Bx = Bx+B_x;
By = By+B_y;
Bz = Bz+B_z;

state = SV9;
p=2;n=2;
x1=-W/2+p*XLattice;              % Width along the X-axis
x2=W/2+p*XLattice;
z1=-L/2+n*ZLattice;              % Length along the z-axis
z2=L/2+n*ZLattice;
[B_x, B_y, B_z] = Bcalculate(X,Y,Z,state,x1,x2,z1,z2,HPy,HCo,space);
Bx = Bx+B_x;
By = By+B_y;
Bz = Bz+B_z;
end

B = sqrt(Bx.^2+By.^2+Bz.^2); % Magnitude of Bfield Vector
[px,py,pz] = gradient(B.^2,(xlimitMax-xlimitMin)/points,step,(zlimitMax-
zlimitMin)/points);
F = 1e12*nonsat*sqrt(px.^2+py.^2+ pz.^2);

XX(:,:) = X(plane,:,:);
YY(:,:) = Y(plane,:,:);
ZZ(:,:) = Z(plane,:,:);
BBx(:,:) = Bx(plane,:,:);
BBy(:,:) = By(plane,:,:);
BBz(:,:) = Bz(plane,:,:);
BB(:,:) = B(plane,:,:);
FF(:,:) = F(plane,:,:);

figure;
subplot(2,1,1);
contourf(1e6*ZZ,1e6*XX,1e3*BB);
for n=0:2:2;
   for p = 0:1:2;
       rectangle('position',[(-L/2+n*ZLattice)*1e6,(-
W/2+p*XLattice)*1e6,L*1e6,W*1e6],'LineWidth',2, 'FaceColor','k');
   end
end
for n=1;
   for p=0:1:2;
       rectangle('position',[(-L/2+n*ZLattice)*1e6,(-
```

```
W/2+p*XLattice+stagger)*1e6,L*1e6,W*1e6],'LineWidth',2, 'FaceColor','k');
   end
end
xlabel('Easy-Axis (um)','FontSize',12);
ylabel('Hard-Axis (um)','FontSize',12);
h=colorbar;
ylabel(h,'|B-Field| (mT)');
subplot(2,1,2);
contourf(1e6*ZZ,1e6*XX,FF);
for n=0:2:2;
   for p = 0:1:2;
      rectangle('position',[(-L/2+n*ZLattice)*1e6,(-
W/2+p*XLattice)*1e6,L*1e6,W*1e6],'LineWidth',2, 'FaceColor','k');
   end
end
for n=1;
   for p=0:1:2;
      rectangle('position',[(-L/2+n*ZLattice)*1e6,(-
W/2+p*XLattice+stagger)*1e6,L*1e6,W*1e6],'LineWidth',2, 'FaceColor','k');
   end
end
xlabel('Easy-Axis (um)','FontSize',12);
ylabel('Hard-Axis (um)','FontSize',12);
h=colorbar;
ylabel(h,'Pull-force (pN)');
```

Appendix C: OOMMF .mif File

```
# MIF 2.1
# Description: Spin valve example
set pi [expr 4*atan(1.0)]
set mu0 [expr 4*$pi*1e-7]

Specify Oxs_MultiAtlas:atlas (
   atlas ( Oxs_BoxAtlas (
        name top
        xrange (0 8e-6)
        yrange (0 1e-6)
        zrange (30e-9 50e-9)
   ) )
   atlas ( Oxs_BoxAtlas (
      name spacer
      xrange (0 8e-6)
      yrange (0 1e-6)
      zrange (20e-9 30e-9)
   ) )
   atlas ( Oxs_BoxAtlas (
      name bottom
      xrange (0 8e-6)
      yrange (0 1e-6)
      zrange (0 20e-9)
   ) )
)

Specify Oxs_RectangularMesh:mesh (
  cellsize (.05e-6 .05e-6 10e-9)
  atlas :atlas
)

Specify Oxs_Exchange6Ngbr:NiFe (
  atlas :atlas
  default_A 13e-12
  A  (
    spacer spacer 0
    spacer top 0
```

```
    spacer bottom 0
  )
)

# Add biasing field to bottom layer. 40e3 A/m \approx 500 (when at 40e3) Oe. Was at 50, now 80
Specify Oxs_TransformZeeman:Bias (
  field ( Oxs_AtlasVectorField (
    atlas :atlas
    default_value (0. 0. 0.)
    values (
          bottom  ( 60e3 0. 0. )
    )
  ))
)

# Add antiferromagnetic exchange coupling across top-bottom layers
Specify Oxs_LinearScalarField:zheight (
vector (0 0 1)
norm   1.0
)

Specify Oxs_TwoSurfaceExchange:AF (
 sigma 0
 comment (sigma2 0)
 surface1 (
         atlas  :atlas
        region  bottom
   scalarfield  :zheight
   scalarvalue  20e-9
    scalarside  -
 )
 surface2 (
         atlas  :atlas
        region  top
   scalarfield  :zheight
   scalarvalue  30e-9
    scalarside  +
 )
)

# Stepped applied field
Specify Oxs_UZeeman "
  multiplier [expr 0.001/$mu0]
```

```
 Hrange (
    (    0  0  0   100   0  0    5 )
    (  100  2  0  -100   2  0   100 )
    ( -100  2  0   100   2  0   100 )
  )

Specify Oxs_Demag ()
Ignore Specify Oxs_EulerEvolve:evolve (
  alpha 0.5
  start_dm 0.01
)

Specify Oxs_RungeKuttaEvolve:evolve (
  alpha 0.5
)

Specify Oxs_TimeDriver (
 basename spinvalve-af
 evolver :evolve
 comment (1 deg/ns = 17453293 rad/sec; If Ms=8.6e5, and lambda is small,
         then mxh=1e-6 translates into dm/dt = 2e5 rad/sec = 0.01 deg/ns)
 stopping_dm_dt .01
 mesh :mesh
 stage_count 207
 stage_iteration_limit 0
 total_iteration_limit 0
 Ms  ( Oxs_AtlasScalarField (
    atlas :atlas
    default_value 0
    values (
       top 800e3
       bottom 800e3
    )
 ))

 m0 ( Oxs_UniformVectorField (
  norm 1
  vector (10 1 0)
 ))
)
```

Appendix D: Fabrication Process Charts

TESTBED4

Start Date: 11 December 2008

Substrates: 3” 1-10 Ohm-cm Si, 300 nm SiN_x

1) SV Deposition DATE: 12/11/08, MT Sputter Chamber, *Base Pressure 6e-9 Torr

- Flat aligned to #1 on chuck
- Gas purifier on
- 250 Oe parallel to flat
- 5 nm Ta, 220 W, 160 sccm Ar, 0.63 A/s
- 5 nm Cu, 100W, 80 sccm, 0.84 A/s
- 10 nm IrMn, 150 W, 130 sccm Ar, 0.82 A/s
- 15 nm NiFe, 400W, 60 sccm Ar, 1.61 A/S
- 5 nm CoFe, 200 W, 80 sccm Ar, 0.63 A/s
- 10 nm Cu, 100 W, 80 sccm Ar, 0.84 A/s
- 5 nm CoFe, 200 W, 80 sccm Ar, 0.63 A/s
- 15 nm NiFe, 400W, 60 sccm Ar, 1.61 A/S
- 5 nm Ta, 220 W, 160 sccm Ar, 0.63 A/s
- 75 nm total stack thickness

3) SV photolith DATE: ?

- Spin on LOR3A, recipe 4 2500 RPM 40 sec
- 4 min 150C bake
- Spin on SPR660, 3200rpm, 40 sec
- 60 s 95C bake
- Expose Stepper

  Job:
  Masks: TESTBED4
  Level: BASE
  Exp.=270 mJ/cm^2
- Autodevelop 70 sec MF701
- DI rinse/inspect, 60 sec 95C bake

4) SV Etch Intelvac chamber DATE: 5/19/06

- Mount sample on 3” stub with dry chuck/
- Base pressure = 5e-8 torr
- Ion beam etch:

  Ic= 8.0 A
  V_d(V) = 40 I_d(A) = 0.43
  Vb=300V I_b(mA)=40
  V_a (V)=400 Ia= 5mA
  I_{ne}(mA) = 50 I_n(A)= 6.4
  Ip= 0.13 mA/cm^2
  Ar flow = 7.5 sccm, P = 3.0e-4T
  Time: 19 minutes
- Ultrasonic in PG remover for 20 min
- Ultrasonic Isoproponal 10 min
- Rinse/inspect
- Etch thickness (nm)

Add SU-8 Channels
Start Date: 12/19/2009
Die Size: SVTestbed is 7 mm x 7 mm, Fluid Mask is for SVWIRE.001 6 mm x 6 mm

5) 75 micron SU-8 DATE:12/19/2010

- Clean wafer with ace/IPA
- Dehydrate on hot plate for 2 min at 100°C
- Spin on SU-8-2025 (Recipe #3):
  - Ramp to 500 rpm at 100 rpm/sec, should take 5 sec
  - Ramp to 1000 rpm at 300 rpm/sec; spin at 1000 rpm for 30 sec
  - Let sit for 2 minutes
- Remove edge bead with SU-8 developer or acetone
- Check that back is clean
- Bake 3 minutes at 65°C, then slowly ramp to 95°C
- Bake 9 minutes at 95°C
- Turn off heat plate and let cool to 50°C (this takes 13 minutes)
- Expose with Carl Suss Mask Aligner for 50 seconds (SU Channel 4 inch mask)
- Bake 1 minutes at 65ºC, then slowly ram to 95°C
- Bake 7 minutes at 95ºC
- Turn off heat plate and let cool to 50ºC
- Develop: 7 min with periodic agitation
- Rinse with SU-8 developer for 15-30 seconds
- Rinse with IPA
- Blow dry
- Inspect: Still some minor cracking and liftoff near the edge of the wafer.

SVWIRE 3.1

Start Date: 10/14/2010
Substrates: 3“ Si, 300 nm LPCVD SiN_x (300 nm Nitride WRA 8/25/2010 SiNx A)
Film ID: SVWIRE3.001
Die Size: 15 mm x 12 mm
Design Modifications: Read wires were simplified, the test SVs with read and write lines were modified to incorporate nearest neighbor SVs and spacing modifications.
Comments: Read wires may be too small…

1) Align Photolith DATE: 10/13/2010

- Notes: It is important to put down the alignments independent of the first mask layer. The alignment will be off if both the PM and layer 1 are exposed at the same time.
- Auto spin on SPR660, 3200 RPM 40 sec
- 60 sec 95C bake
- Expose Stepper
  Job: SVWire
  Masks: ALIGN
  Level: BASE
  Exp.=165 mJ/cm2
  Focus = 0
- 60 sec 95C bake
- Autodevelop 60 sec MF26A
- Inspect:

2) Alignment Mark Etch DATE: 10/13/2010

- Axic etcher, Recipe JM_Nitride
- 2 sccm O_2, 42 sccm CF_4, 75 W, -200 V
- Etch Time: 8 minutes
- Clean with Ace/IPA/N_2

3) Write Wire Photolith DATE: 10/14/2010

- 3 min O_2 ash with 100 watts (this makes the surface hydrophilic, which is necessary for the LOR spin)
- 5 min pre bake at 150C
- Pour 5 mL LOR 5A at 300 rpm for 5 seconds, ramp at 10000 rpm/s to 2500 rpm for 45 sec (use dropper completely filled)
- Remove edge bead with EBR PG (NO ACETONE – failure to remove edge bead may result in the wafer cracking when placed in the IntelVac chuck)
- Bad spin? Clean in Remover PG, IPA, 2 min H_2O wash, then dry. Ash if necessary.
- 5 min 150C bake
- Spin on SPR660, 210 spin setting, 40 sec
- 60 s 95C bake
- Expose with Stepper
  Job: SVWire
  Masks: WRITE, FLOOD (allots for laser)
  Level: BASE
  exp.=165 mJ/cm^2
  focus = 0
- 60 sec 115C bake
- Autodevelop 55 sec MF26A

4) Write Wire Deposition: 5 nm Ti/200 nm Au/ 5 nm Ti DATE: 10/14/2010; Use Lesker

- 5 minute plasma clean
- Deposit 5 nm Ti (2 Å/s: 0.050 kÅ)/200 nm Au (10 Å/s: 2.0 kÅ)/ 5 nm Ti (2 Å/s: 0.050 kÅ)/

- Measure sheet resistance: .041 on ¼ " square
- After deposition, rinse with acetone, IPA, and spin-dry
- Remove residual LOR by 30 minute ultrasonic soak in NMP
- 2 min DI rinse
- 2 min IPA rinse
- Measure thickness using AlphaStep: __Not Measured___ nm
- Inspect:
- Comments: Some issues with Ti deposition (multiple tries)

5) SiN_x Deposition DATE: 10/27/2010
IntelVac

- 80 nm Si_3N_4: rate 3.7 nm/min
  Ar flow = 6 sccm, P = 3e-4 Torr
  Time: 22 minutes

Comments: I'm starting to doubt whether nitride was deposited

6) SV Deposition DATE: 10/25/2010
MT Sputter Chamber, *Base Pressure 6e-9 Torr

- Calibrate targets for at least 100 s
- Flat aligned to #1 on chuck
- Argon gas purifier on
- 220 Oe parallel to flat

Target	Rate (Å/s)	Gas (sccm)	Power (W)
Ru	0.73	19.0	150
CoFe	0.38	15.0	100
Cu	1.32	15.0	100
IrMn	0.92	20.0	100
Ta	0.77	15.0	150
NiFe 80/20	1.21	15.0	250

- Recipe: Ta(5)-Cu(5)-IrMn(10)-NiFe(15)-CoFe(5)-Cu(10)-CoFe(5)-NiFe(15)-Ta(5)-Ru(3)
- 78 nm total stack thickness
- Measure curve with Looper ~80 nm
- Comments:

7) SV layer anneal DATE: 11/4/2010

- Job: Wendy_ann_180C
- Recipe: Ar_5torr_Wendy_180C
  - 5 Torr Argon for 10800 (2 ½ hours) seconds at 235°C (actually 180°C)
  - Ramp up: 10°C per minute, ramp down: 20°C per minute
- Measure with Looper:

8) SV layer photolith DATE: 11/5/2010

- 3 min O_2 ash with 100 watts (this makes the surface hydrophilic, which is necessary for the LOR spin)
- 5 min pre bake at 150C
- Pour 5 mL LOR 5A at 300 rpm (100rpm/s) for 5 seconds, ramp at 1500 rpm/s to 2500 rpm for 45 sec (use dropper completely filled)
- Remove edge bead with EBR PG (NO ACETONE)
- Bad spin? Clean in Remover PG, IPA, 2 min H_2O wash, then dry. Ash if necessary.
- 5 min 150C bake
- Spin on SPR660, (210) 2200 rpm, 40 sec
- 60 s 95C bake
- Expose Stepper
  Job: SVWire
  Masks: SPINVALVE, FLOOD
  Level: BASE
  Exp.=165 mJ/cm^2
  Focus = 0
- 60 sec 95C bake
- Autodevelop 50 sec MF26A
- Comments: Looks good

9) SV Layer Etch Intelvac chamber DATE: 11/5/2010

- Clean wafer edge with Acetone; failure to clean edge makes it difficult for the wafer to fit on the stub resulting in the wafer cracking!

- Mount sample on 3” stub with dry chuck
- Base pressure= 5e-8 torr
- Ion beam etch:
  Angle = 15 °
  Ar flow = 7.5 sccm, P = 3e-4T
  Time: 18 min (probably only needs 16 min)

Property	8 cm
Cathode Filament Current	5.46
Discharge Current	0.32
Discharge Voltage	40
Beam Current	29
Beam Voltage	200
Accelerator Current	2
Accelerator Voltage	100
Neutralizer Emmissions Current	37
Filament Current	6.22

- Rinse with acetone, IPA, and spin-dry
- Remove residual LOR by 2 hours 30 minute ultrasonic soak in NMP
- 2 min DI rinse
- 2 min IPA rinse
- Measure Thickness ~80 nm
- Inspect: There may be some PR baked on the devices. Also, DO NOT put SV in the asher

10) Read Wire Photolith DATE: 11/06/2010

- 3 min O_2 ash with 60 watts (this makes the surface hydrophilic, which is necessary for the LOR spin – may ruin SVs)
- 5 min pre bake at 150C
- Pour 5 mL LOR 5A at 300 rpm (100rpm/s) for 5 seconds, ramp at 1500 rpm/s to 2500 rpm for 45 sec (use dropper completely filled)
- Remove edge bead with EBR PG (NO ACETONE)
- Bad spin? Clean in Remover PG, IPA, 2 min H_2O wash, then dry. Ash if necessary.
- 5min 150C bake
- Spin on SPR660, 2200rpm, 40 sec
- 60 s 95C bake
- Expose Stepper
  Job: SVWire
  Masks: READ
  Level: BASE
  Exp.=165 mJ/cm^2
  Focus = 0
- 55 sec 95C bake
- Autodevelop 55 sec MF26A
- Inspect: Read wires are too thin…redesighn mask

11) Read Wire Deposition DATE: 11/06/2010, Lesker E-Beam

- 5 min clean
- 5 nm Ti/200 nm Au / 10 nm Ti
- Measure sheet resistance: 1.4 ohm
- Remove residual LOR by 5 minute ultrasonic soak in nano EBR
- 2 min DI rinse
- Measure thickness: ~230 nm
- Inspect: OK
- Comments: Some of the thin read wires washed away
- Measure MR using MOKE platform

12) Via 1 Photolith DATE:11/6/2010

- Auto spin on SPR660, 3200 RPM 40 sec
- 60 sec 95C bake
- Expose Stepper
  Job: SVWire
  Masks: VIA, FLOOD
  Level: BASE
  Exp.=165 mJ/cm2
  Focus = 0

- 60 sec 95C bake
- Autodevelop 60 sec MF26A
- Inspect: looks good

13) Via Etch DATE: 11/06/2010

- Axic etcher, Recipe JM_Nitride
- Alighn Laser on open die (didn't have one, so aligned over bare arrays w/good signal)
- 2 sccm O_2, 42 sccm CF_4, 75 W, -200 V
- Etch Time: 4 minutes 20 seconds
- Etch Depth: hopefully over 80 nm
- Clean with Ace/IPA/N_2
- Looks good, Sheet resistance of write Au flood square is 1.63 ohms

14) Passivation Layer Photolith:

- 5 min pre bake at 150C
- Start spinner and pour 5 mL LOR 5A at 300 rpm (100rpm/s) for 5 seconds, ramp at 1000 rpm/s to 2500 rpm for 45 sec (use dropper completely filled)
- Remove edge bead with EBR PG (NO ACETONE)
- Bad spin? Clean in Remover PG, IPA, 2 min H_2O wash, then dry. Ash if necessary.
- 5min 150C bake
- Spin on SPR660, 2200 rpm, 40 sec
- 60 s 95C bake
- Expose Stepper

  Job: SVWire
  Masks: PASS
  Level: BASE
  exp.=165 mJ/cm^2
  focus = 0
- 60 sec 95C bake
- Autodevelop 50 sec MF26A
- Comments:

13) Passivation Layer SiN$_x$ Deposition
DATE: ?, Intelvac chamber

- 100 nm SiN$_x$
- 8 cm: 6.12, 0.3, 25, 3, 31; 40, 100, 200, 7; 0.5sccm Ar and 6.0sccm N_2
- 3 cm: 400 500 100 5.54; 4sccm Ar
- Time ~30 min
- Measure thickness: ~90 nm
- Inspect:

==============================

Start Date: 6/24/2010

Substrates: 3" Mechanical Si, 300 nm SiN$_x$
Film ID: N/A
Comments: The purpose of this wafer is to create a PDMS mold for svwire2.

1) Microfluidic Channel Photolith: 41 micron SU-8 2025
DATE: 6/24/2010

- 3 min O_2 ash
- Clean wafer with ace/IPA
- Dehydrate on hot plate for 2 min at 100°C
- Spin on SU-8-2025 (Recipe #3):
  - Ramp to 500 rpm at 100 rpm/sec, should take 5 sec
  - Ramp to 2000 rpm at 300 rpm/sec; spin at 2000 rpm for 30 sec
  - Let sit for 2 minutes
- Remove edge bead with SU-8
- Check that back is clean
- Bake 2 minutes at 65ºC, then slowly ramp to 95ºC
- Bake 5 minutes at 95ºC
- Turn off heat plate and let cool to 50ºC (this takes 13 minutes)
- Expose with Carl Suss Mask Aligner for 50 seconds (SU Channel 4 inch mask)
- Bake 1 minutes at 65ºC, then slowly ram to 95ºC
- Bake 3 minutes at 95ºC
- Turn off heat plate and let cool to 50ºC

- Develop: 5 min with periodic agitation
- Rinse with SU-8 developer for 15-30 seconds
- Rinse with IPA (check for no white fuzz)
- Blow dry
- Inspect: Some minor cracking and webbing near inlets
- Measure thickness: 39.9 μm

2) Teflon-like coating (optional)

3) PDMS Date: 6/28/2010

- Set oven to 60 ºC
- Clean the petri-dish if it is dirty
- Wear gloves
- Using a metal boat, measure out 4 grams of the viscous base (avoid causing big bubbles)
- Using a pipette, add 0.4 grams (~ 500 μL) of the liquid curing agent to the base (1:10 base to curing agent ratio)
- Gently stir the base and curing agent together. Try to avoid creating big bubbles.
- Let it sit for 20 minutes to allow all the small bubbles to dissipate
- Gently pour onto the wafer/SU-8 mold. The uncured PDMS will spread out evenly onto the wafer after 5-10 minutes
- Cure in the 60 ºC oven for 304 hours (it may be left overnight)
- Wearing gloves to keep the PDMS clean, gently peel the PDMS off the wafer mold. Cut/slice as necessary.
- Punch holes with 14 G blunt needle
- To clean PDMS, use scotch tape then plasma (1 min) or rinse with Ace/IPA/DI H_2O (don't soak!!!)

SVWIRE 6.1

Start Date: 12/10/2010
Substrates: 3“ Si, 300 nm LPCVD SiN_x (250 nm Nitride JM030801b)
Film ID: SVWIRE6.001
Die Size: 15 mm x 12 mm
Design Modifications: More spacing between write lines, added read lines.
Comments: it works!

1) Alighn Photolith DATE: 12/9/2010

- Notes: It is important to put down the alignments independent of the first mask layer. The alignment will be off if both the PM and layer 1 are exposed at the same time.
- Auto spin on SPR660, 3200 RPM 40 sec
- 60 sec 95C bake
- Expose Stepper
  Job: SVWire
  Masks: ALIGN
  Level: BASE
  Exp.=165 mJ/cm2
  Focus = 0
- 60 sec 95C bake
- Autodevelop 60 sec MF26A
- Inspect: Looks good.

2) Alignment Mark Etch DATE: 12/9/2010

- Axic etcher, Recipe JM_Nitride
- 2 sccm O_2, 42 sccm CF_4, 75 W, -200 V
- Etch Time: 8 minutes
- Clean with Ace/IPA/N_2

3) Write Line Photolith DATE: 12/9/2010

- ~~3 min O_2 ash with 100 watts (this makes the surface hydrophilic, which is necessary for the LOR spin)~~
- 5 min pre bake at 150C to dehydrate wafer
- Drop LOR 5A on wafer and spin at 300 rpm for 5 seconds with 500 rpm/sec ramp, ramp at 1500 rpm/s to 2500 rpm for 45 sec (use dropper completely filled)
- Remove edge bead with EBR PG on a q-tip (NO ACETONE – failure to remove edge bead may result in the wafer cracking when placed in the IntelVac chuck)
- Bad spin? Clean in Remover PG, IPA, 2 min H_2O wash, then dry. Ash if necessary.
- 5 min 150C bake
- Spin on SPR660, 210 spin setting, 40 sec
- 60 s 95C bake
- Expose with Stepper
  Job: SVWire
  Masks: WRITE, FLOOD (For laser)
  Level: BASE
  Exp.=165 mJ/cm^2
  Focus = 0
- 60 sec 115C bake
- Autodevelop 55 sec MF26A
- Inspect: Not bad, not great.

4) Write Line Deposition: 5 nm Ti/150 nm Au/ 5 nm Ti DATE: 12/9/2010 Use Lesker

- 5 minute plasma clean
- Deposit 5 nm Ti (2 Å/s: 0.050 kÅ)/150 nm Au (10 Å/s: 2.0 kÅ)/ 5 nm Ti (2 Å/s: 0.050 kÅ)/
- After deposition, rinse with acetone, IPA, and spin-dry
- Remove residual LOR by 10 minute ultrasonic soak in NMP
- 2 min DI rinse

- Auto wash/dry
- Measure thickness using AlphaStep: 200 nm
- Inspect: Looks good.
- Comments:

5) SiN$_x$ Deposition DATE: 12/16/2010 Intelvac

- Add mark with Sharpie on edge of wafer to determine deposition thickness
- 150 nm Si_3N_4: rate 3 nm/min
  N_2 flow = 8 sccm, Ar = 18.5 sccm
  2 mTorr N_2, Ar added until 5mTorr total
  Time: 28 minutes
- Comments: The IntelVac was not behaving. I only got 100 nm of silicon rich SiNx down.

6) SV Deposition DATE: 12/16/2010 MT Sputter Chamber, *Base Presure 1e-10 Torr

- Callibrate targets for at least 100 seconds
- Flat aligned to #3 on chuck (align #1 in chamber)
- Argon gas purifier on
- 220 Oe parallel to flat

Target	**Rate (Å/s)**	**Gas (sccm)**	**Power (W)**
Ru	0.86	19.0	150
CoFe	0.85	15.0	200
Cu	1.97	15.0	200
IrMn	1.08	20.0	150
Ta	0.91	15.0	200
NiFe 80/20	1.51	15.0	300

- Recipe: Ta(3)-Cu(3)-IrMn(10)-NiFe(15)-CoFe(5)-Cu(10)-CoFe(5)-NiFe(15)-Ta(5)
- Measure curve with Looper: Didn't look great…no data collected

7) SV layer anneal DATE: 12/16/2010

- Job: Wendy_ann_180C
- Recipe: Ar_5torr_Wendy_200C
  - 5 Torr Argon for 10800 (2 ½ hours) seconds at 255°C (actually 200°C)
  - Ramp up: 10°C per minute, ramp down: 20°C per minute
- Measure with Looper: Skipped due to time.

8) SV layer photolith DATE: 12/17/2010

- Clean in automated washer/dryer (DO NOT ASH!)
- 5 min pre bake at 150C
- Pour 5 mL LOR 5A at 300 rpm (500 rpm/s) for 5 seconds, ramp at 1500 rpm/s to 2500 rpm for 45 sec (use dropper completely filled)
- Remove edge bead with EBR PG on Q-tip (NO ACETONE)
- Bad spin? Clean in Remover PG, IPA, 2 min H_2O wash, then dry. Ash if necessary.
- 5 min 150C bake
- Spin on SPR660, (210) 2200 rpm, 40 sec
- 60 s 95C bake
- Expose Stepper
  Job: SVWire
  Masks: SPINVALVE, FLOOD
  Level: BASE
  Exp.=165 mJ/cm^2
  Focus = 0
- 60 sec 95C bake
- Autodevelop 50 sec MF26A
- Comments:

9) SV Layer Etch Intelvac chamber DATE: 12/17/2010

- Clean wafer edge with Acetone; failure to clean edge makes it difficult for the wafer to fit on the stub resulting in the wafer cracking!

- Mount sample on 3" stub with dry chuck/vacuum for at least 5 minutes
- Pressure= 2.6e-4 Torr
- Ion beam etch:
  Angle = 15 °
  Ar flow = 7.5 sccm
  Time: 16.5 min

Property	**8 cm**
Cathode Filament Current	9.28
Discharge Current	0.31
Discharge Voltage	40
Beam Current	29
Beam Voltage	200
Accelerator Current	2
Accelerator Voltage	100
Neutralizer Emmissions Current	37
Filament Current	6.21

- Ultrasound in acetone for 10 min (DO NOT ASH)
- Remove residual LOR by 30 minute ultrasonic soak in PG Remover
- 2 min DI rinse
- Clean in automated washer/dryer
- Inspect: The SVs are barely visible on the gold, but the etch looks complete.

10) Read Line Photolith DATE: 12/17/2010

- Clean in automated washer/spinner (DO NOT ASH)
- 5 min pre bake at 150C
- Pour 5 mL LOR 5A at 300 rpm (500 rpm/s) for 5 seconds, ramp at 1500 rpm/s to 2500 rpm for 45 sec (use dropper completely filled)
- Remove edge bead with EBR PG (NO ACETONE)
- Bad spin? Clean in Remover PG, IPA, 2 min H_2O wash, then dry. Ash if necessary.
- 5min 150C bake
- Spin on SPR660, 2200rpm, 40 sec
- 60 s 95C bake
- Expose Stepper
  Job: SVWire
  Masks: READ
  Level: BASE
  Exp.=165 mJ/cm^2
  Focus = 0
- 55 sec 95C bake
- Autodevelop 55 sec MF26A
- Inspect: Looks good

11) Read Line Deposition DATE: 12/17/2010, Lesker E-Beam

- 4 min fast plasma clean (may not be good for SV)
- 5 nm Ti (2 Å/s)/200 nm Au (10Å/s) – skipped Ti cap because no nitride will be deposited on top of the read lines now
- Remove residual LOR by 30 minute ultrasonic soak in PG remover
- 2 min DI rinse
- Clean in automated spinner
- Inspect: OK
- Comments:

12) Via 1 Photolith DATE: 12/17/2010

- Auto spin on SPR660, 3200 RPM 40 sec
- 60 sec 95C bake
- Expose Stepper
  Job: SVWire
  Masks: VIA, FLOOD
  Level: BASE
  Exp.=165 mJ/cm2
  Focus = 0
- 60 sec 95C bake
- Autodevelop 60 sec MF26A
- Inspect: looks good

13) Via Etch DATE: 12/17/2010

- Axic etcher, Recipe JM_Nitride
- Alighn Laser on open die
- 2 sccm O_2, 42 sccm CF_4, 75 W, -200 V
- Etch Time: 16 min (used laser)
- Clean with Ace/IPA/N2 and automated washer/dryer
- Comment: the silicon rich nitride took longer to etch than normal.

14) Passivation Layer Photolith: 12/19/2010

- 5 min pre bake at 150C
- Start spinner and pour 5 mL LOR 5A at 300 rpm (100rpm/s) for 5 seconds, ramp at 1000 rpm/s to 2500 rpm for 45 sec (use dropper completely filled)
- Remove edge bead with EBR PG (NO ACETONE)
- Bad spin? Clean in Remover PG, IPA, 2 min H_2O wash, then dry. Ash if necessary.
- 5min 150C bake
- Spin on SPR660, 2200 rpm, 40 sec
- 60 s 95C bake
- Expose Stepper

  Job: SVWire
  Masks: PASS
  Level: BASE
  Exp.=165 mJ/cm^2
  Focus = 0
- 60 sec 95C bake
- Autodevelop 50 sec MF26A
- Comments: This step needs to be optimized. The exposure or development time is not correct and there is hanging PR on the wafer. The location of this PR is not detrimental to the device, so I'll go ahead to the next step due to time.

13) Passivation Layer SiN_x Deposition DATE: ?, Intelvac chamber

- 100 nm SiN_x Rate 2.75 nm/min
- N_2 flow = 8 sccm, Ar = 18.5 sccm 2 mTorr N_2, Ar added until 5mTorr total

  Time 37 min
- Measure thickness: only 67 nm due to failure of neutralizer filament
- Inspect: bluer than normal, but insolating. Peeled where PR was left

==============================

Start Date: 6/24/2010

Substrates: 3" Mechanical Si, 300 nm SiN_x
Film ID: N/A
Comments: The purpose of this wafer is to create a PDMS mold for svwire 2, 3, 4, 5, and 6

1) Microfluidic Channel Photolith: 41 micron SU-8 2025
DATE: 6/24/2010

- 3 min O_2 ash
- Clean wafer with ace/IPA
- Dehydrate on hot plate for 2 min at 100°C
- Spin on SU-8-2025 (Recipe #3):
  - o Ramp to 500 rpm at 100 rpm/sec, should take 5 sec
  - o Ramp to 2000 rpm at 300 rpm/sec; spin at 2000 rpm for 30 sec
  - o Let sit for 2 minutes
- Remove edge bead with SU-8
- Check that back is clean
- Bake 2 minutes at 65ºC, then slowly ramp to 95ºC
- Bake 5 minutes at 95ºC
- Turn off heat plate and let cool to 50ºC (this takes 13 minutes)
- Expose with Carl Suss Mask Aligner for 50 seconds (SU Channel 4 inch mask)
- Bake 1 minutes at 65ºC, then slowly ram to 95ºC

- Bake 3 minutes at 95ºC
- Turn off heat plate and let cool to 50ºC
- Develop: 5 min with periodic agitation
- Rinse with SU-8 developer for 15-30 seconds
- Rinse with IPA (check for no white fuzz)
- Blow dry
- Inspect: Some minor cracking and webbing near inlets
- Measure thickness: 39.9 µm

2) Teflon-like coating (optional)

3) PDMS Date: 6/28/2010

- Set oven to 60 ºC
- Clean the petri dish if it is dirty
- Wear gloves
- Using a metal boat, measure out 4 grams of the viscous base (avoid causing big bubbles)
- Using a pipette, add 0.4 grams (~ 500 µL) of the liquid curing agent to the base (1:10 base to curing agent ratio)
- Gently stir the base and curing agent together. Try to avoid creating big bubbles.
- Let it sit for 20 minutes to allow all the small bubbles to dissipate
- Gently pour onto the wafer/SU-8 mold. The uncured PDMS will spread out evenly onto the wafer after 5-10 minutes
- Cure in the 60 ºC oven for 304 hours (it may be left overnight)
- Wearing gloves to keep the PDMS clean, gently peel the PDMS off the wafer mold. Cut/slice as necessary.
- Punch holes with 14 G blunt needle
- To clean PDMS, use scotch tape then plasma (1 min) or rinse with Ace/IPA/DI H_2O (don't soak!!!)

SVWIRE Stepper Parameters

Job Name: SVWIRE (in Moreland directory)
Settings for the Stepper

Wafer Layout

- **Alignment Marks**

Item	Value
Number of Primary Marks	2
Field by Field Alignment	NO
Mark Clear Out	Yes

- **Cell Structure**

Item	Value
Cell size	30 x 30
Clearance	R 2 F 0
Wafer Cover	Inner
Min Hor Rect	
Min Ver Rect	
S-Mark to Cell Shift	
Placement Mode	Computer
Matrix Shift X	
# Inner Cells	92
#Edge Cells	0
#Total Cells	92
Next Placement	NO

- **Image Definition**

Item	Value
Image Number	PM
Image ID	ALIGN
Reticle Image	2.065 2.065
Reticle shift	0 0
Masking window	3 x 3
Masking window shift	0 0
Next Image	Yes

Item	Value
Image Number	1
Image ID	BASIC
Reticle Image	30 30
Reticle shift	0 0
Masking window	30 30
Masking window shift	0 0
Update Layers	Yes
Next Image	No

- **Image Distribution**

Item	Value
Cell Indexes	* *
Image Number	1
Image ID	BASIC
Action	Insert
Image to Cell Shift	0 0
Next Image	N
Next Cell	Yes

Item	Value
Cell Indexes	0 10
Image Number	1
Image ID	BASIC
Action	Delete
Image to Cell Shift	0 0
Next Image	N
Next Cell	N

- **View Wafer Layout**
- **Set Graphics**

Layer Layout

- **Process Data**

Item	Value
Number of Layers	1
Layer Selection	0
ID:	
Optical Pre-Alignment	N
Global Wafer align	N
Global Reticle Align	N
Field by Field	Y
Layer Shift	0
Next Layer	Y

Item	Value
Number of Layers	1
Layer Selection	1
ID:	1
Optical Pre-Alignment	Y
Global Wafer align	N
Global Reticle Align	N
Field by Field	Y
Layer Shift	0
Next Layer	

- **Reticle Data**

Item	Value
Layer Selection No.	1
Image Selection No.	PM
Expose Image	Y
Reticle ID	ALIGN
Reticle Image Size	35 35
Masking Window Size	35 35
Energy	165
Focus Offset	0
Next Image	---
Next Layer	Y

Item	Value
Layer Selection No.	1
Image Selection No.	1
Expose Image	Y
Reticle ID	WRITE
Reticle Image Size	35 35
Masking Window Size	35 35
Energy	165
Focus Offset	0
Next Image	N
Next Layer	Y

Item	Value
Layer Selection No.	2
Image Selection No.	1
Expose Image	Y
Reticle ID	NITRIDE
Reticle Image Size	35 35
Masking Window Size	35 35
Energy	165
Focus Offset	0
Next Image	N
Next Layer	Y

Item	Value
Layer Selection No.	3
Image Selection No.	1
Expose Image	Y
Reticle ID	SPINVALVE
Reticle Image Size	35 35
Masking Window Size	35 35
Energy	165
Focus Offset	0
Next Image	N
Next Layer	Y

Item	Value
Layer Selection No.	4
Image Selection No.	1
Expose Image	Y
Reticle ID	READ
Reticle Image Size	35 35
Masking Window Size	35 35
Energy	165
Focus Offset	0
Next Image	N
Next Layer	N

Sample 6

Start Date: 11/10/2010
Substrates: 3“ Si mechanical wafer with SiO_2
Film ID: Sample 6
Die Size: 15 mm x 12 mm, SVWIRE 4

1) SV Deposition: DATE: 11/10/2010 MT Sputter Chamber, *Base Pressure 6e-9 Torr

- Calibrate targets for at least 100 seconds
- Flat aligned to #3 on chuck (align #1 in chamber)
- Argon gas purifier on
- 220 Oe parallel to flat

Target	**Rate (Å/s)**	**Gas (sccm)**	**Power (W)**
Ru	0.73	19.0	150
CoFe	0.38	15.0	100
Cu	1.33	15.0	100
IrMn	0.91	20.0	100
Ta	0.83	15.0	150
NiFe 80/20	1.10	15.0	250

- Recipe: Ta(5)-Cu(5)-IrMn(10)-NiFe(15)-CoFe(5)-Cu(10)-CoFe(5)-NiFe(15)-Ta(5)
- 78 nm total stack thickness
- Measure curve with Looper.

2) SV layer anneal DATE: 11/20/2010

- Job: Wendy_ann_180C
- Recipe: Ar_5torr_Wendy_180C
  - 5 Torr Argon for 10800 (2 ½ hours) seconds at 235°C (actually 180°C)
  - Ramp up: 10°C per minute, ramp down: 20°C per minute
- Measure with Looper:

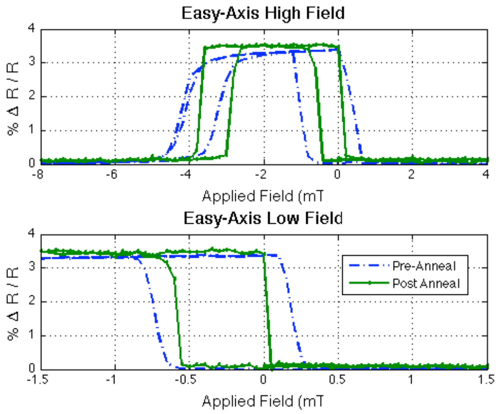

3) Align Photolith DATE: 11/21/2010

- Notes: It is important to put down the alignments independent of the first mask layer. The alignment will be off if both the PM and layer 1 are exposed at the same time.
- Auto spin on SPR660, 3200 RPM 40 sec
- 60 sec 95C bake
- Expose Stepper
  Job: SVWire
  Masks: ALIGN
  Level: BASE
  Exp.=165 mJ/cm2
  Focus = 0
- 60 sec 95C bake
- Autodevelop 60 sec MF26A
- Inspect: OK

4) Alignment Mark Etch DATE: 11/21/2010, Intelvac chamber

- Clean wafer edge with Acetone; failure to clean edge makes it difficult for the wafer to fit on the stub resulting in the wafer cracking!
- Mount sample on 3” stub with dry chuck/
- Pressure= 2.63 x 10^{-4} Torr
- Ion beam etch:
  Angle = 15°

Ar flow = 7.5 sccm,
Time: 16 min

Property	8 cm
Cathode Filament Current	9.28
Discharge Current	0.30
Discharge Voltage	40
Beam Current	30
Beam Voltage	200
Accelerator Current	2
Accelerator Voltage	100
Neutralizer Emmissions Current	37
Filament Current	6.07

- 3 min O_2 ash at 60 W to remove top burnt layer
- Rinse with acetone, IPA, and spin-dry
- Wash with automated washer
- Inspect:

5) SV layer photolith DATE: 11/21/2010

- Rewash with automated spinner
- 5 min pre bake at 150C
- Pour 5 mL LOR 5A at 300 rpm (500 rpm/s) for 5 seconds, ramp at 1500 rpm/s to 2500 rpm for 45 sec (use dropper completely filled)
- Remove edge bead with EBR PG (NO ACETONE)
- Bad spin? Clean in Remover PG, IPA, 2 min H_2O wash, then dry. Ash if necessary.
- 5 min 150C bake
- Spin on SPR660, (210) 2200 rpm, 40 sec
- 60 s 95C bake
- Expose Stepper

  Job: SVWire
  Masks: SPINVALVE, FLOOD
  Level: BASE
  Exp.=165 mJ/cm^2
  Focus = 0
- 60 sec 95C bake
- Autodevelop 50 sec MF26A

6) SV Layer Etch Intelvac chamber
DATE: 11/21/2010

- Clean wafer edge with Acetone; failure to clean edge makes it difficult for the wafer to fit on the stub resulting in the wafer cracking!
- Mount sample on 3” stub with dry chuck/
- Pressure = 2.65 e-4 Torr
- Ion beam etch:

  Angle = 15 °
  Ar flow = 7.5 sccm
  Time: 16.5 min

Property	8 cm
Cathode Filament Current	9.26
Discharge Current	0.31
Discharge Voltage	40
Beam Current	29
Beam Voltage	200
Accelerator Current	2
Accelerator Voltage	100
Neutralizer Emmissions Current	37
Filament Current	6.15

- 30 min ultrasound in acetone
- Remove residual LOR with 60 minute ultrasonic soak in PG Remover
- 2 min DI rinse
- Wash in automated washer/dryer
- Inspect: Looks ok

7) Read Wire Photolith DATE: 11/22/2010

- Rewash in automated washer/dryer
- 5 min pre bake at 150C
- Pour 5 mL LOR 5A at 300 rpm (500 rpm/s) for 5 seconds, ramp at 1500

rpm/s to 2500 rpm for 45 sec (use dropper completely filled)

- Remove edge bead with EBR PG (NO ACETONE)
- Bad spin? Clean in Remover PG, IPA, 2 min H_2O wash, then dry. Ash if necessary.
- 5min 150C bake
- Spin on SPR660, 2200rpm, 40 sec
- 60 s 95C bake
- Expose Stepper

  Job: SVWire
  Masks: READ
  Level: BASE
  Exp.=165 mJ/cm^2
  Focus = 0

- 55 sec 95C bake
- Autodevelop 55 sec MF26A
- Inspect:

8) Read Wire Deposition DATE: 11/22/2010 Lesker E-Beam

- 5 min fast plasma clean
- 5 nm Ti (2 Å/s)/200 nm Au (10Å/s)
- Remove residual LOR by 30 minute ultrasonic soak in PG Remover
- 2 min DI rinse
- Wash in automated washer/dryer
- Inspect: Middle die are bad; problem with auto-PR systems

APPENDIX E: Microfluidics Standard Operating Procedure (SOP)

Date Last Edited: 08/24/2010
Authors: Bruce Han & Wendy Altman

Loading the Syringe – this is the basic procedure to load a syringe with fluid. The main objective of this is to prevent getting air bubbles in the syringe. These decrease accuracy of measurements.

- Put a red tip on the edge of the syringe tube. This red tip will lock with the MFC probe.
- Dip the red tip and the tube together in the desired solution to test.
- Slowly pull the plunger up, allowing time for the pressure to reach equilibrium and bring up the fluid. This takes more time than usual because the fluid has to travel through such a small tube.
- Once the desired volume inside the barrel is achieved, take the tips out of the solution and turn the syringe upside down (facing upward). Flick the barrel a few times or shake the syringe to get all of the air bubbles to float to the top. From there, push the plunger in a little bit to push all of the air bubbles up through the tube and into the atmosphere. The tip will leak a little bit, so make sure if the solution is hazardous to discard properly.
- The syringe is loaded when there are no more air bubbles in either the tube or the barrel of the syringe.

Setting up the Testing Apparatus – this procedure explains how to set up the probe and the chip on the MFC microscope.

- Verify that the isolation table is on.
- Load the microfluidic chip onto the MOKE platform. If possible, turn on the vacuum.

- With the syringe prepared, the system can now be assembled. Attach the tip of the syringe to the blue probes by twisting the red cap into the red import valve in the Microport interface. Twist to its snug, but do not force too hard in risk of breaking it.
- Attach the syringe to the syringe pump. See below for syringe pump protocol.
- With the syringe properly loaded in the syringe pump, position the blue microfluidic probe near the platform so that the tip of the probe is near the inlet of the chip. Lock the magnetic probe onto the steel plate.
- Looking through the microscope, use the X-Y-Z adjustment knobs located on the base of the probe to position the probe directly over the inlet on the chip.
- Once the tip of the probe is directly over the inlet of the chip, begin to lower the Microport interface onto the inlet by turning the Z-adjustment knob located on the top of the probe while looking through the microscope. Watch for the movement of the touchdown indicators on the Microport interface tip seal (three plastic tips on the seal). Once the touchdown indicators have moved back, continue to turn the Z-axis knob approximately one and a half turns past the initial touchdown point to seal the Microport interface against the microfluidic chip.
- **Note: the inlet of the channel is significantly larger than the channel, and movement through the channel will not flow until that well is full. To speed up filling of the inlet, use a flow rate of 2 µL/sec.**

<u>Syringe Pump</u> – In order to have extremely precise control over how much and at what rate fluid is pumped into the channel, a syringe pump is used. The syringe pump is calibrated to the type and size of syringe that is being used and thus can give very accurate and precise control over flow rate and volume of fluid being inserted.

- Turn the syringe pump on. The "ON" switch is located in the back of the pump. When turned on, the analog box will read "Power Failed." Click *Select*.
- To calibrate the machine to the particular syringe being used, click *Select*. A menu should appear on the analog box. Use the arrow buttons to get to the option "Table." Click *Select* to select a menu option. From here, use the arrow keys to find the particular syringe being used in

the experiment, starting with the company name and then the size/diameter of the specific model. Click *Select* to select each choice.

- Once the proper syringe is selected, the volume and the rate can be selected using the same arrow keys and the number pad. Use the arrow keys to change to the desired units as well. When finished, press the *Enter* key next to the number pad.
- To load the syringe into the pump, first release the clutch. This is the knob on the top of the movable part of the apparatus. Turn the knob CCW disengage the clutch and CW to engage it again (It is counter intuitive but the knob feels tight when turned CCW to disengage the pump, and conversely it feels very loose when turned CW and the pump is engaged). When the clutch is disengaged, the movable part (the part that actually presses on the syringe) should be free to move. Move to the desired position.
- Loosen the grips on both the stationary part and the movable part of the syringe pump that hold the syringe in place.
- Place the syringe into the pump. The top of the barrel of the syringe should slide into the little grip at the end of the stationary part, holding the tip so it cannot move. The syringe should fit into the "V" cup and the holder (held by a spring) should clamp down on the syringe. Attach the top of the syringe (the plunger) to the movable part. Slide the top of the plunger into the grip. Tighten both grips gently to the point that the syringe is not easily movable.
- Reengage the clutch by twisting it CW.
- Once everything is set and ready to go, the pump can be started by pressing the *Run/Stop* button. This button also stops the pump at any time.
- **Note: Do not set the volume on the syringe pump over the volume of liquid that is actually in the syringe. This could result in the pump continuing to force the plunger into the barrel of the syringe after the syringe is completely empty. This could damage the syringe beyond repair.**
- The rate can be changed at any time by clicking the *Select* button and using the arrow keys to reach the rate menu. Change it the exact same way as before. When *Enter* is pressed, the rate should change instantaneously.
- Once done, flush out the syringe and turn the pump off.

Cleaning Microport Interfaces – The Microport interface wetted materials consist of PEEK, medical grade silicone and platinum.

- After each use and prior to storing, flush the Microport interfaces with a filtered and dilute solvent to prevent clogging. Standard cleaning procedures compatible with capillary tubing and Microport interface materials are also acceptable.
- In order to avoid the collection of contaminates in your Microport interface, it is safe to clean the Microport interface with an ultrasonic bath or autoclave device. As with any fluid receptable, you may notice a deviation in your experiment results over time that may be caused by a buildup of contaminates in your Microport interface (even with regular cleaning). In this event, you will need to replace the Microport interfaces.
- To clean microport seal, raise the microport and gently wipe using a nonfibrous swab dipped in water or IPA while observing through the microscope.